Computer-Assisted Diagnosis and Therapy Planning in Coronary Artery Disease Based on Cardiac CT and MRI

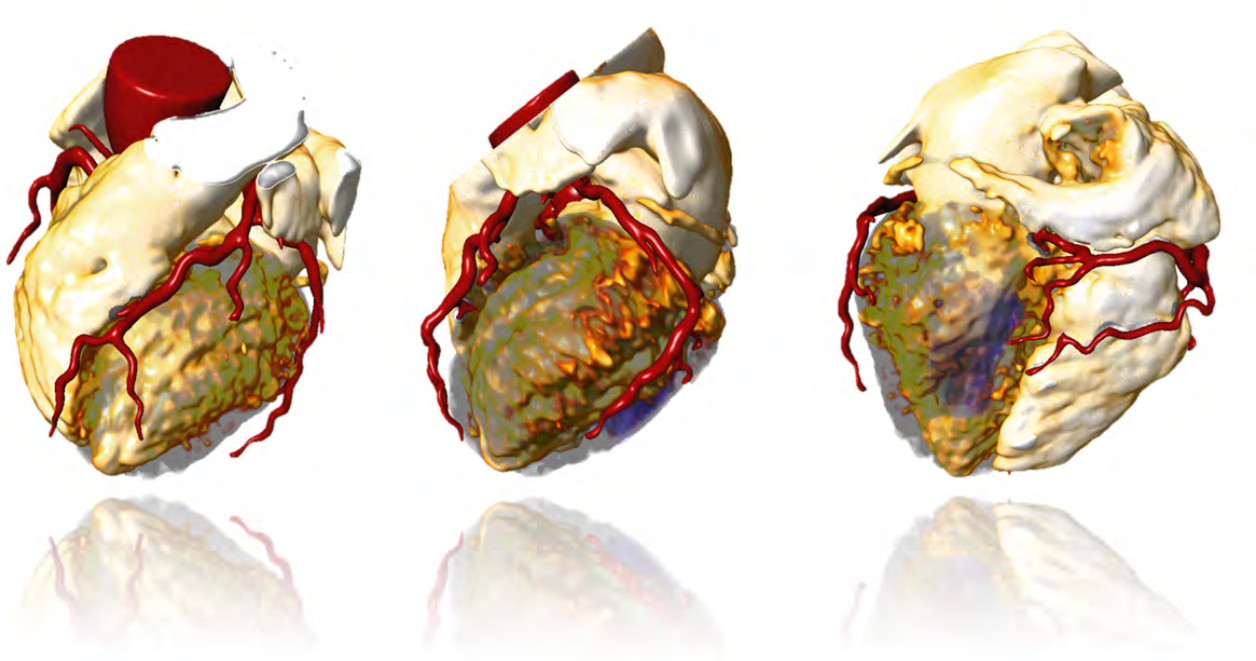

Anja Hennemuth

Fraunhofer MEVIS

A thesis submitted for the degree of

Dr.-Ing.

August 31, 2012

1. Reviewer: Heinz-Otto Peitgen

2. Reviewer: Bernhard Preim

Day of the defense: Friday, August 31, 2012

Abstract

State-of-the-art imaging with CT and MRI allows the acquisition of image data for the evaluation of coronary pathologies, myocardial perfusion, detection of infarctions and myocardial function. Thus, information about the cause, effect and potential progression of coronary artery disease is available. The interpretation of the available image data is a difficult task due to the differences in coverage, resolution and contrast types. The goal of the presented work was the development and evaluation of a set of image processing methods to support this task. These methods include registration methods for the alignment of different datasets as well as compensation methods for the motion, which is caused by breathing or myocardial contraction. Other image processing tasks are the segmentation of the coronary arteries and the classification of the myocardium according to its viability status. The proposed methods are integrated into clinically applicable software prototypes and evaluated with phantom and animal datasets as well as with data from clinical routine. The results show a clear benefit for the diagnosis and therapy prognosis of CAD patients based on CT and MRI image data.

Acknowledgements

The evolution of this dissertation is based on a series of coincidences, key events and encounters. I would like to thank all the people who contributed and made this thesis possible.

First of all, I would like to express my sincere gratitude to my supervisors. I want to thank Prof. Heinz-Otto Peitgen for creating the unique working environment at MeVis, and for providing me with the freedom that enabled the development of the ideas this thesis is based on. Prof. Bernhard Preim has always been open for discussions, joint projects and his encouragement and support was of invaluable assistance to me.

There are many colleagues and project partners, who contributed not only through their scientific input, but also through the enjoyment of common work. Particular thanks are given to my former coworkers Dr. Ola Friman, Caroline Kühnel, and Dr. Tobias Boskamp as well as to Dr. Steffen Oeltze from the AG Vis at University Magdeburg for the fruitful cooperation and support. Furthermore, I want to thank the colleagues, whom I worked with while I was writing this thesis, namely Markus Hüllebrand, Johann Drexl, Lennart Tautz, Michael Schmidt, Dr. Darko Ojdanic, Daniel Demedts and Michael Schwenke for being so understanding and supportive. Dr. Tobias Böhler and Dr. Stefan Wirtz gave valuable input for the design of the implemented registration approaches. I thank Dr. Felix Ritter, Christian Schumann and Christian Rieder for their help with the fused visualizations. I also want to express my gratitude to Daniel Rinck, Dr. Michael Scheuering, Dr. Michael Sühling and Dr. Dominik Bernhard from Siemens CT for the collaboration in the VICORA and Circulation project.

I owe sincere gratitude to the clinical partners, who contributed to this thesis. The collaboration with the partners in the VICORA project inspired most of the work presented here. My sincere thanks go to Prof. Stephan Miller, Dr. med.

Achim Seeger, PD Dr. med. Ulrich Kramer and Dr. med. Bernhard Klumpp from University Hospital Tübingen for the great cooperation in the invaluable input regarding MRI image data. I want to thank Prof. Andreas Mahnken from University Hospital Aachen for the continuous collaboration on the analysis of cardiovascular CT data, the provision of the valuable image data, and the encouragement to write this thesis. Furthermore, I am very grateful for the cooperation with PD Dr. med. Hatem Alkadhi, Dr. med. Paul Stolzmann and Dr. med. Olivio Donati, who provided me with valuable data as well as discussions regarding interaction and data presentation.

There are several people who were not directly involved in the creation of this thesis but inspired and motivated me in important situations of my career path. I want to thank Dr. Werner Cherdron from Karlsruhe Institute of Technology and my former mentor Prof. Bernd Becker from University Freiburg for their encouragement towards an academic career. Prof. Ingrid Schirmer from University Hamburg has been an inspiring example with her never-ending energy and enjoyment of life and her scientific work. For their encouraging remarks regarding my scientific work, I want to thank Dr. Jan Klein, Dr. Jürgen Weese, Dr. Thomas Netsch, Prof. Johan H. C. Reiber and Prof. Boudewijn P. F. Lelieveldt.

I am very grateful for the support of my parents and my friends, who tolerated the shortage of time I could dedicate to them and were always understanding. I particularly thank Sonja, Felix, and Heike for their patient encouragement to finish this document.

Last but not least, I owe my deepest gratitude to my husband Jan-Martin who supported me in all possible ways.

Contents

1

Introduction

The improvement of living conditions and medical care in the western world during the last century has resulted in a notable extension of life expectancy. This process was accompanied by a change of the leading causes of death from infectious diseases toward chronic diseases [Centers for Disease Control and Prevention (CDC), 2003]. Alongside with cancer and stroke, coronary artery disease is one of the most common diseases in the aging society. According to statistics of the World Health Organization (WHO), it caused more than 20% of all deaths in the high-income countries of the world in 2008 [World Health Organization, 2011].

In coronary artery disease, pathological changes of the vessel walls, so-called vessel plaque, can cause narrowings of the vessel lumen. If this hinders the blood flow in such a way that the heart muscle (myocardium) can not be supplied with sufficient oxygen, the muscle tissue starts to degenerate. This is very dangerous, because the heart muscle is the central pump that sustains the blood circulation through the body, and myocardial dysfunctions can result in deathly heart attacks.

Heart muscle tissue does not regenerate. It is thus the major goal to prevent heart muscle damage through insufficient blood supply by means of so-called revascularization therapies. These therapies aim at re-establishing blood supply through surgical insertion of bypass vessel segments or re-widening the vessel lumen at the location of the narrowing, the so-called stenosis.

The preceding diagnosis and therapy planning is a complicated process, because it requires to determine location and relevance of vessel stenoses. The standard method for the inspection of stenoses is the conventional X-ray angiography. This procedure requires the

insertion of a catheter into the vascular system via an incision in the lumbar region. The catheter allows to deliver contrast agent into the artery branch of interest and to measure the vessel diameter in projection images acquired with X-ray imaging. Catheters also allow to determine the pressure drop caused by the stenosis (fractional flow reserve FFR), and recent studies have shown that this parameter is a better indicator for the necessity of an intervention than the diameter change of the lumen [Pijls et al., 2010].

The progress in medical imaging technology during the last 20 years has also made it possible to perform examinations of the coronary arteries supplying the heart muscle as well as the heart muscle perfusion with non-invasive imaging technologies. Computer tomography (CT) scanners nowadays provide volumetric image data with a resolution of less than 0.5 mm^3. Based on these image data coronary artery stenosis can be detected almost as reliably as with conventional catheter angiography. Furthermore it is possible to assess pathological vessel wall changes [American College of Cardiology Foundation Task Force on Expert Consensus Documents, 2010b, Miller et al., 2008]. On the other hand, nuclear imaging technologies like PET and SPECT as well as magnetic resonance imaging (MRI) are suited to provide information on metabolism, perfusion and viability state of myocardial tissue [Mastouri et al., 2010, Greenwood et al., 2012]. It is thus possible to acquire image data that allow detection and relevance assessment of stenoses non-invasively and additionally provide information about the tissue state. However, unlike in local catheter measurements, where anatomical and functional assessment of a stenosis are performed locally in direct succession, the assessment of the non-invasively acquired data is not straightforward. The detection of coronary artery stenoses requires the extraction of the vascular tree from the volumetric image data as a basis for advanced visualizations and measurements. The assessment of the heart muscle perfusion is also based on a segmentation of the myocardium and an advanced analysis of the dynamic image information. Approaches exist for the analysis of the image data from each of the different modalities, but the combination of these data, which is required for a profound therapy decision, is still an open problem. Data is acquired with different reference systems, coverage and intensity distributions, and it is thus not a trivial task to determine the spatial relations between datasets from different image modalities correctly. One approach to overcome this problem is the introduction of hybrid imaging systems like PET-CT or SPECT-CT scanners. These allow the direct combination of anatomic and functional image data acquisition. Another concept for the comparison of different types of image-based cardiac findings is the 17-segment model recommended by

the American Heart Association (AHA) [Cerqueira et al., 2002]. This model provides a standardized segmentation of the coronary arteries and the myocardium as well as a scheme to relate myocardial segments to supplying vessel segments. It is widely used although it has been shown that the assumed segment relations are inadequate for about 23% of all patients [Ortiz-Perez et al., 2008].
To overcome these limitations, it is desirable to provide image processing methods, which allow the fusion of the different types of non-invasively acquired cardiac image data in order to facilitate the inspection of the patient-individual relations of stenoses, undersupplied heart muscle tissue and already necrotic tissue. The inclusion of the tissue viability state allows to decide whether the treatment of a relevant stenosis would result in a benefit for the patient.

Because CT and MRI are nowadays widely available and evolving techniques, the presented work focuses on the analysis of cardiac MRI and CT data. The major goal of this work is the development of a method package, which supports patient-individual diagnosis and treatment planning in coronary artery disease. Essential tasks for this are the determination of the myocardial tissue state (task 1), as well as the correlation between artery stenoses and dependent tissue (task 2).

The differentiation between normally perfused, hypoperfused and non-viable tissue (task 1) can be achieved by a comparison of infarction and perfusion information. Reversibly defective tissue shows a perfusion defect but no infarction. Clinical studies have shown the importance of a classification that differentiates healthy, necrotic, and viable underperfused myocardium occurring in the so-called peri-infarct zone [Saeed et al., 2001, Yan et al., 2006]. Therefore, an advanced analysis of infarcted tissue [Yan et al., 2006] as well as the combined inspection of perfusion and late enhancement MR images [Tsukiji et al., 2006] have been proven suitable.

To address task 2, the spatial relation between the reversibly defective tissue area and the coronary arteries has to be inspected.

The required image processing can be grouped into alignment and analysis problems:

- Image Alignment
  - Alignment of the angiographic volume images, the late enhancement image, and the perfusion sequences.
  - Spatial alignment of the image slices in MR late enhancement datasets.
  - Temporal alignment of the image slices within the perfusion sequences.
- Image Analysis
  - Detection of the coronary artery tree in the whole-heart volume image.
  - Segmentation of infarcted tissue regions in late enhancement images.
  - Identification of underperfused tissue regions in the perfusion image sequences.

The purpose of this work is to develop, compile and validate methods that solve these problems.

To evaluate the applicability of the developed algorithms, all described approaches are integrated in software components, which allow different combinations of processing steps and the integrated visualization of results from all analysis methods. The software assistants composed from these components are applied to different combinations of CT and MRI datasets by experienced radiologists. The results are compared with those achieved with reference methods to evaluate the benefit of the proposed methods for an accurate assessment of the relevance of stenoses and the state of the supplied tissue.

The outline of this work is as follows: Chapter 2 gives an introduction to anatomy and function of the heart. It describes the characteristics of the CT and MR image data that form the basis for this work. Chapter 3 covers existing and proposed methods for the alignment of sparse cardiac images. Chapter 4 discusses existing image analysis approaches and presents the newly developed techniques. This includes coronary artery segmentation methods, the detection of perfusion defects in MR perfusion sequences and the detection of infarctions in late enhancement CT and MR images. Chapter 5 presents and discusses the software components and the workflows for the clinical applications. Three studies are presented, which evaluate the benefit of the proposed methods in comparison with conventional methods. Two criteria are applied for these evaluations: the accuracy in the detection of pathologies and the benefit of the combined analysis. The accuracy of the provided analysis methods

in the identification of the diseased tissue region of the heartmuscle is compared to standard techniques as well as manual analysis. For the assessment of the benefit regarding the determination of the correspondences between defective myocardial tissue and the culprit coronary artery branch, results based on fused visualizations are compared with those based on the application of the AHA segment model as well as those based on side-by-side inspection of the image data.

2

Medical Background

This chapter provides an overview of the clinical problems addressed in this thesis. After a brief introduction into anatomy and function of the heart, the problems caused by coronary artery disease are explained. Section 2.3 describes the application of CT and MR imaging for the assessment of coronary artery disease and the problems in the analysis of these data the work in this thesis is concerned with.

2.1 Anatomy and Function of the Heart

The heart is the central organ responsible for the circulation of blood through the body. It is located in the thorax above the diaphragm and between the lungs as shown in Figure 2.1. The heart connects the pulmonary circulation with the blood circulation through the body. The right heart collects the deoxygenated venous blood from vena cava inferior and vena cava superior and pumps it into the lungs. The oxygenated blood from the lungs enters the left heart via the pulmonary vein. From the left ventricle it is pumped into the aorta and distributed in the whole body, where the oxygen is consumed.

The contraction that ejects the blood into the pulmonary artery and the aorta is triggered by electric impulses. Starting from the sinus node, these impulses are propagated to the ventricles via the AV-node. They can be measured via body surface electrodes and are usually represented as an electrocardiogram (ECG). Figure 2.2 shows a typical ECG. The impulse waves start when the heart muscle is relaxed. In this so-called diastolic phase, the valves between right ventricle and pulmonary artery as well as between the left ventricle and the aorta are closed. The blood enters the ventricles via the atriae. At the end of the diastolic phase, when the electric impulse arrives at the AV-node and the p-wave appears in

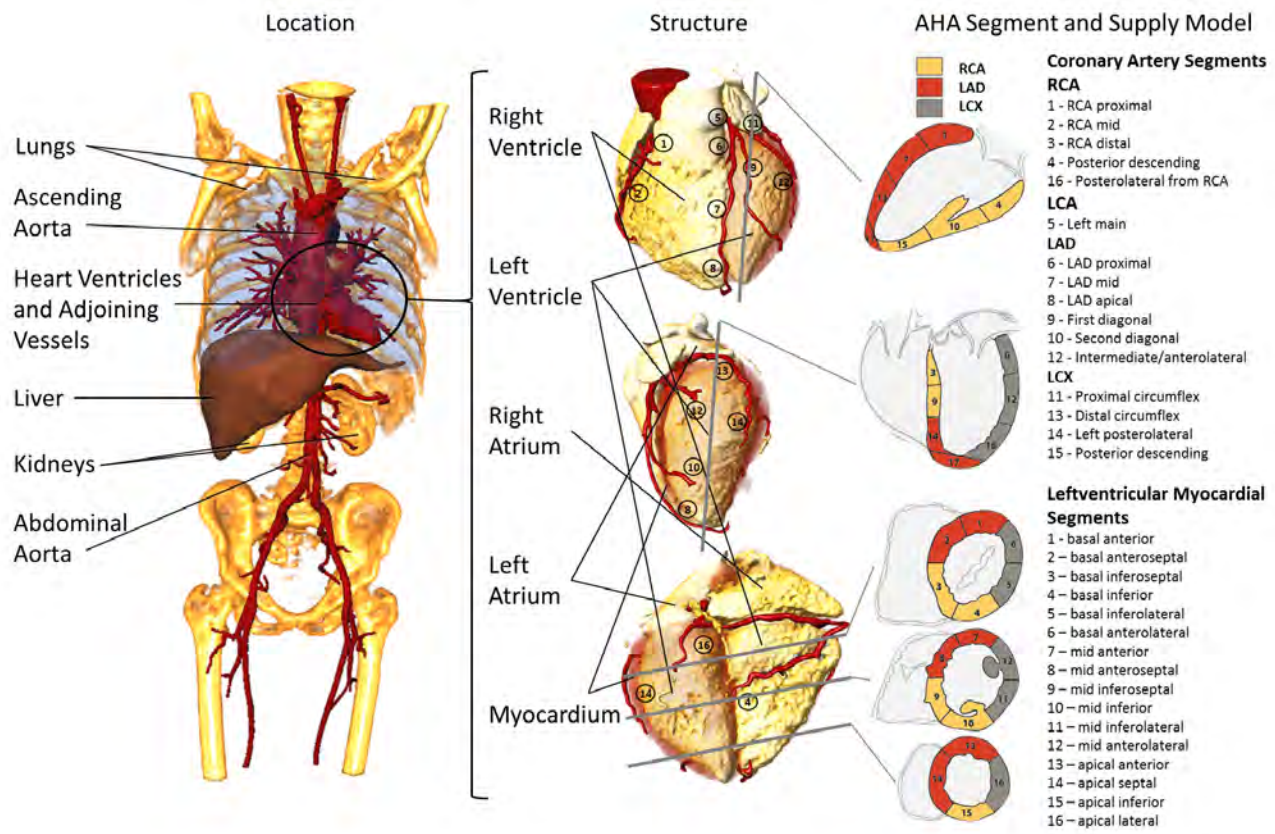

Figure 2.1: Location and anatomy heart. The heart is attached to the diaphragm above the liver and enclosed by the lungs and the ribcage. The middle row shows the heart and the coronary arteries. The American Heart Association has developed a standard model for the segmentation and labeling of coronary arteries and supplied regions in the left ventricular myocardium. The labels and the assumptions about the correlation of coronary branches and the supplied myocardial regions are described in the right columns (image data courtesy of Prof. S. Miller, University Hospital Tuebingen and PD Dr. med. H. Alkadhi, University Hospital Zurich).

the ECG, the atriae start to contract and thereby intensify the inflow into the ventricles. The AV-node is located at the transition between atriae and ventricles. After atrial contraction the atrial pressure drops. The atrioventricular valves float upward (pre-position) and close. In this phase, the ventricles contain the end-diastolic maximal volume (EDV). The arrival of the electric impulse at the ventricle is marked by the so called QRS-complex in the ECG. The heart muscle contracts rapidly, and the increased pressure in the ventricle exceeds the pressure in the pulmonary artery and aorta. This results in the opening of the valves and the ejection of blood into pulmonary and body circulation.

Approximately 200 ms after the start of the ventricular contraction, the T-wave appears

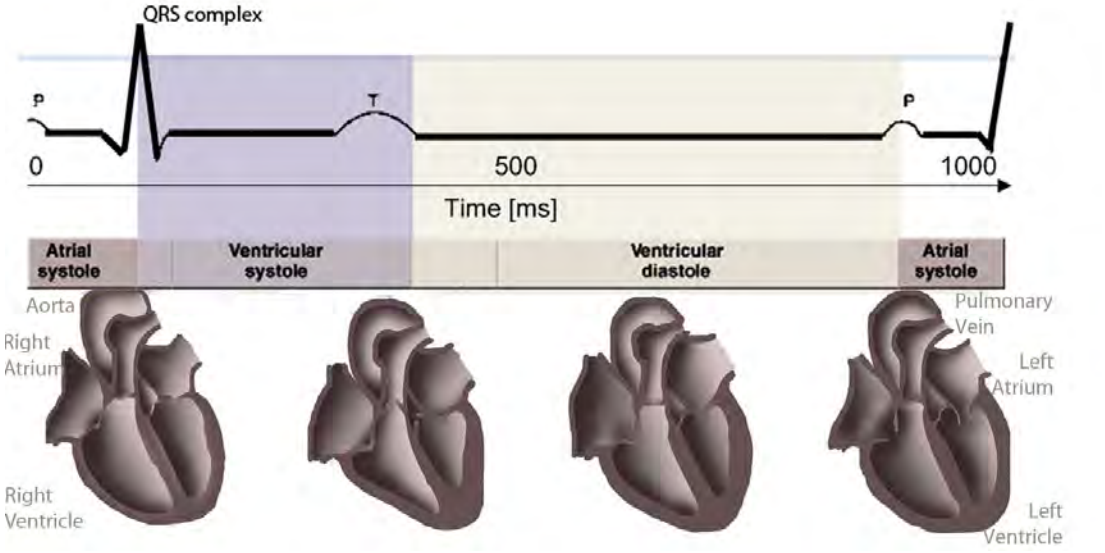

Figure 2.2: The heart cycle phases and the electrocardiogram: The curve represents the ECG signal, the images below depict the corresponding contraction phases of the heart muscle and blood flow.

in the electrocardiogram. The pressure in the atriae increases due to the consistent venous return of oxygenated blood from the lungs and deoxygenated blood from the systemic circulation. The heart muscle starts to relax and the ventricular pressure falls below the pressure in the adjoining vessels making the aortic and pulmonary valve close abruptly. The phase when all valves are closed is called end-systole and the end-systolic volume (ESV) is another important diagnostic parameter. The difference between the EDV and the ESV is the stroke volume.
When the atrial pressure finally exceeds the ventricular pressure, the atrioventricular valves open and the rapid filling phase begins.

The heart muscle itself is supplied by the coronary arteries. The coronary arteries branch off the aorta shortly after the aortic valve. Figure 2.1 shows the typical branching structure of the coronary tree. The assumption of a standard branching scheme was used by the AHA to develop a segment model for the arterial supply territories of the myocardium as shown in Figure 2.1 [Cerqueira et al., 2002]. This model is widely used to relate myocardial and arterial findings from different cardiac examinations. Studies have shown however that these standardized assumptions are not applicable to all patients [Pereztol-Valdes et al., 2005].

Figure 2.3 depicts the structure of the heart wall that is built up in layers. The endothe-

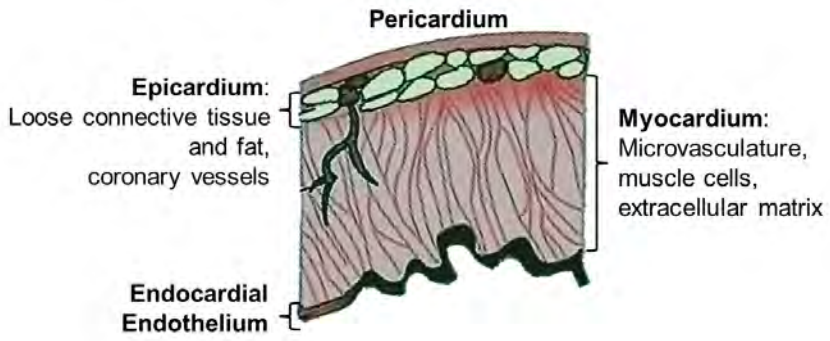

Figure 2.3: Layers of the heart muscle. The myocardium, which contains the myocytes that perform the contraction is separated from the blood pool by a layer of endothelium. The epicardium on the outer side of the myocardium consists of loose connective tissue and fat. It embeds the coronary vessels, which branch into the myocardium.

lial cells at the endocardial surface form the blood-heart-barrier. Normal heart muscle tissue contains different types of cells such as cardiomyocytes, endothelial cells, and fibroblasts. The cardiomyocytes, which accomplish myocardial contraction, amount to 75 % of myocardial volume and 49 % of the number of cells in healthy tissue [Brutsaert, 2003]. The endothelial cells play an important role in the cardiovascular regulation [Furchgott and Vanhoutte, 1989]. The cells of the vascular endothelium regulate the vessel diameters and thereby control the heart muscle perfusion. Fibroblasts synthesize the proteins of the connective tissue and perform the crucial tasks in wound healing. The myocardial cells are located within connective tissue. The so-called *Extracellular Matrix*, consists of laminin, fibronectin, elastin, and collagen. The myocardial collagen is a fibrillar protein that maintains tissue structure. Elastin fibers enable tissue stretching. Laminin proteins form networks of web-like structures and bind other components such as collagen fibers. Fibronectins are glycoproteins. They can bind cells to collagens and facilitate the movement of cells, e.g., during wound healing processes.

2.2 Coronary Artery Disease

As coronary artery disease (CAD) is one of the main causes of death in the western world, diagnosis and therapy planning are tasks of high importance. In the course of this disease, pathologic processes cause the accumulation of plaque in the vessel walls. The mechanisms that lead to plaque formation (atherogenesis) are very complex and subject to current re-

search. Atherogenesis is triggered by bacterial products or other risk factors and starts with a transmigration of leukocytes to the inner vessel wall surface. The leukocytes influence the behavior of smooth muscle cells as well as molecules with lipid content. Inflammation causes smooth muscle cells to migrate from the tunica media into the intima, where they secrete matrix metalloproteinases (MMP) (Fig. 2.4). The MMPs are enzymes that modulate

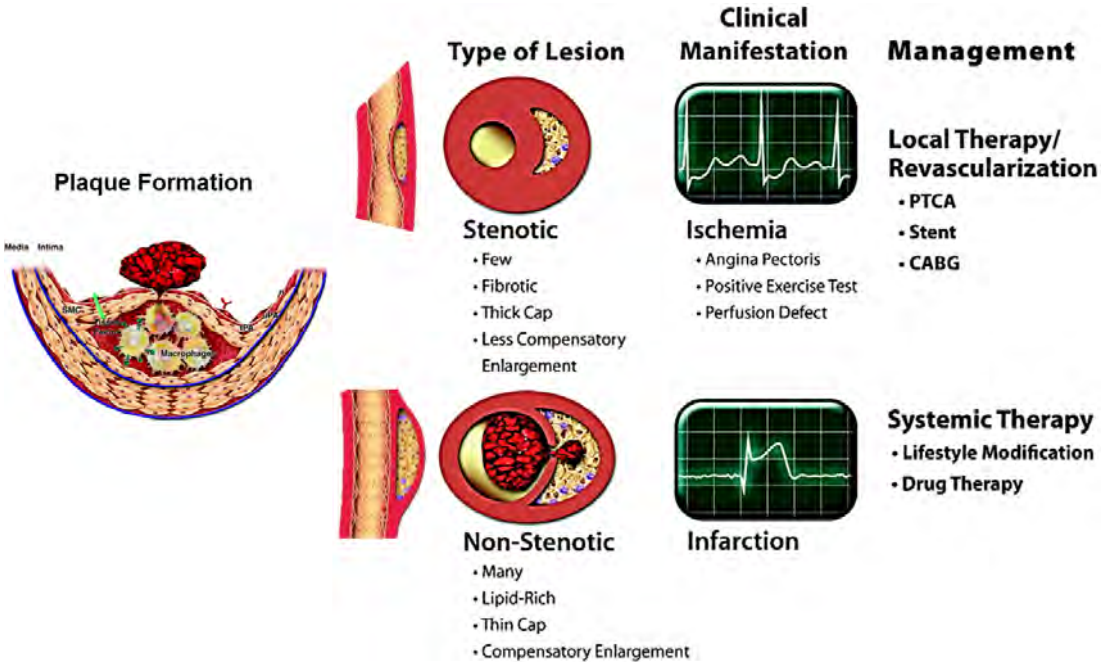

Figure 2.4: Plaque formation. The upper row shows the type of plaque that causes stenosis. The structure of plaques assumed to cause acute myocardial infarction is depicted in the lower row. Image adapted from Libby and Theroux [2005] with kind permission of Wolters Kluwer Health.

several processes such as cell death, vessel formation and remodeling. The extracellular matrix in the intima binds lipoproteins, and calcifications are formed by similar processes as those in bone formation [Libby and Theroux, 2005]. The death of lipid-laden macrophages can lead to the formation of lipid-rich necrotic cores. Lesions grow inward as well as outward. As shown in Figure 2.4, two types of plaque are distiguished regarding risk assessment and treatment strategy. Inward-growing stenotic lesions are assumed to cause stenoses, narrowings in the vessel wall. The plaques that are assumed to cause acute myocardial infarction (AMI), are lipid-rich and have a thin cap that easily ruptures. Plaque content then forms clots with coagulating blood that cause obstructions in dependent smaller vessels. In both cases, as shown in Figure 2.5, the supplied tissue region suffers from an under supply

with oxygenated blood. The undersupply of the myocardial cells with oxygen first occurs at

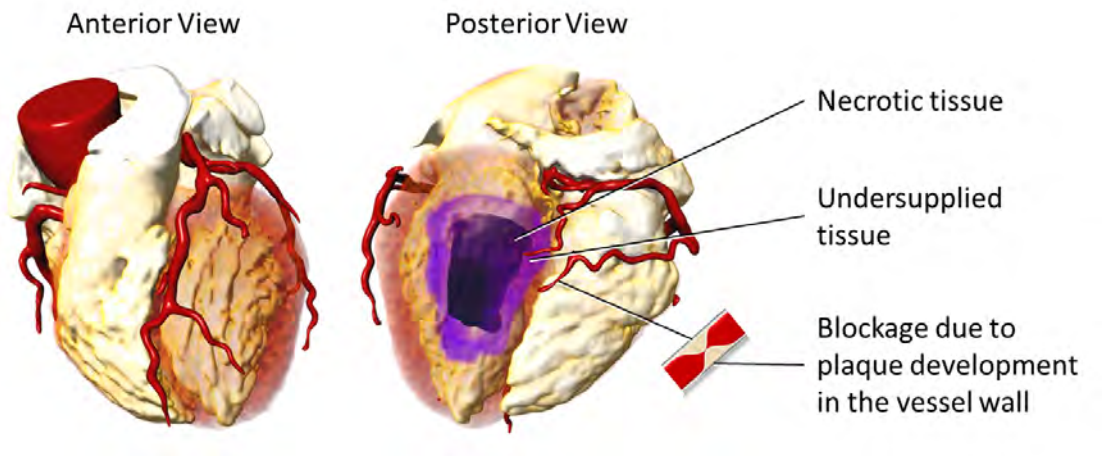

Figure 2.5: Local effect of coronary artery disease: The image shows two views of a heart. The anterior side is healthy, but due to plaque development in the posterior descending branch of the RCA, the supply of the dependent myocardial tissue is reduced. The black region shows the core zone of the undersupplied region, which is already necrotic. The violet zone is viable but at risk if the undersupply persists (image data courtesy of PD Dr. med. Hatem Alkadhi, University Hospital Zurich).

the endocardial surface. It results in cardiomyocyte necrosis and apoptosis. Inflammatory cells (macrophages) immediately infiltrate the infarcted region to remove necrotic cells. Interstitial edema and the necrosis of microvessels occur. The collagen degrades and to avoid a rupture of the myocardium, fibroblasts become active. In order to stabilize the myocardial tissue, they build a new collagen network. This process is usually completed within weeks. Figure 2.6 shows how the remodeling process can change the heart muscle. In the optimal case a quick local tissue stabilization avoids an alteration of the tissue in the infarct vicinity.

According to the so-called *ischemic cascade*, disturbances due to stenoses become apparent in myocardial perfusion prior to myocardial function [Nesto and Kowalchuk, 1987]. The states of myocardial tissue that frequently appear in CAD patients [Futterman and Lemberg, 2000] are listed in Table 2.1. Since only viable underperfused tissue can benefit from reperfusion therapy, the state of tissue is an important parameter for therapy decisions.

CAD patients are treated pharmaceutically, interventionally and surgically. Pharmaceutical therapies aim at decreasing the risk of undersupplied myocardial tissue. To this end, oxygen consumption in the heart muscle is reduced with nitrates or beta blockers. To

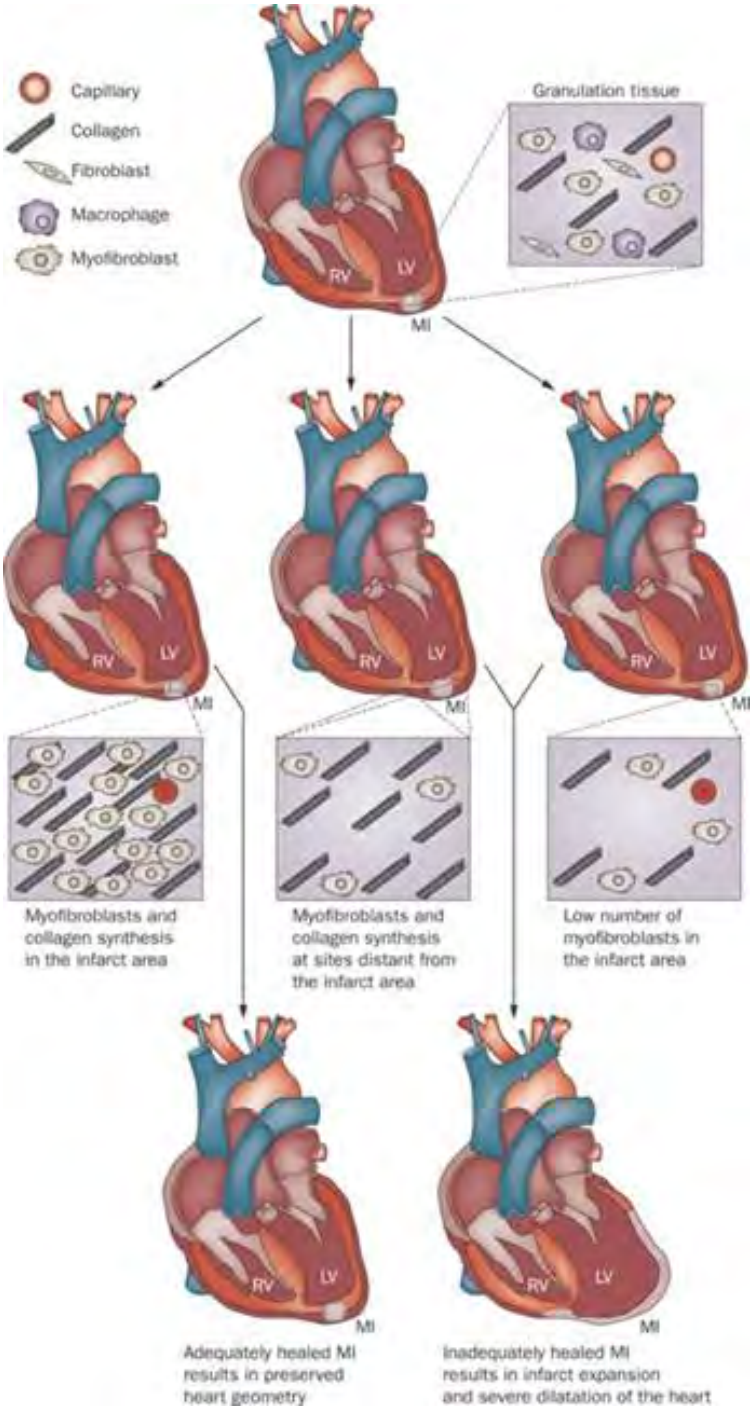

Figure 2.6: Myocardial Remodeling according to van den Borne et al. [2010] (illustration used with kind permission of Nature Publishing Group). It is assumed that local activity of fibroblasts in healing after infarction results in geometry preservation (left row) whereas insufficient and remote fibroblast activity results in undesired cardiac remodeling (middle and right row).

Table 2.1: Clinically relevant states of tissue in CAD patients

Viability	Term	Description
Viable	Normal	Healthy myocardium with normal perfusion and function
	Stunned	Normally perfused myocardium with a dysfunction that is persistent for max. 2 weeks after acute ischemia
	Underperfused	Underperfused myocardium with normal function
	Hibernating	Underperfused dysfunctional myocardium
Non-viable		Necrotic tissue with neither perfusion nor function

prevent constriction of vessels through thrombi and plaque, patients are treated with antiplatelet drugs and cholesterol lowering statins [Donner-Banzhoff et al., 2010]. If the conservative pharmaceutical therapy does not prevent shortage of oxygen supply sufficiently, patients receive interventional stenting therapy to reopen stenosed vessel segments or bypass surgery if a reopening of the occluded vessel segment is impossible. This can, e.g., happen in case of restenosis of already stented vessel segments. In contrast to pharmaceutical therapy, which affects the whole heart muscle and body vasculature, revascularization therapies have a locally restricted effect. Thus, it is crucial to know about the location and extent of the undersupplied myocardium as well as the responsible myocardial segment to perform a successful therapy. Modern imaging methods already provide means to acquire image data, which can serve for the non-invasive assessment of the coronary vessels as well as the myocardial tissue. Based on these data, the following tasks have to be addressed for diagnosis and therapy planning in CAD:

1. The detection and assessment of stenoses and plaque in the coronary arteries.
2. The detection of underperfused viable myocardial tissue.
3. The correlation between the underperfused viable tissue and the supplying vessel.

2.3 CT and MRI in Coronary Artery Disease

Both CT and MR imaging allow the assessment of coronary vasculature, myocardial perfusion and necrotic tissue regions. Contrast agents are applied intravenously to enhance

the image intensity in vessels or monitor the intensity change in tissue regions induced by perfusion or diffusion processes.

As described in Section 2.2, vessel occlusions caused by CAD first affect the blood transport into the dependent tissue. Thus, regions, which are at risk of infarction, can be identified by observing the time-intensity-curve of the myocardial tissue after intravenous contrast agent application [DallArmellina et al., 2010]. The intensity enhancement in underperfused tissue is significantly reduced. At the same time, cell necrosis and scar tissue formation increase extracellular space and thus the distribution volume of extracellular contrast agents. In damaged tissue the contrast-agent wash-in is therefore delayed, but the contrast agent is accumulated due to increased distribution volume and delayed wash-out [Hunold, 2009]. This effect is observed 5 to 30 minutes after contrast injection. Edema as well as injuries of the microvasculature can cause so-called no-reflow [Niccoli et al., 2009]. This means that even after a reopening of the artery occlusion, blood can not enter a tissue region, and the prognosis for the affected tissue is worse than in other ischemic tissue regions. In no-reflow areas also the effect of late contrast enhancement is delayed, and thus these regions can be identified in contrast-enhanced CT and MRI.

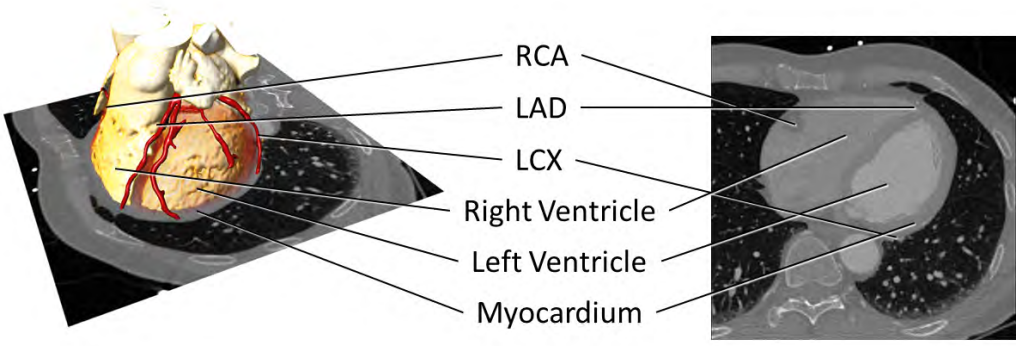

Figure 2.7: CT Coronary Angiography: The image shows a slice from a volumetric image of the contrast enhanced coronary arteries (image data courtesy of Prof. S. Miller, University Hospital Tuebingen).

Current imaging technology does not allow the inspection of plaque composition and rupture risk yet, but molecular imaging research will hopefully provide means for the non-invasive plaque assessment in the near future [Eagle et al., 2010, Matter et al., 2009].

CT: CT scanners currently used in clinical practice range from 16- to 256-slice systems. The multislice CT technology allows the acquisition of volumetric image data with sub-

milimeter resolution, if the captured objects are stationary. Typical CT coronary angiograms have an extent of 512×512×400 voxels with a voxel size of 0.4-0.5 mm^3 [Abbara et al., 2009]. The image data is organized as a set of axial slices. CT imaging enables the quantitative

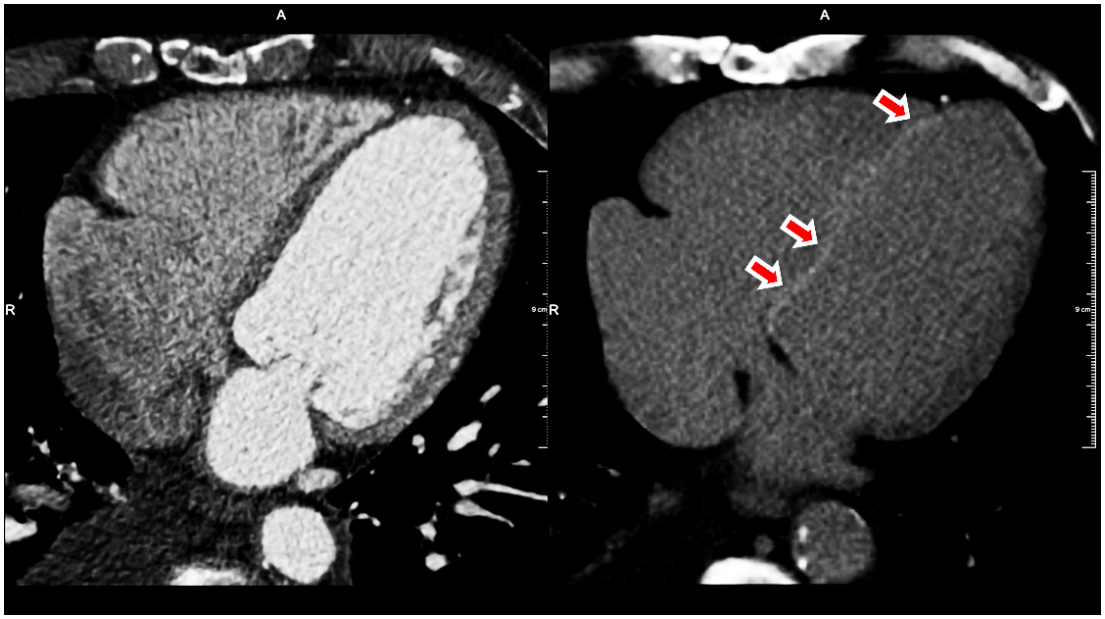

Figure 2.8: Corresponding slices in a CT coronary angiography and a late enhancement CT image. The arrows point at the infarcted myocardium (image data courtesy of Prof. A. Mahnken, University Hospital Aachen).

assessment of calcifications in the vessel walls as well as stenosis measurements, which are almost as accurate as those performed with conventional X-ray angiography [American College of Cardiology Foundation Task Force on Expert Consensus Documents, 2010b, Miller et al., 2008]. To avoid blurring artifacts in moving objects, a high temporal resolution is required in cardiac image acquisition. The coronary arteries are affected by respiratory motion as well as by the contraction of the heart muscle [Husmann et al., 2007, Yang et al., 2010]. To avoid respiratory motion, patients are asked to hold their breath during the acquisition. The contraction speed is often controlled with beta blockers. The achievable temporal resolution with current CT scanner technology is about 83 ms per slice [Flohr et al., 2006]. To enable the assessment of the vascular lumen, iodine-based contrast agents (≥ 300 to 350 mg I/ml) are intravenously injected prior to image acquisition at an injection rate of about 6 ml/s. This is supposed to result in an enhancement of the Hounsfield units (HU) in the vessel lumen to 300 to 350 HU. The timing of the acquisition is very important to ensure

the desired contrast enhancement in the regions of interest. To this end, methods like automatic bolus tracking or test bolus evaluation can be applied [Dewey, 2009].

The determination of necrotic and undersupplied myocardial tissue through imaging the late enhancement of contrast agent with CT has been proven to be feasible [Mahnken et al., 2010b, Bauer et al., 2010] and is now recommended if there are contraindications for other established techniques [Taylor et al., 2010]. This imaging technique is based on the accumulation of contrast agents in extracellular space in infarcted myocardium [Allard et al., 1988, Mahnken et al., 2005]. Five minutes after contrast agent injection the infarcted tissue is visible as an enhanced area on the CT image. Figure 2.8 shows corresponding slices of a CTCA and the late low dose scan. The late enhancement (LE) in the infarcted myocardium is clearly visible. New scanner technology allows the acquisition of myocardial perfusion sequences [Ho et al., 2010], but due to the high radiation doses these methods are not applied in clinical practice.

The data is reconstructed in axial slices (Fig. 2.7). The heart phase that is chosen for the assessment of the arteries is typically selected according to its quality regarding motion artifacts.

CT image data used in this work were acquired at endinspiratory breathhold. For coronary CT angiography, an arterial phase acquisition was performed after intravenous administration of iodine-based contrast agent. As shown in Figure 2.9, the late phase Dual Source CT (DSCT) data was obtained six minutes after injection of contrast agent for the assessment of late myocardial contrast enhancement [Mahnken et al., 2009b]. The applied reconstruction method depended on the clinical indication for the CT scan. So-called smooth reconstruction kernels reduce noise and resolution and thus facilitate the detection of connected tissue regions. On the other hand, sharp reconstruction kernels produce noisier images but facilitate the distinction of small image features. For CTCA, smooth or medium-smooth kernels were applied in most cases. If stents had to be assessed, CTCA data was reconstructed with medium-sharp kernels. To reduce noise, late enhancement datasets were reconstructed with a smooth kernel.

MR: As magnetic resonance imaging (MRI) provides a non-invasive and radiation-free means to inspect coronary arteries, myocardial infarction, function and perfusion dynam-

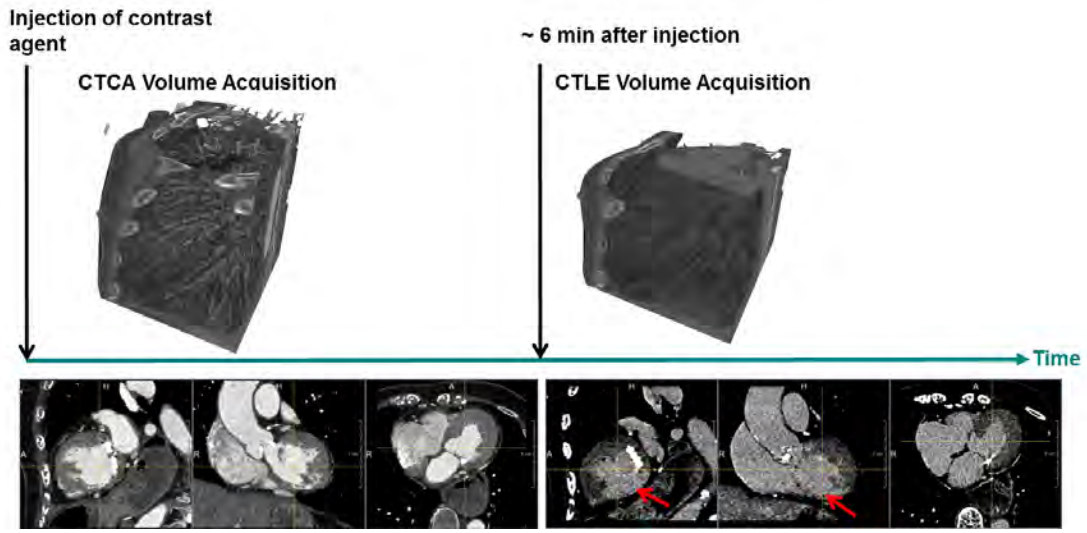

Figure 2.9: Acquisition of CT coronary angiography and late enhancement image data (image data courtesy of Prof. A. Mahnken, University Hospital Aachen).

ics, it is recommended for these diagnostic tasks by the American Heart Association (AHA) and the American College of Cardiology (ACC) [American College of Cardiology Foundation Task Force on Expert Consensus Documents, 2010a]. Typical acquisition protocols as, e.g., proposed by Plein et al. [2002] contain:

- Cardiac function cine sequences in 4-chamber and short-axis orientation
- Stress/rest perfusion sequences in short axis orientation
- Late enhancement images with similar orientations as the cine sequences
- Volumetric coronary angiogram

By means of the navigator technology [Ehman and Felmlee, 1989], MR coronary angiograms can nowadays be acquired as volumetric datasets with a resolution of about 1 mm^3, but the long scan time of 5 to 10 minutes, lower resolution and problems with local drop-out artifacts from stents are still considerable drawbacks when compared with CTCA [Bluemke et al., 2008].

Function, perfusion, and late enhancement datasets are often acquired slice-wise. Figure 2.10 shows the typical slice orientations for the examination of the myocardium. Image planes are either perpendicular to or oriented along the main axis of the left ventricle. The

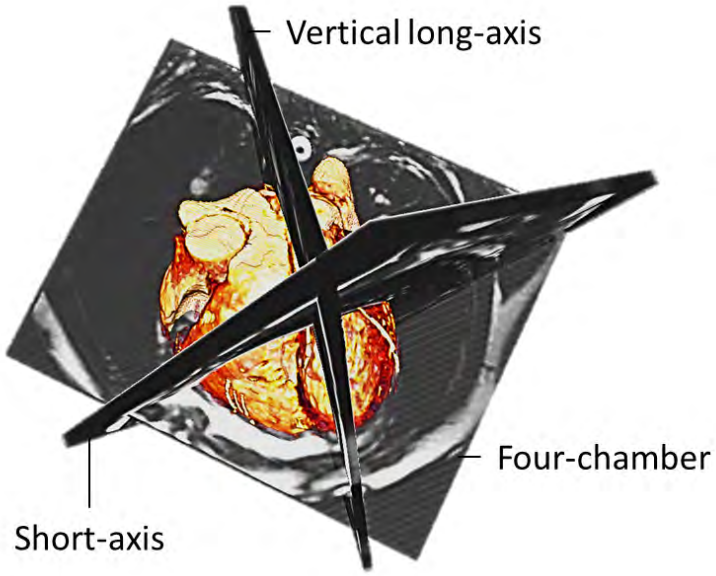

Figure 2.10: Typical slice orientations for the analysis of myocardial viability with MRI (image data courtesy of Prof. S. Miller, University Hospital Tuebingen).

contrast agents used for perfusion and late enhancement imaging in MRI consist of smaller molecules than the ones applied for CT and can thus leave the arteries easier. This is a drawback for the application of quantitative perfusion analysis techniques, but it results in clearer enhancement in necrotic or fibrotic tissue regions. Figure 2.11 shows typical perfusion and late enhancement slices and their location in relation to the left ventricle. It becomes clear that the contrast is considerably higher than that achieved with corresponding CT techniques, whereas the image data is much sparser. MR image data for the assess-

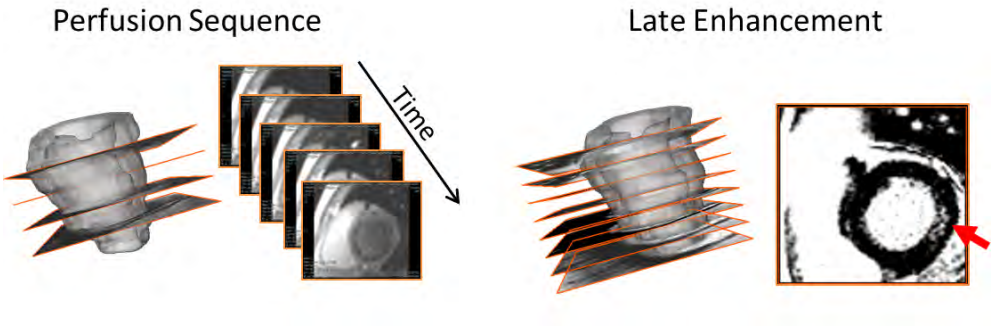

Figure 2.11: MR perfusion and late enhancement slices and their position relative to the left ventricular myocardium. The red arrow shows a myocardial region, where the late enhancement effect is visible (image data courtesy of Prof. S. Miller, University Hospital Tuebingen).

ment of coronary artery disease consist of different images for morphological and dynamic analysis. Image data for the examination of the myocardium are typically acquired as bright-blood images with fast gradient-recalled echo (GRE) or balanced steady state free precession (SSFP) scanning sequences. These techniques allow an acquisition with high speed and a high SNR. Fluid and fat with their comparable T1- and T2-values show high intensities in these images. Both acquisition types can form the basis for the analysis of myocardial function, perfusion, late enhancement and coronary arteries [Shah et al., 2005, Bluemke et al., 2008].

Cardiac function: According to the guidelines of the Society for Cardiac Magnetic Resonance (SCMR) the analysis of myocardial function requires the acquisition of cine sequences with a temporal resolution of less than 45 ms between the depicted phases [Kramer et al., 2008]. Image data is acquired in long-axis and short-axis orientation with a slice thickness of 6 to 8 mm and interslice gaps of 2 to 4 mm with or without the use of parallel imaging techniques [Finn et al., 2006]. Figure 2.10 presents an image example with four-chamber and vertical long-axis slices as well as a short-axis slice to depict the typical orientations.

Perfusion images: Myocardial perfusion sequences are usually acquired in short-axis orientation and contain at least three slices with 8 mm thickness and an in-plane resolution of less than 3 mm [Kramer et al., 2008]. Images are mostly acquired with parallel imaging. Per heartbeat every slice is scanned. Gadolinium-based contrast agent is injected intravenously at 3 to 7 ml/s. The image sequence covers 35 to 60 heartbeats in order to show the first pass of the contrast agent through the myocardium. It is acquired under breathhold. Figure 2.12 shows example images of a perfusion sequence, which correspond to characteristic time points in the intensity course. The contrast agent first enters the right ventricle (RV), and then the left ventricle (LV) before it is washed into the myocardium (MC) via the coronary arteries.

To determine perfusion deficits or wall motion abnormalities that can occur under physical stress conditions, additional cine and perfusion sequences are acquired under pharmacologically induced stress. For the assessment of the myocardial perfusion reserve, patients are usually treated with adenosine to widen the arteries and thereby increase the perfusion. To examine the contractile reserve, dobutamine or atropine are given to increase the patient's heart rate [Kramer et al., 2008]. If the ECG triggering is not adapted, the accelerated

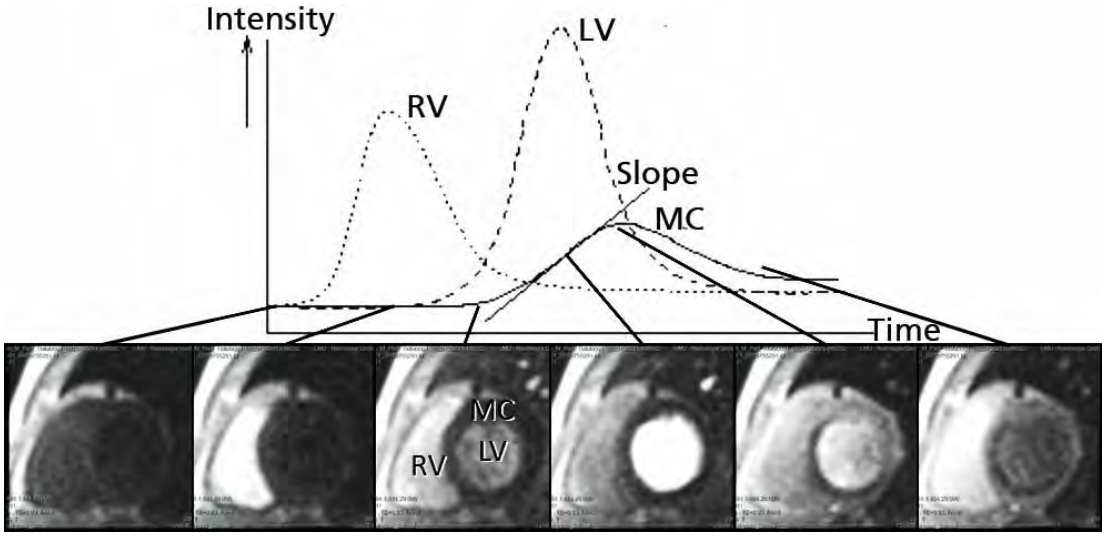

Figure 2.12: Perfusion sequence: The diagram shows the typical intensity course in the right ventricle (RV), left ventricle (LV) and myocardium (MC). The images below are taken from a perfusion sequence to illustrate the corresponding image contrast at characteristic time points of the perfusion sequence (image data courtesy of Dr. med. A. Seeger, University Hospital Tuebingen).

contraction results in imaging different contractile phases in rest and stress perfusion. As depicted in Figure 3.1, a direct comparison of the images is rather difficult.

Late Enhancement Image Slices: Late enhancement can be imaged 10 minutes after the contrast bolus injection using an inversion recovery turbo flash sequence. As defective tissue has a higher distribution volume for the Gadolinium-based contrast agent (see Sec. 2.2), infarcted areas take on high intensities in the image slices [Arheden et al., 1999, 2000]. Slice thickness and orientation are chosen according to the settings for the cardiac function cine sequences. An in-plane resolution of 1.4 to 1.8 mm is recommended [Kramer et al., 2008]. If image data is acquired in 2D, displacement of image slices acquired at different time points may occur due to breathing motion.

Whole-Heart Coronary Angiography: The acquisition of high resolution volumetric image data with MRI takes too long for one breathhold. Thus, image data is usually acquired with ECG-gating and navigator technology [Ehman and Felmlee, 1989, Scott et al., 2009]. Navigators are small images placed perpendicular to the moving structure of interest and

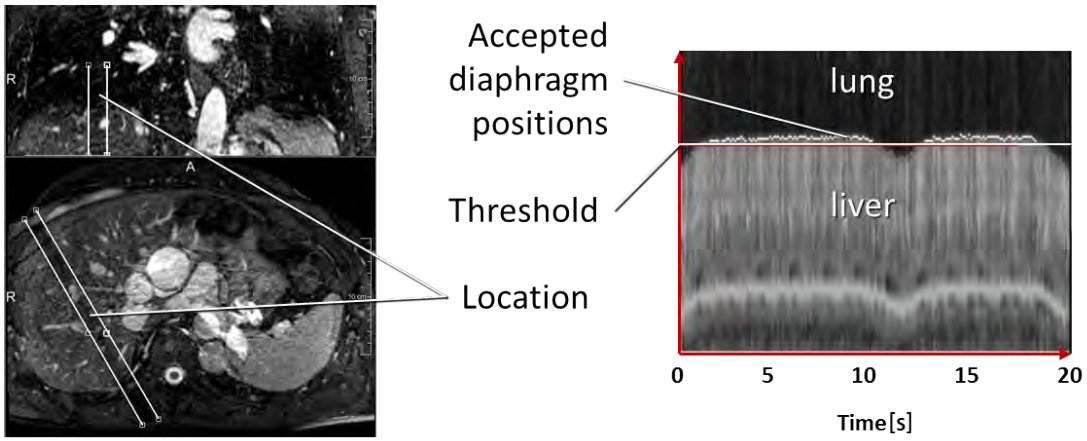

Figure 2.13: Placement, position and signal sequence of a navigator measuring the position of the diaphragm (image data courtesy of Dr. med. A. Seeger, University Hospital Tuebingen).

rapidly acquired before the effective image acquisition. For whole heart imaging, the navigator is placed perpendicular to the diaphragm and image data is defined to be acceptable if the navigator shows the diaphragm position within a window of 3 to 5 mm from its endexspiratory position [Bluemke et al., 2008]. Figure 2.13 shows an example for the ECG-signal and the navigator of a whole heart image acquisition. The imaging process for the whole heart with these technologies takes 5 to 15 minutes on a 1.5 Tesla scanner. The use of contrast agent for the enhancement of the coronary arteries in MR angiographies is difficult because of the long acquisition time opposed to the short turnaround time of the contrast agent in the vascular system. Thus, most clinically used techniques do not use contrast agent, but apply T2 preparatory pulses to enhance the contrast between the vascular lumen and surrounding structures [Botnar et al., 1999]. Furthermore, steady-state-free-precessing (SSFP) sequences are applied to achieve a good contrast [Deshpande et al., 2001]. The image slices have axial orientation and a resolution of 1 mm^3 is recommended [Kramer et al., 2008]. A major problem of MRA data are perturbations induced by metallic objects like stents, clips, wires, prosthetic valves and supporting struts or rings. Even if these objects do not cause problems for the patient such as, e.g., heating-up, they often cause local signal loss or artifacts that hinder the image interpretation and quantification.

Comparative studies between CTCA and MRCA show that due to the high resolution achievable with current state-of-the-art scanner technology, CT outperforms MR in the detection of CAD [Wagner et al., 2011], but this may change with further advances in MR technology.

3

Alignment Problems in Cardiac Image Data

The integrated analysis approach of coronary arteries and myocardial viability, as proposed in this thesis, is based on separately acquired image data scanned at different time points. The examination of spatial correspondences, e.g., between necrotic and underperfused tissue requires however that the image regions depicting the myocardium are aligned. Therefore, different registration problems have to be solved. First, the coordinate systems of different modalities must be aligned. Second, misalignment between images acquired with the same system at different time points must be matched. The types of displacement induced by the image acquisition described in Section 2.3 pose several problems that need to be solved before a comprehensive combined analysis of all relevant images is possible:

- Matching of the whole-heart volume, the late enhancement image and the perfusion images to allow a visualization of spatial relations between healthy, hypoperfused and infarcted tissue and the supply through the coronary arteries as described in Section 2.2.
- Alignment of late enhancement image slices in order to correct slice displacements and to allow 3-D image analysis.
- Motion compensation of perfusion image sequences in order to enable the analysis of the contrast-agent-induced local intensity change over time.

This chapter presents an overview of general registration approaches and the specialized implementations described in literature for related problems. A detailed description of the

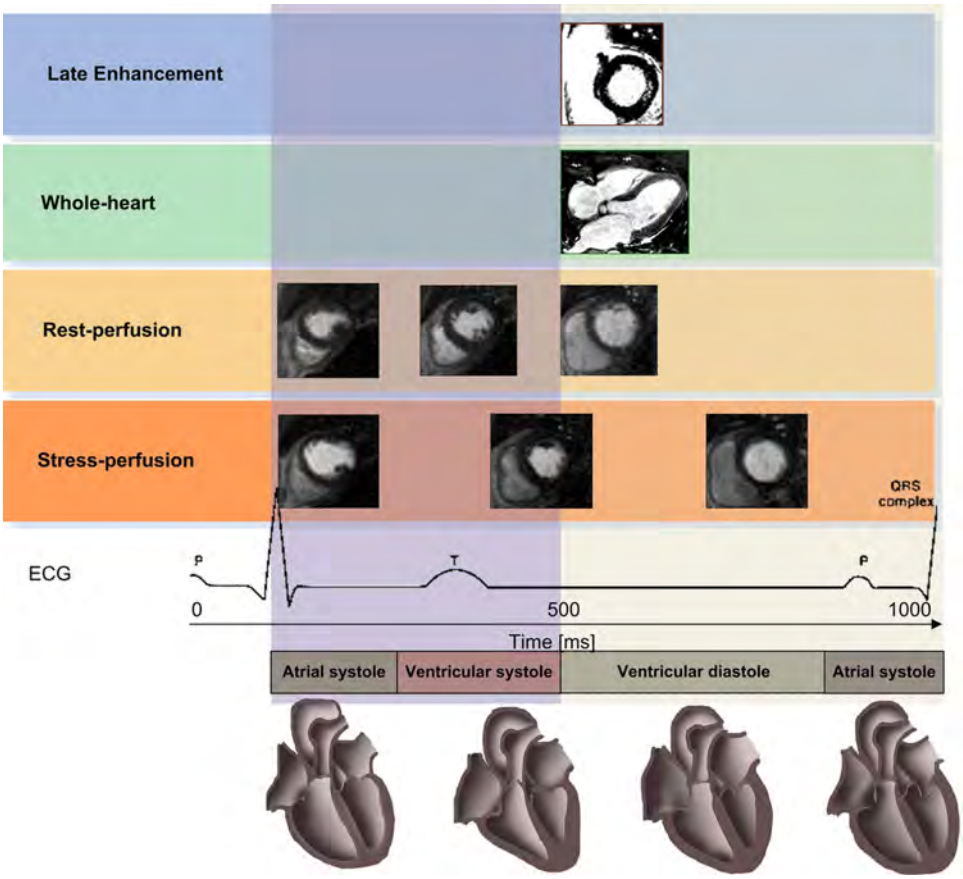

Figure 3.1: Temporal position of images in the heart contraction cycle (based on image data kindly provided by Prof. S. Miller, University Hospital Tuebingen).

implemented methods and the achieved results is given in Section 3.2. It is divided into subsections according the problems described above.

3.1 Existing Approaches for the Alignment of Cardiac Images

The general task in alignment problems of a reference image I_R and a so-called template image I_T is the search for a transformation function tf, which changes the coordinates of the voxels of I_T in such a way that $tf(I_T)$ better matches I_R according to certain criteria. In cardiac image registration, the goal is usually to match corresponding regions of the myocardium. Typical approaches to find a suitable transformation tf are point-based registration techniques and intensity-based registration methods [Makela et al., 2002].

Extraction and comparison of feature points These methods derive the transformation tf from corresponding keypoint sets P_R and P_T. The keypoints can be defined interactively or derived from image features like surfaces, edges or corners. An overview of proposed keypoint extraction methods is given by Schmid et al. [2000]. In medical image registration approaches, keypoints are often detected with the Harris corner detector, which is related to the autocorrelation function [Harris and Stephens, 1988]. Detected keypoints can be characterized by means of the so-called scale invariant feature transform (*SIFT*), which results in a feature description vector v_i summarizing the relative gradient orientations in the neighborhood of a keypoint p_i [Lowe, 1999]. If no feature information is available for the points

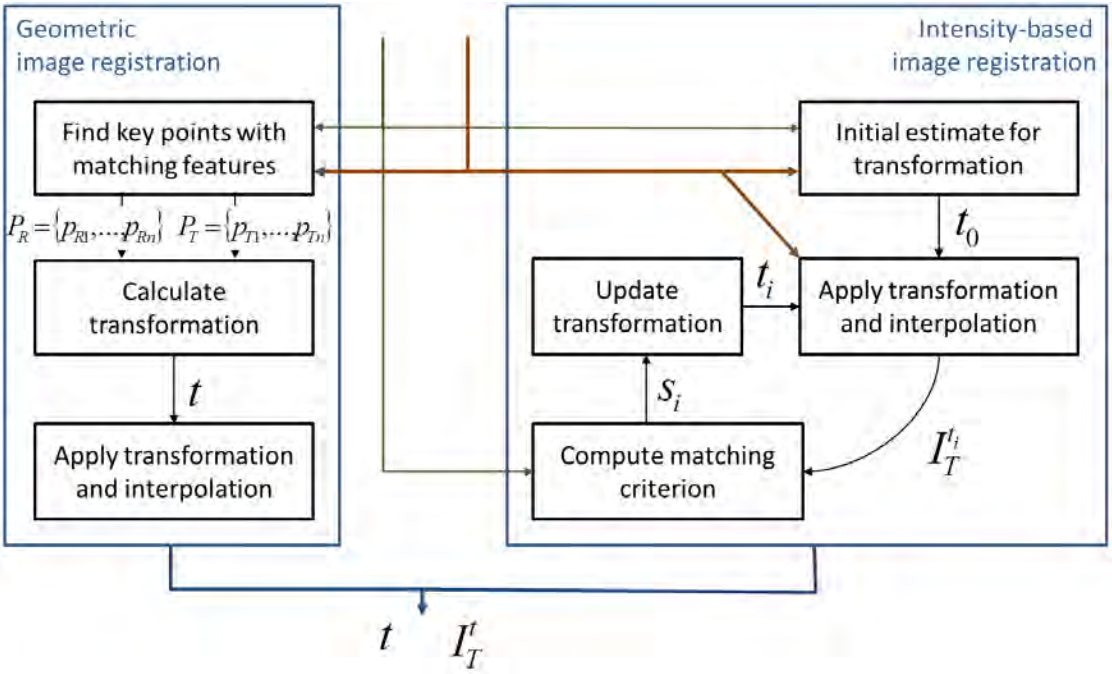

Figure 3.2: Types of registration methods used in cardiac image registration.

in P_R and P_T, the *head-and-hat algorithm* or the iterative closest point algorithm (*ICP*) can be applied to calculate the transformation for the alignment of P_R and P_T [Pelizzari et al., 1989, Yang and Medioni, 1992]. These methods are often used to align extracted surface points [Declerck et al., 1997, Sinha et al., 1995].

Feature descriptors can be used to search for direct point-to-point correspondences through the calculation of the feature descriptor distance $\|v_{Ri}, v_{Tj}\|$ of keypoints p_{Ri} and p_{Ti}. This method has been applied to match projection images of arteries from different time points

and different modalities [Pechaud et al., 2008, Gatta et al., 2011].

Image similarity measurement Intensity-based registration methods directly use certain similarity measures to assess how well the images I_R and $tf(I_T)$ match. These similarity measures can be grouped into three categories:

Linear intensity relation Proposed methods for the direct global comparison of voxel intensities are the Sum of Squared Differences (*SSD*), the Sum of Absolute Differences (*SAD*) and the Normalized Cross Correlation (*NCC*).

SSD and *SAD* measure the similarity of I_R and $tf(I_T)$ using the voxel intensity differences in the overlap of the corresponding image domains D_R, D_T^{tf}:

$$SSD\big(I_R, tf(I_T)\big) = \frac{1}{\left|D_R \cap D_T^{tf}\right|} \sum_{\boldsymbol{x} \in D_R \cap D_T^{tf}} \left\| I_R(\boldsymbol{x}) - tf(I_T(\boldsymbol{x})) \right\|^2 \tag{3.1}$$

$$SAD\big(I_R, tf(I_T)\big) = \frac{1}{\left|D_R \cap D_T^{tf}\right|} \sum_{\boldsymbol{x} \in D_R \cap D_T^{tf}} \left| I_R(\boldsymbol{x}) - tf(I_T(\boldsymbol{x})) \right| \tag{3.2}$$

They are best suited for intra-modality registration of images with intensity differences that stem from Gaussian noise [Makela et al., 2002]. On the other hand, they are very sensitive to structures, which appear only in one of the images, e.g., due to presence of contrast agent or pathological changes in the anatomy. *SAD* performs better in these cases [Slomka et al., 1995]. Surprisingly, these measures were also successfully applied for the registration of MR perfusion images, which exhibit strong intensity differences in corresponding regions through the pass of the contrast agent [Bidaut and Vallee, 2001].

NCC determines the similarity of I_R and $tf(I_T)$ from the correlation coefficient:

$$NCC\big(I_R, tf(I_T)\big) = \frac{Cov\big(I_R, tf(I_T)\big)^2}{Var(I_R)\, Var\big(tf(I_T)\big)} \tag{3.3}$$

It is a good similarity measure if the relationship between the intensity values in I_R and I_T is linear. Because of the non-linear relationship between intensity values in images from different modalities, *NCC* is mainly applied in intra-modality registration. *NCC* can be applied in the spatial as well as in the frequency domain. Castro and Morandi proposed to use the phase correlation to estimate the relative shift between two image blocks with *NCC* computed in the spatial Fourier domain [Kuglin and Hines, 1975, De Castro and Morandi, 1987]. The underlying principle is the Fourier

Shift theorem. A relative shift between I_R and I_T in the spatial domain results in a linear phase term in the Fourier domain:

$$I_T(x,y) = I_R(x+\Delta x, y+\Delta y) \tag{3.4}$$

$$F_T(u,v) = e^{-j(u\Delta x+v\Delta y)} F_R(u,v) \tag{3.5}$$

The inverse Fourier transform of the normalized power spectrum results in the cross-correlation function, which equals an impulse if the images match. The cross-correlation has been used to align cardiac image sequences from MRI and ultrasound [Gallippi and Trahey, 2001].

Non-linear intensity relation Information theory provides means for the registration of images with non-linear relations between the intensity values in I_R and I_T. The goal is to maximize the shared information of I_R and $tf(I_T)$ [Wells et al., 1996]. According to the *Shannon Entropy*, the average information supplied by the image I is defined via the probabilities of the appearance of the intensity values in the range R_I of I:

$$H_I = -\sum_{I_i \in R_I} p_I(I_i) \log p_I(I_i) \tag{3.6}$$

The probability $p_I(I_i)$ is usually estimated as the histogram value $h_I(I_i)$. The joint entropy of I_R and $tf(I_T)$ is defined as

$$H(I_R, tf(I_T)) = -\sum_{I_r \in R_{I_R}} \sum_{I_t \in R_{I_T}} p_{I_R tf(I_T)}(I_r, I_t) \log p_{I_R tf(I_T)}(I_r, I_t) \tag{3.7}$$

Because this value highly depends on the spatial overlap of I_R and $tf(I_T)$, Mutual Information (*MI*) considers the information content of I_R and $tf(I_T)$ in the overlap domain $D_R \cap D_T^{tf}$ as well:

$$MI\big(I_R, tf(I_T)\big) = H_{I_R tf(I_T)}(I_R) + H_{I_R tf(I_T)}(tf(I_T)) - H(I_R, tf(I_T)) \tag{3.8}$$

The so-called Normalized Mutual Information (*NMI*) proposed by Studholme and Hill [1999] further diminishes the influence of the overlap by the following formulation:

$$NMI\big(I_R, tf(I_T)\big) = \frac{H_{I_R tf(I_T)}(I_R) + H_{I_R tf(I_T)}(tf(I_T))}{H(I_R, tf(I_T))} \tag{3.9}$$

These similarity measures are well suited for the registration of images from different modalities [Maes et al., 1997].

Incorporation of spatial information In order to incorporate local image features like gradients, additional similarity measures have been introduced. Modersitzki et al. propose the comparison of Normalized Gradient Fields (*NGF*) for multimodal medical image registration, assuming that intensity changes occur at corresponding locations Haber and Modersitzki [2007]. Wollny et al. also used *NGF* in combination with *SSD* for the alignment of cardiac MRI perfusion sequences [Wollny et al., 2008].

The cross-correlation is also proposed as a local similarity measure. The Local Cross Correlation (*LCC*) is then calculated for the neighborhoods of single voxels.

Frequency-based optical flow methods use the phase information in the output of velocity-tuned filters [Heeger, 1988, Fleet, 1992]. Through the application of band-pass quadrature filters the input signal is decomposed according to scale, speed and orientation [Jaehne, 2005, Boukerroui et al., 2004]. Because of it's stability under scale perturbations and contrast variations, Heeger and Jepson proposed the usage of the phase for image comparison. In the analysis of cardiac motion, Becciu et al. [2009] worked with Gabor-filtered images to compensate intensity changes.

Transformation types The transformation $tf : D_T \rightarrow D_R$ to match I_T with I_R can be defined via formulae, grids or directly as vector fields.

Affine transformations are usually formulated as multiplications of the voxel coordinates $\boldsymbol{x}$ with a transformation matrix M. In 3D space, M is a 4×4-matrix which is built from the motion component matrices, which describe translation, scaling, rotation, and shearing through matrix multiplication. Altogether, the transformation matrix can have up to 15 parameters, which have to be determined in the registration process. Rigid (translation and rotation only) and affine transformations have been applied in cardiac applications, e.g., for the alignment of MR perfusion images [Bidaut and Vallee, 2001]. However if local deformations occur, other types of transformations are usually preferable. Approaches to describe deformable registration use, e.g., radial basis functions such as Thin-plate Splines (*TPS*) and Cubic B-Splines [Goshtasby, 1988, Bookstein, 1989]. The transformation function is formulated as a linear combination of translated radially symmetric functions added to a polynomial of low degree and depends on the set of control points $CP = \{\mathbf{p_i}, ..., \mathbf{p_n}\}$:

$$tf(\mathbf{x}) = \mathbf{A}\mathbf{x} + \sum_{i=1}^{n} c_i \, d\left(\mathbf{x}, \mathbf{p_i}\right) \tag{3.10}$$

The computational effort for the calculation of these transformations largely depends on the number of control points $|CP|$. For *TPS* $d\left(\mathbf{x}, \mathbf{p_i}\right)$ is defined as

$$d(\mathbf{x}, \mathbf{p_i}) = \left(\left\|\mathbf{x} - \mathbf{p_i}\right\|^2 + c^2\right) \ln\left(\left\|\mathbf{x} - \mathbf{p_i}\right\|^2 + c^2\right) \tag{3.11}$$

TPS perfectly match the key points. For other points, the error increases with distance from the nearest key point. The parameter c can be used to change the stiffness of the interpolating volume. To achieve robustness against key point localization errors, Rohr et al. [2001]. also suggested to use approximated instead of interpolated *TPS*. *TPS* are based on the physical model of a metal plate. Davis et al. suggested, that a physical model based on elastic material could better describe the deformations in the female breast [Davis et al., 1997]. They suggested the usage of the Navier-PDE-based Elastic Body Splines (*EBS*) for applications with small deformations. For the same application, cubic-B-Spline-based Free Form Deformations (*FFD*) have been suggested, arguing that local control of the B-splines makes them computationally efficient even for large numbers of control points [Unser et al., 1991, Rueckert et al., 1999]. *FFD* is defined as the 3D tensor product of 1D cubic B-splines:

$$\begin{aligned} tf(\mathbf{x}) &= \sum_{l=0}^{3}\sum_{m=0}^{3}\sum_{n=0}^{3} B_l\left(\frac{x}{n_x} - \left\lfloor\frac{x}{n_x}\right\rfloor\right) B_m\left(\frac{y}{n_y} - \left\lfloor\frac{y}{n_y}\right\rfloor\right) B_n\left(\frac{z}{n_z} - \left\lfloor\frac{z}{n_z}\right\rfloor\right) \boldsymbol{x}_{i+l,j+m,k+n} \\ \text{with } i &= \left\lfloor\frac{x}{n_x}\right\rfloor - 1,\ j = \left\lfloor\frac{y}{n_y}\right\rfloor - 1,\ k = \left\lfloor\frac{z}{n_z}\right\rfloor - 1 \end{aligned} \tag{3.12}$$

The basis functions B_j are defined as follows:

$$B_0(x) = \frac{(1-x)^3}{6} \tag{3.13}$$

$$B_1(x) = \frac{3x^3 - 6x^2 + 4}{6} \tag{3.14}$$

$$B_2(x) = \frac{-3x^3 + 3x^2 + 3x + 1}{6} \tag{3.15}$$

$$B_3(x) = \frac{x^3}{6} \tag{3.16}$$

This approach has also been used for the myocardial motion estimation from cardiac sequences [Perperidis et al., 2003, Cammin and Taguchi, 2010].

The application of finite element meshes as a basis for the motion description allows to include tissue properties such as the elasticity of biological tissue types into the transformation modeling [Hagemann et al., 1999, Ferrant et al., 2002].

The most complex transformations are those with independent transformations per voxel.

These are usually described as vector fields and thus consist of a set of parameters three times the size of the template image I_T.

Transformation parameter search The complexity of the search for the transformation tf depends on the amount of points included in the search. The comparison of a small set of feature points is easier than the calculation of the similarity of two complete images. The search effort is further influenced by the number of parameters as well as the characteristics of the selected transformation type. It is usually formulated as an optimization problem, which is solved iteratively. The parameters X_{tf} of the transformation function tf are adapted in such a way that the objective function s, which represents the similarity measure, is maximized or minimized respectively. The major classes of optimization algorithms, which are applied in medical image registration, are:

Local optimization methods These methods iteratively change the steps towards an optimum, which is not necessary the global optimum. Thus, they strongly depend on the shape of the objective function s and the initial estimate for the parameter set X_{tf}. To avoid getting trapped in local minima, these methods are often used as multi-resolution or multi-scale approaches. Depending on the characteristics of s, typically one of the following optimization types is chosen: *Gradient-based Methods* require an exact calculation of the derivative of the objective function with respect to the parameters X_{tf}. Typical gradient-based methods applied in medical image registration are gradient descent, Levenberg-Marquardt, quasi-Newton, and nonlinear conjugate gradient [Maes et al., 1999]. The major difference between these methods is the way they choose the step for the parameter change in an iteration step. A detailed description of the algorithms, step width control and implementation concepts can be found in the book by Nocedal and Wright [Nocedal and Wright, 2006].

Derivative-free Methods, which are often applied to medical image registration, are the algorithms proposed by Powell [Powell, 1964] and Nelder and Mead [Nelder and Mead, 1965] [Bernon et al., 2001]. These approaches are robust for functions s that have peculiar gradients or that are discontinuous and thus often preferable to gradient-based methods.

Global optimization methods To overcome the limitations of the local optimization methods, which can get trapped in local optima, it is possible to use global optimization

methods. These include simulated annealing [Dekkers and Aarts, 1991], genetic algorithms and evolutionary strategies. The algorithms are inspired by physical and biological models. Simulated annealing mimics the cooling process of heated metal, genetic algorithms use competitive characteristics of biological evolution and particle swarm optimization models cooperative and social aspects of animal swarms. The applicability of these methods for medical image registration has been proven in many publications [Ait-Aoudia and Mahiou, 2007, Rouet et al., 2000, Wachowiak et al., 2004]. However, their major drawback compared to the local optimization methods are the high computational costs through the many evaluations of the objective function and the concomitant interpolations.

Optical flow So-called optical flow methods derive the motion between two image frames that represent time points t_i and $t_{i+1} = t_i + \delta t$, corresponding to the template and the reference image, at every voxel position. The differential methods are based on local Taylor series approximations of the image intensity and use partial derivatives with respect to the spatial and temporal coordinates. They are based on the assumption that the image intensities do not change over time and thus $\frac{\partial}{\partial t} I(x, y, t) = 0$. The calculation of plausible solutions requires advanced approaches [Barron et al., 1994]. Differential approaches estimating the flow field based on partial derivatives and additional constraints were proposed by Horn and Schunck, Lucas and Kanade, and Nagel [Horn and Schunck, 1981, Lucas and Kanade, 1981, Nagel, 1983]. Advancements of these methods have, e.g., been proposed for the analysis of myocardial motion based on MRI tagging sequences [Suinesiaputra et al., 2003, Florack and van Assen, 2010].

An overview and evaluation of optimization methods for cubic B-Splines in combination with Mutual Information as similarity measure is presented by Klein et al. [2007]. The highest accuracy was achieved with the gradient-based optimizers here.

Interpolation The calculation of the image intensity of a transformed template image $tf(I_T)$ at the image coordinates $\boldsymbol{x}_R \in D_R$ of the reference image I_R requires an interpolation between intensity values defined for the transformed voxel coordinates $tf(\boldsymbol{x}_T)$ with $\boldsymbol{x}_T \in D_T$ of the template image. Usually, there is a considerable trade-off between the quality and the computational costs of interpolation methods. For medical image registration, nearest-neighbor, linear, trilinear, and spline-based interpolations have been proposed [Lehmann

et al., 1999]. According to Meijering et al. [2001], best results with respect to the preservation of the original image intensities are achieved with spline-based interpolation techniques.

3.1.1 Spatial Alignment of Slices of one Image Series

The problem of misalignment between stacked image slices in cardiac MRI data often occurs when these slices are acquired in different heart cycles (see Fig. 3.1) as well as in the presence of patient or breathing motion. Hence, data often has to be analyzed slice-wise. The effect is seen in cardiac images in general, and there are some approaches to correct the misalignment in order to allow a 3D analysis of the image data. In cardiac MR examinations, slice alignment problems typically occur in the sequences for the assessment of cardiac function and late enhancement. These image slices are acquired under constant contrast conditions and with ECG triggering. Thus proposed methods use intensity-based similarity measures and rigid transformations. The methods proposed by Lotjonen et al. [2004] and Barajas et al. [2006] both include long-axis images in the alignment procedure and they apply translations in 3D to correct the misalignment. The methods differ in the handling of slice distances and the applied optimizer. Rotational motion is neglected in both approaches. Chandler et al. suggested to correct slice misalignment through the alignment with a high-resolution 3D reference dataset [Chandler et al., 2008]. Their approach is superior with regard to motion from 3D translation and rotation.

3.1.2 Temporal Alignment of Perfusion Sequences

To assure spatial correspondence of regions of interest, the displacement errors between time frames of the perfusion sequence due to patient motion, contraction, and breathing have to be corrected. For this purpose, classical intensity-based as well as model-based registration methods have been proposed, e.g., based on squared differences [Bidaut and Vallee, 2001], normalized cross-correlation [Breeuwer et al., 2004, Gupta et al., 2003], mutual information [Bansal and Funka-Lea, 2002, Bracoud et al., 2003] and a measure based on gradient strength and direction [Sun et al., 2004]. Classes of transformations applied for correction are translation [Gupta et al., 2003, Bansal and Funka-Lea, 2002, Bracoud et al., 2003], rigid transformations (translation and rotation) [Bidaut and Vallee, 2001, Breeuwer et al., 2004, Gupta et al., 2003] and affine transformations (translation, rotation, shearing and scaling). More tailored approaches apply model assumptions to support the registration. Such assumptions relate to the shape of the myocardium [Bansal and Funka-Lea, 2002,

Sun et al., 2004, Gallippi and Trahey, 2001] as well as to the expected intensity change over time in the image regions of interest [Stegmann et al., 2005, Discher et al., 2005, Rougon et al., 2005]. Unlike the late enhancement slices, which are acquired over multiple heart cycles, perfusion slices, which represent one temporal position, are acquired in straight succession. Thus, spatially adjacent slices, which represent one time point, assumingly do not differ strongly regarding their displacement. All the above mentioned approaches perform a per-slice correction which does not account for the long-axis connectivity of the slices at one temporal position.

3.1.3 Spatial Alignment to a Reference Dataset

The alignment of different datasets is of high interest, if complementary information, e.g., anatomy and function are shown. In cardiac images, this is generally a difficult problem, because the heart muscle does not provide characteristic markers and different image types tend to differ regarding coverage, resolution, visible structures, etc..

There are only few approaches that address the alignment of different cardiac images. Breeuwer et al. assume that the AHA-model segmentations, which divide the myocardium into radial segments within three slices [Cerqueira et al., 2002], spatially correspond to each other in all inspected images [Breeuwer et al., 2003], while other strategies consider anatomical landmarks [Swingen et al., 2003] or previously segmented image structures such as the epicardial surface [Sturm and Stillman, 2003, Setser et al., 2005]. Since local image information is not taken into account, these methods can only provide relatively imprecise information about spatial relations between image structures from different datasets. The problem of aligning single slices with an image that shows a different coverage, resolution or even intensity distribution occurs in different application areas. In particular, the application of mutual information was found to be successful for the alignment of short-axis and long-axis images with a pre-procedural image volume in MR-guided cardiac interventions [Smolíková-Wachowiak et al., 2005]. The fusion of processed cardiac CT and MRI images is addressed by Kirisli et al. [2011]. In their approach, epicardial contours are extracted from the different images and used as input for a registration with the iterative closest points method.

3.2 Spatial Alignment of Cardiac CT and MR Images

The methods described in this section aim at solving the alignment problems, which are necessary to perform an integrated analysis of the coronary arteries and myocardial viability. This requires the fusion of the angiographic dataset, the late enhancement dataset and the perfusion dataset. This is a problem if data has been acquired with different modalities and will be addressed in Section 3.2.1. Furthermore, the misalignments of images within one coordinate system caused by patient motion, breathing or myocardial contraction have to be compensated. This includes, e.g., the alignment of late enhancement image slices and the motion compensation within the myocardial perfusion sequence.

3.2.1 Initial Alignment of CT and MRI Data

For the comparison of angiographic data from CT and perfusion or late enhancement information from MRI, the coordinate systems have to be aligned. Because of the differences in coverage, orientation and contrast distribution, an intensity-based registration is not applicable to these data. Thus characteristic landmarks are identified in one CT and one MRI dataset and used for an initial rigid alignment. Three landmarks are placed per dataset and the transformation consists of a translation, which is defined through the first marker and a rotation to align the directions defined through the other two landmarks (see Algorithm 1).

Algorithm 1 Calculation of the Rigid Transformation Based on Three Landmarks

{Determine direction vectors from reference landmarks $\boldsymbol{p}_{R1}, \boldsymbol{p}_{R2}, \boldsymbol{p}_{R3}$ and template landmarks $\boldsymbol{p}_{T1}, \boldsymbol{p}_{T2}, \boldsymbol{p}_{T3}$}
for $i \in \{R, T\}$ **do**
$\boldsymbol{d}_{i1} := \boldsymbol{p}_{i2} - \boldsymbol{p}_{i1} / \left|\boldsymbol{p}_{i2} - \boldsymbol{p}_{i1}\right|$
$\boldsymbol{d}_{i2} := \boldsymbol{p}_{i3} - \boldsymbol{p}_{i1} / \left|\boldsymbol{p}_{i3} - \boldsymbol{p}_{i1}\right|$
$\boldsymbol{d}_{i3} := \boldsymbol{d}_{i1} \times \boldsymbol{d}_{i2}$
{Create matrix $\boldsymbol{M}_i$ from direction vectors $\boldsymbol{d}_{i1}, \boldsymbol{d}_{i2}, \boldsymbol{d}_{i3}$ }

$$\boldsymbol{M}_i := \begin{pmatrix} \boldsymbol{d}_{i1}{}^T \\ \boldsymbol{d}_{i2}{}^T \\ \boldsymbol{d}_{i3}{}^T \end{pmatrix}$$

end for
{Calculate rotation matrix $\boldsymbol{R}$}
$\boldsymbol{R} := \boldsymbol{M}_R^{-1} \cdot \boldsymbol{M}_T$
{Calculate transformation $\boldsymbol{t}$ for input point $\boldsymbol{x}$}
$\boldsymbol{t}(\boldsymbol{x}) := \boldsymbol{p}_{R1} - \boldsymbol{R} \cdot \left(\boldsymbol{x} - \boldsymbol{p}_{T1}\right)$

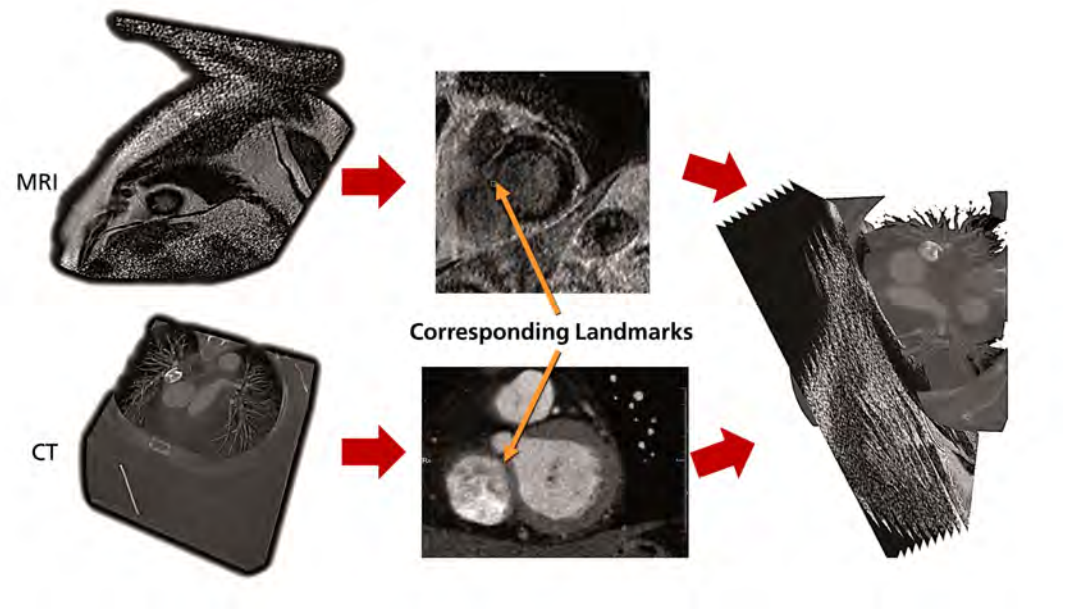

Figure 3.3: Initial alignment of CT and MRI datasets based on anatomical landmarks. This aligns the image coordinate systems without changing the image content (image data courtesy of PD Dr. med. H. Alkadhi, University Hospital Zurich).

3.2.2 Motion Correction in Cardiac Images

The major causes for misalignment in cardiac image datasets with corresponding coordinate systems are differences in the contraction or respiration phase. These are likely to occur in patients with cardiac arrhythmias or when long breathholds are required.

3.2.2.1 CT Angiography and CT Late Enhancement

Thanks to the ECG gating in the image acquisition, a rigid transformation can be assumed appropriate for the alignment of the arterial and late phase datasets. Intensity differences occur in the blood-filled regions, which are enhanced in the arterial phase and in the necrotic myocardium, which shows increased intensity values in the late phase volume. Therefore a mutual information based rigid registration is applied to align the volumes.

3.2.2.2 Alignment of MR Image Slices with Angiography Volume Image

A major problem in the analysis of late enhancement and perfusion images is the relatively low spatial resolution and the related partial volume effects. Additional smoothing is intro-

duced by interpolation when spatial transformations are applied. Therefore, the purpose of the proposed approach is to solve the intra- and inter-image alignment problems described above with a minimum of transformations. To this end the workflow depicted in Figure 3.4 is applied. The whole-heart dataset serves as reference, because it shows the highest image information density and it is already aligned due to the acquisition technique.

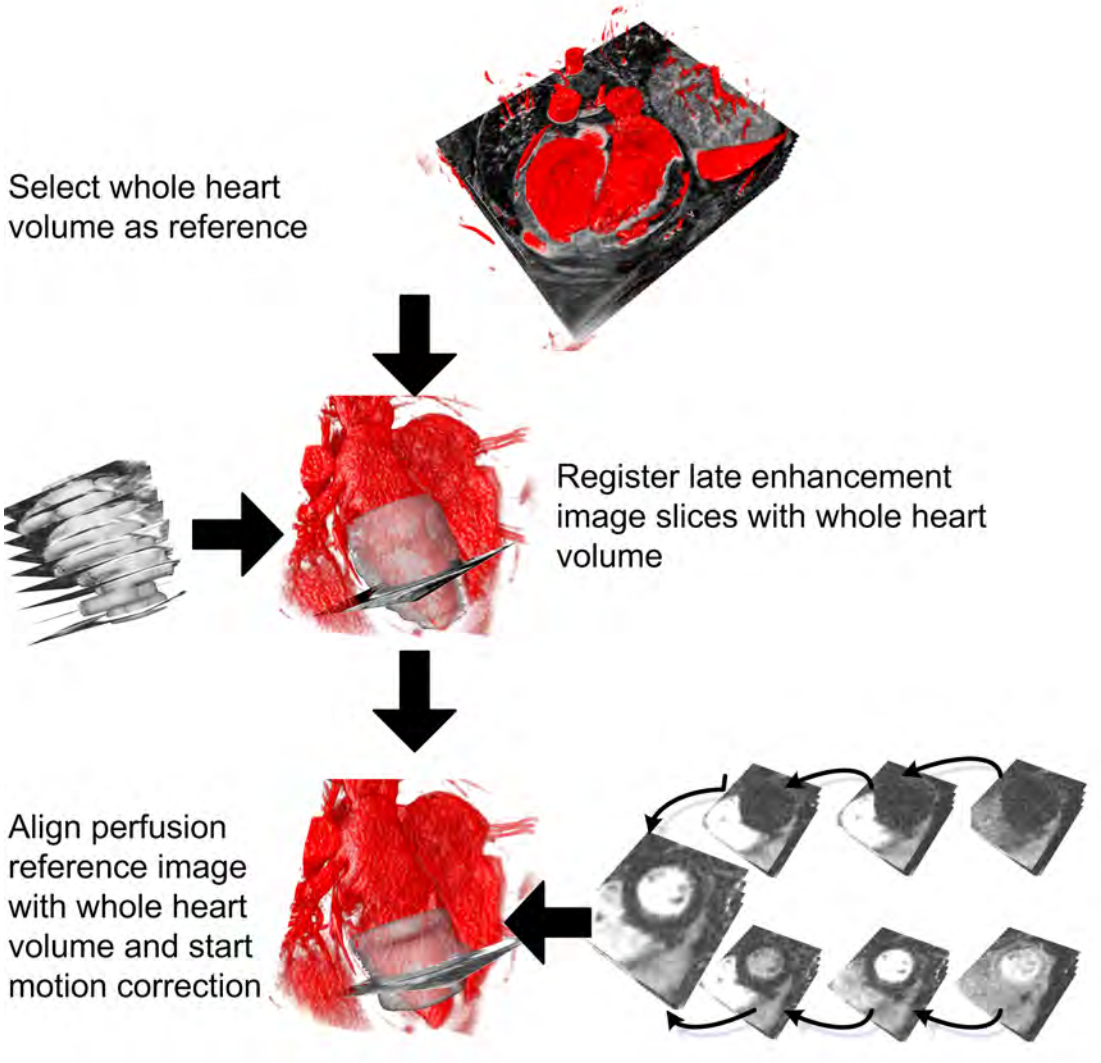

Figure 3.4: Workflow of image preprocessing for a combined analysis of coronary angiography, MR late enhancement and MR perfusion (image data courtesy of Dr. med. A. Seeger, University Hospital Tuebingen).

To correct slice misalignment in the late enhancement image, the image slices are matched

separately onto the whole-heart image volume. Images are acquired in the same cardiac contraction phase. Any displacement between the images is therefore caused by patient- or breathing-motion. This displacement can be described by rigid transformations, which are volume preserving and do thus not change the results of subsequent quantification steps. When matching a single slice I_{LE_i} of the late enhancement image I_{LE} with the whole-heart image I_{WH}, only the overlapping image parts $I'_{\mathrm{LE}_i}, I'_{\mathrm{WH}}$ have to be compared. That is, for every evaluation step, the computation of the similarity measure is restricted to the intersection of the domains $D^{tf}_{\mathrm{LE}_i} \cap D_{\mathrm{WH}}$, where $D^{tf}_{\mathrm{LE}_i}$ is the domain of the transformed late enhancement slice i and D_{WH} is the domain of the whole-heart volume. To find a suitable similarity measure S we evaluate the following approaches [Lotjonen et al., 2004, Barajas et al., 2006, Smolíková-Wachowiak et al., 2005]:

- **Normalized Cross Correlation (NCC)**

$$S\left(tf\left(I_{\mathrm{LE}_i}\right), I_{\mathrm{WH}}\right) = \mathrm{NCC}\left(tf\left(I_{\mathrm{LE}_i}\right)', I'_{\mathrm{WH}}\right) \tag{3.17}$$

$$\tag{3.18}$$

- **Normalized Mutual Information (NMI)**

$$S\left(tf\left(I_{\mathrm{LE}_i}\right), I_{\mathrm{WH}}\right) = \mathrm{NMI}\left(tf\left(I_{\mathrm{LE}_i}\right)', I'_{\mathrm{WH}}\right) \tag{3.19}$$

$$\tag{3.20}$$

with

$$tf\left(I_{\mathrm{LE}_i}\right)' = tf\left(I_{\mathrm{LE}_i}\right)|_{D^{tf}_{\mathrm{LE}_i} \cap D_{\mathrm{WH}}} \tag{3.21}$$

$$I'_{\mathrm{WH}} = I_{\mathrm{WH}}|_{D^{tf}_{\mathrm{LE}_i} \cap D_{\mathrm{WH}}} \tag{3.22}$$

Both methods have the term *normalized* in their name. Regarding *NCC* this refers to the use of $Var(I)$ to achieve scale invariance, whereas for *NMI* the integration of the marginal entropies $H(I)$ provides a certain robustness to changes of the overlapping regions $D^{tf}_1 \cap D_2$ due to the transformation t [Studholme and Hill, 1999]. Optimization is performed with the Simplex algorithm by Nelder and Mead [Nelder and Mead, 1965].

3.2.2.3 Evaluation

Two experts fused 20 datasets of patients with known CAD (57.6±7.7 years, range 43 - 69), who underwent low-dose CTCA and MRI on the same day. CTCA data were acquired with a dual-source CT scanner (Siemens Somatom Definition) using prospective ECG-gating after the injection of 80-100 ml iodine-based contrast agent (Iopromidum). Non-overlapping CTCA images were reconstructed with a slice thickness of 0.6 mm, using a medium smooth-tissue convolution kernel (B26f). Additional reconstructions were performed using a sharp-tissue convolution kernel (B45f) to compensate for blooming artifacts.
The CMR examination was performed with a 1.5 T clinical MR system (Philips Achieva). Late enhancement images were acquired ten minutes after the injection of 0.1 mmol gadobutrolum-based contrast agent (Gadovist) per kilogram of body weight. Images were oriented in short-axis view and an inversion-recovery gradient-recalled echo MR sequence with the parameters shown in Table 3.1 was applied. The observers initialized the alignment with three

Field of view	350-400 mm
Repetition time/echo time	7.4/4.3 ms
Inversion time	200-350 ms
Flip angle	20°
Matrix	240 x 240
Slice thickness	10 mm

Table 3.1: MR acquisition parameters

interactively placed landmarks. After the automatic registration step, alignment quality was evaluated by comparing the left ventricle segmentation results from the different images in the fused images. The corresponding CT and MR segmentations of the left ventricles were compared regarding their principal axis (PA) orientation as well as the overlap and the surface distance. Figure 3.5 depicts an example for the comparison of the bloodpool segmentation. The distance of the MRI bloodpool segmentation from the CT segmentation is shown color-coded on the surface.

Results The complete fusion procedure took 42.54±6.31 s for observer 1 and 39.91±5.47 s for observer 2 and was performed successfully for all datasets. Table 3.2 shows the results for the comparison of the segmented bloodpool regions.

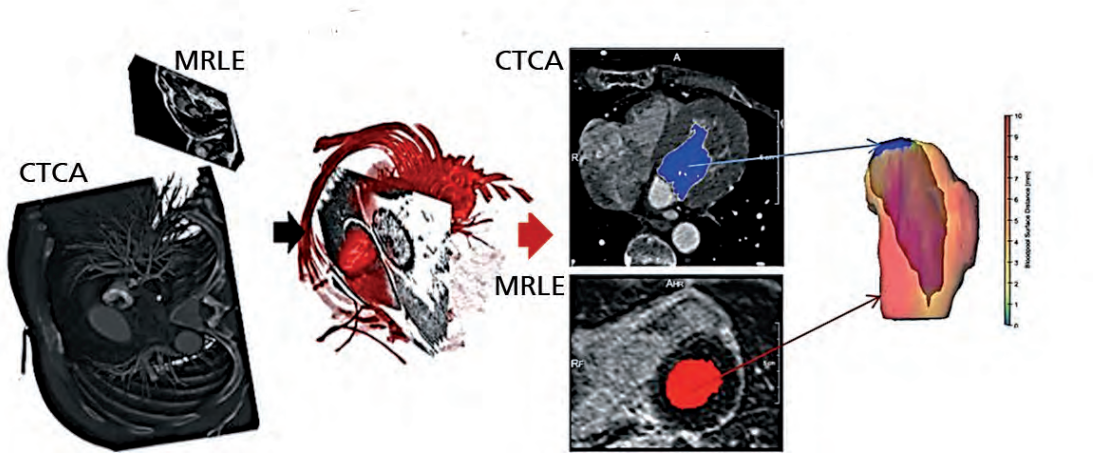

Figure 3.5: Assessment of the CT-MRI image alignment via the bloodpool segmentations. The images on the left show the bloodpool segmentations as overlay on the original image data. The image on the right shows the aligned corresponding bloodpool surfaces. In the presented case, the heartphases of the processed datasets do not match (image data courtesy of PD Dr. med. H. Alkadhi, University Hospital Zurich).

Observer	Angular Orientation Deviation		Dice Coefficient		Surface Distance	
	Mean	Std.Dev	Mean	Std.Dev	Mean	Std.Dev
1	11.11°	4.51	0.81	0.03	3.63 mm	0.31
2	12.71°	6.73	0.73	0.13	4.30 mm	2.27

Table 3.2: Comparison of the segmented bloodpool regions for observer 1 and observer 2. The deviation of the orientation is measured as the angle between the main axes of the bloodpool segmentations derived from the CT and the MR image data. The Dice coefficient measures the overlap of the segmented regions. The Hausdorff distance between the bloodpool regions is determined from the surface points of the segmentation masks.

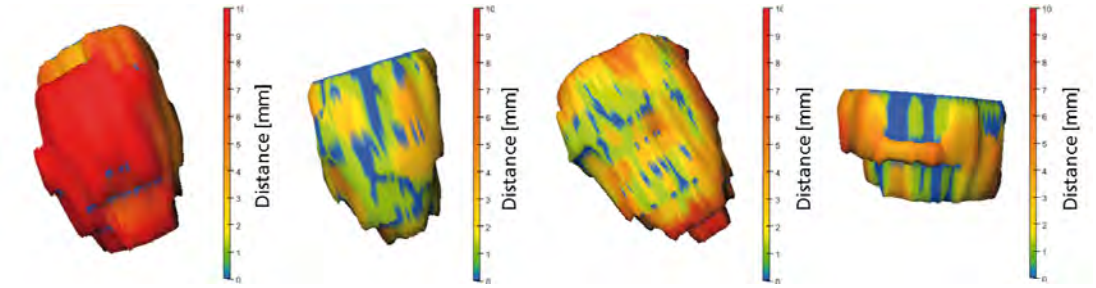

Figure 3.6: Comparison results of the segmented bloodpools for the fused datasets. The images show the local distances of the MRI bloodpool surface from the CT segmentation after image fusion.

Discussion The results shown in Table 3.2 appear acceptable considering the low resolution of the MR images. The visualization of the surface distance measurement in Figure 3.6 shows the problem of the thick MRI slices, which result in a coarse resolution in the long-axis direction. Another factor that limited the measurable accuracy was the incomplete coverage of the left ventricle segmentation in the MR images as indicated in the rightmost image of Figure 3.6. In this case, the experts included only very few image slices in the late enhancement analysis and thus the segmentation covers only a part of the left ventricle.
A general problem, which caused the bad result in the leftmost image of Figure 3.6 is presented in more detail in Figure 3.5. In this case, the users tried to fuse CT and MRI datasets from non-matching heart phases. This should be prevented and future improvements will include a heart phase check.

3.2.2.4 Motion Compensation in Perfusion Sequences

Perfusion sequences consist of about 40 time points depicting the pass of the contrast agent through the right ventricle, the left ventricle and the myocardium. To enable the analysis of the local time-intensity-curves, the motion induced through breathing and contraction has to be compensated. Image sequences are often acquired with a large field of view. As shown in Figure 3.7, only a small image region is relevant for the myocardial perfusion analysis. To speed up the motion correction as well as the subsequent image analysis step, it is therefore useful to crop the image in a pre-processing step. Existing approaches simply determine the right and left ventricle as blobs of high intensity in space and time [Spreeuwers and Breeuwer, 2001]. Unfortunately, this approach is not applicable to the datasets we work with, because high intensity changes occur also in aorta, kidney or moving fatty regions. Thus, the proposed method uses the intensity variation during a time interval T_{circ}, which represents the average time from the venous contrast agent injection to tissue enhancement in order to suppress regions with constant high intensities.

As only the myocardial first pass is needed for the derivation of semi-quantitative perfusion parameters (see Section 4.3), the motion correction starts from the end of the baseline of the myocardial time-intensity-curve. Because of its central temporal position in the perfusion sequence and its intensity distribution, the reference time point is defined as the intersection time of the right and left ventricular intensity curves. Figure 3.7 shows a screenshot of an input slice with markers at the detected gravity centers of the ventricles. For registration, this reference image is matched to the whole-heart image dataset with the method

Algorithm 2 Detection of heart ROI and reference time point

{Determine voxels with strong intensity changes during first pass of contrast agent}
for $\boldsymbol{x} \in D_I$ **do**

$$\sigma^2_{\max}(\boldsymbol{x}) := \max_{t_s \in [3,9]} \frac{1}{T_{circ}-1} \sum_{t=t_s}^{t_s+T_{circ}} \left(I_t(\boldsymbol{x}) - \overline{I_t(\boldsymbol{x})} \right)^2$$

end for

$X_{ic} := \left\{ \boldsymbol{x} \in D_I | h\left(\sigma^2_{\max}(\boldsymbol{x})\right) < th_\sigma \right\}$

{Find two largest voxel clusters C_{LV}, C_{RV} in X_{ic}}

{Return extended bounding box of C_{LV}, C_{RV} as heart ROI}

{Set reference time point to intersection of intensity curves at gravity centers of C_{LV}, C_{RV}}

$$t_{ref} := t : I_t \left(\frac{\sum_{\boldsymbol{x} \in C_{LV}} \boldsymbol{x}}{|C_{LV}|} \right) \equiv I_t \left(\frac{\sum_{\boldsymbol{x} \in C_{RV}} \boldsymbol{x}}{|C_{RV}|} \right)$$

that is described for late enhancement slice alignment in the previous section (Fig. 3.4). As the images are not acquired in the same heart phase, scaling and shearing are added and thus affine transformations are allowed.

As shown by Rogers et al. [1991], myocardial tissue moves up to 13 mm in the long-axis direction during contraction exceeding the usual slice thickness. As depicted in Figure 3.8 perfusion image sequences are often spatially sparse, and thus 3D alignment of the image slices is neither possible nor useful. The analysis of perfusion data is based on the analysis of voxel intensity curves and can thus only be performed if enough time points are available for a location. Eliminating outliers is thus more useful than searching for their correct location in 3D. The time frame that is aligned with the whole-heart image serves as reference I_R for the motion correction. Diseased patients often tend to show arrhythmias, which can give rise to misalignment due to extrasystolic contractile motion. Figure 3.9 shows typical types of motion that frequently appear in perfusion image sequences. As depicted in Figure 2.12 on page 21 the intensity changes over time in the different anatomic sections are asynchronous. Thus, we have to select a similarity measure, which is invariant to intensity differences. Furthermore, the motion to compensate for is known to be a combination of breathing and contractile motion. Breathing moves the heart location by changing the the diaphragm position. The shape of the heart does thereby not change significantly. The contractile motion of the heart muscle on the other hand mainly induces local deformations.

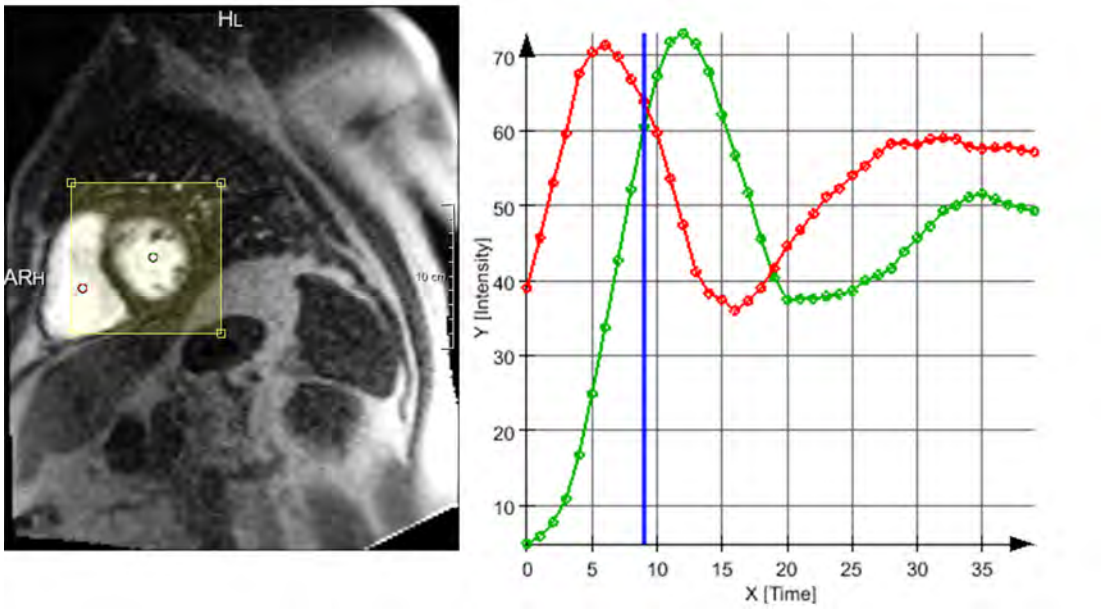

Figure 3.7: Pre-processing steps: The yellow box shows the relevant subimage of the perfusion sequence I_P at the reference time point t_M, which is determined by the intersection of the curves in the diagram on the right. The colors of the intensity curves correspond to the markers defining the subjacent image regions in the left image (image data courtesy of Dr. med. A. Seeger, University Hospital Tuebingen).

Two different approaches are evaluated for the motion compensation between subsequent time frames in the image sequences.

Intensity-based Motion Correction The first approach uses normalized mutual information as similarity measure. The motion correction consists of two steps. First, rigid transformations are applied to compensate the displacement and deformation caused by breathing and patient motion. To address slight contractile motion, cubic B-spline transformations are considered in the second phase. To this end, we apply a regular grid of five points in both directions, and thus the parameter set $X_{i,j}$ to be optimized for an image slice s_i at time

Figure 3.8: Example for a sparse perfusion image data. The image shows a volume rendering of a CTCA dataset combined with the corresponding perfusion data. Perfusion data is acquired with a slice thickness of 10mm and a slice distance of 20mm. Thus, for a considerable part of the myocardium there is no perfusion information available (image data courtesy of PD Dr. med. H. Alkadhi, University Hospital Zurich).

point j is composed as follows:

$$
\begin{aligned}
X_{i,j} &= \{TR_x, TR_y, R, S_x, S_y, B_{11}, ..., B_{15}, B_{21}, ..., B_{55}\} \\
i &= 1, ..., z_{max} \\
j &= t_M, ..., t_{max} \\
TR_x, TR_y &: \text{translation in x- and y-direction, respectively} \\
R &: \text{rotation angle} \\
S_x, S_y &: \text{scaling} \\
B_{x,y} &: \text{de Boer point coordinates specifying the} \\
&\quad \text{B-Spline transformation}
\end{aligned}
$$

To register every slice $s_{i,j}$ of the perfusion sequence I_P with its corrected temporal predecessor $s^t_{i,j-1}$ the parameter set $X_{i,j}$ is optimized by applying *NMI*, which is described on page 27, to the intersection of the corresponding domains $D^{tf}_{i,j-1}$ and $D^{tf}_{i,j}$ that result from

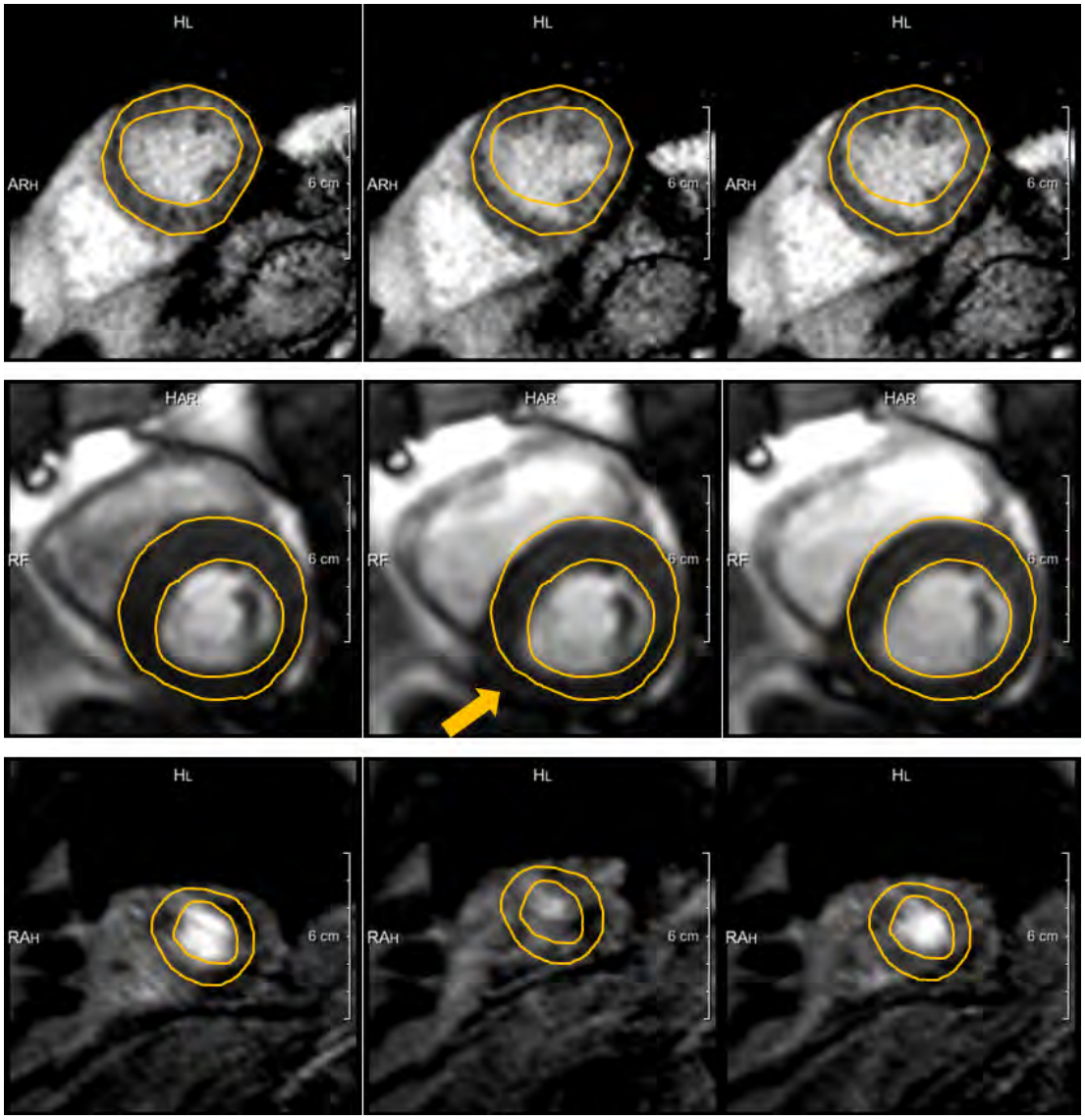

Figure 3.9: Different types of motion in perfusion sequences: The upper row shows three consecutive time frames of perfusion sequence 44 with out-of-plane motion: the ventricle almost disappears in the middle image. In the middle row (sequence 5) the diaphragm moves and thereby changes the heart position. Sequence 57 in the last row shows myocardial deformation.

the application of the transformation tf with the parameter sets X_{ij-1}^{opt} and X_{ij}:

$$\begin{aligned} S\left(tf\left(s_{i,j-1}\right)', tf\left(s_{i,j}\right)'\right) & \quad \text{with} \\ tf\left(s_{i,j}\right) &= tf\left(X_{i,j}, s_{i,j}\right) \\ tf\left(s_{i,j'-1}\right)' &= tf\left(s_{i,j-1}\right)|_{D_{i,j-1}^{tf} \cap D_{i,j}^{tf}} \\ tf\left(s_{i,j}\right)' &= tf\left(s_{i,j}\right)|_{D_{i,j-1}^{tf} \cap D_{i,j}^{tf}} \end{aligned}$$

As described in Section 2.3, perfusion slices are acquired over the course of one heart beat. We assume the displacement between the slices of one heartbeat to be minimal and propagate the optimal transformation parameters found for the first slice as start parameters for its spatial successors:

$$X_{ij}^{0} = X_{i-1j}^{opt}, i > 1 \tag{3.23}$$

Phase-based Motion Correction The other approach for the alignment of perfusion sequences uses the local phase, which represents image features such as edges and lines but is invariant to their magnitude. The *Morphon* implementation by Tautz et al. is based on the Fourier Shift Theorem explained on page 27 [Tautz, Hennemuth, Andersson, Seeger, Knutsson, and Friman, 2010, Knutsson and Andersson, 2005]. It is related to the seminal work by Fleet and Jepson, which is mentioned in Section 3.1. As proposed by Jepson and Fleet, the analytic signal is estimated by applying a quadrature filter, $q(x)$, which has a band-pass character that determines the scale of the structures or shifts of interest. The generalization of the analytic 1D signal to higher dimensions is achieved with a set of quadrature filters $q^{(i)}(\mathbf{x})$ with different orientations $\mathbf{n}_i$, and the generalized analytic signal in direction $\mathbf{n}_i$ for an image $I(\mathbf{x})$ is then obtained as $(I * q^{(i)})(\mathbf{x})$. The spherically separable quadrature filters used in the *Morphon*-implementation have a radial frequency function that is Gaussian on a logarithmic scale.

$$R_i(u) = e^{-\frac{4}{B^2 \ln 2} \ln^2\left(\frac{u}{u_i}\right)} \tag{3.24}$$

An example of the application of a log-normal filter set $q^{(i)}$ with orientations 135°, 90°, 45°, 0°, bandwidth $B = 1.5$, and center frequency u_i to two time points of a perfusion sequence is shown in Figure 3.10. To capture the different types of motion, the actual implementation of the *Morphon* uses a multi-resolution approach. The applied algorithm is described on page 48. In the deformation field calculation, the displacement estimation as well as

Algorithm 3 Motion Correction with rigid and B-Spline transformations

for $t \in \{t_M + 1, ..., t_{max}\}$ **do**
  for $i \in \{1, ..., z_{max}\}$ **do**
    {**Initialization of parameters** X^0_{i,t_M}}
    $$X^0_{i,t} := \begin{cases} id & , i = 1 \\ X^{\text{opt}}_{i-1,t} & , i > 1 \end{cases}$$
    {**Find transformation parameters for correction**}
    {Optimize rigid transformation parameters XA}
    repeat
      {Determine overlap regions for current parameters XA^j_i}

$$\begin{aligned} tf\left(I_{P_{i,t}}\right) &:= tf\left(I_{P_{i,t}}, XA^j_{i,t}\right) \\ tf\left(I_{P_{i,t}}\right)' &:= tf\left(I_{P_{i,t}}\right)|_{D^{tf}_{P_{i,t}} \cap D^{tf_{\text{opt}}}_{P_{i,t-1}}} \\ tf_{\text{opt}}\left(I_{P_{i,t-1}}\right)' &:= tf_{\text{opt}}\left(I_{P_{i,t-1}}\right)|_{D^{tf}_{P_{i,t}} \cap D^{tf_{\text{opt}}}_{P_{i,t-1}}} \end{aligned}$$

      {Calculate new parameters $XA^{j+1}_{i,t}$}
      $$XA^{j+1}_{i,t} := O_{\text{Simplex}}\left(XA^j_{i,t}, NMI\left(tf\left(I_{P_{i,t}}\right)', tf_{\text{opt}}\left(I_{P_{i,t-1}}\right)'\right)\right)$$
    until convergence
    {Optimize B-Spline transformation parameters XB}
    repeat
      {Determine overlap regions for current parameters $X^k_{i,t} = \{XA^{\text{opt}}_{i,t}, XB^k_{i,t}\}$}

$$\begin{aligned} tf\left(I_{P_{i,t}}\right) &:= tf\left(I_{P_{i,t}}, X^k_{i,t}\right) \\ tf\left(I_{P_{i,t}}\right)' &:= tf\left(I_{P_{i,t}}\right)|_{D^{tf}_{P_{i,t}} \cap D^{tf_{\text{opt}}}_{P_{i,t-1}}} \\ tf_{\text{opt}}\left(I_{P_{i,t-1}}\right)' &:= tf_{\text{opt}}\left(I_{P_{i,t-1}}\right)|_{D^{tf}_{P_{i,t}} \cap D^{tf_{\text{opt}}}_{P_{i,t-1}}} \end{aligned}$$

      {Calculate new parameters $XB^{k+1}_{i,t}$}
      $$XB^{k+1}_{i,t} := O_{\text{Simplex}}\left(XB^k_{i,t}, NMI\left(tf\left(I_{P_{i,t}}\right)', tf_{\text{opt}}\left(I_{P_{i,t-1}}\right)\right)\right)$$
    until convergence
  end for
end for

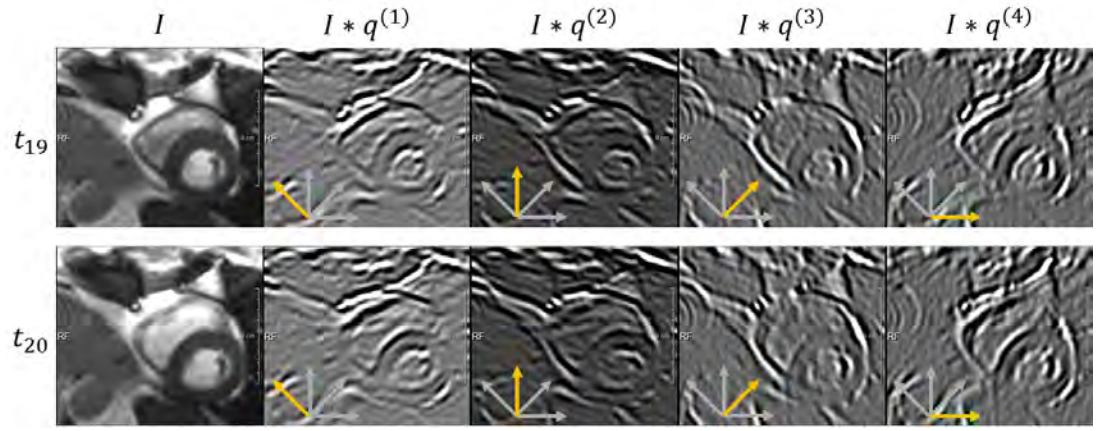

Figure 3.10: Application of a set of log-normal filters $q^{(i)}$ with orientations $135°, 90°, 45°, 0°$ and bandwidth 1.5 to two successive time points of a perfusion sequence.

the certainty of that estimate are considered. Furthermore, it is assumed that plausible tissue deformations are relatively smooth. Therefore, spatial regularization is applied with a Gaussian kernel. The parameters, which have to be selected for this method, are

- the scales, which are realized through a resampling of the image
- the maximum number of iterations per scale
- the bandwidth and center frequency of the quadrature filters
- the kernel size of the Gaussian

The proposed implementation uses three resolution levels to capture the displacement and contractile motion. The resampling factor between the scales was chosen as 0.63, which is a reasonable compromise between the number of scales and the size of perceivable deformations, and avoids artifacts due to dyadic resampling [Tautz, Hennemuth, Andersson, Seeger, Knutsson, and Friman, 2010]. Two different quadrature filter sets with center frequencies u_0 of $\frac{\pi}{4}$ and $\frac{\pi}{2\sqrt{2}}$ are used, so that deformations on six different scales are considered in total.

The process of the sequence alignment is organized similar to the intensity-based methods. Starting from the reference image $I_k(\mathbf{x})$, the deformation fields $\mathbf{d}_{k-1}(\mathbf{x})$ and $\mathbf{d}_{k+1}(\mathbf{x})$ are calculated, which align the neighboring slices with $I_k(\mathbf{x})$. In this way for every time frame the motion field for the alignment with its already aligned neighbor in the direction of the reference frame $I_k(\mathbf{x})$ is calculated and applied.

Algorithm 4 Motion Correction with the *Morphon* algorithm

{Perform calculation on all scales sc}
for $sc \in \{sc_1, ..., sc_m\}$ **do**
{$it(sc)$ iterations on scale sc}
for $j \in \{1, ..., it(sc)\}$ **do**
{Consider filters in directions $\boldsymbol{n}_i$}
for $i \in \{1, ..., n\}$ **do**
{Apply log-normal quadrature filter for current direction}
$I^{(i)}_{R_{sc}}(\mathbf{x}) := \left(I_{R_{sc}} * q^{(i)}\right)(\mathbf{x})$
$I^{(i)}_{T_{sc}}(\mathbf{x}) := \left(tf\left(I_{T_{sc}}\right) * q^{(i)}\right)(\mathbf{x})$
{Estimate displacement along the current filter orientation}
$C^{(i)}_{RT_{sc}}(\mathbf{x}) := I_{R_{sc}}(\mathbf{x})\,\overline{tf\left(I_{T_{sc}}(\mathbf{x})\right)}$
$d_i(\mathbf{x}) \approx \arg\left(C_{RT_{sc}}(\mathbf{x})\right)$
{Calculate confidence measure}
$c_i(\mathbf{x}) := \sqrt{\left|C_{RT_{sc}}(\mathbf{x})\right|}\left(1 + \cos\left(\arg\left(C_{RT_{sc}}(\mathbf{x})\right)\right)\right)$
end for
{Calculate accumulated confidence measure}
$c_j(\mathbf{x}) := \sum_{i=1}^{n} c_i(\mathbf{x})$
{Estimate current deformation field}
$$\mathbf{d_{sc}}(\mathbf{x}) := \frac{\sum_{i=1}^{n} c_i(\mathbf{x})\, d_i(\mathbf{x})\, \mathbf{n_i}}{c(\mathbf{x})}$$
{Regularize current deformation field}
$$\mathbf{d^{reg}_{sc}}(\mathbf{x}) := \frac{(\mathbf{d_{sc}}(\mathbf{x})\, c(\mathbf{x})) * g(\mathbf{x};\sigma)\, \mathbf{n_i}}{c(\mathbf{x}) * g(\mathbf{x};\sigma)}$$
{Add regularized deformation to total deformation}
$$\mathbf{d}_{\text{tot}}(\mathbf{x}) := \mathbf{d}_{\text{tot}}(\mathbf{x}) + \frac{c(\mathbf{x})}{c_{\text{tot}}(\mathbf{x}) + c(\mathbf{x})}\mathbf{d^{reg}_{sc}}(\mathbf{x})$$
{Update confidence measure}
$$\mathbf{c}_{\text{tot}}(\mathbf{x}) := \frac{c_{\text{tot}}(\mathbf{x})^2 + c(\mathbf{x})^2}{c_{\text{tot}}(\mathbf{x}) + c(\mathbf{x})}$$
{Warp $I_{T_{sc}}$ with current deformation field to calculate new $tf\left(I_{T_{sc}}\right)$}
end for
end for

3.2.2.5 Evaluation

The evaluation of motion correction algorithms for MRI perfusion data is almost as challenging as the motion correction itself. Neither software nor physical phantoms are found in literature. That is because the combination of tissue perfusion properties, the different types of motion and the rapid artifact-prone image acquisition constitute a very complex modeling problem.

The achievable image resolution does not provide structure information within the heart muscle, and thus landmark-based evaluation approaches use the blood pool or myocardium segmentation. It is very popular to assess the left ventricles gravity center movement in the corrected sequence [Bracoud et al., 2003, Milles et al., 2008, Xue et al., 2008, Tautz et al., 2010]. This measure is actually too coarse to provide information about the result's eligibility for a clinical interpretation, because it does not provide information about the matching of the voxels within the myocardium. It is important that myocardial perfusion curves are not disturbed by voxels belonging to the blood pool. As shown in Figure 2.12 on page 21, these curves differ strongly, and a mixed curve could lead to wrong conclusions. Thus, some authors propose to calculate the overlap of the myocardium segmentation at different time points or the distances of the segmented contours [Xue et al., 2008, Li and Sun, 2009]. The result of this evaluation strongly depends on the myocardium segmentation.

The actual interpretation of the perfusion sequence is based on the characteristics of the time-intensity-curves of the myocardium. It is thus obvious to base the assessment of the motion correction on the resulting time-intensity-curves. An expert assessment has been suggested for the qualitative assessment [Spreeuwers and Breeuwer, 2001, Milles et al., 2008, Hennemuth et al., 2008b]. A quantitative curve assessment was introduced by Gupta et al. [Gupta et al., 2003]. It is based on the assumption that the intensity curves are smooth and accumulates the deviations of intensity values from the mean intensity of their pre- and postdecessors. Thus, peaks and valleys also contribute to the error measure. This measure has been applied to selected ROIs in previous studies.

One problem of all the proposed evaluation methods is the dependence on manual input. Because of the high effort for segmenting the myocardium in 3 to 6 slices on 30 to 60 time points, most evaluations are based on only few datasets.

Evaluation Methods In order to provide a quantitative user-independent quality measure, this approach provides an automatic curve assessment. For all voxels in the region of interest, a model curve is fitted. The deviation from this model curve is then used to assess the plausibility of the motion correction result. Based on indicator dilution theory, Thompsen et al. proposed to model tracer concentration curves through the gamma variate function [Thompson et al., 1964, Mischi et al., 2008]. Although it can not be motivated physically, this model was found to be suitable for modeling ventricular and myocardial time-intensity curves during the first pass of the contrast agent [Jerosch-Herold et al., 2004]. The gamma variate can be formulated as follows:

$$C(t) = \begin{cases} s_0 + \gamma\,(t-t_0)^{\alpha}\, e^{-\frac{t-t_0}{\beta}} & , t > t_0 \\ s_0 & , t \leq t_0 \end{cases} \tag{3.25}$$

Because compartments with different time-intensity-curves, such as left ventricular blood pool, right ventricular blood pool, myocardium, lung, or liver can be present in the inspected region of interest, fit parameters are estimated separately for every voxel. The end of the baseline t_0 as well as the mean baseline intensity s_0, the maximum intensity $s_{\max}$, and the time point of maximum intensity $t_{\max}$ are derived directly in a first curve analysis step (see Figure 3.11). If α is also known, β and γ can be initialized as described in Equations 3.26 and 3.27 [Madsen, 1992].

$$\beta = \frac{(t_{\max} - t_0)}{\alpha} \tag{3.26}$$

$$\gamma = \begin{cases} (s_{max} - s_0)\left(\frac{e}{|\alpha-\beta|}\right)^{\alpha} & , t_{\max} > t_0 \\ 0 & , t_{\max} \leq t_0 \end{cases} \tag{3.27}$$

Here, α is initialized with $\alpha = 1,8$, which was considered a good first estimate after initial experiments. The final parameters are calculated by means of least squares minimization with the *Minpack* library [Cowell, 1984]. The gamma variate can only describe the first pass of the contrast agent and thus the fitting procedure only considers the first 25 time points of the image sequence.

For this interval, the difference between original and fitted image is then calculated and the mean difference between the original and the fitted voxel intensity curves is used as quality measure.

For an assessment of the diagnostic benefit of the provided motion correction methods, for a subset of the inspected cases, derived results are compared with those acquired by

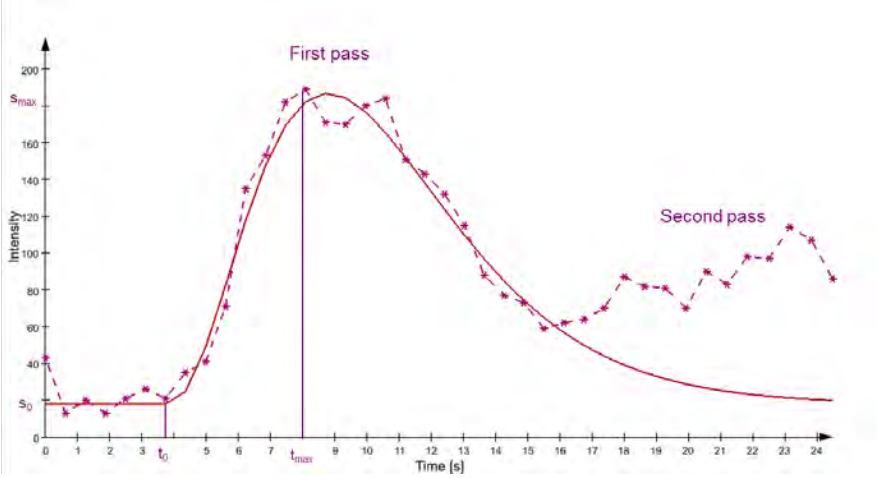

Figure 3.11: Example for a measured time-intensity curve (asterisks) and the fitted gamma variate function. The fitted function describes the first pass well but does not consider the second pass of the contrast agent.

other modalities such as late enhancement MRI and conventional coronary angiography. Spatial relations are assumed to correspond to the AHA segment model [Cerqueira et al., 2002].

Experiments The proposed methods have been applied to 60 clinical datasets from two different hospitals. The datasets were acquired with 1.5T scanners from two manufacturers. All patients had suspected or proven coronary artery disease. 53 sequences were acquired with the Philips Intera scanner after an intravenous injection of gadobutrol (Gadovist 1.0; Bayer Schering Pharma, Berlin, Germany). Contrast media was dosed at 0.1 mmol/kg of body weight at an injection rate of 5 ml/s, followed by a 40 ml saline flush. K-t sensitivity encoding perfusion MRI imaging was combined with a saturation recovery gradient-echo pulse sequence. Three slices were acquired sequentially per R-R interval with 10 mm slice thickness, and a reconstructed in-plane resolution of 1.25×1.25 mm^2. Six patients were examined with the Siemens Sonata scanner and one patient with the Siemens Avanto scanner. These patients received an injection of gadopentetat-dimeglumin (Magnevist; Bayer Schering Pharma, Berlin, Germany), which is also based on a gadolinium complex and has similar contrast-enhancing properties [Pintaske et al., 2006]. Here, the resolution was between 1.25 and 1.98 mm^2 in-plane.

All datasets were processed automatically with the algorithms described on pages 41, 46,

and 48. In order to provide results comparable with those in other publications, for 10 datasets with different types and amounts of motion, expert segmentations of the myocardium were provided for the original and corrected image sequences. Only those time points, which represent the first pass of the contrast agent through the myocardium were selected for this purpose. Surface distance and center-of-gravity movement were derived from the segmentations as proposed in previous studies. Two datasets were given to the expert twice to enable the assessment of the intraobserver variability of the manual segmentation.
For all datasets, gamma variate fitting was performed in the region of interest considered in the motion correction. The mean difference between the original time-intensity-curve and the fitted gamma variate was calculated for every voxel of the original image and the motion corrected images. The myocardium was segmented from the temporal maximum intensity projection (MIP) of the original and corrected image sequence as depicted in Figure 3.12.

Results A detailed list of the processed datasets is presented in Table A.1 on page 154 in the appendix. Table 3.3 presents the results for the segmentation-based comparison of two subsequent timepoints as proposed by Xue et al. [2008]. On average, the gravity center distance was decreased by all methods. In those cases, where the gravity center distance was increased, the value was below the in-plane resolution. The maximum surface distance was elevated by the method based on *NMI* and a fixed reference image. The methods using a floating reference image decreased this value, but the maximum distance between the segmented surfaces was still in the range of three voxels. The Dice coefficient was enhanced by the floating reference methods. It improved most with the *Morphon* algorithm. The assess-

			Dice				Surface Distance				Gravity Center Distance			
♯	SNR_{max}	SNR_{avg}	O	M1	M2	M3	O	M1	M2	M3	O	M1	M2	M3
5	6,27	2,71	0,74	0,76	0,86	0,88	9,67	9,67	5,64	8,32	2,53	2,03	1,91	1,36
11	9,43	2,63	0,77	0,74	0,81	0,87	6,98	6,98	6,98	6,98	2,29	2,29	2,01	1,83
22	10,08	5,56	0,54	0,54	0,77	0,81	9,52	11,52	6,25	6,37	6,89	3,43	2,67	2,24
29	6,37	2,61	0,79	0,81	0,85	0,86	8,29	8,29	5,62	8,29	1,14	0,69	1,62	2,15
33	10,07	1,98	0,76	0,75	0,85	0,87	7,60	10,08	6,37	5,15	2,95	2,75	2,06	1,64
36	7,67	3,62	0,79	0,79	0,90	0,87	6,73	7,60	5,15	7,60	3,23	2,34	0,77	1,15
38	7,90	2,77	0,82	0,77	0,84	0,83	6,37	7,60	6,25	6,37	1,69	1,48	1,60	1,77
54	7,85	2,47	0,85	0,84	0,84	0,87	11,05	7,97	7,97	6,44	1,85	2,11	2,67	1,59
57	8,77	2,24	0,77	0,83	0,81	0,86	5,30	6,37	6,37	5,30	3,16	1,89	2,67	2,86
58	6,65	2,97	0,82	0,80	0,84	0,88	7,57	9,94	8,55	9,94	2,01	2,72	1,78	1,51
Average			0,76	0,76	0,84	0,86	7,91	8,60	6,52	7,08	2,77	2,17	1,98	1,81

Table 3.3: Results of segmentation-based assessment of motion correction results. O means the original image sequence. The applied methods are M1: NMI-based non-rigid registration with fixed reference image, M2: NMI-based non-rigid registration with a floating reference image, M3: *Morphon* registration with floating reference image.

ment of the left ventricular movement through the average motion of the gravity center in

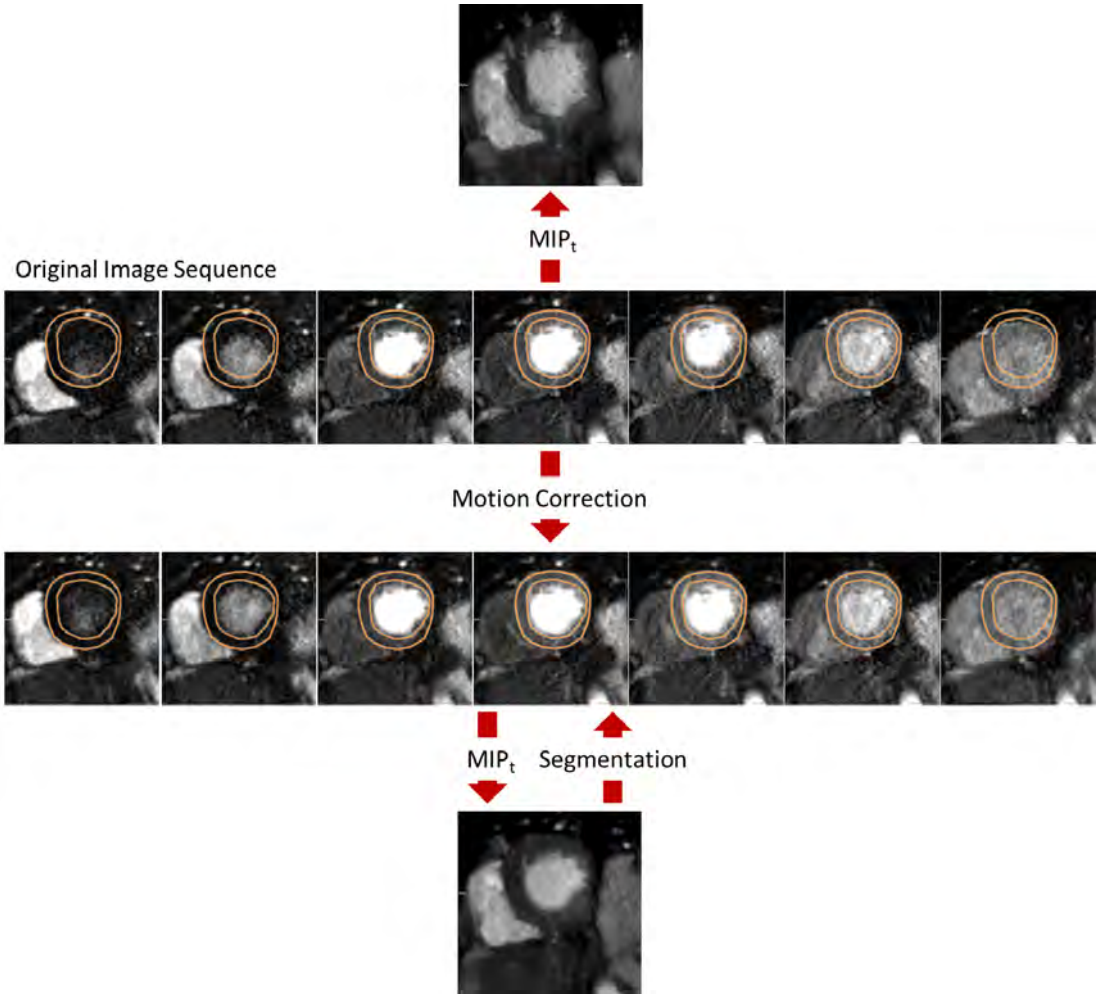

Figure 3.12: Myocardium segmentation based on temporal maximum intensity projection (MIP$_t$). The upper image sequence represents time frames of the original image data. The lower sequence shows the corresponding time frames after motion correction with the *Morphon* algorithm. The contours of the segmentation, which was performed on the temporal MIP of the corrected sequence, are shown as overlays on both sequences. The MIP-based segmentation mismatches most timeframes of the original sequence whereas it is suitable for all timeframes after motion correction.

the relevant part of the image sequences provided the results shown in Table 3.4. The best

	Gravity Center Distance			
#	O	M1	M2	M3
8	2,49	2,05	1,85	1,58
11	1,41	1,50	1,53	1,52
22	2,99	1,89	2,47	2,36
29	1,98	1,57	1,65	1,67
33	2,36	3,18	2,20	2,30
36	5,70	2,28	2,87	2,61
38	1,28	1,31	1,41	1,28
54	1,73	1,94	1,97	1,70
57	3,21	1,78	1,93	1,58
58	1,46	1,37	1,35	0,95
Avg.	2,46	1,89	1,92	1,76

Table 3.4: Average motion of the left ventricle in the original image sequence (O) and the corrected sequences M1-M3.

improvement was achieved with the *Morphon* method, which reduced the average motion almost to one voxel. All presented values depend on the segmentation of the left ventricle in the perfusion by an expert. The maximum intraobserver difference between myocardial contours on one image defined at two different timepoints was about 6 mm in average, meaning a deviation of two to three voxels. Strongest deviations occured in those regions where the papillary muscles are attached to the myocardium as well as in those regions with a low contrast between different tissue types. An example of two different segmentations provided for the same image is shown in Figure 3.13.

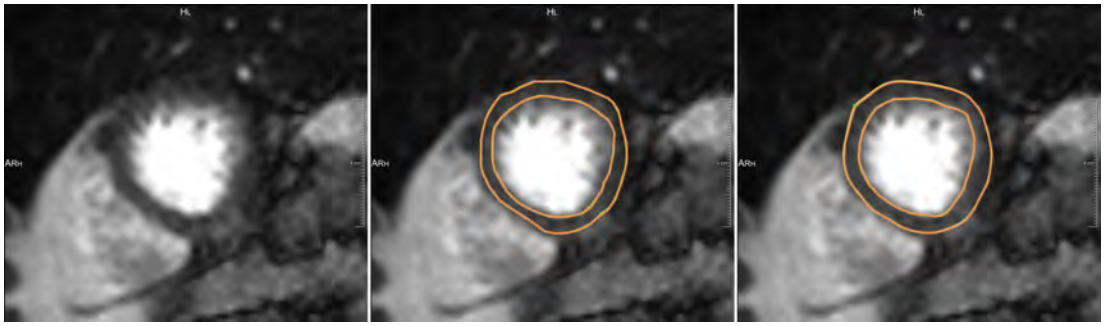

Figure 3.13: Intraobserver variation of segmentation. The leftmost image shows the a timeframe without segmentation. The middle and right images present segmentations of the myocardium performed by the same observer at different timepoints. Although both segmentations appear plausible, they differ significantly.

In all datasets the myocardium was segmented in the temporal MIPs as suggested by Milles et al. [2008] and the average error of the gamma variate fit was calculated for the myocardium region. For segmentations performed in the processed sequences the error was compared to

that, which occured before motion correction for this region. Because the intensity ranges of the images varied strongly ([0, 213] to [0, 3459]), the intensity-related results listed in Table 3.5 are presented in percentage of the intensity range of the corresponding image sequence. Because the myocardial image intensities are relatively low in comparison to the hight intensities in blood-filled compartments, errors may also appear low. The detailed results are presented in Table A.2. On average, the number of voxels, which were identified as myocardium, increased through all three motion correction methods. The *NMI*-based method using a fixed reference frame (M1) increased the dectected myocardial volume by 20%. The methods, which use a floating reference image, resulted in a notably higher increase of the detected myocardial volume. For the *NMI*-based method (M2) as well as for the *Morphon* algorithm (M3) the increase was 33%. The average error of the gamma variate fit to these regions was 3.18, 3.13, 3.03 and 3.12% of the image sequences intensity range for original sequence and correction methods M1 to M3 respectively.

As shown in Table 3.5 all methods achieved a decrease of the myocardial intensity range,

		M1	M2	M3
Increase of Myocard. Volume [%]		20.00	33.00	33.00
Decrease of Myocard. Intensity Range [%]		3.14	9.88	12.48
Avg. Fit Error	Rel. Intensity Deviation [% of Intensity Range]	3.13	3.03	3.12
	Rel. Error Decrease [% of Intensity Range]	0.50	0.56	0.51
	Rel. Error Decrease [% of Initial Value]	12.94	16.44	14.91
Max. Fit Error	Rel. Intensity Deviation [% of Intensity Range]	20.84	30.34	23.74
	Rel. Error Decrease [% of Intensity Range]	5.92	5.57	8.62
	Rel. Error Decrease [% of Initial Value]	0.73	8.74	12.77

Table 3.5: Results of myocardium segmentation and gamma fit after correction. All intensity related values are given as percentages of the image intensity range.

meaning that after motion correction the separation between myocardium, bloodpool and lung worked better. The average decrease of the gamma variate fit error in the segmented regions of the corrected sequences was 0.5, 0.56 and 0.51% of the intensity range for methods M1 to M3. This means that the average error decreased by 12.94, 16.44 and 14.91%. The maximum error of the gamma variate fit in the detected myocardium decreased by 0.73, 8.74 and 12.77%. This means, that while the region that was identified as myocardium increased most, the maximum error of the gamma variate fit also decreased most in this area for method M3. However, for method M1 the error increased in five cases. For method M2

this only happened in two cases, and for method M3 an error increase occured in one case. For sequence 8, which is presented in Figure 3.14, there was a strong increase in segmented

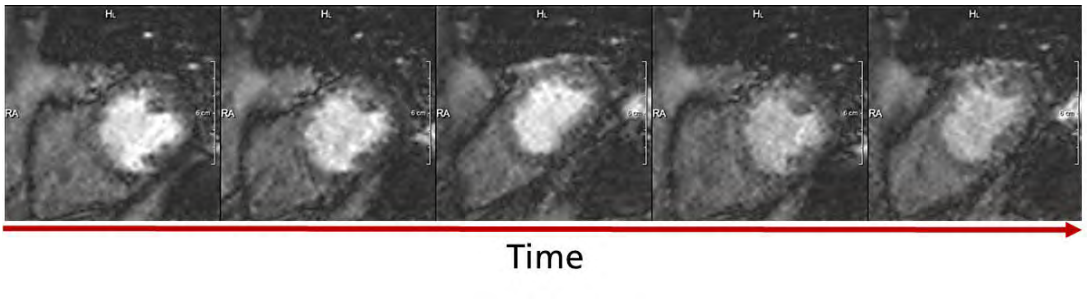

Figure 3.14: Myocardial first pass of contrast agent in image sequence 8. Strong deformation through in-plane motion and out-of-plane motion is visible. The myocardium moves up and down with the diaphragm. Furthermore the bloodpool changes its shape due to the deformation.

myocardial volume for the methods that use a floating reference image. This is clearly explained through the temporal MIP images presented in Figure 3.15. In the projection images of the original image sequence and the correction with the fixed reference (M1), major parts of the myocardium can not be identified. However, the average gamma variate fit er-

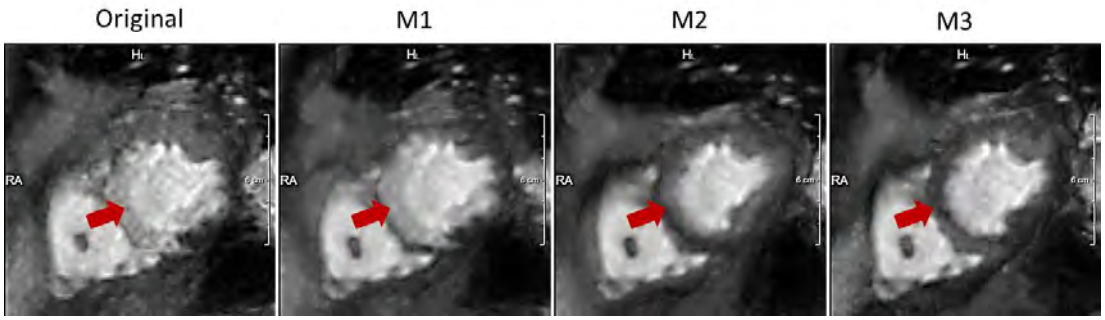

Figure 3.15: Temporal MIP images for sequence 8 before and after correction. In the MIP of the original sequence and the sequence corrected based on *NMI* and a fixed reference image (M1), parts of the myocardium are not detectable. The red arrows point to the image region where high image intensities of the bloodpool appear in the myocardium region due to uncorrected motion in the two images on the left.

ror increased for both methods using a floating reference image. Figure 3.16 depicts, that the segmentation, which is more comprehensive than in the other sequences, also includes small regions with a large average fit error, especially in the area of the diapragm.

Sequence 6 is another example with strong in-plane motion as depicted in Figure 3.17.

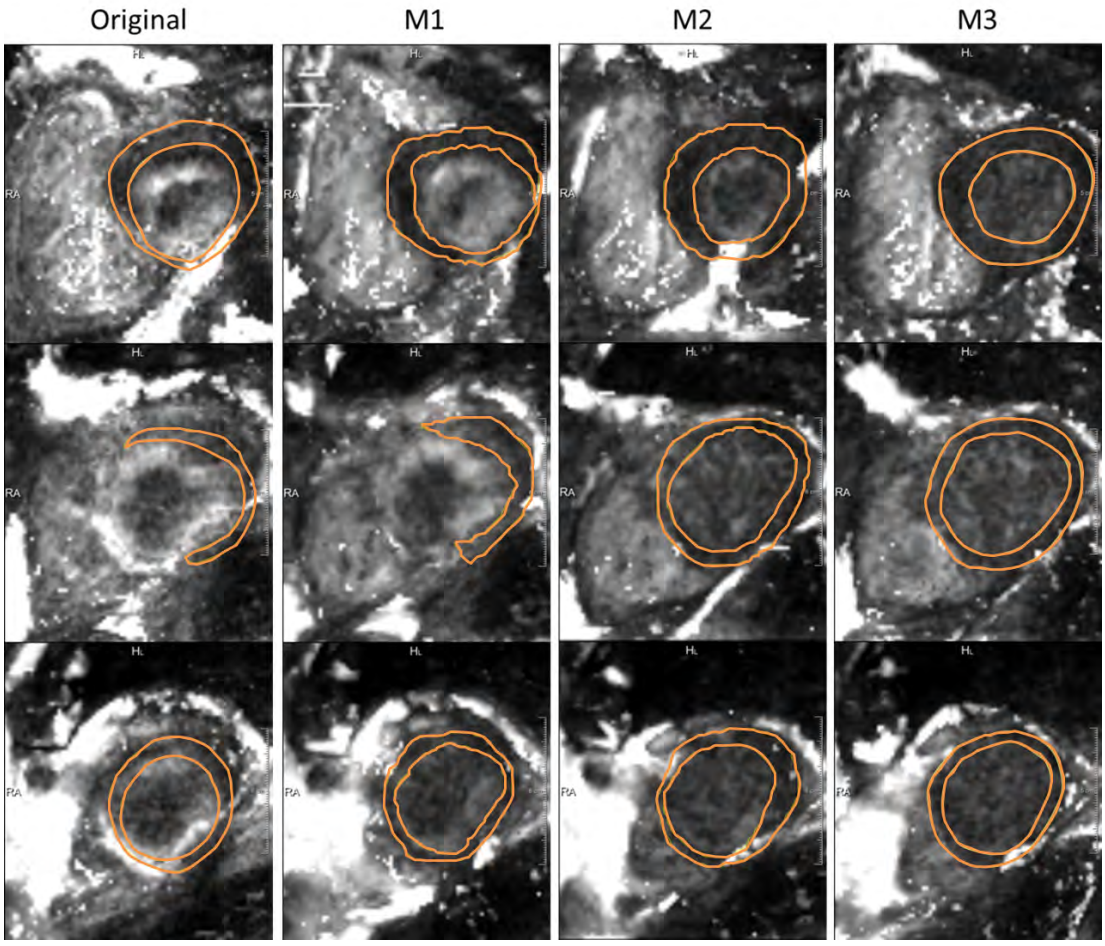

Figure 3.16: Average gamma variate fit error for image sequence 8 before and after correction. Bright image regions indicate a strong deviation of the local intensity curves from the fitted gamma variate function. The orange contours show the myocardium regions that could be detected in the temporal MIPs of the corresponding sequences. At the myocardial borders, the segmentations of corrected sequences produced with method M1 and M2 include voxels with a high average fit error. For the correction with methods M3 the myocardial region appears relatively dark, meaning that the average fit error is low after correction. It can thus be assumed, that the analysis of the myocardial time-intensity curves will provide reasonable results here.

For this case, the motion correction with the fixed reference frame resulted in a clear decrease of the detectable myocardium. The temporal MIPs in Figure 3.18 shows that this method resulted in a degenerated image sequence, which is not suitable for a further analysis. Only parts of the myocardium are identifyable here.

For the datasets of four patients (sequences 3, 28, 34, 38 and 44), AHA-segment-model-

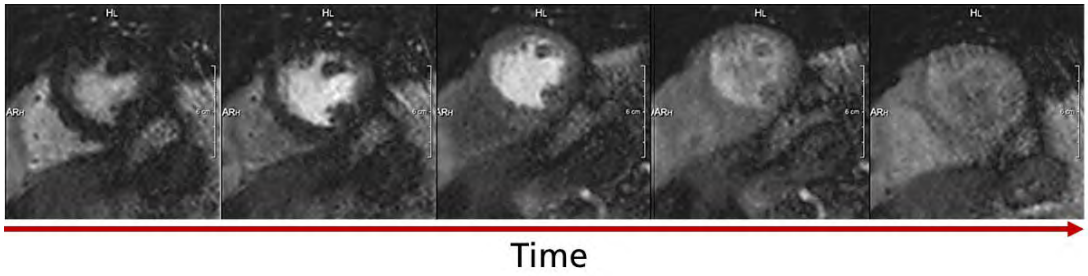

Figure 3.17: Relevant timepoints of image sequence 6 with strong in-plane motion. It can be observed, that the bloodpool moves up and down. It does however not change it's shape as would be the case for deformation or out-of-plane motion.

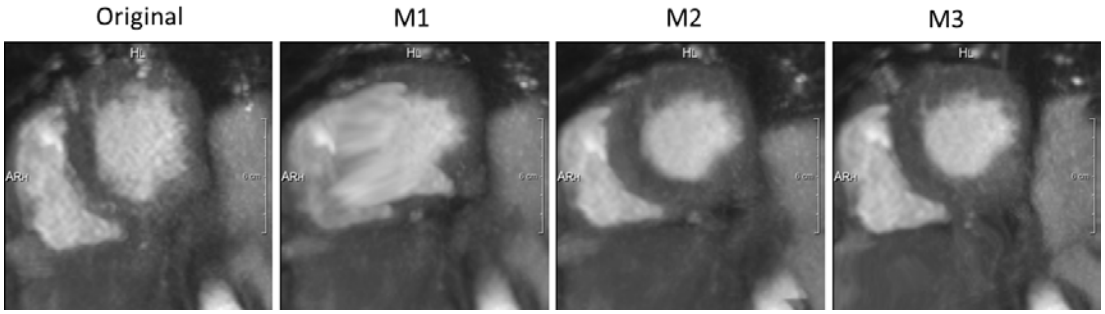

Figure 3.18: Temporal MIPs of the original and the corrected image sequence 6. The application of the *NMI*-based correction with fixed reference frame (M1) clearly resulted in a degenerated image.

based results are calculated to assess myocardial bloodvolume (MBV) and myocardial bloodflow (MBF). For all cases the intensity range within the AHA segments was reduced significantly through all motion correction methods. Figures 3.19 to 3.21 present the results achieved with the original image sequence compared with those derived from the motion-corrected sequence from the *Morphon* algorithm.

Discussion The evaluations presented in the previous paragraph have shown that *NMI*- and B-Spline-based methods as well as the phase-based *Morphon* algorithm have the potential to compensate for breathing and contractile motion of the heart muscle in myocardial perfusion MRI sequences. However, the comparison of successive timepoints resulted in a much better alignment than the sequence registration with a fixed reference image.

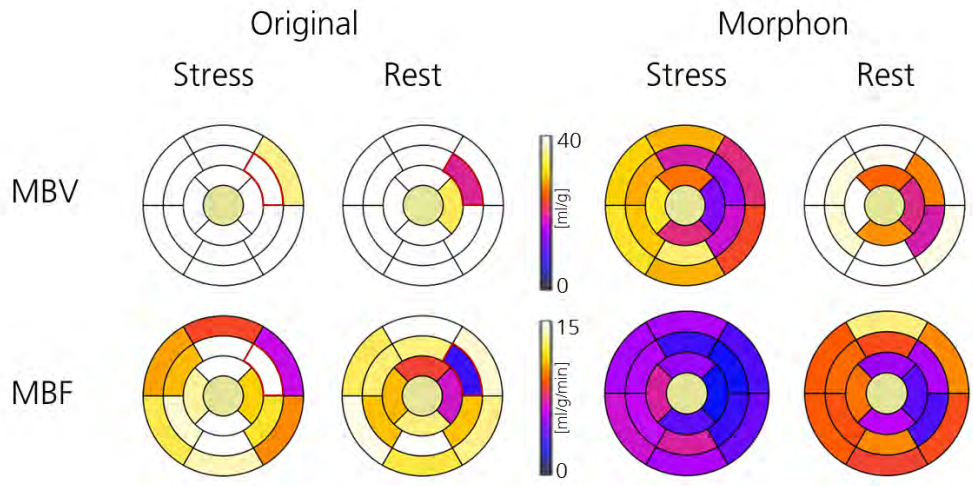

Figure 3.19: Comparison of AHA-segment-based results of bloodvolume (MBV) and blood flow (MBF) for sequence 28 derived from the original data and after motion correction with the *Morphon* algorithm. The patient has a known LAD stenosis > 75%. In the results derived from the corrected image sequence, suspicious segments show lower values (darker colors) in stress as well as rest perfusion bulls-eye-plots. In the original sequences, results of stress and rest perfusion analysis are contradictory, e.g., for segment 12 (red border), which shows very low myocardial bloodflow under rest but a high value under stress.

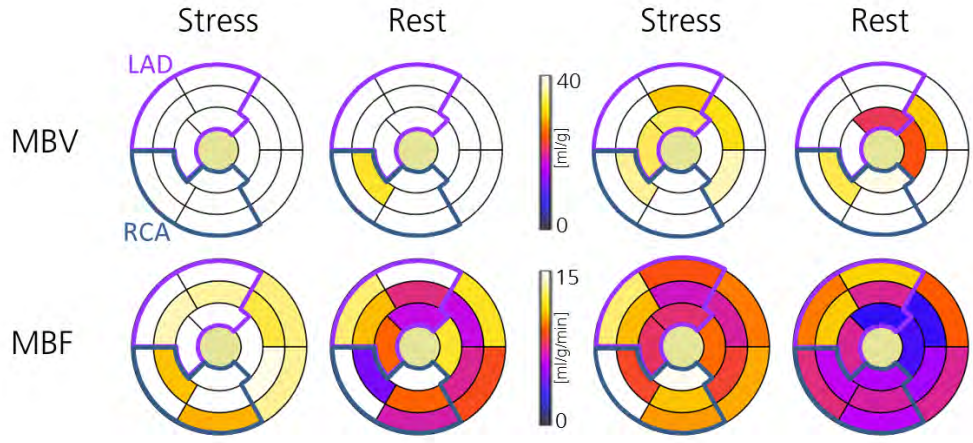

Figure 3.20: Comparison of AHA-segment-based results for case 38, calculated for original and *Morphon*-corrected image sequence. The patient suffers from a LAD stenosis > 50% and late enhancement was detected in the RCA-supplied tissue region. The corresponding AHA supply regions are marked by pink (LAD) and blue (RCA) contours. Based on the original data no suspicious segments are found in the LAD supply region. The *Morphon*-corrected examination shows suspicious segments in the RCA region, the LAD region and the direct vicinity of the LAD region.

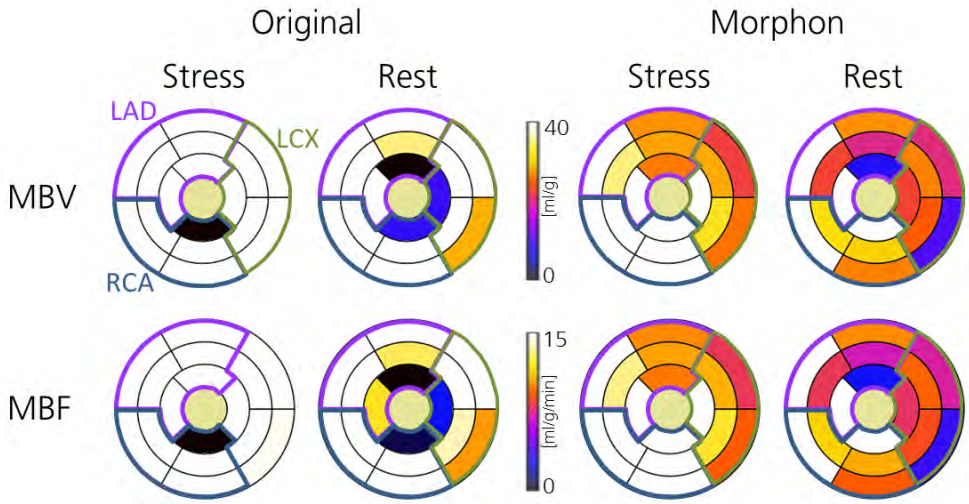

Figure 3.21: Comparison of AHA-segment-based results for case 45, calculated for original and *Morphon*-corrected image sequence. Stenoses > 75% are known to be present in RCA and LCX, LAD stenosis is > 50% and late enhancement was detected in the LCX region. In the original image sequences, apical segments (black) could not be analyzed. Segment 5, which represents the late enhancement region can clearly be identified by the dark blue color in the bulls-eye-plots of the rest perfusion after Morphon-based correction.

Comparison with State-of-the-Art The comparison of two selected time frames per sequence as proposed by Xue et al. [2008] showed that the best improvement was achieved with the *Morphon* algorithm. The average Dice coefficient and the left ventricle motion after registration with this method are almost comparable to their results.
The left ventricular motion within the relevant part of the sequence has also been assessed as suggested in previous publications. With an average motion of 1.76 mm after motion compensation even the *Morphon* method seems to perform worse than even the rigid motion correction methods suggested by Bracoud et al. [2003]. However, in their evaluation the segmentation was performed via a rigid adaptation of the template segmentation and thus the comparability of the results is limited. Furthermore, the intraobserver variation test showed that the reproducibility of the manual segmentation is limited. The distance between the contours produced for the same image was up to 6 mm.

Evaluation Based on Temporal MIP and Gamma Variate Fit The segmentation of the myocardium in the temporal MIPs was also suggested by Milles et al. as a first step for the

assessment of the time-intensity-curves in the corrected image sequence. Their evaluation approach however used the averaged curves based on the myocardium segmentation of the uncorrected image sequence as reference and thereby again depends on the error-prone user delineation of the myocardium in the relevant time frames [Milles et al., 2008]. The new quality measures suggested here consist of the amount of identifiable myocardium and the describability of the intensity change over time through an indicator dilution model, which describes the contrast agent's first pass. This idea is related to the idea of Adluru et al. [2006], who apply a compartment model to generate template images for the registration. The results of this evaluation, which are shown in Table A.2, also indicate that the motion correction with a floating reference is superior to the usage of a fixed reference image. The identifiable myocardium increased most with the *Morphon* algorithm and the deviation from the fitted model curve decreased by 15% on average in these regions.
These newly suggested parameters for the quality assessment of the motion correction aim at a more objective assessment of motion compensation methods. This was achieved through the restriction of the user input to the segmentation on the temporal MIP, which provides stronger contrast than most sequence time frames, and the automatic calculation of the gamma variate fit error. A further improvement would be the automatization of the myocardium segmentation in the MIP image, which is related to the myocardium detection in cardiac function MRI.

Comparison of Results with Other Clinical Findings The actually relevant question is, whether the suggested correction method provides sequences, which are suitable for the detection of underperfused myocardial regions. This is difficult to assess, because the gold standard methods for the detection of perfusion defects are conventional X-ray angiography, which does not directly deliver perfusion information, as well as nuclear imaging with PET or SPECT. The latter methods on the other hand deliver data with a very coarse resolution. The presented assessment of the diagnostic benefit of the motion correction of the given datasets was based on reference results from coronary angiography and late enhancement MRI. These methods provide complementary results. From the angiographic data, possible causes of perfusion defects can be detected. If the stenosis is relevant for the myocardial perfusion, it can be expected that a perfusion defect is visible at least in the stress sequence.

The late enhancement MRI data on the other hand shows tissue defects, which correspond to regions with no perfusion. It is thus expected that in the rest perfusion sequence, regions with known late enhancement show almost no perfusion. For these regions, the later acquired stress perfusion sequence is disturbed by the beginning late enhancement effect, the contrast agent accumulation in the fibrotic and necrotic tissue.

The presented results have shown that the decrease of the intensity variations within the myocardial segments through the motion correction did not result in a decrease of the distinguishability of healthy and diseased tissue. In all inspected cases, known defects were clearer perceivable after motion correction. Figure 3.22 shows screenshots of the original and the corrected parameter images of sequence 52. The infarcted myocardium as identified in the late enhancement MRI image can clearly be distinguished in the corrected image.

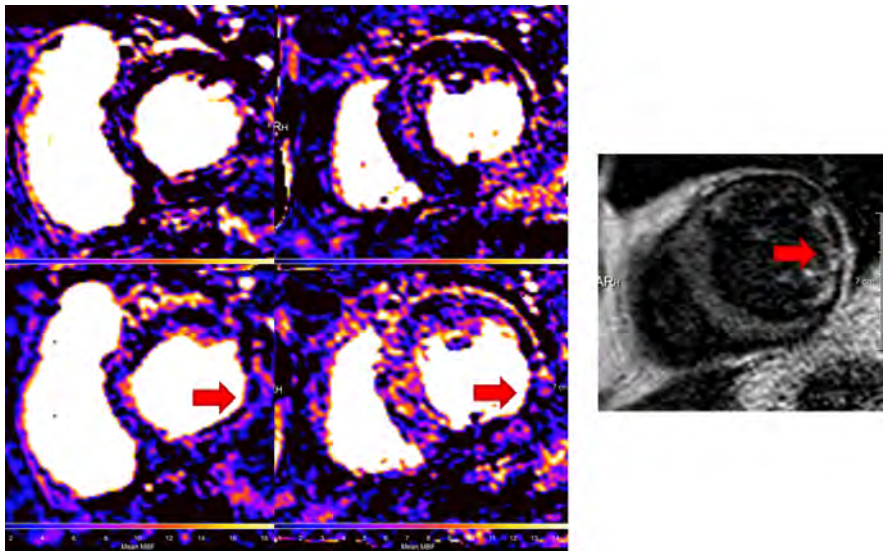

Figure 3.22: Comparison of parameter maps before (upper row) and after motion correction with the *Morphon* (lower row). The location of the infarct region in the lateral wall is shown in the late enhancement image on the right. The parameter map in the upper row does not allow a clear identification of the infarct region whereas in the lower row images the infarct region is distiguishable as a dark region with low parameter values.

3.3 Discussion

In the previous section a new composition of methods and evaluation results for the fusion of cardiac images and the compensation of misalignment due to breathing and contractile motion was presented. The proposed methods consist of

1. A landmark-based fusion of data acquired in different reference systems.
2. An intensity-based slice-to-volume registration for the additional alignment of image slices, which are impaired by motion.
3. Intensity- and phase-based registration techniques for the compensation of movement and deformation within myocardial perfusion sequences.

For registration of the sparse arbitrarily oriented and time-dependent MRI datasets, the existing registration methods, which had been designed for high resolution volume data were adapted. Furthermore, interaction and workflow concepts were developed to enable the landmark setting and the fusion of the different datatypes. This included the reformatted views of the volume data in the sparse data orientation. Furthermore the identification of the perfusion reference timepoint suitable for the fusion registration was added.
The evaluation with datasets from clinical routine has shown that good results can be achieved with the methods presented for task 1 and task 2. The achievable accuracy is limited, if the contraction phases that are represented through the images do not correspond. Because the provided methods aim at leaving the volumes of the structures of interest unchanged, deformation is not compensated. A desirable future improvement is the automatic detection of contraction phase mismatches. For the motion compensation in perfusion MRI sequences two methods have been evaluated. The first method is based on a conventional approach with an intensity-based similarity measure and the search for suitable transformation parameters. It uses *NMI* and a combination of rigid and B-Spline transformations. This method is closely related to approaches by other authors, whereas the application of the second approach, the phase-based *Morphon* algorithm introduced by Knutsson and Andersson [2005] for MRI perfusion data is new. Here, a deformation field is derived directly from the comparison of quadrature filter responses in reference and template time frame. The comparison with previously published results based on expert segmentations in the original and corrected sequences indicate that both methods are suitable if used with a

floating reference image. The *Morphon* however delivered slightly better results than the *NMI*-based motion compensation with B-Splines.
In order to achieve a higher objectivity and to better assess the suitability for clinical interpretation two new quality measures have been suggested here, namely the amount of identifiable myocardium in the temporal MIP of the image sequence as well as the deviation of the voxels' time-intensity-curves from a fitted model. These parameters also indicate that the *Morphon* method is well suited for the motion compensation in perfusion MRI sequences.

The major contribution of this chapter is the compilation of a suitable method set for the combination and motion correction of cardiac CT and MRI datasets for the integrated analysis of the myocardial perfusion. For the motion compensation of myocardial perfusion MRI sequences, a phase-based method has been compared with a conventional approach using methods proposed in literature as well as new quality assessment parameters. The objective of the introduction of these new parameters is to provide more objective results than those achieved with conventional measures based on expert segmentations.

4

Image Analysis

There are two major goals in the analysis of the cardiac CT and MRI data. The first goal is to provide visualizations, which assist the clinician in the detection and the assessment of the patient-individual anatomy and the pathological changes. The second goal is to support the quantification of these changes.

Regarding the coronary arteries, this requires the extraction of the coronary tree from the angiographic dataset (CTCA or MRCA). The coronary artery centerlines can then be used to generate visualizations for the inspection of the vessel wall and form the basis for the lumen diameter measurement.

The perfusion defects caused by lumen decreases due to vessel wall pathologies can be assessed through the analysis of the myocardial intensity curves in the perfusion MRI sequences. Here, regions that exhibit pathological intensity curves have to be detected. Finally, already infarcted tissue has to be detected in the late enhancement image datasets. For these data, it is important to provide accurate information about the transmurality of the infarction, which is an important indicator for the muscle's ability to recover after revascularization therapies.

Angiographic as well as late enhancement data can be acquired using CT as well as MRI. Therefore, methods have been developed in such a way that they can be applied to data from both modalities.

The first section of this chapter describes methods for the detection of coronary arteries in CTCA and MRCA data. Section 4.2 and 4.3 describe the segmentation methods developed for the analysis of the myocardial viability status based on late enhancement images and perfusion sequences.

4.1 Coronary Tree Analysis in CT and MR Angiograms

The examination of the coronary tree requires the visualization of the patient-individual coronary anatomy, the visualization of selected vessel branches in curved, stretched and cross MPRs and the quantification of stenoses via diameter and area measurements. Figure 4.1 depicts typical volume rendering and MPR visualizations. Because the ribcage and

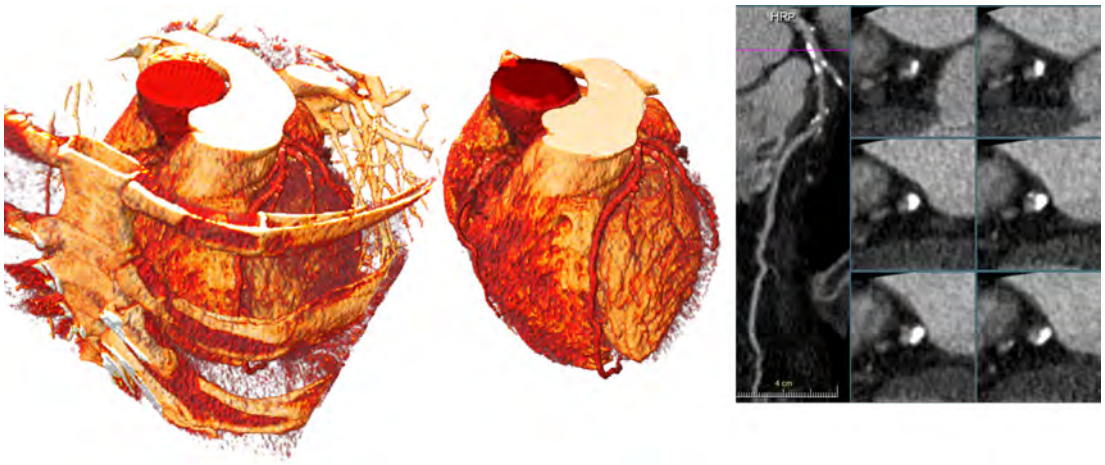

Figure 4.1: Data visualization for coronary artery analysis. The 3D images depict the volume rendering of the dataset with and without ribcage removal. The 2D images depict reformatted views along and perpendicular to the LAD centerline to support the inspection of plaque and stenoses (image data courtesy of Prof. A. Mahnken, University Hospital Aachen).

other surrounding structures cloak the heart in volume rendering views, a segmentation of the heart and it's surroundings are important to enable meaningful 3D visualizations. The reformatted views are based on the vessel centerlines, and the stenosis quantification and advanced vessel wall analysis requires a lumen extraction. So, the major components of vessel analysis algorithms are:

1. Pre-processing of the image volume
2. Extraction of the coronary artery centerlines
3. Segmentation of the coronary artery vessel lumen

4.1.1 Existing Approaches for Coronary Artery Analysis

An overview of algorithms for vessel analysis in CTA and MRA data was given by Lesage et al. [2009b]. Figure 4.2 presents a simplified version of their vessel extraction scheme di-

agram that covers only coronary tree analysis approaches. The description of algorithmic

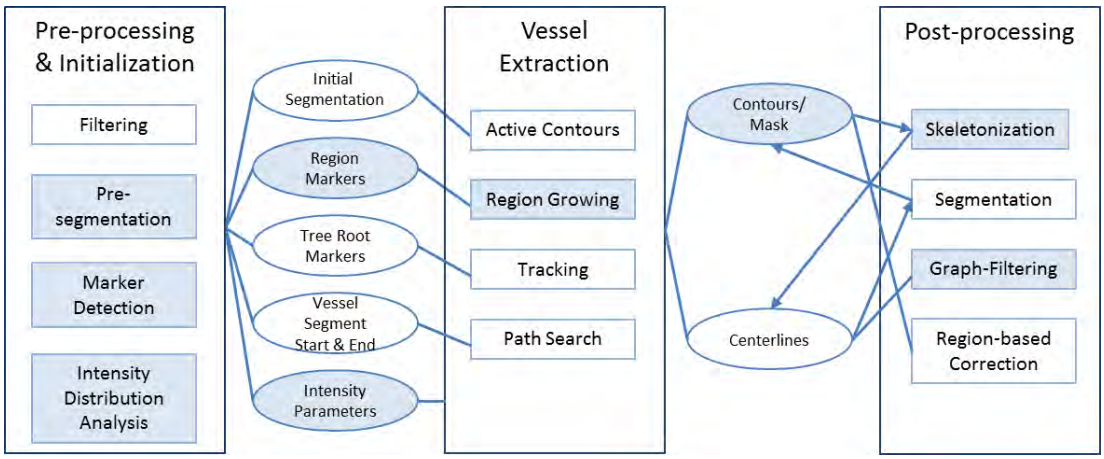

Figure 4.2: Structure and types of algorithms for coronary artery analysis. The ellipses indicate results whereas the rectangles mark algorithms. The algorithmic steps, which are implemented for the approach described in this work are highlighted in light blue.

approaches for the given tasks follows the structure shown in Figure 4.2. The paragraphs describe the algorithmic approaches for the components listed in the subboxes of the processing steps. Actual solutions are always composed from these components. The two major strategies differ in the order of the extraction of the centerline and the vessel lumen.

Pre-processing and Initialization An optional first step for the analysis of the coronary arteries is the isolation of the heart and the automatic initialization of the detection of centerlines or lumen respectively. Dedicated approaches are usually based on knowledge about intensity distributions and anatomy. A straightforward method is the combination of search ray profile analysis with basic assumptions on the structure and intensity of the regions of interest. The ray analysis approach can be used for the detection of the descending aorta as well as for the myocardium [Saur et al., 2008, Lorenz et al., 2004]. The approach by Wang and Smedby [2008] first removes the ribcage through a combination of a lung segmentation with a live wire method. The aorta detection is based on 2D Hough transformations. Florin et al. apply an initial graph cut segmentation to detect the heart, which is then approximated by a spheroid to cut out the heart [Florin et al., 2004]. A related approach combines the graph cut segmentation with automatic seed region detection [Funka-Lea et al., 2006]. This seed region is then used to determine appropriate edges and prevent leakage. Many

approaches apply shape models for the heart detection. Kitslaar et al. use the Hough transform for circles to detect the aorta and apply a 2D balloon model to determine the heart slice-wise [Kitslaar et al., 2008]. 3D shape models have also been used successfully. Zheng et al. combine marginal space learning (MSL) with an active shape model. With this advanced machine learning method they achieve better results than the earlier graph-cut-based approaches [Zheng et al., 2010b]. The *Depth First Model Fit* uses an anatomical model of the complete heart to locate the coronary ostia [Zambal et al., 2008].
The algorithm by Tek et al. detects the ostia from a segmentation of the left ventricle and the aorta, which are detected via brightness and shape assumptions [Tek et al., 2008].

The vessel extraction is often supported by a prefiltering step to avoid artifacts and enhance tubular structures. To this end Hessian-based filters [Frangi et al., 1998, Wink et al., 2002, Olabarriaga et al., 2003, Zhou et al., 2010] as well as anisotropic diffusion have been successfully applied [Metz et al., 2007].

Vessel Extraction: The vessel extraction techniques are roughly grouped into lumen detection methods and centerline detection methods.
Lumen Detection Based on Image Information The algorithmic approach described in the next section uses an adapted region growing approach and was one of the first dedicated to the problem [Hennemuth et al., 2005]. Further developments based on the presented concept tried to improve the segmentation depth and avoid leakage by controlling the growth fronts separately [Bock et al., 2008, Metz et al., 2007]. Closely related to this approach are wave-front propagation methods which correspond to a segmentation with a lens-shaped growth front. Lorenz et al. apply Fast Marching with uniform Euclidean speed and binary inclusion criterion to detect the coronary arteries [Lorenz et al., 2003].
The application of active contour methods, especially level-set-based approaches, have been proven to be applicable for the segmentation of small vessels [Lorigo et al., 2001, Vasilevskiy and Siddiqi, 2002, Nain et al., 2004, Holtzman-Gazit et al., 2006], and few authors published the application of 2D and 3D level set segmentation to the coronary arteries and calcified plaque [Toumoulin et al., 2003, Mueller and Maeder, 2008]. All previously described methods aim at the detection of the vessel lumen. The vessel centerline is then derived in a post-processing step.
Centerline Detection Based on Image Information This class of methods is dedicated to the

direct extraction of the artery centerlines. Minimal path approaches determine an optimal path between two initialization points with respect to certain quality features such as image intensities, path length, curvature, vesselness, etc.. To this end, graph-based path search methods like the Dijkstra algorithm [Dijkstra, 1959] as well as the faster *A**-algorithm have been applied to find a discrete optimal path [Olabarriaga et al., 2003, Wink et al., 2000]. Due to the discretization, the accuracy of these graph-based algorithms is limited by the image resolution. Better results can be achieved with the *Fast Marching* approach, which can be used to determine centerlines with subvoxel accuracy [Yang et al., 2004].
In contrast to path search algorithms, which require the input of start and destination, centerline tracking methods can be used to build trees a starting point. Centerline tracking is an iterative process. One step consists of a path prediction based on model assumptions or image features and a re-centering based on local optimizations. Woerz et al. apply a cylindrical intensity model with Kalman filtering to segment the arteries in MRA images [Gong et al., 2003, Wörz and Rohr, 2007]. A moment-based approach for centerline detection is proposed in Larralde et al. [2003]. Features used to recenter the inital centerline points are determined on cross sections [Wesarg and Firle, 2004] or derived from three dimensional models [Friman et al., 2010, Zambal et al., 2008]. Due to the incorporation of model assumptions, tracking methods are more robust to noise and image artifacts than region-based methods or shortest-path approaches. On the other hand, these methods are sensitive to derivations from the underlying model such as different intensity distributions.
Recent approaches proposed stochastic modeling to enhance the robustness of the vessel detection. Particle filters and recursive Bayesian estimation schemes are used to model the centerline detection as a recursive estimation problem. The parameter sets and models, which are predicted using this approach, concern the shape of crossections [Florin et al., 2005] or a medial-based geometric model [Lesage et al., 2009a]. Friman et al. achieved a high accuracy and robustness with a 3D template and multiple hypothesis tracking in the Coronary Artery Tracking Challenge (http://coronary.bigr.nl/) described below [Friman et al., 2010]. This approach has also been successfully applied to MR coronary angiography data [Velut et al., 2010].

Post-processing: Few approaches directly combine centerline and lumen surface detection [Li and Yezzi, 2006, Benmansour and Cohen, 2009]. In all other approaches, a post-processing step is applied to derive either the tree skeleton or the vessel lumen, respectively.

Skeletonization Voxel masks such as provided by the region growing or wave front propagation methods are most often processed with homotopic thinning [Palagyi and Kuba, 1998]. This means that the created skeleton is topologically equivalent to the mask it was based on and thus inherits connectivity properties. The basic thinning approach is combined with distance transformations [Metz et al., 2007] and pruning strategies [Boskamp et al., 2004]. These methods solely work on the segmentation result.

Lumen Detection based on Centerlines The extraction of the vessel lumen based on the previous centerline detection however requires the analysis of the centerline surrounding in the image. Simpler approaches perform ray casting or construct the 3D surface from cross sectional 2D segmentations. Recent 3D approaches apply deformable models and graph cuts [Mille and Cohen, 2009, Schaap et al., 2009b].

Graph Construction Other important post-processing steps are concerned with the generation of plausible vascular trees from the initial analysis results. Jomier et al. propose the usage of the Mahalanobis distance with criteria like distance, radius ratio and ridgeness to derive minimum spanning trees from segmented tubular structures [Jomier et al., 2005], whereas Szymczak et al. use heuristics on segment lengths and branching angles to clean up and restructure the vessel graph [Szymczak et al., 2005, Szymczak, 2008].

Schaap et al. have developed a framework for training and evaluation of coronary artery centerline detection [Schaap et al., 2009a]. This framework offers a training set of contrast enhanced low-dose CT datasets from 64-slice scanners with centerlines derived from the manual input of four experts by applying the Mean Shift algorithm for open curves. The evaluation framework provides three overlap measures, namely the total overlap as given by the Dice coefficient, the overlap until the first error occurs, and the overlap with the clinically relevant part of the vessel. The accuracy of the centerline is measured via the distance from the observer input. This framework is provided via the internet and allows the comparison of different algorithms. These are grouped into fully automatic methods, methods with manual initialization, and interactive approaches. The highest accuracy so far was achieved by interactive approaches. The *Multiple Hypothesis Tracking* as well as the related *Bayesian Maximum Path* approach provided the best results regarding coverage as well as local distance when compared with expert reference delineations [Friman et al., 2010, Lesage et al., 2009a]. Another successful approach was the *Tracer* method that builds a tree from candidate points that are determined on the 2D slices [Szymczak, 2008]. The automatic ap-

proaches could not provide the same level of accuracy so far [Zambal et al., 2008, Tek et al., 2008, Kitslaar et al., 2008].

There are many quality criteria for choosing a suitable algorithm in clinical applications. If the coronary artery extraction is simply used as a pre-processing step for the visual inspection of the coronary artery branches and image quality is good, the automatic algorithms by Zambal, Tek and Kitslaar are well suited. If on the other hand a wide applicability independent of field of view and anatomical anomalies is required, most algorithms, which are based on anatomical models will fail. In this case, interactive centerline tracking approaches or lumen segmentation methods might be a good solution, because they can be applied to arbitrary vessel branches. The same accounts for the image intensity distribution. Segmentation methods, which are based on assumptions about the intensity distribution in the surrounding of the coronary arteries might not work on other modalities or in datasets acquired with different parameters. There is generally a tradeoff between automatization and computation time and accuracy.
For a quantitative assessment of stenoses it is highly desirable to provide a segmentation of the vessel lumen. It is well known, that voxel-based approaches are not suitable for this task, because the provided segmentation is too coarse, but it is difficult to assess the performance of the more advanced approaches. There will hopefully be a challenge for the quantification of the vessel lumen in the future.

4.1.2 Coronary Artery Segmentation in CT and MR Angiograms

When this work started, there existed only few publications on the analysis of the coronary arteries in volumetric CT and MR angiographies [Lorenz et al., 2003, Larralde et al., 2003]. That was, because the scanner technology had just started to make volumetric cardiac CT and MR imaging applicable to CAD patients. The presented work was developed with data from 16-slice CT scanners and later adapted for volumetric MRI and low dose CT data from 64-slice scanners. The highlighted boxes in Figure 4.2 show the implemented components. The pre-processing and initialization are new developments, whereas the segmentation and tree analysis are established with adapted algorithms by Boskamp et al. and Siemens SCR [Boskamp et al., 2004].

The pre-segmentation and initialization is based on assumptions concerning shape and size of aorta and coronary arteries on CT and MR image data. First, the cross-section of the

aorta is considered to be nearly elliptic. According to recent studies the aortic lumen diameter is between 27 and 50 mm for adult people [Mao et al., 2008]. The second assumption is, that the coronary arteries arise more or less radially from the aorta. These assumptions are independent from actual intensity distributions and were thus applicable to CT and MRI images.
The proposed algorithm works in three steps. In the initialization step, the region of interest, aorta and the orifices of the coronary arteries are detected. The following artery segmentation step applies a region growing algorithm with automatic threshold control and forms the basis for the centerline detection in the final step.

4.1.2.1 Initialization of the Coronary Tree Detection

The image intensities in the vessel regions of the CTCA datasets depend strongly on the contrast agent dose, application and the timing of the image acquisition [Ramos-Duran et al., 2010]. Figures 4.3 and 4.4 show histograms of CT scans from four different clinical sites, which depict the variability of the intensity distributions. Furthermore, the field of view and the reconstruction kernel, which determines the smoothness of the reconstructed image may be different. The initially applied assumptions about image data and anatomy in CT and MR coronary angiographic images are:

1. The image coordinate system is oriented in such a way that the xy-plane corresponds to an axial slice.
2. The blood filled vessel lumen exhibits high intensity values.
3. On axially oriented image slices, ascending and descending aorta appear as circular regions with diameters between 24 and 45 mm.
4. The length of the ascending aorta amounts up to 6 cm.

These assumptions are applied to find a region of interest, that allows a visualization of the heart without blanketing structures. Furthermore, the seed points for the initialization of the actual vessel segmentation are detected in this step. The ascending and descending aorta are determined using the Hough transformation for circular objects with an approach related to the method proposed by Kovacs et al. [2006]. The original Hough transform performs a projection of possible border points P_b into the Hough space where all possible circle center points P_{bc} for these points are accumulated. Detecting all circular objects is thus

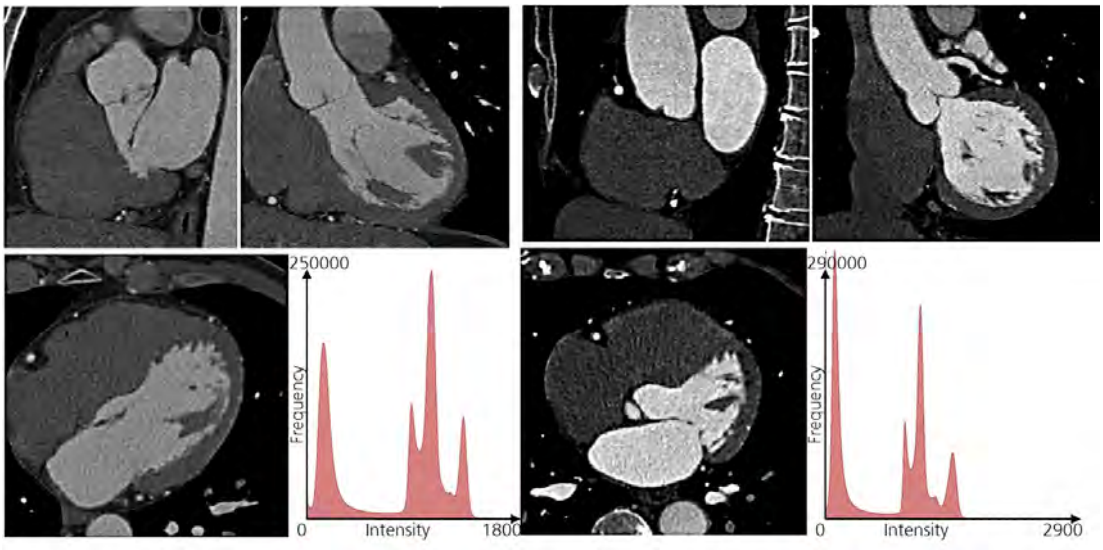

Figure 4.3: Examples for datasets with quality class 1: Reconstruction was performed with a smooth kernel, images display good contrast, clear histogram peaks and almost no artifacts.

very memory- and time-consuming. The determination of appropriate markers for the descending and ascending aorta is therefore only performed on axial slices s_i with a distance d_i between two successive slices in an image volume with resolution (rx, ry, rz):

$$s_i(x,y) = I_{x,y,z_{\max}-i\cdot\left\lfloor\frac{d_i}{rz}\right\rfloor}, i = 1,2,\ldots \tag{4.1}$$

To speed up the calculation the Hough transform in *ITK* allows to consider the gradient direction at a border point and limit the accumulation of possible circle centers to the points on this line. By incorporating the a-priori knowledge of the aortic diameter, the method can be written as presented in Algorithm 5. Figure 4.5 shows an example with an input image I, the gradient directions $\left(\frac{\partial I}{\partial x}(x,y), \frac{\partial I}{\partial y}(x,y)\right)$, the accumulator image I_a and the detected circle centers (x_{c0}, y_{c0}) and (x_{c1}, y_{c1}).

Following the assumption, that the blood filled vessel lumen appears bright, the thresholds t_l and t_u are chosen in such a way that the interval $[t_l, t_u]$ includes the upper 80% of the image intensity range.

The Hough transform on the selected slice s_i results in circle center points (x_{cl}, y_{cl}), which are located either in the ascending aorta, the descending aorta, the pulmonary artery or the spine. To differentiate these regions, the detected points X are grouped into clusters C according to their distance from the regression line $\mathbf{m}$ defined by the current cluster

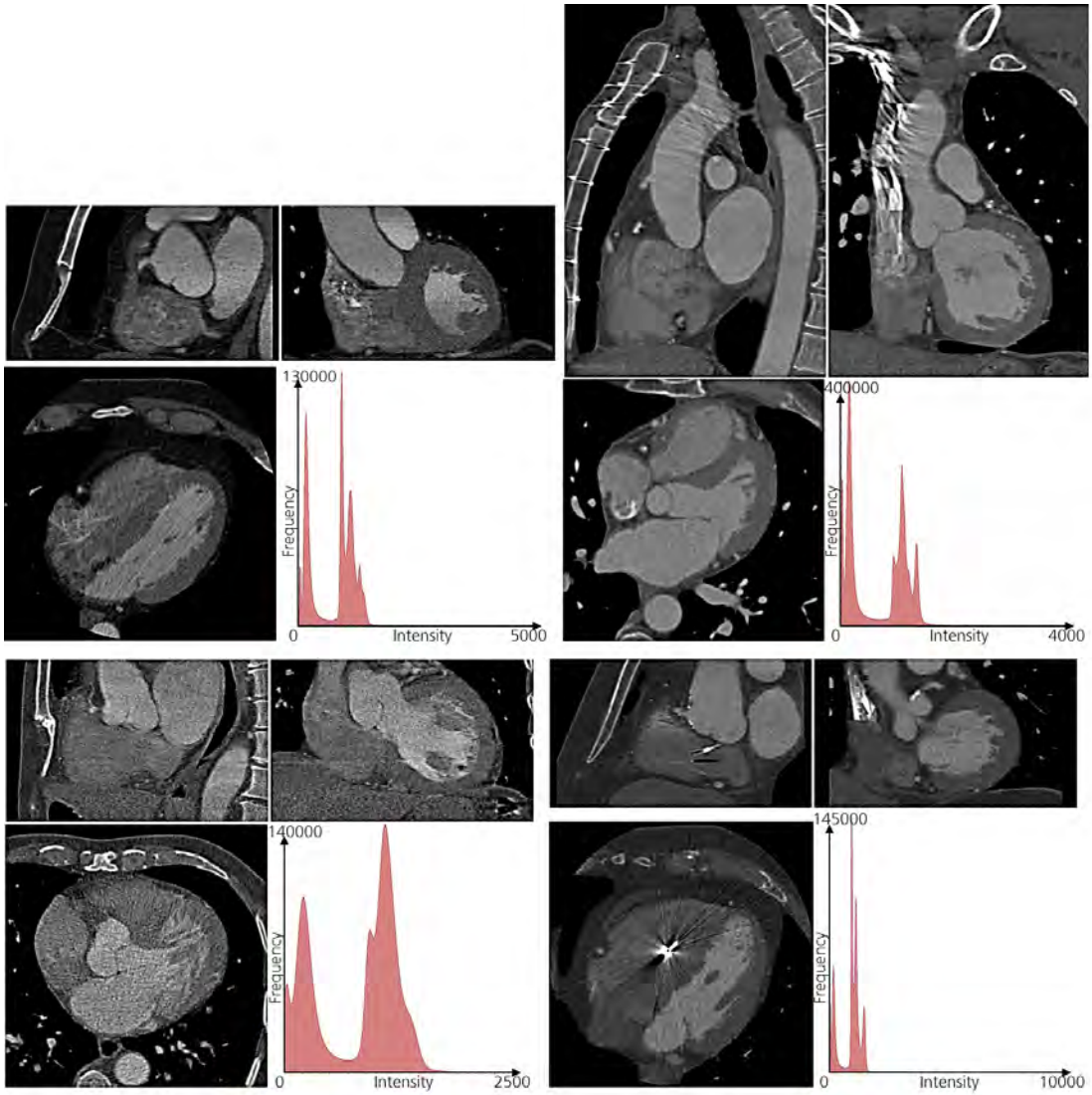

Figure 4.4: Examples for datasets with different coverage, reconstruction kernels and scanner types.
Upper row/quality class 2: The left dataset is noisy (medium-smooth kernel) and has some artifacts from contrast agent inflow. The right dataset covers a bigger volume in order to inspect bypasses. It has streaky artifacts in the aorta.
Lower row/quality class 3: The image on the left shows low contrasted vessels, noise and a step artifact. It's histogram has fewer peaks than observed for images in higher quality categories. The image on the right is strongly disturbed by artifacts which cause unusually high intensity values in the image.

Algorithm 5 Initial detection of the ascending aorta candidates

for all x, y: **do**
{Select image voxels in intensity interval of interest}
if $s_i(x,y) \in [t_l, t_u]$ **then**
{Update accumulator image values of within the given radius interval $[r_{\min}, r_{\max}]$ along gradient direction}
for $\alpha \in [r_{\min}, r_{\max}]$: **do**
$I_a\left(x + \alpha \frac{\partial s_i}{\partial x}(x,y), y + \alpha \frac{\partial s_i}{\partial y}(x,y)\right) := I_a\left(x + \alpha \frac{\partial s_i}{\partial x}(x,y), y + \alpha \frac{\partial s_i}{\partial y}(x,y)\right) + 1$
end for
end if
end for
{Select coordinates of voxels with highest intensities in accumulator image}
$(x_{cl}, y_{cl}) := (x,y) : \max_l \left(I_a(x_l, y_l)\right)$

Algorithm 6 Seed point clustering

for all $\mathbf{x} \in X$ **do**
{Add seedpoint x to cluster C if the distance to the main axis $\mathbf{m}_C$is below the threshold t_C}
for all $C \in \Omega$ **do**
if $\frac{|\mathbf{m}_C \times (\mathbf{x} - \bar{x_C})|}{|\mathbf{m}_C|} < t_C$ **then**
$X_C := X_C \cup \{\mathbf{x}\}$
$\mathbf{m}_C :=$ main axis (X_C)
end if
end for
{Create new cluster, if x could not be added to an existing cluster}
if $\mathbf{x} \notin \bigcup X_C$ **then**
$C_{\text{new}} := \{\{\mathbf{x}\}, \text{main axis}\,(\{\mathbf{x}\})\}$
$\Omega := \Omega \cup C_{\text{new}}$
end if
end for

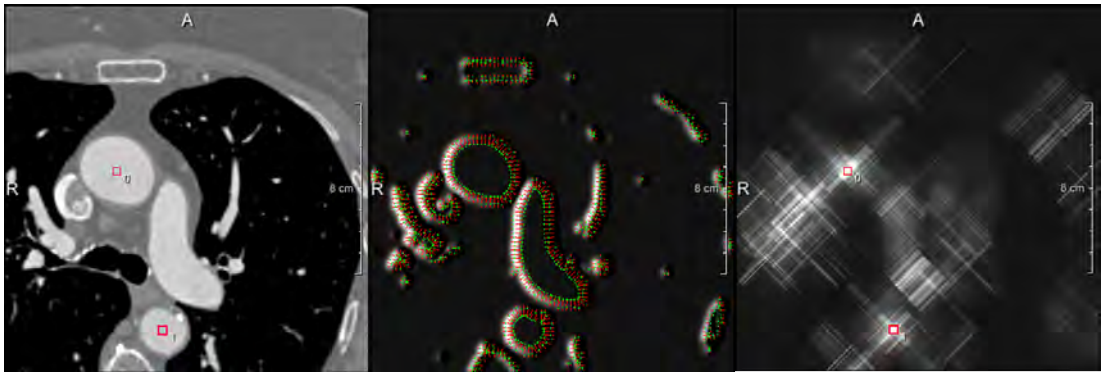

Figure 4.5: Application of the Hough transform for the detection of the aorta. Left: Original image data with canditate markers for the aorta. Middle: Gradient directions. Right: The resulting accumulator image with the detected aorta center canditate markers.

points X_C with a threshold t_C as explained in Algorithm 6. The main axis $\mathbf{m}_C$ of a cluster C is initially set to the slice stacking direction. In case of two points, it is defined by the difference vector. For sets with more points, the cluster's main axis is calculated with the singular value decomposition (SVD) provided within the *numpy* library [Hugunin and Oliphant, 2010]. The SVD calculates a factorization of the $m \times 3$-matrix M_C:

$$M_C = \begin{pmatrix} \mathbf{x}_{C1} - \bar{\mathbf{x}_C} \\ \dots \\ \mathbf{x}_{Cn} - \bar{\mathbf{x}_C} \end{pmatrix} \tag{4.2}$$

$$M_C = U\Sigma V^T \tag{4.3}$$

$$M_C^T M_C = V\Sigma^T U^T U\Sigma V^T \tag{4.4}$$

$$= V\left(\Sigma^T\Sigma\right)V^T \tag{4.5}$$

U and V^T are unitary matrices with dimension $m \times m$ and 3×3 respectively. The right singular vectors, which are the columns of V are eigenvectors of $M_C^T M_C$ and thus represent the main axes of the cluster C. Clusters with more than one circle center point are usually detected for the ascending and descending aorta as well as for the spine. The cluster closest to the origin of the voxel coordinate system is chosen to initialize the segmentation of the ascending aorta.

The seed points in the ascending aorta are used to determine a 3D surrounding from which the threshold interval for the initial region growing is computed. To segment the aorta, a slice-by-slice region growing algorithm is performed, which uses statistical information about the gray value distribution in a predefined neighborhood. This means, that

the neighborhood information is stored in an accumulator image I_a that represents the image region $N_a(x_c, y_c) = \bigcup_{x \in [x_c - 2\rho_{\max}, x_c + 2\rho_{\max}], y \in [y_c - 2\rho_{\max}, y_c + 2\rho_{\max}]} (x, y)$ around the current seed point (x_c, y_c). The size $\rho_{\max}$ of the neighborhood to consider is an input parameter, which is chosen in such a way that it is smaller than the coronary ostia diameter but bigger than small noisy structures or artifacts, which could cause a leakage of the segmentation. In the segmentation step, a 2D region growing is performed on the accumulator array I_a starting with the seed point (x_c, y_c) and applying a threshold $t_a = \frac{3}{4} v_n$ based on the actual number of voxels v_n in the defined neighborhood region $N_{8(2D)}(x, y)$ to determine the voxel set S_z on the current slice z (Eq. 4.6).

$$N(S) = \bigcup_{(x_i, y_i) \in S} N_{8(2D)}(x, y) \setminus S \tag{4.6}$$

$$S_z^i = \begin{cases} (x_c, y_c), & i = 0 \\ S_z^{i-1} \cup \bigcup_{(x,y) \in N(S_z^{i-1}) \wedge I_a(x,y) > t_a} (x, y), & i > 0 \end{cases} \tag{4.7}$$

The segmentation is propagated to the next slice via the center of the fitted ellipse. As the aorta cross-section is assumed to be nearly elliptic, a moment based shape analysis is performed on S_z, which corresponds to fitting an ellipse to the segmented region. The normalized central moments $\mu_{11}, \mu_{20}, \mu_{02}$ are used to determine the eccentricity η, the radii α, β, the orientation ϕ and the area A of the fitted ellipse (Eq. 4.8).

$$\mu_{ij} = \frac{1}{n} \sum_{(x_l, y_l) \in S_z} (x_l - \bar{x})^i \left(y_l - \bar{y}\right)^j, i + j = 2 \tag{4.8}$$

$$\eta = \frac{\sqrt{\mu_{20} - \mu_{02}} + 4\sqrt{\mu_{11}}}{\sqrt{\mu_{20} + \mu_{02}}} \tag{4.9}$$

$$\alpha / \beta = 1{,}05 \sqrt{2 \left(\mu_{20} + \mu_{02}\right) \left(1 \pm \sqrt{\eta}\right)} \tag{4.10}$$

$$\phi = \begin{cases} 0, & \mu_{11} = 0 \wedge \mu_{20} \geq \mu_{02} \\ \frac{\pi}{2}, & \mu_{11} = 0 \wedge \mu_{20} < \mu_{02} \\ \frac{1}{2} \arctan\left(\frac{\mu_{20} - \mu_{02}}{\mu_{11}}\right) \pm \frac{\pi}{4}, & \mu_{11} \neq 0 \end{cases} \tag{4.11}$$

$$A = \pi \alpha \beta \tag{4.12}$$

The center of the ellipse as well as the size and compactness of the segmented region are used to recognize leakage or the start of the left ventricle. The segmentation of the aorta stops if the center coordinates differ significantly between two slices, the ellipse fit does not correspond well with the segmented region, or if the volume increases rapidly (Eq. 4.13).

$$\left|(x_{cz-1}, y_{cz-1}) - (x_{cz}, y_{cz})\right| > d_{\max} \vee \frac{S_z \setminus A_z}{A_z} > c_{\max} \vee \frac{A_{z-1}}{A_z} < a_{\min} \tag{4.13}$$

The parameters $d_{\max}, c_{\max}$ and $a_{\min}$ that control these conditions are chosen according to heuristics derived from example datasets. To enable the detection of coronary arteries in regions located closely to the ventricle, the growth of the segmented region is controlled with two thresholds for $a_{\min}$. If the relation between the segmented region in the preceding slice and the actual segmentation falls below $a_{\min 1}$, only the intersection of the ellipse on the preceding slice and the segmented region of the current slice is considered as part of the aorta. If this relation falls below $a_{\min 2}$, the algorithm stops.

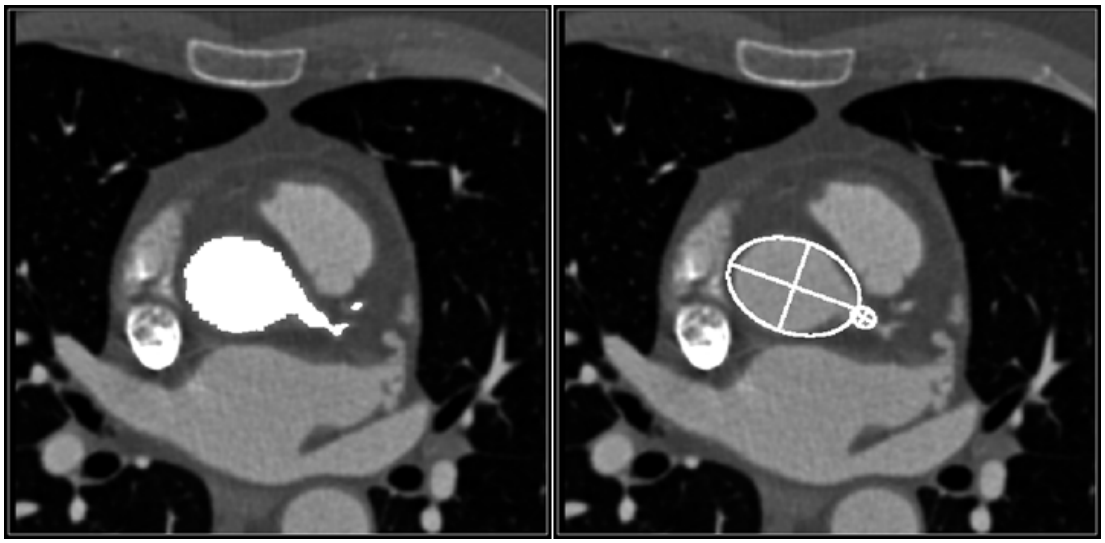

Figure 4.6: Segmentation with shape control. The left image shows the result of the initial region growing. In the right image the ellipse fits for the aorta and the potential ostium are overlaid on the original image slice.

The coronary arteries are detected via an examination of those voxels, which have been segmented by the region growing step but do not belong to the aorta. For this purpose connected regions are detected and a moment-based analysis is performed for these voxel clusters (Fig. 4.6). Considering the size, the center of gravity, the eccentricity and the orientation, the algorithm then chooses the clusters that meet best the conditions derived from the model assumptions (eq. 4.14).

$$\eta < 0,2 \vee \arccos\left(\frac{\cos(\phi)\bar{x}_d + \sin(\phi)\bar{y}_d}{\sqrt{\bar{x}_d + \bar{y}_d}}\right) < \frac{\pi}{4} \tag{4.14}$$

This means that longish voxel clusters outside the aorta ellipse are only accepted, if they point away from the aorta.

4.1.2.2 Segmentation of Coronary Arteries

The selected clusters are used as seed points for a subsequent 3D-region-growing-based on the algorithm described by Selle and Boskamp [Selle et al., 2002, Boskamp et al., 2005]. This method uses a progressive approach that organizes the segmented voxels according to the threshold t_s applied to reach them. In an iterative process, this threshold is decreased until the volume of the segmented region increases rapidly as displayed in Figure 4.7. The

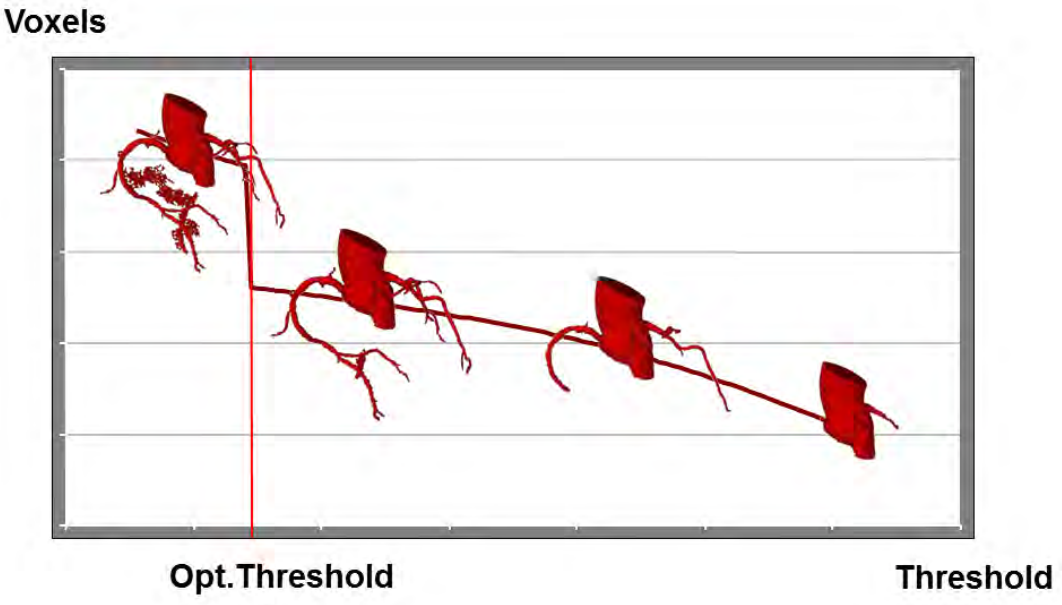

Figure 4.7: Detection of the lower threshold for the coronary artery segmentation. The last value before the volume leaps is chosen as the final threshold t.

presented approach is not capable of detecting the full course of heavily stenosed vessels, because it depends on the direct neighborhood of voxels belonging to the segmented region. However, it is possible to place additional seed points interactively to add missing vessel segments. The region growing algorithm results in a binary image that forms the basis for the derivation of the vessel centerlines. As described by Selle [1999], homotopic thinning is performed to determine the vessel skeleton. This method computes a skeleton for each connected component of the segmentation mask. Therefore, vessel branches with stenoses, which are segmented using different seed points may not be recognized as one vessel branch. To enable the visualization of complete vessel branches in curved and stretched CPR views as shown in Figure 4.8, vessel segments are joined with a path search

approach.

Figure 4.8: Vessel centerline detection for the generation of CPR views. The leftmost image depicts the segmentation result. The LAD is not segmented completely. The second image from the left shows the skeleton with distance dilation, which is used for the path search. The images on the right present the detected centerline and the stretched CPR of the LAD.

4.1.3 Evaluation

The described methods have been tested with datasets from CT and MRI. To evaluate the quantitative measurements, a software phantom as well as a physical phantom have been provided by Siemens Healthcare. The evaluated patient datasets stem from clinical routine and are selected in order to cover a wide range of different scanners, reconstruction kernels and anatomical variation. The subsequent paragraphs give an overview of the method's performance with regard to the automatic detection of aorta, ostia and bypasses.

4.1.3.1 Software Phantom

The software phantom consists of two volumes representing the enddiastolic and endsystolic contraction phases of the heart. Figure 4.9 shows volume renderings as well as orthogonal cuts through these volumes. The image intensities correspond to the typical Hounsfield values of the simulated anatomical structures. The volumes represent a simplified heart with two ventricles and atriae as well as the ascending aorta and three coronary arteries. The coronary arteries exhibit typical abnormalities caused by coronary artery disease and the corresponding therapies. There are darker regions at the vessel wall, which represent soft plaque as well as very bright spots that simulate calcifications. Stents, which have very high

Algorithm 7 Path detection on skeleton/distance image

{Initialize end points}
endpoints := endpoints $\cup \{p_1, p_2\}$
{Explore neighborhood of start point p_1 until endpoint p_2 is reached}
cost(p_1) := 1, priorityqueue = p_1
while ‖priorityqueue‖ > 0 **do**
  pos := top(priorityqueue), priorityqueue = priorityqueue \ {pos}
  if pos ∈ endpoints: **then**
    reachedEndpoints := reachedEndpoints ∪ {pos}
    if ‖reachedEndpoints‖ = 2 **then**
      break
    end if
  end if
  for all $v \in N$(pos) **do**
    if $dist(v,$skeleton$) < t$ **then**

$$\text{penalty} := \begin{cases} 1, & v \in \text{skeleton} \\ 1 + \frac{1}{\text{dist}(v,\text{skeleton})}, & v \notin \text{skeleton} \end{cases}$$

    newCost(v) := cost(pos) + $\|v - \text{pos}\| \cdot$ penalty

$$\text{cost}(v) := \begin{cases} \max(\text{cost}(v), \text{newCost}(v)), & v \in \text{priorityqueue} \\ \text{newCost}(v), & v \notin \text{priorityqueue} \end{cases}$$

    if $v \notin$ priorityqueue: **then**
      priorityqueue := priorityqueue $\cup \{v\}$
    end if
  end if
  end for
end while
{Backtracking to determine minimal cost path}
pos := p_2
while pos $\neq p_1$ **do**
  path := path ∪ pos
  for all $v \in N$(pos) **do**
    if cost(v) < cost(pos) **then**
      pos := v
    end if
  end for
end while
{Smooth path}

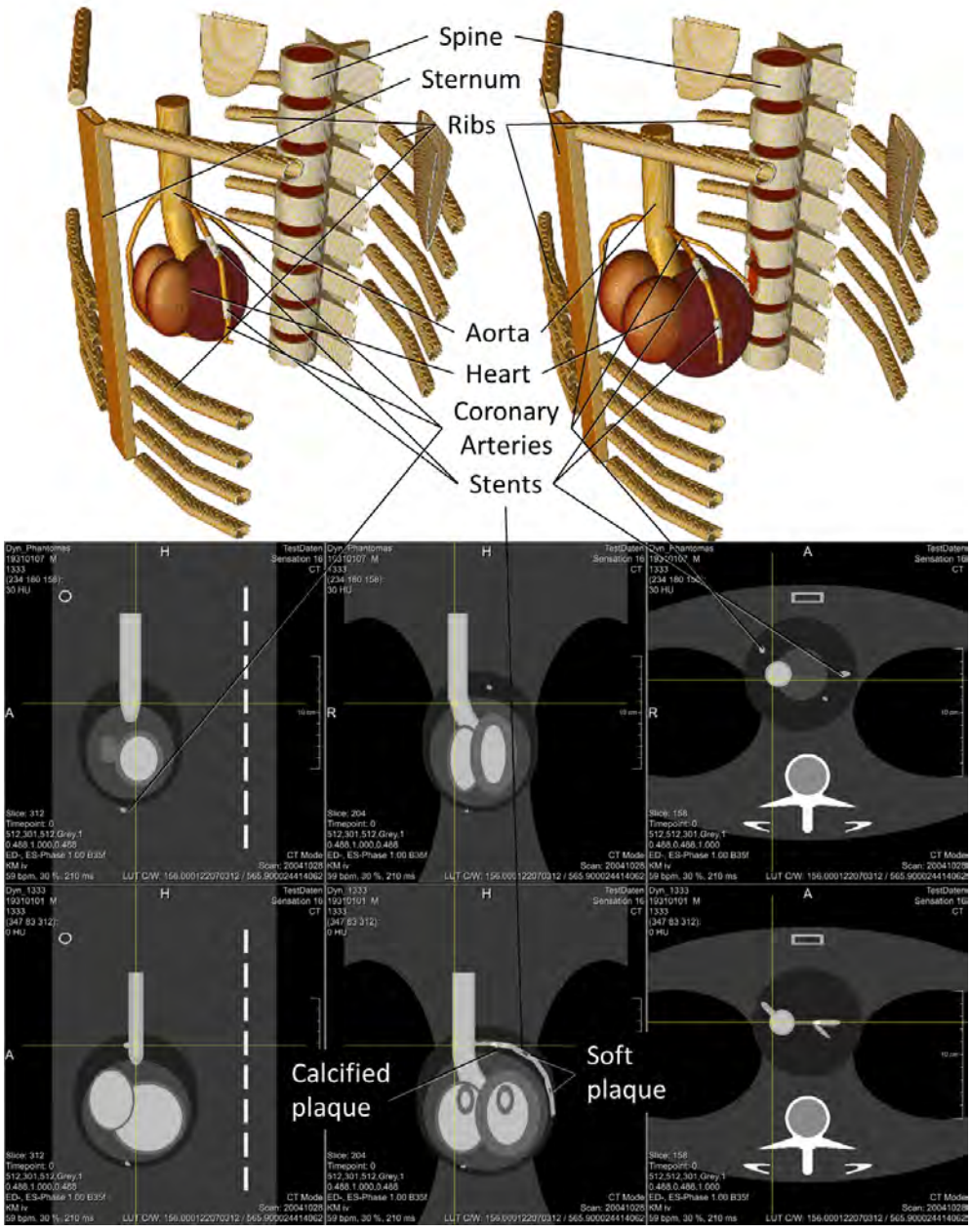

Figure 4.9: Software phantom for the evaluation of the coronary artery detection. The upper row shows volume renderings of the simulated endsystolic and enddiastolic heart phase applying a typical lookup table. The middle row displays orthogonal cut planes through the endsystolic volume, whereas the corresponding views of the enddiastolic volume are presented in the lower row.

intensities in CT images, are also simulated. The simplified heart is surrounded by a simplified ribcage model consisting of spine, sternum, ribs, collar bones and scapulae. These simulated volumes have an extent of $512 \times 512 \times 301$ and the voxelsize is $0.49 \times 0.49 \times 1.00$ mm^3. The coronary artery tree lumen has a volume of 34.28 ml, 2.61 ml in the left coronary artery and 2.07 ml in the right coronary artery.

Results The described method was applied with the standard parameterization for CT datasets. The automatic detection found the aorta and coronary arteries correctly in both volumes. The volumes of the respective segmented arteries were determined through the multiplication of the number of the corresponding voxels with the voxel volume. The segmentation resulted in a volume of 2.61 ml for the left coronary artery and 2.07 ml for the right coronary artery. Figure 4.10 shows the the surface rendering of the segmentation result of the enddiastolic time point.

Figure 4.10: Result of the automatic coronary tree segmentation in the simulated dataset of the enddiastolic heart phase. The volume rendering shows the original image. The aorta is depicted as a yellow surface rendering, whereas the coronary artery segmentation is represented by the red surface.

4.1.3.2 Physical Phantom

The physical phantom is based on the anthropomorphic thorax phantom provided by *QRM* (www.qrm.de). This phantom allows the insertion of cylinders for different calibration and evaluation purposes (Fig. 4.11). For the evaluation of the coronary artery segmentation, a

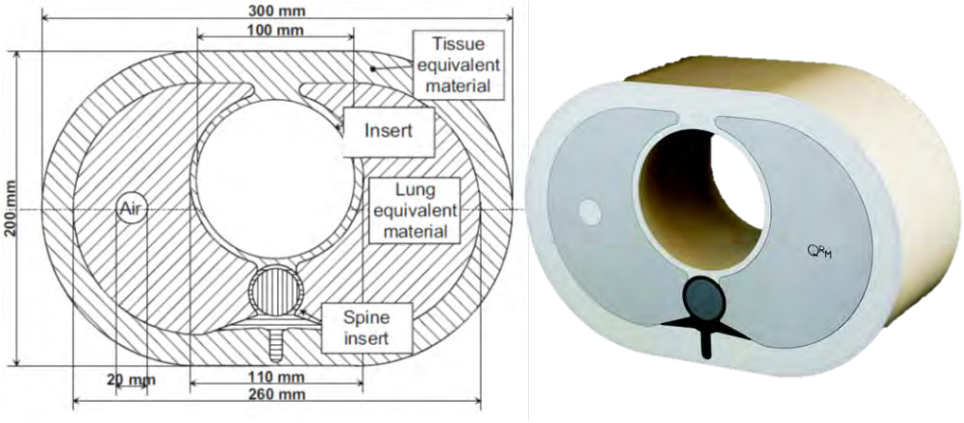

Figure 4.11: Basic thorax phantom. The bore hole allows the insertion of different cylinders.

custom made insert has been developed which contains a simulated coronary tree. The physical phantom has been scanned with a *Siemens Sensation 64* and reconstructed with different slice thickness and reconstruction kernels as described in Table 4.1. The resulting

Index	Extent	Voxel Size	Reconstruction Kernel
1	$512 \times 512 \times 301$	$0.391 \times 0.391 \times 0.400$	B25f
2	$512 \times 512 \times 241$	$0.391 \times 0.391 \times 0.500$	B25f
3	$512 \times 512 \times 241$	$0,391 \times 0.391 \times 0.500$	B30f
4	$512 \times 512 \times 41$	$0.391 \times 0.391 \times 3.000$	B30f

Table 4.1: Parameters of physical phantom scans

image datasets are presented in Figure 4.12. It is clearly visible that the signal to noise ratio is worse than in typical cardiac CT datasets.

Results The aorta was detected correctly in all four datasets, but as shown in Fig. 4.13, the right coronary artery was detected in none of the provided volumes. In dataset 1, which has an almost isotropic voxelsize of 0.4 mm^3, the artery segmentation stopped earlier than in dataset 2 and 3, which have a slice thickness of 0.5 mm. The very thick 3 mm-slices of

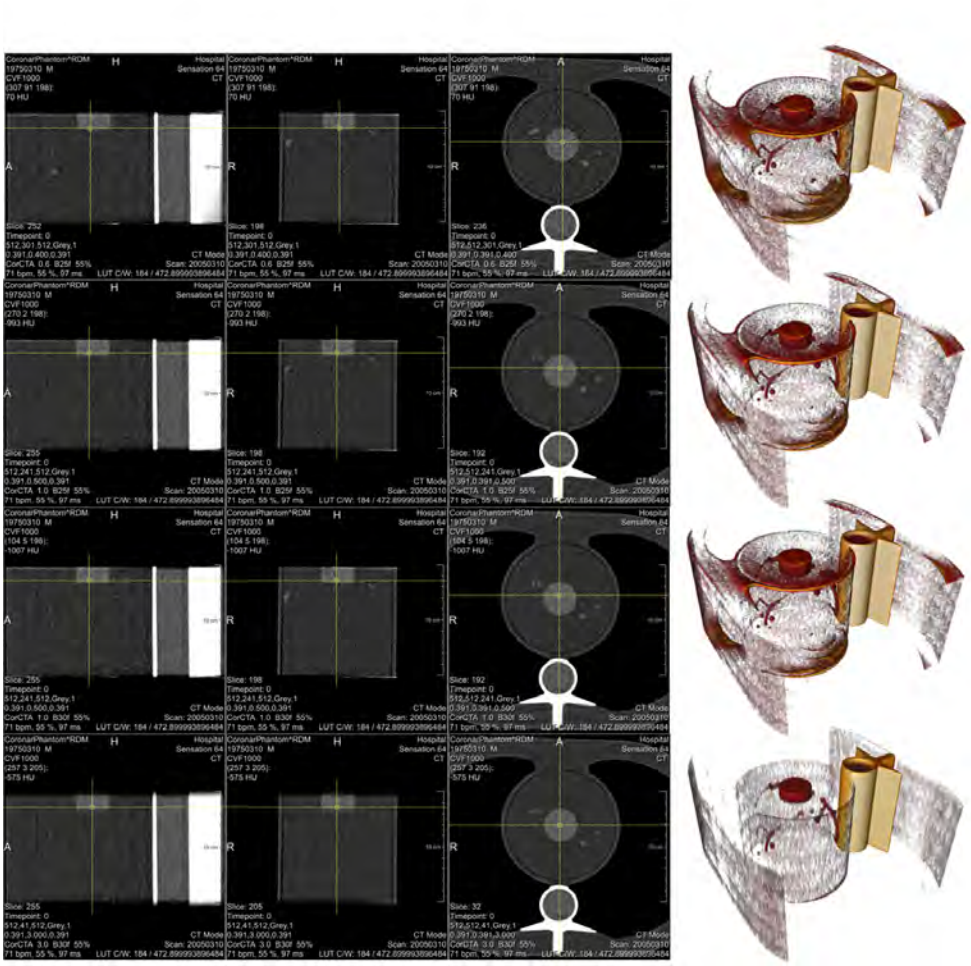

Figure 4.12: Image datasets of the physical phantom for different slice thickness and reconstruction kernel settings. The volume rendering is performed with a typical lookup table for contrast-enhanced cardiac CT datasets.

dataset 4 resulted in a segmentation of the aorta only. Dataset 2 and 3 were reconstructed with kernels of different smoothness. The segmentation achieved a better coverage of the coronary tree in the dataset 2, for which the smoother kernel had been applied.

4.1.3.3 CT Coronary Angiography

To evaluate the performance in clinical practice, 160 CT coronary angiographies of patients with proven or suspected coronary artery disease have been analyzed. In these datasets, soft and calcified plaque as well as stents and bypasses occur at different localizations. 138

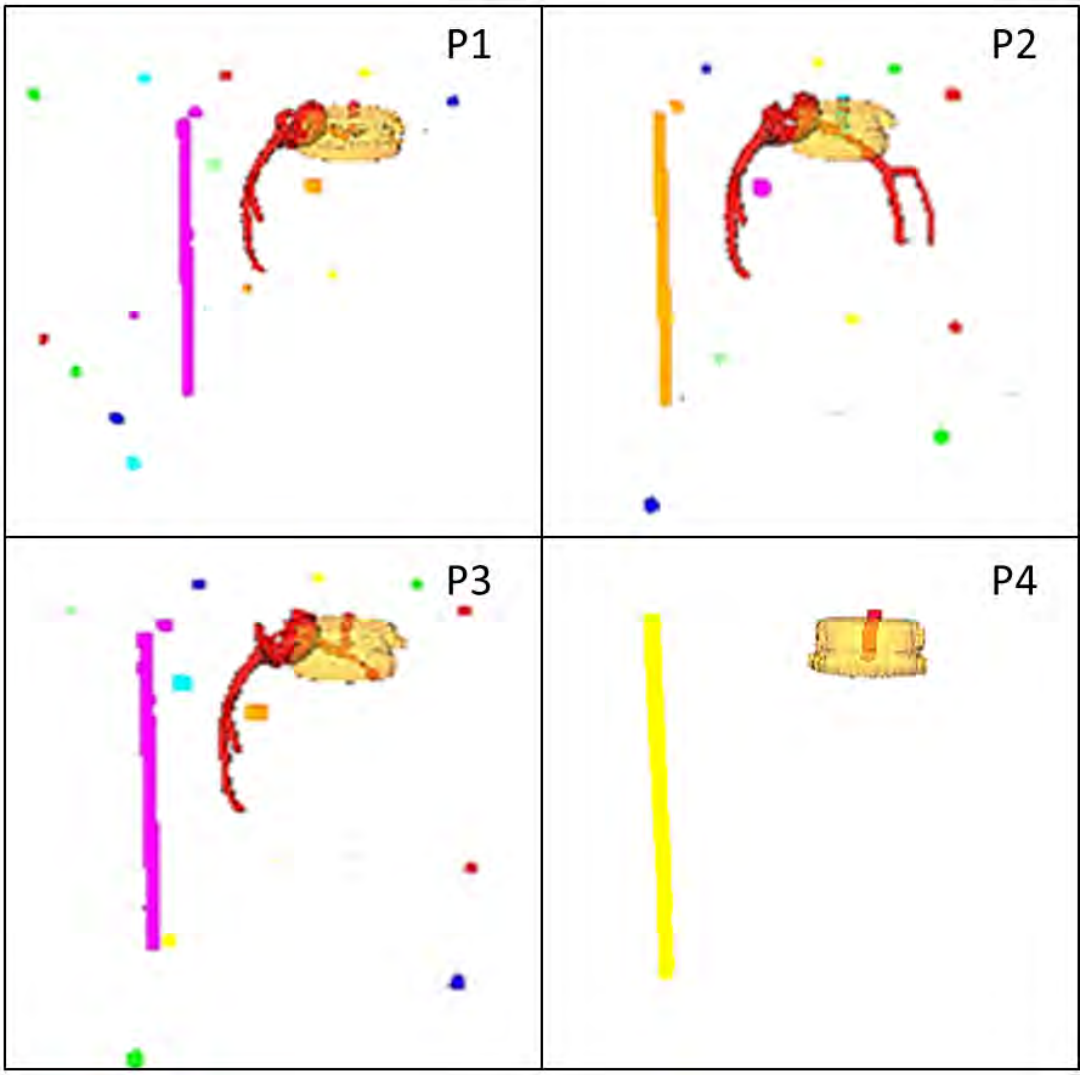

Figure 4.13: Result of the automatic tree detection in the image volumes acquired for the physical phantom. The markers represent the positions of detected circles and are colored according to the cluster they are assigned to. The aorta is shown as a yellow surface rendering whereas the coronary arteries are colored red. The indices in the images correspond to the dataset description in table 4.1. The aorta was detected in all datasets. The detection of the coronary arteries worked best on the image data with 0.5 mm slice thickness and the smooth B25f reconstruction kernel. This indicates that besides a resolution below the coronary artery diameter the signal-to-noise ratio is an important factor for the algorithm's success.

image data sets stem from different clinics, who participated in research projects and are thus acquired with different scanners and different parameterizations. 22 datasets have been provided by the organizers of the vessel tracking challenge at MICCAI 2008. Tables A.3

to A.5 give an overview of the evaluated datasets with scanner, size, resolution, reconstruction kernel and data quality. The reconstruction kernel applied for coronary angiograms often depends on the purpose of the examination. The inspection of the vessel anatomy is easier in images reconstructed with smoother kernels (B20f to B35f on Siemens scanners), but the analysis of small high intensity structures like stents requires the application of a sharper reconstruction kernel like for example B46f. This results in a higher noise level and the enhancement of ray artifacts in the image. For the 138 datasets, which were received directly from clinical partners, the quality assessment was done in cooperation with a medical technical assistant according to the grading proposed in [Hennemuth et al., 2005]:

Category I: Good image quality and easily segmentable arteries (89)

Category II: Image artifacts, inhomogeneous contrast or abnormal anatomy (61)

Category III: Vessels even manually very difficult to segment (10)

Examples for datasets of these quality categories are presented in Figures 4.3 and 4.4 on page 73. The datasets from the coronary artery centerline extraction challenge were delivered in *MetaImage* format, which is used within *ITK* and *VTK* [Chandra and Ibanez, 2001], and do thus not contain detailed DICOM information. As described by Schaap et al. [2009a] these data were acquired with the Siemens Sensation 64 and the Siemens Definition Scanner. The enddiastolic phase was reconstructed with a sharp (B46f) kernel in three cases and a medium-to-smooth (B30f) kernel for all other cases. The datasets were graded following the proposed scheme. Figures 4.3 and 4.4 show examples for the three quality types rated here. Altogether, 89 datasets have been categorized as high quality datasets, 61 image volumes are in category 2 and only 10 datasets were graded as very difficult. Bypasses occured in 8 datasets. As shown in Table A.3 to A.5, resolution, size and thereby coverage differ strongly between datasets. Some volumes contain the carotid arteries and the whole thorax, whereas in other images, only the heart and a short section of the aorta are visible.

Results Figures A.1 to A.3 present the results of the automatic coronary tree detection for all 160 datasets. The ascending aorta was detected correctly in 158 (99%) cases and the ostium the left coronary artery was found in 148 (93%) datasets. The orifice of the right coronary artery was detected in 149 (93%) datasets. However, as clearly visible in the result

images of dataset 132 and 133, the segmentation stopped early in many cases. The algorithm was more successful in the images graded with better quality. In category 1 91% of the left coronary arteries (LCA) and 98% of the right coronary arteries (RCA) were detected. In category 2 the detected ostiae amounted to 95% for the LCA and 90% for the RCA whereas in category 3 the detection rate was 90% for the LCA and 70% for the RCA orifice.

Regarding the reconstruction kernels, the algorithm was most successful in the datasets with the sharp reconstruction kernel (B46f). The detection rate was 96% for the LCA and 100% for the RCA. Most datasets were reconstructed with the medium smooth (B30f) and smooth kernels (B25f, B26f). Here, 94% of the LCA and 91% of the RCA ostia were detected. Few datasets were reconstructed with a very smooth kernel (B20f). In these volumes, 88% of the LCA and 75% of the RCA were found automatically. Dataset 88 and 89 are reconstructions of the same acquisition, the first one applying a smooth and the second one using a sharp kernel. Ostia were detected at the same locations, but the segmentation results differ.

Datasets 11, 14, 24, 48, 88, 89, 128, 136 contain bypasses, which are affixed to the aorta above the coronary ostia. Ten of the twelve bypasses in these datasets were found automatically.

4.1.3.4 MR Coronary Angiography

The whole-heart volume datasets for the inspection of the coronary arteries were acquired with a navigator-gated 3D SSFP sequence with T2 preparation on 1.5T scanners. The parameters are describe in Table 4.2. The acquisition of the slice stack takes around 5 minutes

Table 4.2: Sequence parameters used for the MR image acquisition.

	Whole-heart Volume
Repetition / Echo Time [ms]	4/1.71
Flip Angle	90°
Matrix	256x173
Field of View [mm^2]	320x240
Bandwith [Hz/Pixel]	601
Slice Thickness [mm]	ca. 1.1

and the image data consist of axial slices with about 1.2 mm thickness and a resolution of up

to 0.6 mm × 0.6 mm in plane. Extracellular gadolinium-based contrast agent was applied in 10 cases. An overview of the processed datasets is presented in Table A.6.

Discussion The presented results demonstrate the strengths and weaknesses of the presented method very clearly. The basic assumptions on the coverage of the image volume and the anatomic features resulted in very good overall detection rates for the aorta and the coronary ostia. However, there were also cases, where these assumptions did not apply. In datasets, which cover a very big volume up to the neck, the algorithm detected the truncus brachiocephalicus, which fits the basic assumptions on size and orientation of the aorta. Figure 4.14 also shows a slice of dataset 84 with an aorta diameter of 59 mm. With the initial parameterization, which was searching vessels with a diameter of 25 mm to 45 mm, the aorta could not be detected in this dataset, but with adapted settings this case was also successfully segmented. Another problem is presented in Figure 4.15, where the ostium of the

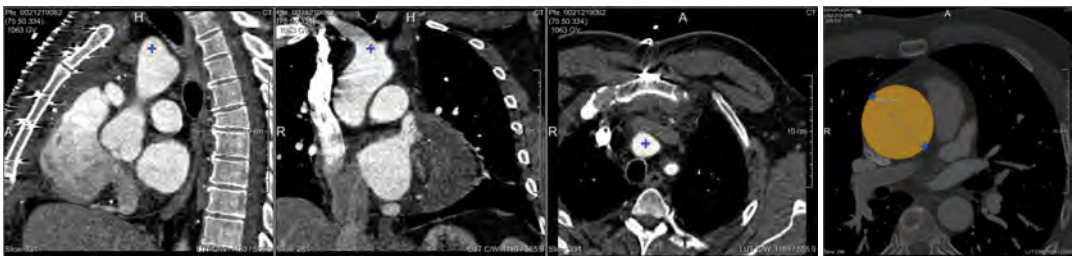

Figure 4.14: Cases, which require an adapted parameterization. In the image on the left (dataset 3) the normal parameterization results in the detection of the truncus brachiocephalicus. The dataset on the right depicts an unusually wide aorta that is not detected with the standard parameters.

left coronary artery points upward and is thus not detected by the slice-wise region growing. For this type of cases, the approach of Zheng et al., which uses steerable features to detect ostia at probable locations might be more appropriate [Zheng et al., 2010a]. One major problem for the ostia detection in the physical phantom were the construction artifacts depicted in Fig. 4.16. These result in contrast barriers, which do not occur in the model the algorithm is based on, and thus hinder the segmentation of the artery tubes.
The detection of 10 out of 12 bypasses was successful. Bypasses were not or only indirectly detected, if they were attached to the aortic arch as shown in dataset 3. This occured in two of the processed datasets (3 and 136). Figure 4.17 shows the positions of the additional ostia in dataset 3. The bypass attached to the ascending aorta is detected automatically

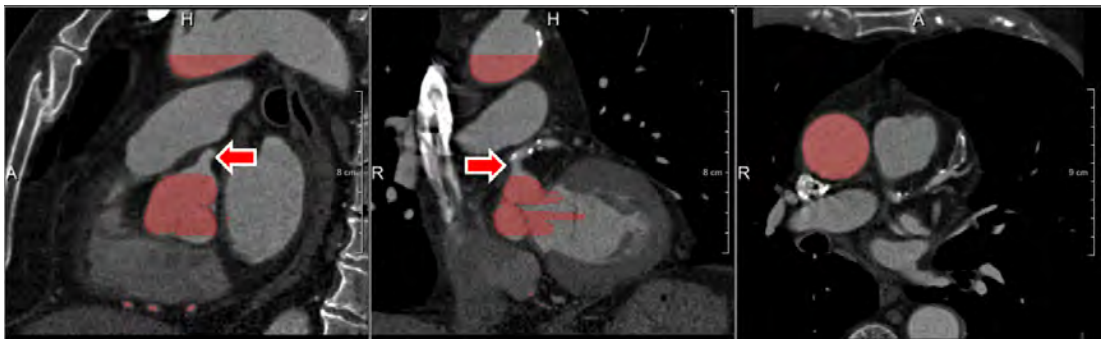

Figure 4.15: Dataset 84. The ostium is not detected by the algorithm because its orientation is upward instead of sideward.

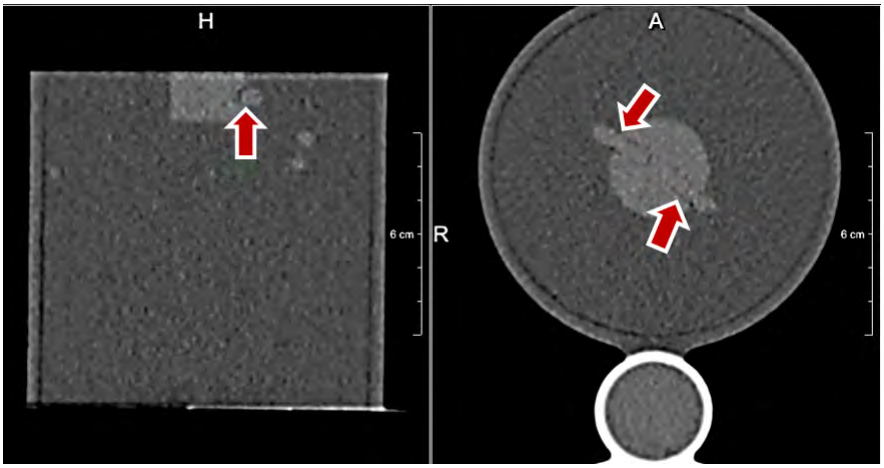

Figure 4.16: Coronary ostia in the physical phantom. The tubes that represent the coronary arteries reach into the aorta tube and thereby and create contrast barriers in the image.

(Fig. A.1), whereas the vessel attached to the carotid artery is only found via the region growing. In unusual cases like this one, other model-based ostia detection algorithms like the one by Zheng et al. [2010a] or the method by Wang and Smedby [2008] would also fail, because ostia are only searched for in the ascending aorta.

Figure 4.17: Volume rendering of dataset 3. The arrows indicate the positions of the additional ostia. While the bypass graft attached to the ascending aorta is detected automatically, the ostium attached to the coronary artery is missed.

The main weakness of the presented method is the inaccuracy of the artery extraction, which is inherent in the voxel-based approaches. The high noise level in the phantom images also poses a problem for the presented method, because the segmentation is based on neighborhood and threshold information. In very noisy data, this results in frayed segmentations or an early termination of the region growing. Bock et al. tried to improve the peripheral segmentation through locally adaptive thresholds and the blockage of detected leakages [Bock et al., 2008], but the initial segmentation is still not reproducible for different images of the same patient. In the phantom data as well as in dataset 88 and 89, one clearly recognizes that the results differ for different scans and reconstructions of the same subject. Thus, the initial segmentation is only used for a first overview and the generation of the vessel centerlines. For an accurate vessel analysis it could be beneficial to combine this initial segmentation with a centerline detection method as proposed by Friman et al. [2010]. for the segmentation of the liver arteries. Because the multiple hypothesis tracking was also very successful in the detection of the coronary artery centerlines, this approach appears very promising.

4.2 Necrotic Tissue Detection in Late Enhanced CT and MR Images

As described in Section 2.3, the contrast agents applied in cardiac CT and MRI accumulate in necrotic and fibrous tissue. Thus, these regions can be identified in CT and MR images, which are acquired 5 to 30 minutes after contrast agent administration. This section addresses the automatic detection and quantification of defective myocardial tissue in these so-called late enhancement image data.

4.2.1 State of the Art in Late Enhancement Detection

Viability assessment with MR imaging has become a gold standard for the detection of necrotic and fibrotic myocardial tissue. For the segmentation and quantification of myocardial regions, which exhibit late enhancement, commercially available tools offer basic methods such as thresholding two or three standard deviations above the average intensity value of a healthy myocardial region [Kim et al., 1999]. An extension of this method, which applies a combination of both thresholds, is used to further classify infarctions into core and peri-infarct regions [Yan et al., 2006].

There exist different approaches to compute a threshold automatically [Breeuwer et al., 2003, Kolipaka et al., 2005], apply clustering methods [Positano et al., 2005], or classify myocardial voxels based on support vector machines [O'Donnell et al., 2003].

The arterial vessels supplying the myocardium run from the epicardial surface inward. A shortening of blood supply is strongest at the vessel endings close to the endocardial surface. Therefore, in coronary artery disease infarctions start subendocardially and grow from the inner to the outer part of the myocardium. This fact has been considered in the approach of Hsu et al. [2006], who perform a feature analysis after the initial thresholding. In addition to checking the subendocardial distance, a 3D connectivity analysis is applied to remove false positive segmentations.

For therapy decisions, it is important to know the transmurality, the degree of penetration of myocardium with infarction from endocardium to the outer surface [Choi et al., 2001]. For this purpose, many approaches simply determine the portion of segmented voxels per radial segment [Noble et al., 2004, Positano et al., 2003a]. This method does not consider the position of the segmented voxels relative to epi- and endocardium.

Newer approaches combine simple thresholding with the proposed assumptions about the

typical scar shape and location [Tao et al., 2010]. Elagouni et al. combine the proposed mixture model approach with a so-called *Fast Region Competition* [Elagouni et al., 2010]. This corresponds closely to an automatic seed detection with a subsequent region growing applying the threshold model derived from the mixture model.
The segmentation of microvascular obstructions, which occur in scans acquired in the early late enhancement phase are only covered by few approaches. Hsu et al. include microvascular obstructions into the late enhancement segmentation via the assumption that they must be included in the outmost contour of the segmentation [Hsu et al., 2006]. Saering et al. add the assumption of an intensity below two standard deviations of healthy myocardium [Saering et al., 2006].

For the analysis of delayed enhancement in CT data, no special approaches have been published so far. Previous clinical studies applied thresholds derived from the standard deviation as proposed by Kim et al. [1999],[Mahnken et al., 2009a].

4.2.2 Late Enhancement Detection with a Mixture Model and Shape Constraints

In contrast to most approaches described in Section 4.2, we do not only want to measure the portion of infarcted tissue in a predefined tissue region, but also to locate the surface of the infarcted region. This information is used to visualize location, shape and transmurality of the infarction, and to compare it with the hypoperfused tissue regions derived from the perfusion images. The algorithm proposed to this end combines a histogram analysis with a constrained watershed segmentation [Hennemuth et al., 2008c, Hahn and Peitgen, 2003]. The method is based on four fundamental assumptions about the processed images and the characteristics of myocardial infarctions:

1. The intensity values of the myocardium in MR images are distributed according to the Rician distribution. The intensity value distribution of CT images can be approximated by Gaussian distributions.

2. Late enhancement is most likely to appear subendocardially.

3. Relevant late enhancement regions are compact crescent-shaped areas of a certain size.

4. Dark regions surrounded by late enhanced tissue are no-reflow-areas and thus belong to the infarct.

Considering these assumptions, the algorithm consists of two major steps, the analysis of the myocardial intensity distribution and the following segmentation.

Analysis of the Myocardial Intensity Distribution in CT and MR Late Enhancement Datasets
The first step in late enhancement detection is the segmentation of the myocardium. This is accomplished semi-interactively with a Live-Wire-algorithm [Schenk et al., 2000]. Segmentations can be interpolated between slices and optimized using a predefined cost function. Once the myocardium has been segmented, the intensity distribution is analyzed by fitting a mixture model of two probability distributions.
The intensity distributions in CT image data result from weighted linear combinations of different X-ray projections. The noise in these projections is known to follow a Poisson process, because the intensities correspond to the number of photons captured during a defined time interval. For the CT image intensities, which result from a combination of a multitude of projections, the central limit theorem applies [Gravel et al., 2004]. This theorem indicates that the mean of a sufficiently large number of independent random variables, each with finite mean and variance, tends to be close to a Gaussian distribution. Thus, CT image intensities are assumed to be Gaussian-distributed [Lei and Sewchand, 1992].
In MRI, acquired image data are intrinsically complex-valued. In conventional acquisitions, the noise in these data can be described by complex Gaussians. The actual data considered for late enhancement assessment shows the magnitudes A_i of the complex values $c_i = A_i\left(\cos\phi_i + \sin\phi_i \mathrm{i}\right) = A_i e^{\mathrm{i}\phi_i}$ as image intensities. Thus, the frequency of an intensity A_i in the late enhancement image is the sum of the frequencies of all complex values c_i with magnitude A_i and arbitrary angles ϕ. If the probability density function (PDF) in the acquired complex data is a complex Gaussian with $\mu = A_\mu e^{\mathrm{i}\phi_\mu}$ the PDF in the corresponding magnitude image is thus a Rician distribution (Eq. 4.15) [Gudbjartsson and Patz, 1995, Hahn, 2005].

$$p(A|\mu,\sigma) = \frac{A}{2\pi\sigma^2}\int_0^{2\pi} e^{-\frac{A_\mu^2+A^2-2A_\mu A\cos\phi}{2\sigma^2}}\,d\phi \tag{4.15}$$

$$p(A|\mu,\sigma) = \frac{A}{\sigma^2}e^{-\frac{A_\mu^2+A^2}{2\sigma^2}} I_0\left(\frac{A_\mu A}{\sigma^2}\right) \text{ with} \tag{4.16}$$

$$I_0(x) = \frac{1}{2\pi}\int_0^{2\pi} e^{x\cos\alpha}\,d\alpha \tag{4.17}$$

I_0 is the modified zeroth order Bessel function the first kind. For $A_\mu = 0$, corresponding with low intensities in the magnitude image, the Rician function takes the simpler form of the

Rayleigh function (Eq. 4.18).

$$p(A|\sigma) = \frac{A}{\sigma^2} e^{-\frac{A^2}{2\sigma^2}} \tag{4.18}$$

For large x the asymptotic form of the Bessel function is [Abramowitz and Stegun, 1965]:

$$I_0(x) \approx \frac{e^x}{\sqrt{2\pi x}} \left[1 + \frac{1}{8x} + \frac{1 \cdot 9}{2!(8x)^2} + \frac{1 \cdot 9 \cdot 25}{3!(8x)^3} + \cdots \right] \tag{4.19}$$

Thus, for large values of $\mu P(A|\mu,\sigma)$ approximates a Gaussian (Eq. 4.20).

$$\begin{aligned} p(A|\mu,\sigma) &\approx \frac{A}{\sigma^2} e^{-\frac{A_\mu^2 + A^2}{2\sigma^2}} \frac{e^{\frac{A_\mu A}{\sigma^2}}}{\sqrt{2\pi \frac{A_\mu A}{\sigma^2}}} \left[1 + \underbrace{\frac{1}{8\frac{A_\mu A}{\sigma^2}} + \frac{1 \cdot 9}{2!\left(8\frac{A_\mu A}{\sigma^2}\right)^2} + \frac{1 \cdot 9 \cdot 25}{3!\left(8\frac{A_\mu A}{\sigma^2}\right)^3} + \cdots}_{\longrightarrow 0} \right] \\ &\approx \frac{1}{\sqrt{2\pi}\sigma} e^{-\frac{(A-A_\mu)^2}{2\sigma^2}} \sqrt{\frac{A}{A_\mu}}, \text{with} A \approx A_\mu \\ &\approx \frac{1}{\sqrt{2\pi}\sigma} e^{-\frac{(A-A_\mu)^2}{2\sigma^2}} \end{aligned} \tag{4.20}$$

Generally, the mixture model fit can be formulated as the task of maximizing the likelihood of a given set of observations $X = \{x_1, ..., x_N\}$ with frequencies $h(x)$ by optimizing the parameters of the applied mixture model. Assuming that we have a set of two classes $C = \{c_{myo}, c_{LE}\}$ with a corresponding parameter set $\Omega = \{\theta_{myo}, \theta_{LE}\}$ that defines the fitted distributions, the likelihood to optimize is:

$$L(\Omega|X,C) = \ln\left(\prod_{x \in X} p(x,C|\Omega)^{h(x)} \right)$$

and the expected log-likelihood can be formulated as follows:

$$\begin{aligned} E_c\left[\ln(L)\right] &= E_c\left[\ln\left(\prod_{x \in X} p(x,C|\Omega)^{h(x)} \right) \middle| x \right] \\ &= E_c\left[\sum_{x \in X} h(x) \ln\left(p(x,C|\Omega)\right) \middle| x \right] \\ &= \sum_{x \in X} h(x) E_c\left[\ln\left(p(x,C|\Omega)\right)\right] \\ &= \sum_{x \in X} h(x) \sum_{c \in C} p(c|x,\Omega) \ln(p(x|c,\Omega) p(c|\Omega)) \end{aligned}$$

Figure 4.18 shows two example datasets from CT and MRI. It is clearly visible that the histogram patterns are different and following assumption 1 on page 94 the CT histogram is

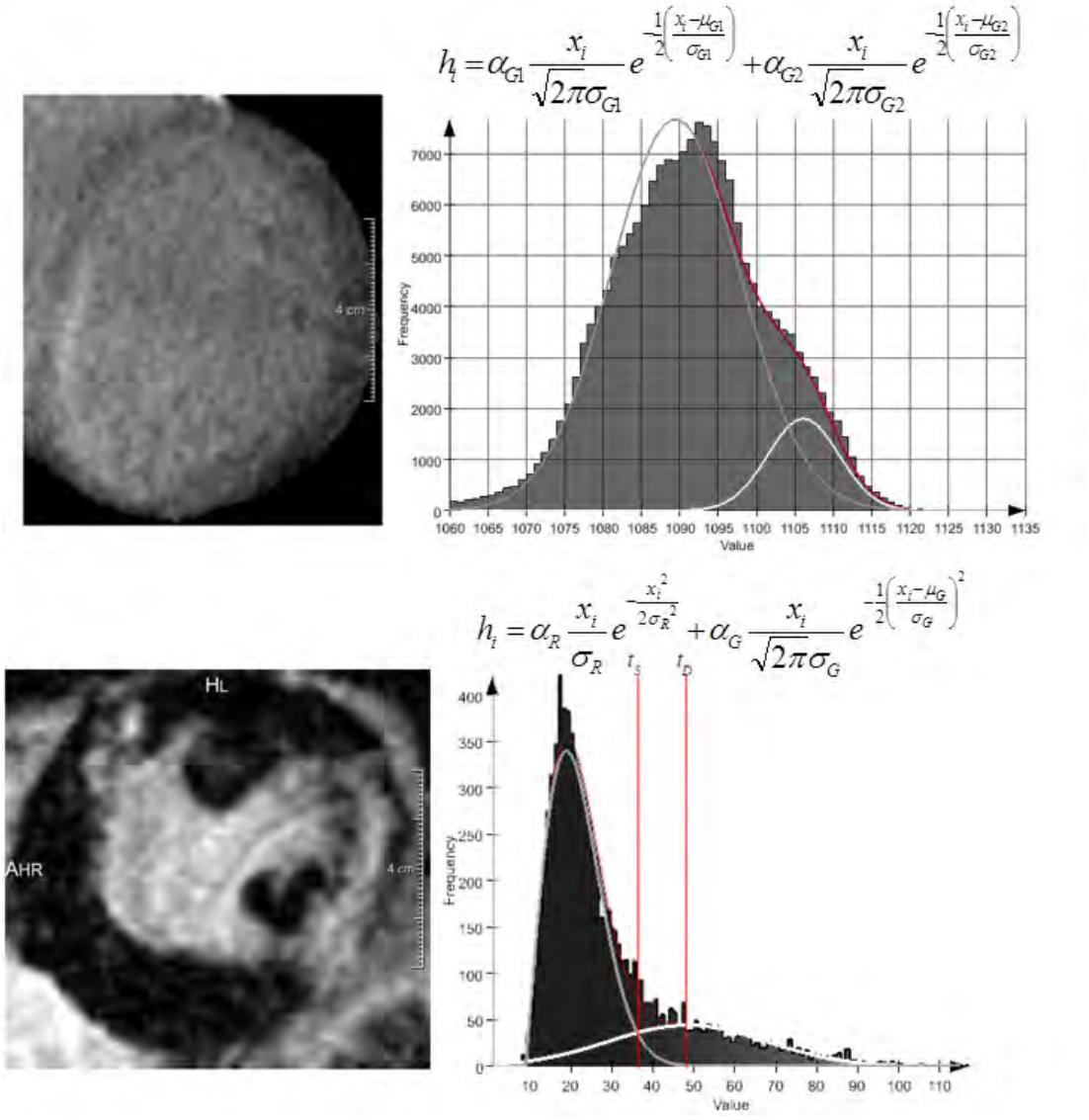

Figure 4.18: Intensity distributions in late enhancement images. The upper row presents a CT late enhancement image with the corresponding myocardial histogram and a fitted mixture model. The row below shows such a histogram analysis for a MR image.

described as a mixture of two Gaussians with class probabilities $p(c|\Omega) \in \{\alpha_{myo}, \alpha_{LE}\}$. For MR image data, this model consists of a Rayleigh distribution representing low intensities and a Gaussian distribution for the bright late enhanced regions (Eq. 4.21):

$$h(x) = \underbrace{\alpha_{myo} \frac{x}{\sigma_{myo}} e^{-\frac{x^2}{2\sigma_{myo}^2}}}_{\text{Rayleigh distribution}} + \underbrace{\alpha_{LE} \frac{1}{\sqrt{2\pi}\sigma_{LE}} e^{-\frac{1}{2}\left(\frac{x-\mu}{\sigma_{LE}}\right)^2}}_{\text{Gaussian distribution}} \tag{4.21}$$

The expectation values can then be formulated as follows.

$$
\begin{aligned}
E_c^{CT} &= \sum_{x\in X} h(x)\left(p(c_{myo}|x,\Omega)\ln\left(\alpha_{myo}\frac{1}{\sqrt{2\pi}\sigma_{myo}}e^{\frac{1}{2}\left(\frac{x-\mu_{myo}}{\sigma_{myo}}\right)^2}\right)+\right.\\
&\quad \left. p(c_{LE}|x,\Omega)\ln\left(\alpha_{LE}\frac{1}{\sqrt{2\pi}\sigma_{LE}}e^{\frac{1}{2}\left(\frac{x-\mu_{LE}}{\sigma_{LE}}\right)^2}\right)\right)\\
E_c^{MR} &= \sum_{x\in X} h(x)\left(p(c_{myo}|x,\Omega)\ln\left(\alpha_{myo}\frac{x}{\sigma_{myo}}e^{-\frac{x^2}{2\sigma_{myo}^2}}\right)+\right.\\
&\quad \left. p(c_{LE}|x,\Omega)\ln\left(\alpha_{LE}\frac{1}{\sqrt{2\pi}\sigma_{LE}}e^{\frac{1}{2}\left(\frac{x-\mu_{LE}}{\sigma_{LE}}\right)^2}\right)\right)
\end{aligned}
$$

To maximize $E_c\left[\ln\left(L(\Omega|X,C)\right)\right]$ the partial derivatives are calculated with respect to the variables μ_{myo} (only CT), $\sigma_{myo},\mu_{LE},\sigma_{LE},\alpha_{myo},\alpha_{LE}$ assuming $\alpha_{myo}+\alpha_{LE}=1$:

$$
\begin{aligned}
\frac{\partial}{\partial\mu_{myo}}E_c^{CT} &= \frac{1}{\sigma_{myo}}\sum_{x\in X} h(x)p(c_{myo}|x,\Omega)\left(\mu_{myo}-x\right)\\
\frac{\partial}{\partial\sigma_{myo}}E_c^{CT} &= \frac{1}{\sigma_{myo}}\sum_{x\in X} h(x)p(c_{myo}|x,\Omega)\left(\left(\frac{x-\mu_{myo}}{\sigma_{myo}}\right)^2-1\right)\\
\frac{\partial}{\partial\sigma_{myo}}E_c^{MR} &= \frac{1}{\sigma_{myo}}\sum_{x\in X} h(x)p(c_{myo}|x,\Omega)\left(\left(\frac{x}{\sigma_{myo}}\right)^2-2\right)\\
\frac{\partial}{\partial\mu_{LE}}E_c &= \frac{1}{\sigma_{LE}}\sum_{x\in X} h(x)p(c_{LE}|x,\Omega)\left(\mu_{LE}-x\right)\\
\frac{\partial}{\partial\sigma_{LE}}E_c &= \frac{1}{\sigma_{LE}}\sum_{x\in X} h(x)p(c_{LE}|x,\Omega)\left(\left(\frac{x-\mu_{LE}}{\sigma_{LE}}\right)^2-1\right)\\
\frac{\partial}{\partial\alpha_i}E_c &= \frac{1}{\alpha_i}\sum_{x\in X} h(x)p(c_i|x,\Omega)-\frac{1}{1-\alpha_i}\sum_{x\in X} h(x)p(c_j|x,\Omega),\\
&\quad i,j\in\{myo,LE\}, i\neq j
\end{aligned}
$$

The formulae for the *Maximization*-step are deduced by setting these partial derivatives

to 0. For the application to MR data, this results in the following formulae:

$$
\begin{aligned}
\alpha_{myo}^{j+1} &= \frac{\sum_{x\in X} h(x)p(c_{myo}|x,\Omega^j)}{\sum_{x\in X} h(x)} \\
{\sigma_{myo}^{j+1}}^2 &= \frac{\sum_{x\in X} h(x)p(c_{myo}|x,\Omega^j)x^2}{2\sum_{x\in X} h(x)p(c_{myo}|x,\Omega^j)} \\
\alpha_{LE}^{j+1} &= \frac{\sum_{x\in X} h(x)p(c_{LE}|x,\Omega^j)}{\sum_{x\in X} h(x)} \\
\mu_{LE}^{j+1} &= \frac{\sum_{x\in X} h(x)p(c_{LE}|x,\Omega^j)x}{\sum_{x\in X} h(x)p(c_{myo}|x,\Omega^j)} \\
{\sigma_{LE}^{j+1}}^2 &= \frac{\sum_{x\in X} h(x)p(c_{LE}|x,\Omega^j)(x-\mu_{LE}^{j+1})^2}{\sum_{x\in X} h(x)p(c_{myo}|x,\Omega^j)}
\end{aligned}
$$

The values for $p(c_i|x,\Omega^j), x \in X$ are calculated in the *Expectation*-step as follows:

$$
\begin{aligned}
p(c_{myo}|x,\Omega^j) &= \frac{\alpha_{myo}\frac{x}{\sigma_{myo}^2}e^{-\frac{1}{2}\left(\frac{x}{\sigma_{myo}}\right)^2}}{\alpha_{myo}\frac{x}{\sigma_{myo}^2}e^{-\frac{1}{2}\left(\frac{x}{\sigma_{myo}}\right)^2} + \alpha_{LE}\frac{1}{\sqrt{2\pi}\sigma_{LE}}e^{-\frac{1}{2}\left(\frac{x-\mu_{LE}}{\sigma_{LE}}\right)^2}} \\
&= \frac{p_{myo}(x)}{p_{myo}(x)+p_{LE}(x)} \\
p(c_{LE}|x,\Omega^j) &= \frac{\alpha_{LE}\frac{1}{\sqrt{2\pi}\sigma_{LE}}e^{-\frac{1}{2}\left(\frac{x-\mu_{LE}}{\sigma_{LE}}\right)^2}}{\alpha_{myo}\frac{x}{\sigma_{myo}^2}e^{-\frac{1}{2}\left(\frac{x}{\sigma_{myo}}\right)^2} + \alpha_{LE}\frac{1}{\sqrt{2\pi}\sigma_{LE}}e^{-\frac{1}{2}\left(\frac{x-\mu_{LE}}{\sigma_{LE}}\right)^2}} \\
&= \frac{p_{LE}(x)}{p_{myo}(x)+p_{LE}(x)}
\end{aligned}
$$

Other than the Gaussian distribution, which can be centered around arbitrary points defined through μ_{LE}, the offset of the Rician distribution is fixed at the origin and the parameter σ_{myo} defines the shape (Fig. 4.19). The myocardial tissue intensity values are normally higher than 0 and thus we introduce an offset x_s for the mixture model:

$$
x_s = \arg\max_{h(x)<0.05h_{max}} x
$$

The algorithm can then be implemented as described on page 100.

Algorithm 8 Mixture Model Fitting with Expectiation Maximization

{Parameter Initialization}

$$
\begin{aligned}
x_s &= \underset{x \in \{x_i | h(x_i) < 0.05 h_{max}\}}{\arg\max} x \\
\sigma^0_{myo} &= \underset{x \in X}{\arg\max}\, h(x - x_s) \\
\alpha^0_{myo} &= \max_{x \in X} h(x) \\
\mu^0_{LE} &= \sigma^0_{myo} + \frac{1}{2}\left(x_{max} - \underset{x \in X}{\arg\max}\, h(x)\right) \\
\sigma^0_{LE} &= \sqrt{\frac{1}{3}\left(x_{max} - \mu^0_{LE}\right)} \\
\alpha^0_{LE} &= h(\mu^0_{LE})\sqrt{2\pi}\sigma^0_{LE}
\end{aligned}
$$

repeat

{Expectation-Step}

$$
\begin{aligned}
p(c_{myo}|x,\Omega^j) &= \frac{p_{myo}(x)}{p_{myo}(x) + p_{LE}(x)} \\
p(c_{LE}|x,\Omega^j) &= \frac{p_{LE}(x)}{p_{myo}(x) + p_{LE}(x)}
\end{aligned}
$$

{Maximization-Step}

$$
\begin{aligned}
\alpha^{j+1}_{myo} &= \frac{\sum_{x+x_s \in X} h(x+x_s)\, p(c_{myo}|x,\Omega^j)}{\sum_{x+x_s \in X} h(x+x_s)} \\
{\sigma^{j+1}_{myo}}^2 &= \frac{\sum_{x+x_s \in X} h(x+x_s)\, p(c_{myo}|x,\Omega^j)\, x^2}{2 \sum_{x+x_s \in X} h(x+x_s)\, p(c_{myo}|x,\Omega^j)} \\
\alpha^{j+1}_{LE} &= \frac{\sum_{x+x_s \in X} h(x+x_s)\, p(c_{LE}|x,\Omega^j)}{\sum_{x+x_s \in X} h(x+x_s)} \\
\mu^{j+1}_{LE} &= \frac{\sum_{x+x_s \in X} h(x+x_s)\, p(c_{LE}|x,\Omega^j)\, x}{\sum_{x+x_s \in X} h(x+x_s)\, p(c_{myo}|x,\Omega^j)} \\
{\sigma^{j+1}_{LE}}^2 &= \frac{\sum_{x+x_s \in X} h(x+x_s)\, p(c_{LE}|x,\Omega^j)(x - \mu^{j+1}_{LE})^2}{\sum_{x+x_s \in X} h(x+x_s)\, p(c_{myo}|x,\Omega^j)}
\end{aligned}
$$

until convergence

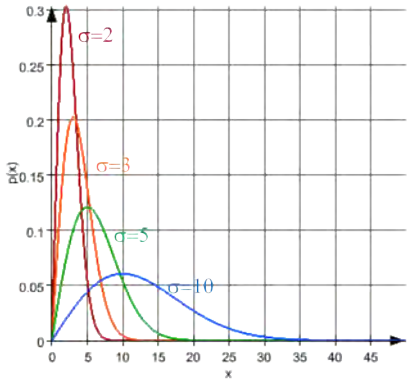

Figure 4.19: Examples for the Rayleigh distribution $\alpha_{myo}\frac{x}{\sigma^2_{myo}}e^{-\frac{1}{2}\left(\frac{x}{\sigma_{myo}}\right)^2}$ with parameters $\sigma_{myo} = 2,3,5,10$.

Figure 4.21 presents the example of a myocardial intensity distribution and the adapted mixture model. The thresholds t_M and t_D define the locations of the distribution of normal and enhanced myocardium, and t_S defines the intersection between these densities in the adapted model. Based on this mixture model, all myocardium voxels are assigned an estimated portion $p(x)$ of late enhanced tissue according to their intensity value x. A linear partial volume model is assumed:

$$p(x) = \begin{cases} 0 & \text{if } x \leq t_M, \\ \frac{x-t_M}{t_D-t_M} & \text{if } t_M < x \leq t_D, \\ 1 & \text{if } t_D < x. \end{cases} \tag{4.22}$$

Late Enhancement Segmentation with Assumptions on Shape and Location The actual segmentation of the tissue regions that exhibit late enhancement uses the partial volume model derived in the previous section. It is combined with a watershed-based segmentation approach that is derived from the assumptions 2 to 4 on page 94. A final closing step includes tissue, which shows no enhancement due to microvascular obstruction. Figure 4.20 displays the typical progression of myocardial infarction due to CAD. Necrotic tissue regions, which are visible in late enhancement images, are usually attached to the subendocardial border and form compact crescent shaped regions [Hunold et al., 2006]. Taking this into account, in a first step seed voxels v with an intensity value x higher than the determined threshold t_D are determined in the subendocardial layer of the myocardium. For

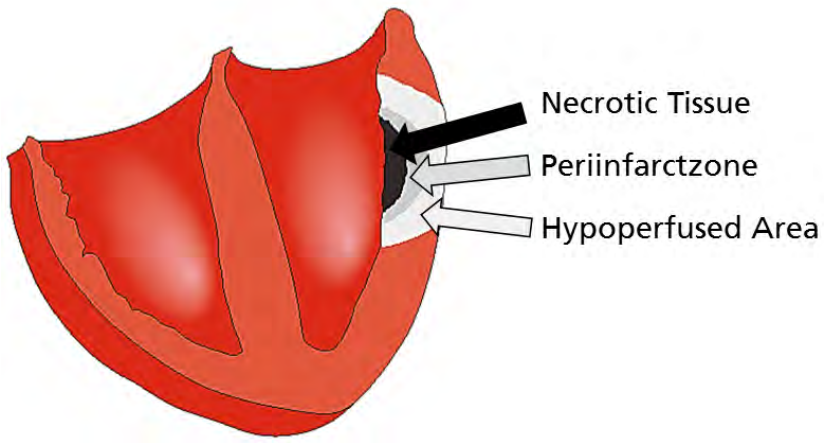

Figure 4.20: Progression of myocardial infarctions. Due to the location of the arteries on the outer border of the myocardium, infarctions are normally located subendocardially and grow towards the epicardium. The core infarct zone is surrounded by the periinfarct zone, which still partially consists of viable tissue. The outer undersupplied tissue is at risk but still healthy and does not exhibit late enhancement.

these voxels the distance d from the endocardial wall ($endo$) is shorter than that from the epicardial wall (epi):

$$\left(\frac{d(v,endo)}{d(epi,endo)} \leq 0.5\right) \wedge \big(p(x) = 1\big) \tag{4.23}$$

In the special case where the intersection t_S of the two fitted distributions is not located between the maxima t_M and t_D we apply $t_S := t_D$. The seed voxels v are used to define the basins included into the initial segmentation mask.
In an ensuing connected-component analysis, small noisy structures are identified and removed from the segmentation result. The resulting mask is used to visualize the extent of the infarcted tissue (Fig. 4.21).

Microvascular obstructions are not included in the initial segmentation. To add these so-called no-reflow-areas, I is divided into the sets I_S, I_B, and I_H. $I_S = S_{WT} \cup S_{BP}$ is the combination of the initial segmentation mask S_{WT} delivered by the watershed transform and the bloodpool mask S_{BP}. I_B contains the voxels not included in I_S with a path to the image border that does not contain voxels of I_S, whereas $I_H = (I \setminus I_S) \setminus I_B$ contains those voxels of $I \setminus I_S$ without such a path. The final segmentation $I_R(v)$ can then be described as

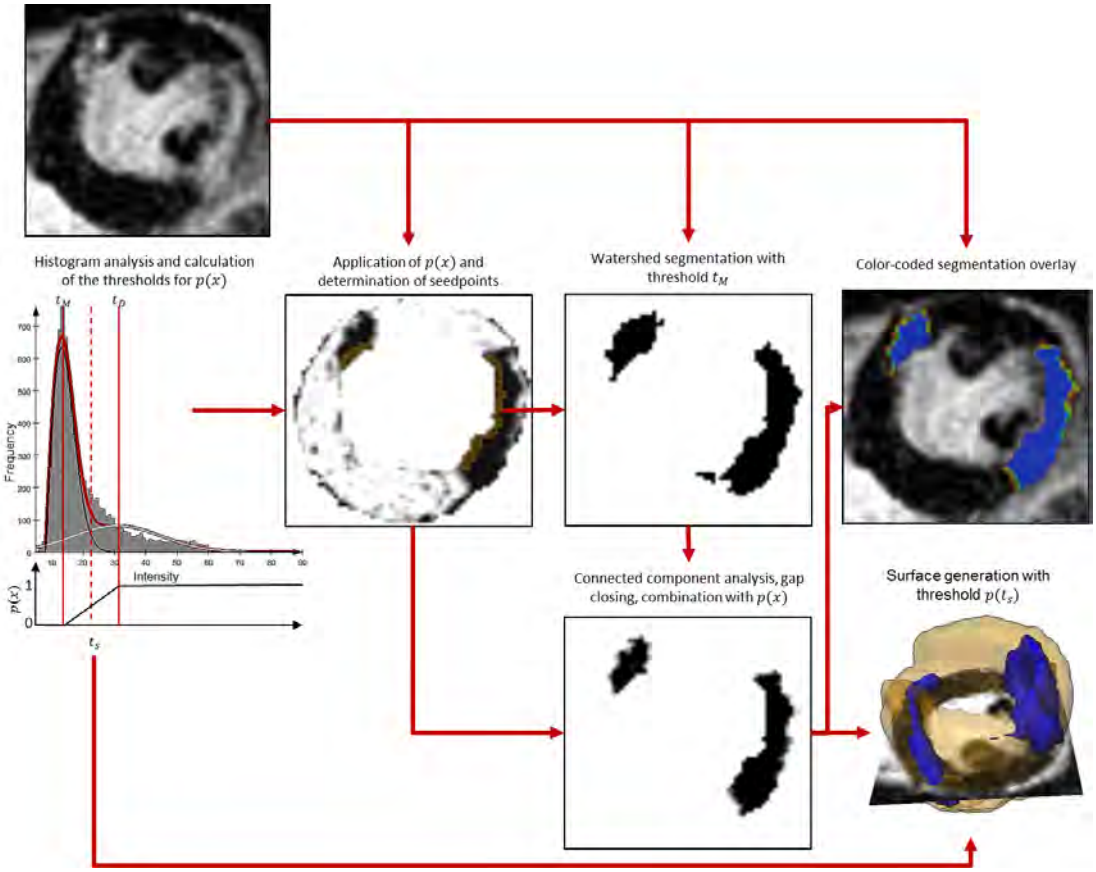

Figure 4.21: Late enhancement segmentation procedure. The thresholds t_M, t_D and t_S that are derived from the initial histogram analysis are used to control the watershed segmentation and to determine a function for the potential portion of hyperenhanced tissue $p(x)$ for an intensity value x. This function is applied for the detection of the initial seed voxels v (white markers) as well as for the final quantification. t_S defines the threshold for the 3-D surface generation. The red circles show locations where the original watershed segmentation was changed by the subsequent connected-component analysis and the closing of gaps.

follows:

$$I_R(v) = \begin{cases} 1, & (v \in S_{WT} \cup I_H) \wedge (d(v, I_B) > 3) \\ p(x), & (v \in S_{WT} \cup I_H) \wedge (d(v, I_B) \leq 3) \\ 0, & v \notin S_{WT} \cup I_H \end{cases}, \; d(v, I_B) = \min_{v_i \in I_B} d(v, v_i) \tag{4.24}$$

$d(v, I_B)$ calculates the minimal voxel distance of the v to the outer voxel set I_B. This method results in the filling of holes in the segmentation. Furthermore, the function $p(x)$ calculates wrong values for the late enhancement portion of the voxel at the transition from late enhancment to no-reflow-areas. I_R corrects these values as well. Figure 4.22 presents the

application of this method to an MRI dataset with severe microvascular obstructions.

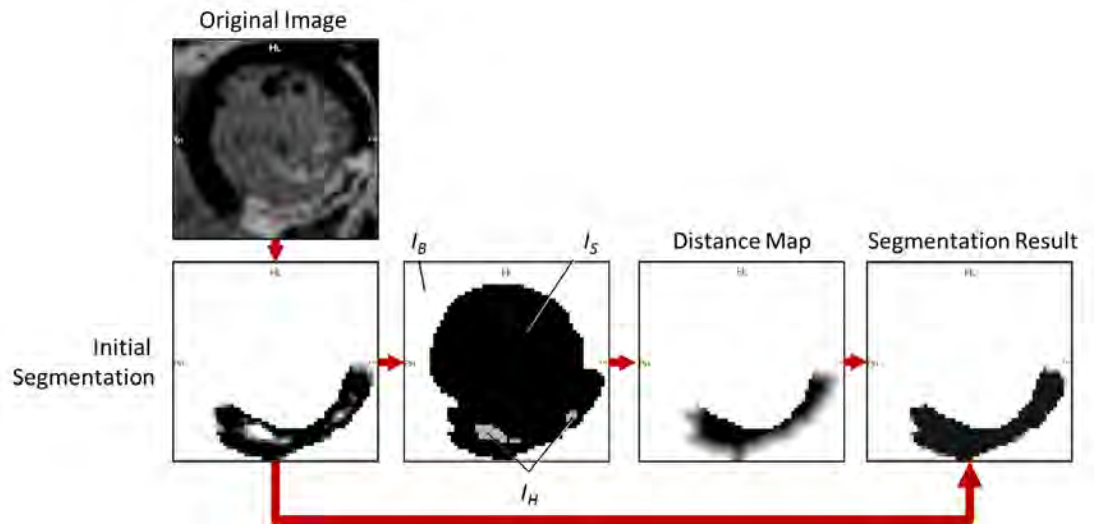

Figure 4.22: Inclusion of microvascular obstructions into the late enhancement segmentation. The left column shows an original image slice and the resulting segmentation, which contains holes at the locations of the microvascular obstruction. The next columns depict the partition into the voxel sets I_B, I_S, I_H and the calculation of the distances $d(v, I_B)$ for the voxels of $S_{WT} \cup I_H$. The resulting segmentation $I_R(v)$ is displayed in the rightmost image.

4.2.3 Evaluation

The described methods have been applied to laboratory datasets with known artificial infarctions in order to evaluate the reliability and accuracy in the detection of infarctions. The applicability to datasets of patients with coronary artery disease has then been tested with image data from clinical practice and compared to expert annotations.

Laboratory Datasets The analysis was performed on datasets of seven domestic pigs (55.2±7.3 kg), which had been acquired for another study by Mahnken et al. [2009a]. After the preparation with anesthesia and mechanical ventilation, acute reperfused myocardial infarction had been induced in these pigs. To this end, a coronary artery was occluded with a balloon catheter for 60 minutes. Imaging started 60 minutes after the removal of this catheter. 10 minutes after the injection of a gadolinium-based contrast agent (Magnevist, Bayer-Schering) MR image acquisition was performed with a clinical 1.5 T whole body MR scanner (Gyroscan Intera, Philips Medical Systems, Best, the Netherlands), resulting in image volumes with a

256×256-matrix and a reconstructed voxel size of 1.48×1.48×6 mm^3.
CT imaging was performed with a 64-slice DSCT scanner (SOMATOM Definition, Siemens). Ten minutes after the injection of the contrast agent, the late enhancement scan was acquired. Double-oblique, 6-mm-short-axis images without intersection gap were reconstructed with a field of view of 150×150 mm^2, a 512×512-matrix, and a smooth convolution kernel (B20f).
All subjects were killed after the imaging procedure and the hearts were sectioned into 6 mm thick short-axis slices, which were stained with 2% 2,3,5-triphenyltetrazolin-chloride (TTC) solution and photographed after 15 minutes.

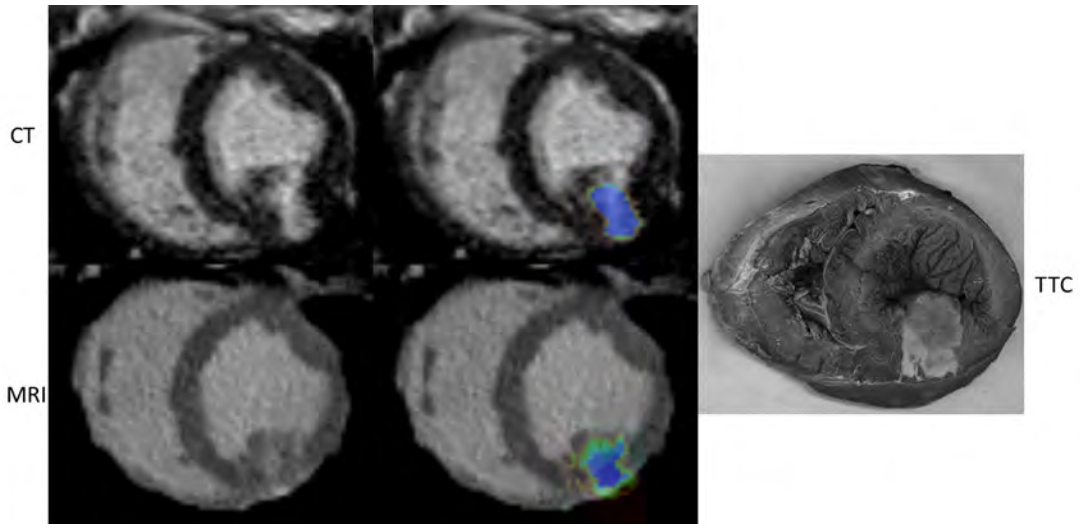

Figure 4.23: Comparison of corresponding slices of the aligned MRI and CT datasets. The leftmost column shows the raw images, whereas the middle column displays the segmentation results as overlays. The photo on the right depicts the TTC-stained slice of the heart muscle, which best corresponds to the image slices on the left.

Image analysis was based on the segmentation of the myocardium, which was performed semi-interactively with a live wire method by a clinical expert. Based on this initialization, the late enhancement region was detected automatically in both, CT and MRI datasets. If the automatic segmentation was considered insufficient by the expert, missing regions were added via the interactive watershed transformation.
To enable also a visual comparison of the segmentation results from CT and MRI, the CT volumes were aligned with corresponding MRI datasets by interactive rigid registration. The segment-based analysis was then performed with the same orientation point, and 3D visu-

alizations were created to examine the correspondence of the segmented regions' shape.

Results The inflicted infarctions were detected automatically at the correct locations. Figure 4.23 presents the comparison of the segmentation results for case 5 with the photograph of the myocardium slice that best matches the depicted image slice. 3D visualizations as well as the volume portions of the AHA segments are depicted in Figure 4.24 for two cases with different locations of the inflicted infarction. Results for all cases can be inspected in Figures A.5 to A.7 on page 164 in the appendix.

Table 4.3 presents the quantitative results of this segmentation. In three datasets, the initial late enhancement segmentation was extended interactively. The volumes of the detected regions differed between 0.08 and 2.58 ml between the CT and MRI datasets. The average difference was 1.3 ml.

Case	Interactive Extension	Volume[ml]		
		CT	MRI	Diff
1		18.40	20.98	2.58
2		11.52	11.30	0.22
3		15.44	16.05	0.61
4	X	9.51	11.41	1.91
5	X	12.46	12.54	0.08
6	X	5.16	3.86	1.30
7		9.48	11.86	2.38

Table 4.3: Late Enhancement Volumes in CT an MRI datasets of pigs with inflicted infarctions.

MRI Datasets of CAD Patients To evaluate the applicability of the algorithm for the assessment of datasets from patients with coronary artery disease, the described method was compared with expert segmentation as well as with the commonly used threshold method. Datasets from 21 patients with known or suspected CAD were inspected. The image data were acquired with the settings listed in Table 4.4. The segmentation was performed automatically with the methods described in the previous section. The experts were then allowed to change the segmentation manually. Furthermore, the experts drew regions into myocardial tissue that they assumed to be healthy. These were analyzed to determine a threshold three standard deviations (3σ) above the average.

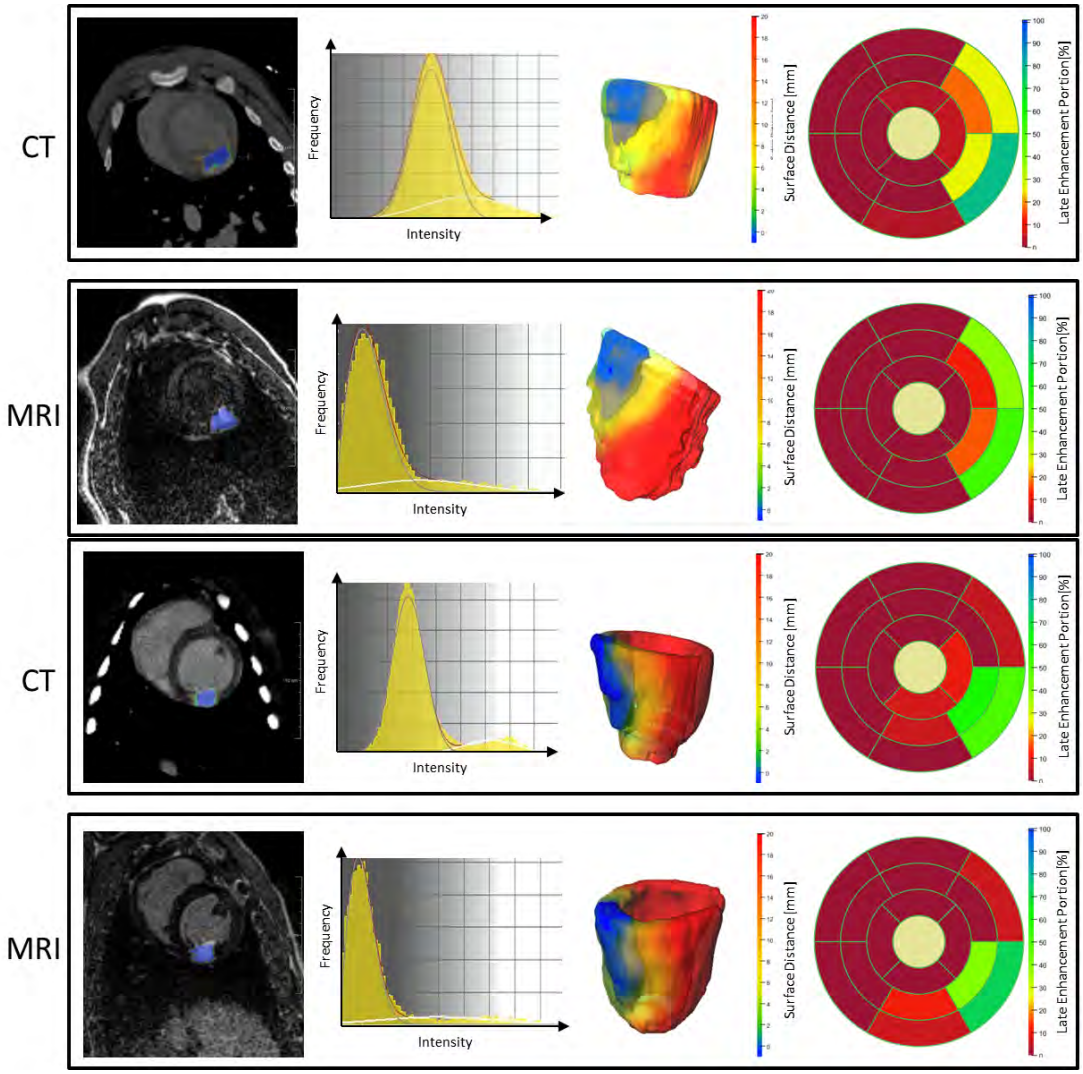

Figure 4.24: Late enhancement segmentation results for case 2 and 7. The leftmost column shows the segmented region as an overlay with the original image data. The myocardial histogram with the fitted mixture model is presented in the next column. The second column from right depicts the segmentation result in 3D. The late enhancement region is colored blue whereas the surface color of the myocardium corresponds to the distance from the infarction to indicate the transmurality. The rightmost column shows the late enhancement volume portions according to the AHA segment model.

Table 4.4: Sequence parameters used for the image acquisition.

	Late Enhancement
Repetition / Echo Time [ms]	11.04/4.4
Flip angle	30°
Matrix	192x256
Field of View [mm^2]	293x360
Bandwith [Hz/Pixel]	140
Slice Thickness [mm]	5 - 8

Results Figure 4.26 presents the comparison of the determined late enhancement volume portions per AHA-segment with all performed segmentations using Bland-Altman and scatter plots. The correlation between the manual and the automatic segmentations proposed here was better than between the manual and the 3σ-method segmentation. Furthermore, the 95% confidence interval is significantly smaller for the comparison of automatic and manual segmentations than for the inter-observer comparison of the 3σ-method. The correlation between the applied segmentations is shown in Table 4.5. The observers agreed on the non-existence of late enhancement in five cases. As depicted in Figure 4.25, the automatic segmentation method detected false-positive late enhancement regions in two of these cases. For the other three cases the automatic segmentation agreed with the observers' segmentations. For cases 5, 6, 7 and 16, observer 1 determined bright regions, which could possibly represent late enhancement. These regions were neither detected by the automatic method nor considered relevant by observer 2.

Table 4.5: Correlation of late enhancement segmentation results

	Observer	**Manual**		**3σ-Method**	
Observer		1	2	1	2
Automatic		0.95	0.94	0.69	0.78
Manual	1		0.93	0.70	0.80
	2			0.67	0.76
3σ-Method	1				0.89

The Dice similarity coefficient (Eq. 4.25) was computed to determine the mutual overlap between the results obtained by the mixture model segmentation with manual segmenta-

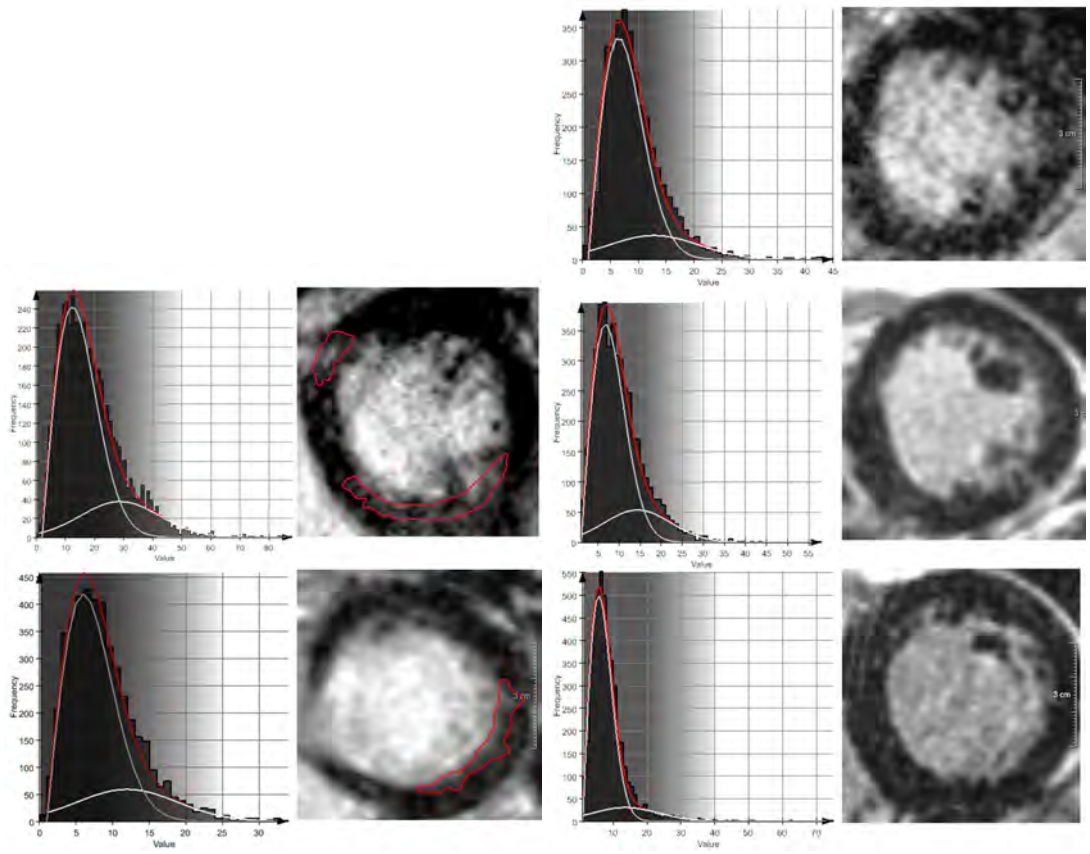

Figure 4.25: Left column: False-positive late enhancement segmentation for patient 9 (upper row) and 10 (lower row). The results of the histogram analyses are shown on the left, whereas the corresponding segmentation results are represented by the gray contours in the images on the right.
Right column: Correct results for patient 3, 8 and 17. No late enhancement regions are detected by the automatic histogram-based method.

tion being defined as the standard of reference. It calculates the overlap between two sets of voxels and provides values between 0 (when there are no mutual voxels) and 1 (when the segmented voxel sets fully match) [Dice, 1945].

$$D = \frac{2\,|V_{\text{man}} \cap V_{\text{auto}}|}{|V_{\text{man}}| + |V_{\text{auto}}|} \tag{4.25}$$

Table 4.6 presents the Dice coefficient as well as the average surface distance and its standard deviation for the 16 cases, where both observers detected late enhancement.

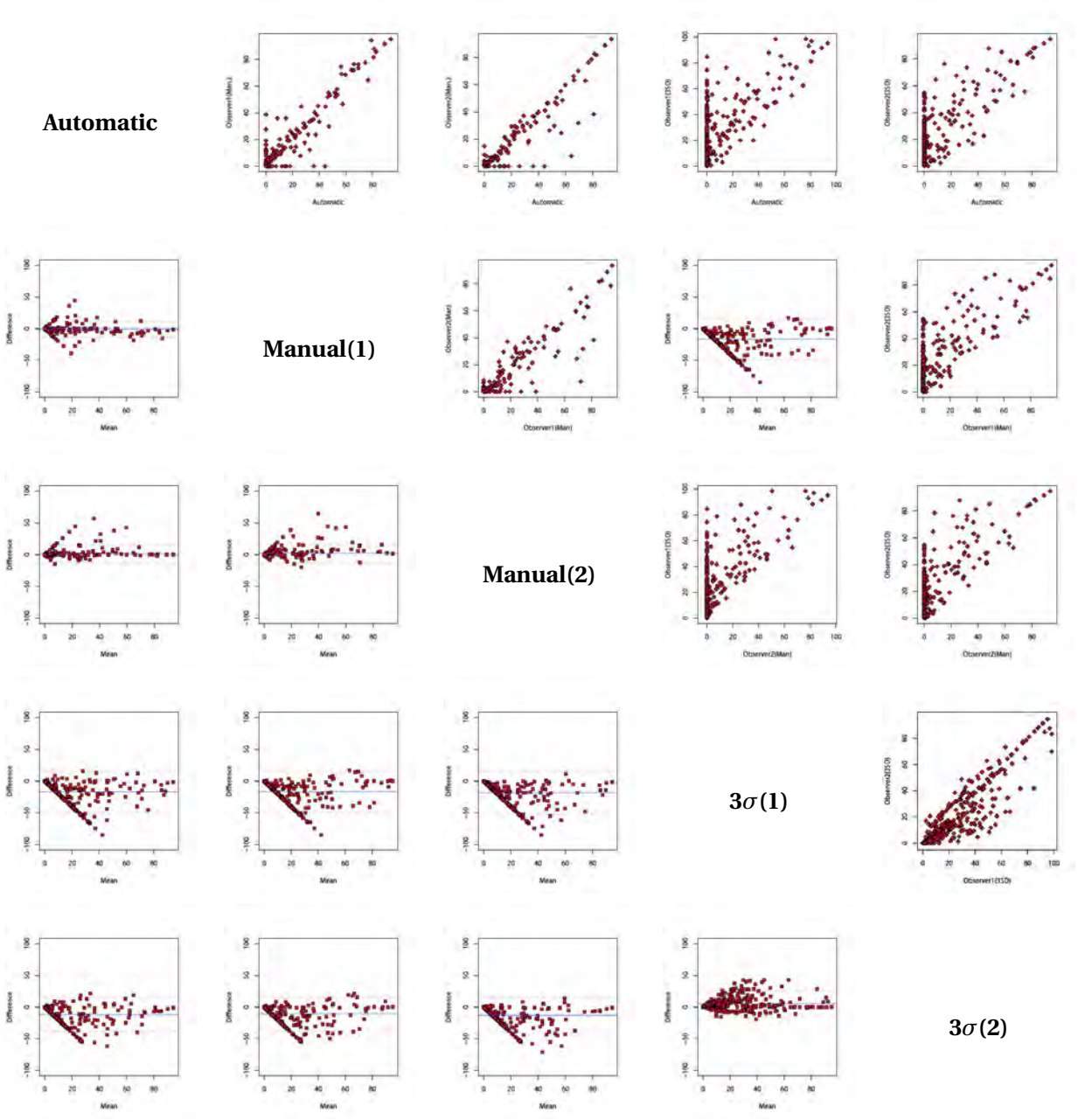

Figure 4.26: Comparison of the portion of segmented tissue per AHA segment for automatic and expert segmentation. The upper triangular matrix shows scatter plots corresponding to the results achieved with the methods stated in the corresponding diagonal elements. The opposite elements in the lower triangular matrix present these results in Bland-Altman plots. (1) and (2), respectively, indicate which expert did the segmentation.

Pat	Dice Coeff.	Surface Distance	
		Average	Std. Dev.
1	0.90	1.52	0.16
2	0.95	1.65	0.55
3	0.79	1.55	0.28
5	1.00	-	-
6	0.97	1.74	0.83
7	0.94	2.66	2.40
8	0.00	-	-
9	0.98	1.50	0.00
10	0.97	4.50	4.07
11	0.75	4.26	4.07
12	0.97	2.58	2.85
13	1.00	-	-
14	0.96	1.99	0.77
15	0.73	1.85	1.24
16	0.74	3.25	2.19

Table 4.6: Overlap measurement between manual and mixture model segmentation using Dice coefficient and surface distances.

CT Datasets of CAD Patients The described method was also applied to CT datasets from 6 patients with chronic myocardial infarction, who were scheduled for revascularization therapy. The data were acquired with a 64-slice Dual Source CT scanner system (SOMATOM Definition, release VA20, Siemens, Forchheim, Germany) at end-inspiratory breath hold with the standardized acquisition protocol, which had also been applied for the examination of the laboratory pigs [Mahnken et al., 2010a]. 120 ml Iopromide 300 (Ultravist 300, Bayer-Schering Pharma AG, Berlin, Germany) were injected at a flow rate of 6.2 ml/s followed by a 50 ml saline chaser bolus at the same flow rate, and after six minutes the late enhancement data were acquired. The scan range varied between 9.6 to 11.9 cm, resulting in an average CT data acquisition duration scan time of 5.4±1.4 s. Data were reconstructed in double-oblique 6 mm short-axis slices at 70% of the RR interval with a field of view of 180 ×180 mm^2, a 512 ×512 reconstruction matrix and a smooth convolution kernel (B20f).

Results Similar to the analysis of the MRI datasets, the detection of regions that exhibit delayed contrast enhancement was performed by a clinical expert both manually using de-

lineation and automatically with the 3σ threshold method and the proposed mixture model approach. The Dice coefficient was calculated for both, the mixture model and the 3σ-method. Figure 4.27 shows a visualization of the segmentation results and their overlap for patient 2.

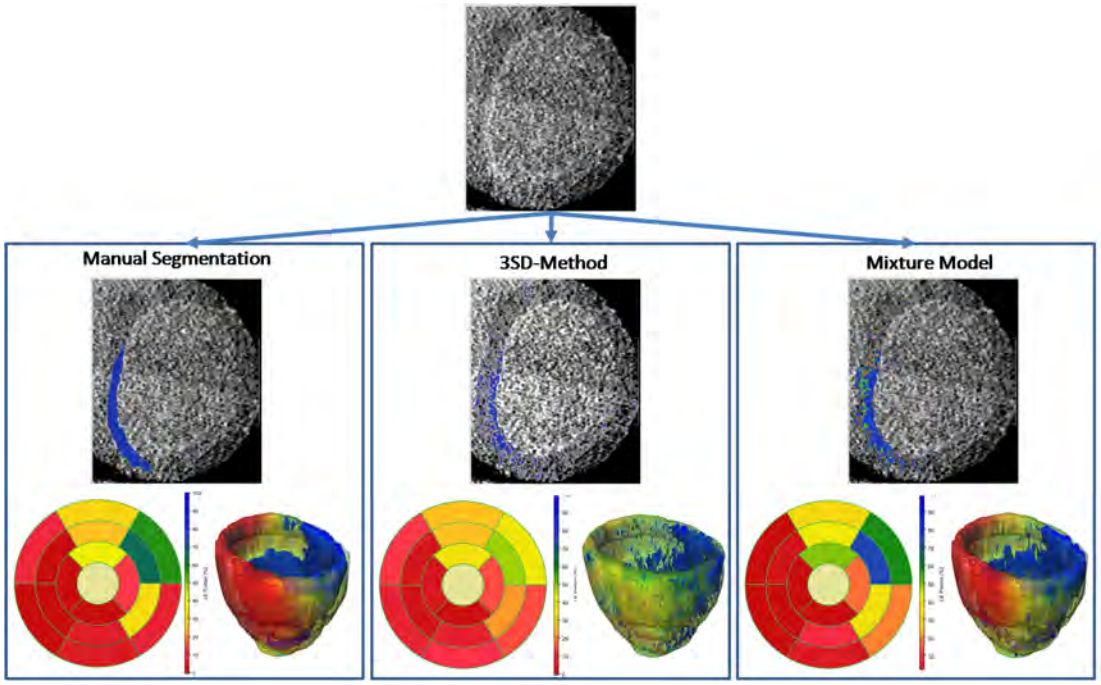

Figure 4.27: Comparison of late enhancement segmentation methods for the analysis of the CT dataset of patient 2. The overlap between the mixture model segmentation and the manual segmentation is much better than that between the 3σ threshold segmentation and the expert delineation.

Discussion The late enhancement segmentation delivered promising results in almost all applications. In the laboratory datasets, all inflicted infarctions were detected at the correct locations in the MRI as well as the CT datasets. False-positive results occured however in two MRI patient datasets as displayed in Figure 4.25. In these cases, the intensity of the falsely detected myocardium is slightly increased. This can partly be explained by partial volume effects at the border to the myocardium. The region thus fulfills the criteria for late enhancement. Segmentation errors like this one could probably be avoided through the introduction of a minimal difference between the peaks of the fitted myocardium and late enhancement intensity curves or an improvement of the myocardium segmentation.

Considering the identification of affected AHA-segments, the proposed method delivered

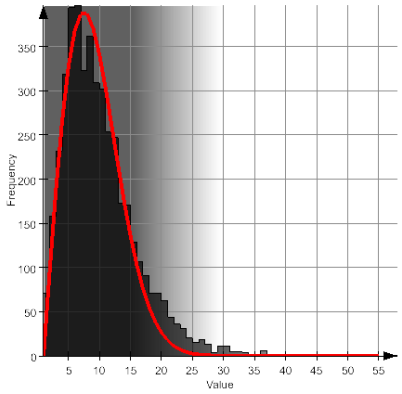

Figure 4.28: Histogram and fitted Rayleigh distribution (red curve) for patient 8. Although there is no late enhancement, the red curve does not perfectly describe the histogram. This might be due to partial volume effects at the myocardial borders.

much clearer results than the 3σ threshold method for both, MRI and CT datasets. The examination of the detected regions resulted in a good agreement between the differently acquired datasets of the laboratory pigs. However, the comparison of these segmentations is problematic for the myocardium close to the valves. As depicted in Figure 4.24, the orientation and coverage of the CT and MRI datasets do not fully correspond. Thus, the segmentation and the AHA segment quantification disagree most in the basal segments.

In the patient datasets the Dice coefficient revealed a very good agreement of the automatically detected regions with the expert segmentations. The inspection of the difference voxelsets indicates that deviations mainly occur at the cuspidal ends of crescent-shaped clusters. Outliers occur in apical regions (mainly segments 12-16), where data are distorted by artifacts. These segments are more strongly affected by myocardial motion than the basal segments, and the segmentation accuracy for these regions could probably be improved through the inclusion of long-axis slices into the analysis.

The inclusion of the microvascular obstructions resulted in a very good agreement of the segmentations in the laboratory datasets from MRI and CT. Due to the early acquisition and the large contrast agent molecules, the CT images exhibit larger regions of microvascular obstruction than the corresponding MRI images. Figure 4.29 presents corresponding slices from CT and MRI for laboratory pig number 5. Though the no-reflow-effect makes the infarct region appear differently, the segmentation results correspond well as shown in Fig-

ure A.6. Unenhanced regions like this would be missed by most standard techniques [Tao et al., 2010, Elagouni et al., 2010].

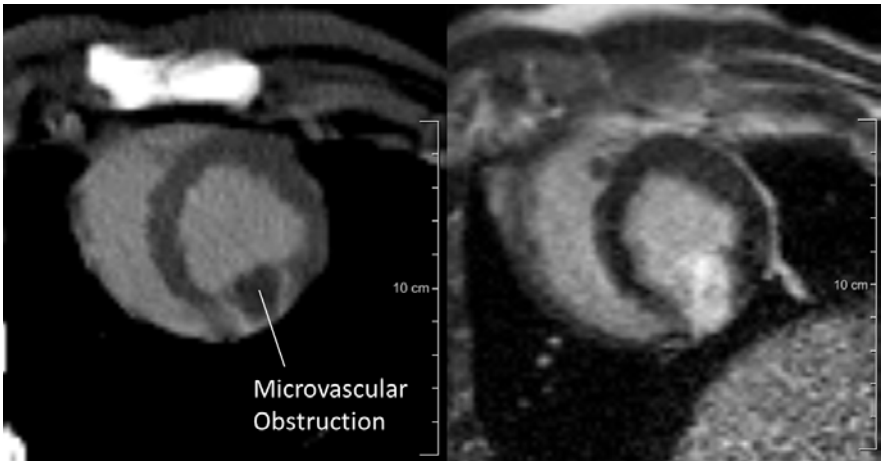

Figure 4.29: Microvascular obstruction in CT dataset. The screenshots represent corresponding image slices from CT and MRI for laboratory pig 5. On the CT image, the infarct consists of a dark region surrounded by a zone, which exhibits late enhancement. On the MRI image, the whole infarct region displays late enhancement.

The major contribution of the presented method are the mixture-model approach for the intensity distribution and the consideration of the shape characteristics of myocardial infarctions for the segmentation. Both ideas have been adapted by newer approaches [Elagouni et al., 2010, Tao et al., 2010]. Furthermore, there currently exists no other approach for the late enhancement detection in CT datasets.

4.3 Analysis of Myocardial Perfusion Defects in CE-MRI Sequences

The inspection of the myocardial perfusion is based on the analysis of the time-intensity-curves of image regions or single voxels (cf. Fig. 4.30). Parameters computed from these curves are used to assess the local perfusion. These parameters can be so-called *semi-quantitative* descriptive curve parameters or quantitative parameters. Descriptive parameters used for semi-quantitative perfusion analysis are *Peak Enhancement (PE)*, *Up-Slope*, *Contrast Agent Arrival*, *Time to Peak (TTP)* and *Area Under Curve (AUC)* (Fig. 4.30) [Al Saadi et al., 2001, Keijer et al., 1995, Klocke et al., 2001]. Quantitative parameters such as the regional myocardial blood flow (*MBF*), the regional myocardial blood volume (*MBV*) and the

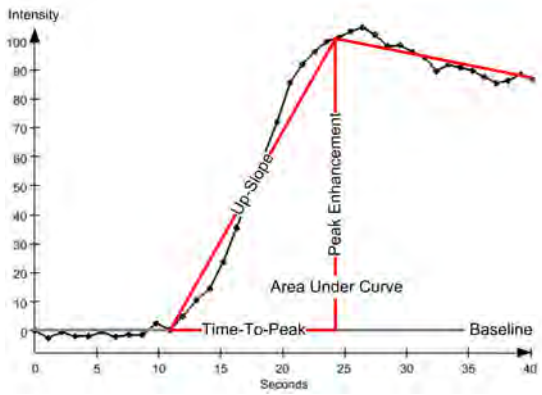

Figure 4.30: Typical time-intensity-curve and its descriptive curve parameters

mean transit time (MTT) are usually calculated based on a model that describes a pharmacological process using assumptions about the imaged tissue compartments [Schwitter, 2006, Ritter et al., 2006]. Typically, two compartments, namely arteries and myocardial tissue are considered [Larsson et al., 1994]. The assumed underlying relationship between the image intensity values $I(t)$ and the contrast agent concentration $C_t(t)$ in tissue for the calculation of these parameters based on T1-weighted MRI image sequences is:

$$I(t) = I_0 + kC(t) + \varepsilon \tag{4.26}$$

k denotes a constant, and ε is the noise parameter. The relation of the myocardial contrast agent concentration $C_t(t)$ and the concentration in the supplying artery $C_a(t)$ is described as a convolution with the impulse response function $h(t)$ and the constants describing the tissues flow properties :

$$C_t(t) = C_a(t) \otimes \underbrace{\frac{hem_{\text{cap}}}{hem_{\text{art}}} MBF h(t)}_{h(t)} \tag{4.27}$$

hem_{cap} and hem_{art} are estimates for the hematocrit values in the bloodpool and the capillaries. The published approaches differ regarding the constraints and methods applied for the calculation of $h(t)$. Physiologically-derived tracer kinetic models are often applied to make sure that a sensible solution for $h(t)$ is calculated in the deconvolution process. Most recent publications are based on a model-free approach as proposed by Jerosch-Herold et al. [2002]. They differ mainly regarding the formulation of the constraints for $h(t)$ and the technique applied to calculate the deconvolution. The method comparison by Neyran et al. [2002]. demonstrated that results achieved with different model-based approaches

and algebraic methods using *ARMA* or singular value decomposition (SVD) do not differ significantly.

4.3.1 Existing Methods for the Analysis of Myocardial Perfusion MRI

To reduce the influence of noise on the parameter calculation, many approaches fit model curves of pharmacokinetic processes like the so-called gamma variate before parameters are calculated from the given curves [Schmitt et al., 2002, Sainsbury and Ashley, 1986, Thompson et al., 1964]. To assess the effect of a stenosis on the myocardial perfusion, sequences acquired at rest are compared with sequences acquired under pharmacologically induced stress [Al Saadi et al., 2002]. The ratio of curve parameters derived for spatially corresponding regions from the different image sequences is used to assess the ability to increase perfusion under stress. Studies have demonstrated that *Up-Slope* is the most appropriate parameter for this computation [Al Saadi et al., 2001], and the myocardial perfusion reserve index (MPRI) has been proven suitable for locating hypo-supplied myocardial regions [Positano et al., 2006]. As the resolution in myocardial perfusion images is very low and distortions from motion and acquisition artifacts are likely to be present, myocardial perfusion parameters are often calculated for image regions rather than for single voxels to achieve more stability through averaging [Positano et al., 2003b, Breeuwer et al., 2003]. However, more accurate information about location, size and degree of a hypoperfusion are of clinical interest, and there are some approaches to segment suspicious regions based on the inspection of voxel intensity curves. These use different classification approaches like factor analysis, fuzzy K-means [Di Bella and Sitek, 2001] and support vector machines [Hansen et al., 2007], but they do not incorporate spatial constraints given for the location of infarctions relative to the myocardial surface (see Section 4.2).

4.3.2 Parameter-based Analysis of Myocardial Perfusion MRI

The purpose of the perfusion analysis is to objectively determine hypoperfused tissue. As the range of intensity values and the point of intensity saturation vary with the particular acquisition settings of the individual examinations, it is difficult to define an objective measure for the degree of a hypoperfusion. Some publications have listed ranges for quantitative myocardial perfusion parameters in animals and humans [Muehling et al., 2003, Jerosch-Herold et al., 2002, Ritter et al., 2006]. However, the relationship between measured intensities and contrast agent concentration is non-linear and depends strongly on the contrast

agent, local contrast agent concentration, field inhomogeneites, etc. [Jerosch-Herold, 2010]. Thus, there are no standardized values, which could be used for a threshold-based detection of perfusion defects using quantitative parameters, and the proposed segmentation approach uses a histogram analysis to determine suitable thresholds. The developed method allows the usage of the descriptive parameters *Peak Enhancement (PE)*, *Up-Slope*, and *Time to Peak (TTP)* [Hennemuth et al., 2007] as well as the quantitative parameters *regional myocardial bloodflow (MBF)* and *regional myocardial bloodvolume (MBF)*. These are calculated as basis for the detection of suspicious regions. Both parameter calculation methods depend on initial parameter estimates. Therefore, the first processing step is the detection of a region in the left ventricular bloodpool as well as a myocardial tissue region. To this end the left ventricle ROI is detected through an analysis of the local intensity variation as described in the algorithm on page 41. The inner myocardial boundary is then defined as the convex hull of this ROI. The outer myocardial contour is defined semi-automatically with a live wire contouring method applied to the temporal maximum intensity projection (MIP_t) of the intensity sequence [Schenk et al., 2000]. Averaged intensity curves are extracted for both regions.

For the calculation of the descriptive parameters, the initial estimates for the start of the upslope, the timepoint of maximum enhancement and the end of the relevant time course are derived from the average myocardial intensity course. Parameter images are then calculated with existing MeVisLab modules.

For the calculation of the quantitative parameters with the singular value decomposition (*SVD*) implementation by Kohlmann et al. as proposed by Ostergaard et al. [1996], the so-called arterial input function (*AIF*) is required. In the given application, this is set to the contrast agents first pass through the left ventricle, which is represented by the gamma variate fit to the time intensity curve of the left ventricular bloodpool. The deconvolution is calculated with a block-circulant deconvolution matrix as suggested by Wu et al. [2003].

The concept of the perfusion defect detection is based on similar assumptions as those applied for the segmentation of necrotic of fibrotic tissue from late enhancement MRI described in Section 4.2.2 (cf. Fig. 4.20). The segmentation is based on the myocardium delineation determined in the preceeding step. Suitable seedpoints are detected in the subendocardial part of the myocardium applying a threshold one standard deviation below the average intensity in the myocardium. These seedpoints are then used as input for the watershed transform by Hahn and Peitgen [2003]. The preflooding height is constrained by the

initial threshold and the segmentation threshold is initially chosen as the mean intensity of the myocardium. This restricts the expansion of the segmentation in inhomogeneous regions. The threshold constraining the segmentation can be manipulated interactively. The resulting masks are filtered in such a way that only those regions with a minimum contour length are kept.

4.3.3 Evaluation

The presented method was evaluated towards the following quality criteria:

1. Plausibility of the detected region with regard to findings from other examinations.
2. Increase of information compared to the AHA-segment-based analysis.

To this end, a subset of ten datasets (3, 7, 20, 28, 32, 34, 36, 38, 44, 50) from the image sequences described in Table A.1 on page 154 have been processed. The datasets were acquired with the 1.5T Philips Intera scanner after an intravenous injection of gadobutrol (Gadovist 1.0; Bayer Schering Pharma, Berlin, Germany). Contrast media was dosed at 0.1 mmol/kg of body weight at an injection rate of 5 ml/s, followed by a 40 ml saline flush. K-t sensitivity encoding perfusion CMR imaging was combined with a saturation recovery gradient-echo pulse sequence. Three to four slices were acquired sequentially per R-R interval with 10 mm slice thickness, and a reconstructed in-plane resolution of $1.25 \times 1.25\,\mathrm{mm}^2$. Perfusion sequences were acquired after Gadolinium contrast agent bolus injection over 40 to 65 consecutive heartbeats, and they illustrate the contrast agent's first pass through the myocardium. For all patients, findings from coronary artery inspection as well as late enhancement MRI were available based on the AHA segment model.

Results For all image sequences, parameter maps were calculated with the deconvolution method after motion correction with the *Morphon* method described in Section 3.2.2.4. The segmentation was performed automatically on these images. Sequences 32, 36, 38 had known infarctions proven by late enhancement MRI. In these images, seedpoints were detected automatically in all regions where late enhancement had been detected as shown in Figure 4.31. For those regions associated with stenosed arteries but not with late enhancement, defects were detected in sequence 28, 36, 38, and 34. Figure 4.32 shows the results for case 34. The combination with the coronary artery tree enables the inspection of the perfusion state downstream of diseased vessel segments. Figure 4.33 presents the segmen-

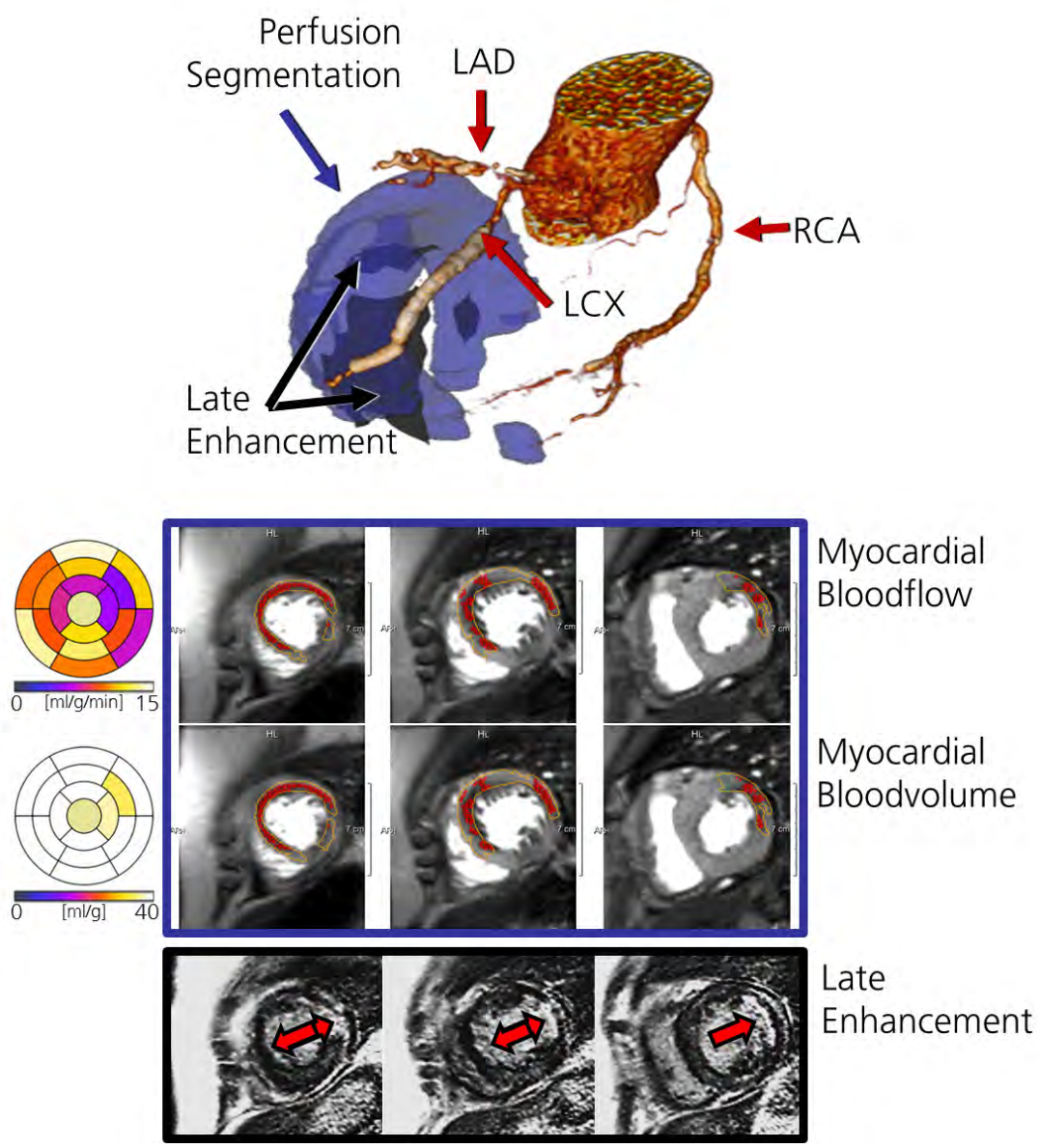

Figure 4.31: Comparison of automatic segmentation in perfusion parameter images with findings from coronary artery inspection and late enhancement MRI for sequence 32. For LAD and LCX stenoses ≥ 75% were reported, the RCA stenosis is ≥ 50%. The results clearly display that seedpoints (red markers) were detected in those regions with tissue defects proven by late enhancement. Compared with the AHA segment analysis, more accurate information about the defect's extent (yellow contours) is presented. The 3D visualization at the top shows a volume rendering of the coronary artery tree. The late enhancement segmentation is colored black, and the perfusion segmentation result represented by the blue surface. This visualization allows the assignment of the defective tissue regions to the supplying artery branches. Shape and location of the perfusion defect indicate that the LAD and LCX stenoses are relevant whereas the RCA stenosis does not cause a strong perfusion deficit.

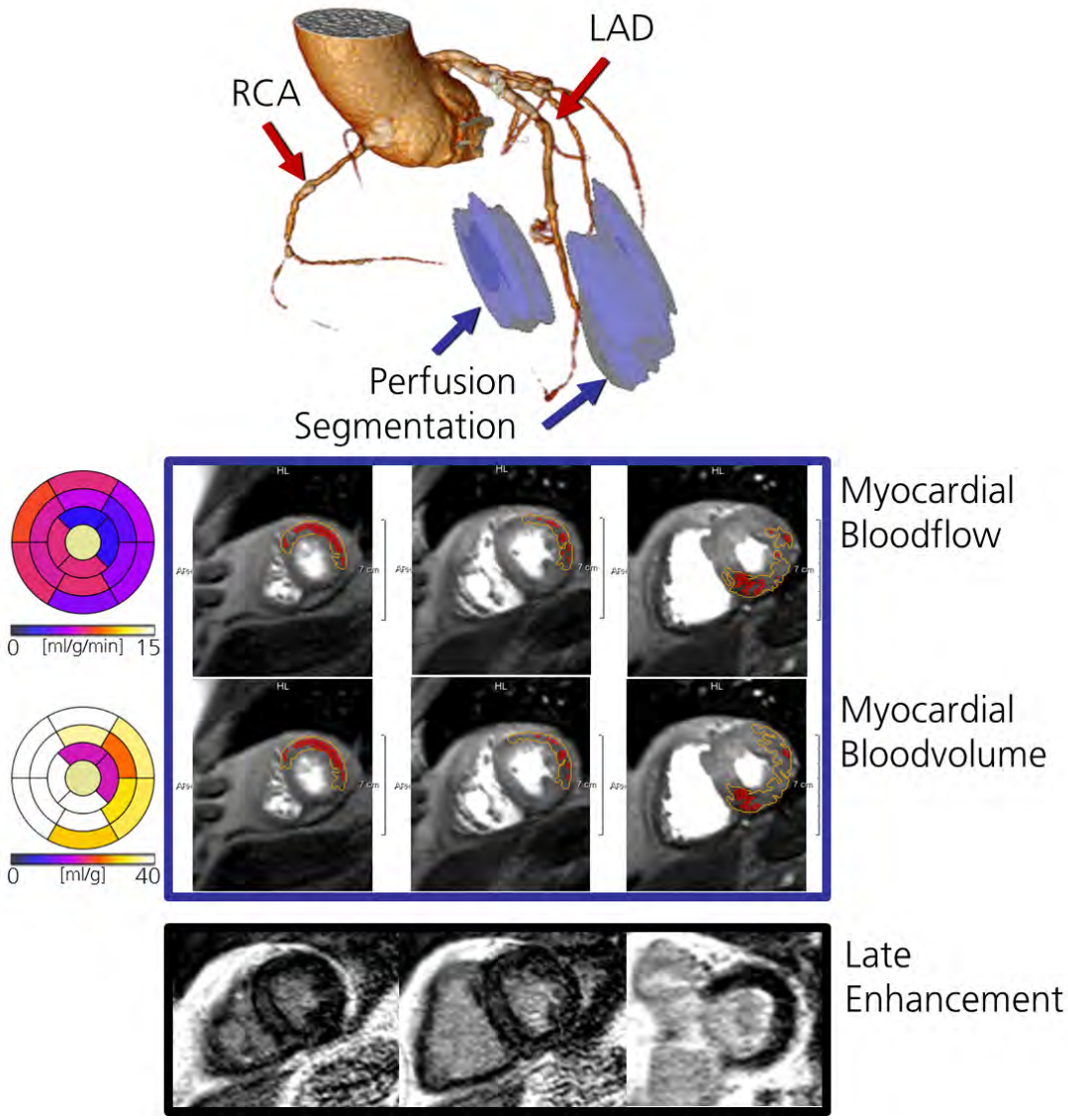

Figure 4.32: Comparison of automatic segmentation in perfusion parameter images with findings from coronary artery inspection and late enhancement MRI for sequence 34. LAD and RCA of this patient are known to have stenoses ≥ 75%. Model-based as well as segmentation-based analysis indicate perfusion defects. Based on the AHA model the defect is assigned to LAD and LCX. The direct 3D visualization at the top shows however, that the defect could also be caused by the RCA stenosis.

tation results for sequences 28 and 36. These segmentation enable the assessment of the real transmurality of the perfusion defect.

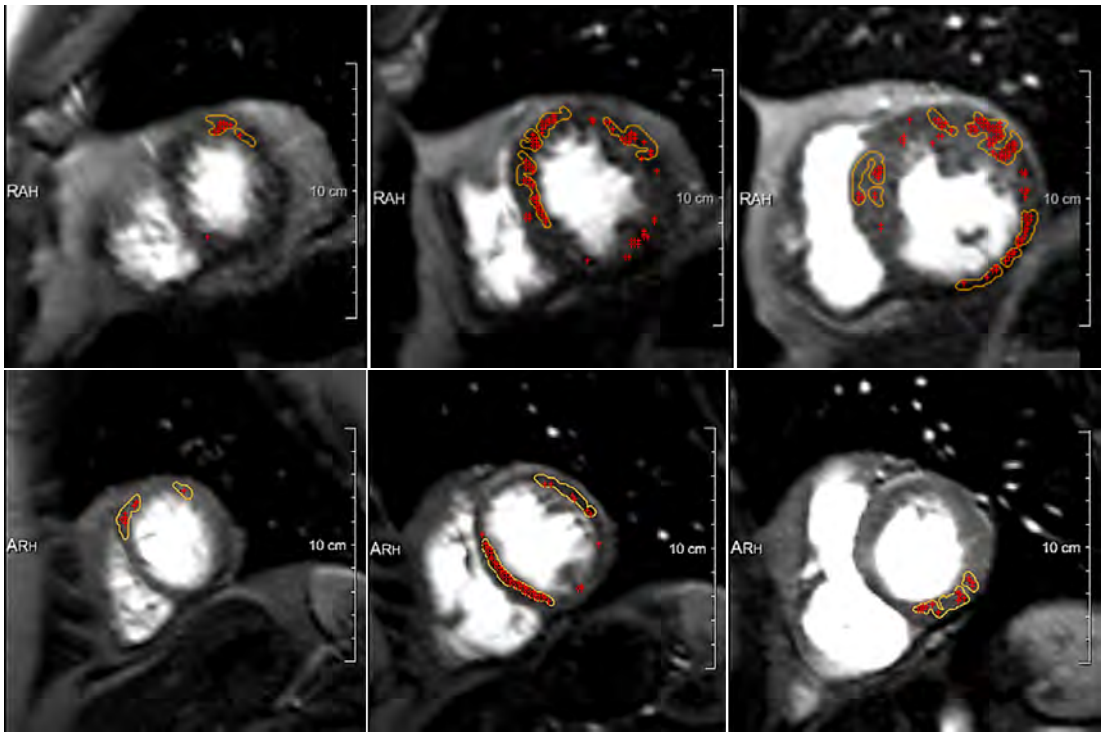

Figure 4.33: Segmentation results for sequences 36 and 38. The presented contours display clear outline and transmurality information.

Discussion The presented combination of perfusion parameter calculation and the detection of suspicious regions have been successfully tested with ten datasets from clinical practice. The comparison with findings from other modalities showed that all results were plausible. The clear delineation of the underperfused region is very promising and indicates the potential for a region detection, which allows a better inspection of extent and transmurality of perfusion defects. In combination with the coronary artery tree, the detection of the coronary arteries provide a promising non-invasive means for the assessment of coronary stenosis relevance. However, the significance of the presented evaluation is limited, because of the high uncertainty in the underlying data. The calculation of the parameter maps strongly depends on the preceeding motion correction. Furthermore, the reference information from the coronary artery inspection can not directly be compared with the perfusion analysis. On the one hand, there is patient-specific variation in the anatomy [Pereztol-

Valdes et al., 2005] that limits the accuracy of the assumption on spatial relations between arterial branches and corresponding supply territories. On the other hand, it is known that the degree of stenosis in a vessel is not directly related with its relevance [Tonino et al., 2009]. Thus, the detection of an underperfused region as well as no region detection are plausible in myocardium associated with a stenosed vessel and no infarction. Therefore, the segmentation of perfusion defects, which are not related to late enhancement regions is difficult to assess.
In the context of studies that are concerned with the clinical impact of cardiac MRI, such as MR-INFORM [Hussain et al., 2012], perfusion MRI will be compared with pressure wire measurements. These are assumed as the gold standard for stenosis relevance measurements. Besides the assessment of the MR measurement methods, it will hopefully also be possible to evaluate perfusion analysis postprocessing methods based on these data.

4.4 Discussion

This chapter has been concerned with the extraction of the relevant structures for the assessment of the coronary artery tree and the myocardial viability based on contrast-enhanced cardiac CT and MRI. This included the development of methods for

1. The segmentation of the coronary artery tree and the extraction of the arterial branches centerlines in CT and MR coronary angiography datasets.

2. The automatic delineation and quantification of myocardial regions which exhibit late contrast enhancement in late phase CT and MRI datasets.

3. The automatic detection and delineation of perfusion defects based on motion corrected perfusion MRI sequences.

The basic idea in the development of these methods was to separately model geometrical knowledge about shape and location of the structures of interest and modality-specific knowledge about their appearance in the examined image data.
For the extraction of the coronary arteries, an automatic detection of aorta and coronary ostia was developed based on the description of the aorta as a tubular structure with a given range of plausible diameters. The coronary ostia are assumed to be thin structures pointing away from the aorta center. This concept has been combined with an automatic threshold

range detection, which allows the application to CT and MRI data. To finally extract the coronary arteries the existing methods by Selle, Boskamp and Rasch for vessel segmentation and centerline extraction have been integrated.
The evaluation of the automatic coronary tree detection with datasets from different hospitals and scanners as well as varying levels of quality revealed good results for the datasets with medium to good quality regarding the tree detection and provided computation results very quickly. Because it was amongst the first approaches concerned with this problem, the implemented approach have been adapted and improved by other authors, e.g., Wang and Smedby [2008]. Compared to current state-of-the-art methods, the major drawback is the lower accuracy in the calculation of the coronary centerline, which is derived from the segmentation mask.

The shape assumptions applied for the late enhancement and perfusion defect detection are based on the knowledge about the progression of ischemia in coronary artery disease. The models applied to the intensity analysis are derived from the principles of contrast agent distribution in blood and different tissue types as well as modality-specific noise characteristics. The implementation of these concepts is partly based on existing methods such as the watershed method by Hahn and Peitgen [2003] and the deconvolution methods for the calculation of quantitative perfusion parameters by Kohlmann et al..
The automatic late enhancement detection was compared to histological findings from laboratory animals as well as expert delineations. The methods performed better on MRI data, which provides higher contrast-to-noise in the regions of interest, but was successful on CT data as well. The idea of the description of the myocardial intensity distribution through a Rayleigh-Gaussian mixture model has been adapted in other approaches for the same problem [Elagouni et al., 2010] as well as for the generation of phantom datasets [Tobon-Gomez et al., 2010]. The major advantages over other state-of-the-art methods are the successful inclusion of microvascular obstructions as well as the applicability to CT datasets [Hennemuth et al., 2008a, 2012a].
For the automatic delineation of perfusion defects, which is implemented as a segmentation on the automatically determined parameter maps, a limited evaluation has been performed. The comparison of the results with findings from coronary angiography and late enhancement MRI revealed promising results towards the accurate segmentation of myocardial perfusion defects, the assignment to the supplying artery and the non-invasive assessment of stenosis relevance.

The major contribution of this chapter is the development of suitable methods for the fast extraction of the structures of interest. The approaches for the segmentation of coronary tree and delayed enhancement have inspired other authors and are used in products and clinical studies respectively. Future work should focus on the automatic detection of the myocardium, which would enable a completely automatic viability analysis. Furthermore, within current studies such as *INFORM* [Hussain et al., 2012] data is acquired, which will allow to compare the results of MR perfusion analysis with catheter-based measurements of the fractional flow reserve (FFR). These are currently considered to be the gold standard in the quantitative assessment of stenosis relevance, and the comparison will hopefully provide the means to better assess the suitability of the provided perfusion analysis techniques for the detection and segmentation of relevant perfusion defects.

5

Software Application and Clinical Evaluation

The combination of the described methods to a software application, which provides a benefit for clinical practice is a non-trivial task. On the one hand the applicability of the provided methods depends strongly on their integration into a suitable workflow concept. On the other hand, it is necessary to support the interpretation of provided results through meaningful visualizations and exploration methods.

5.1 Software for Integrated Cardiac Image Analysis

There exist many commercially available software packages for the analysis of cardiac CT and MRI image data. Most software packages perform modality-specific tasks separately. Myocardium-related findings are stored by means of the AHA segment model and combined in a report, which shows the bulls-eye-plots with results from different examinations side by side. Some commercial as well as freely available research tools like *SEGMENT* or *OsiriX* allow the fusion of arbitrary images without supporting any disease specific analysis [Heiberg et al., 2010, Rosset et al., 2006]. In these tools, images are either overlaid on each other in 2D views or volume renderings with different transfer functions are fused. For hybrid imaging systems such as PET/CT or SPECT/CT there exist software for combined inspections. These provide overlays of the color-coded parameter maps from the nuclear imaging modality on the CT images and 3D volume renderings of the CT image data with colored parameter maps mapped on the heart surface. Clinical studies showed that these visualizations provide additional meaningful information for the assessment of

correspondences between vascular pathologies and myocardial perfusion defects [Nakaura et al., 2005, Gaemperli et al., 2007, Fricke et al., 2009].

There are few scientific research projects concerned with advanced concepts for the visualization and exploration of cardiac image data and derived results. An overview of recent approaches is given in Gupta et al. [2012]. The works by Oeltze, Termeer, Kuehnel and Kirisli are all concerned with the visualization of results derived from MR or CT coronary angiography and myocardial examinations [Oeltze et al., 2006, Kuehnel et al., 2008, Termeer et al., 2007, Kirisli et al., 2011]. Oeltze et al. proposed to use the bulls-eye plot as an active element of the graphical user interface. In their prototype, the selection of AHA segments triggered a 3D animation, which rotated the corresponding 3D region into the user focus. The concept

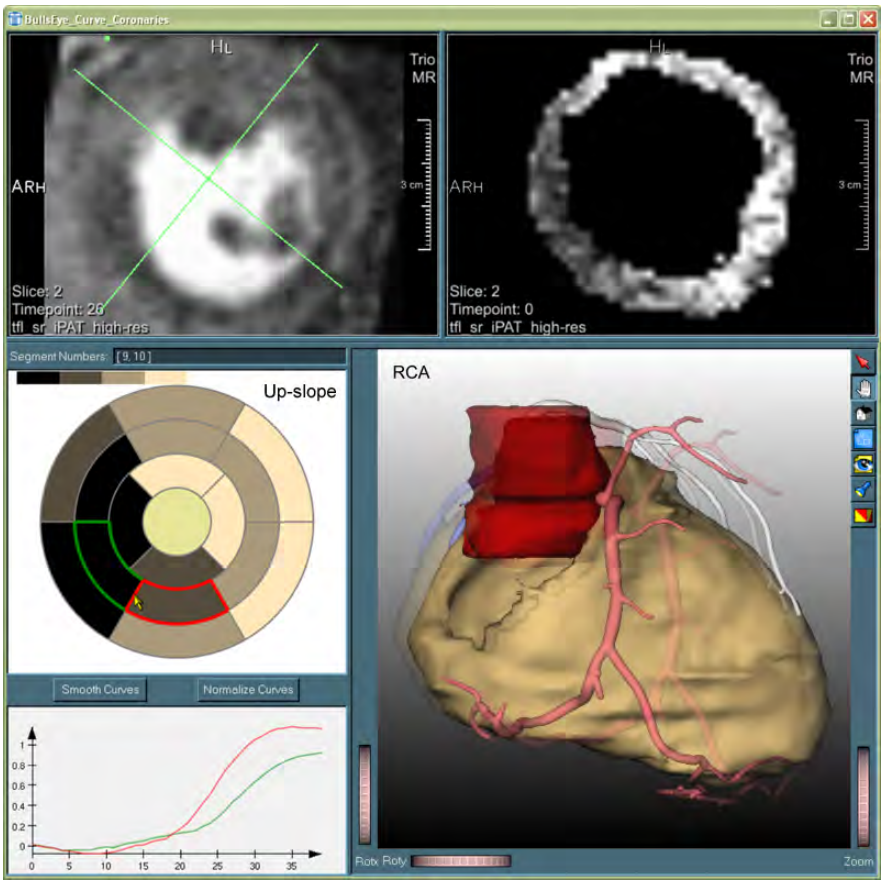

Figure 5.1: Combined inspection of CT coronary angiography and myocardial perfusion as proposed in Oeltze et al. [2006]. The 2D parameter map and the 3D visualization are automatically chosen such that the region corresponding with the segment selected in the bulls-eye-plot is shown.

of a synchronized 2D/3D exploration of an abstract result presentation is also used in the

CoViCAD software for the comprehensive visualization of coronary artery disease [Termeer et al., 2007]. Termeer developed an advanced concept for user-individual bulls-eye-plots as an abstract map of the myocardium. Like proposed in many commercial products, parameters as well as the coronary arteries are projected directly into the bulls-eye-plot. To provide additional information on transmurality, the bulls-eye plot is transformed into a 3D object. The user can then navigate through selecting the focus point in either the 3D visualization or the 2D bulls-eye-plot map.

These approaches use the coronary angiography volume data to provide information on

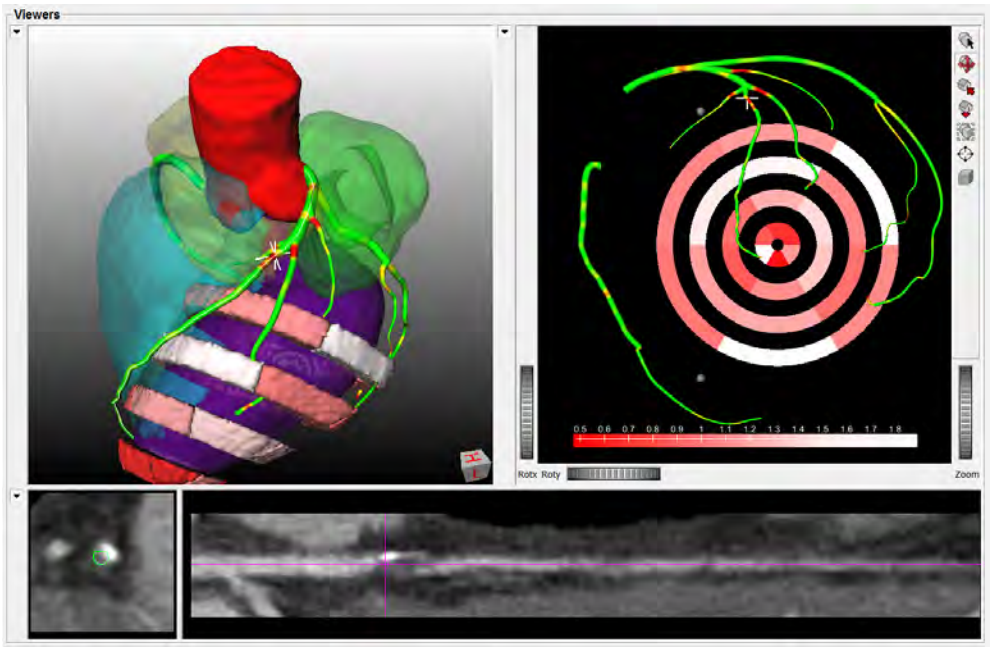

Figure 5.2: The *SMARTVis* software by Kirisli et al. couples a idealized 2D and 3D visualizations with an inspection of the original image data for the interactive result exploration.

the anatomical relations in 3D. The interaction is based on the analysis results derived from the myocardial examinations. The concept we provided in Kuehnel, Hennemuth, Oeltze, Boskamp, and Peitgen [2008] also includes vessel-related measurements. It is an extension of the approach by Oeltze et al. and based on the concept of results provided as findings. These findings are measurement results based on myocardial defect or coronary stenosis inspections. Thus they contain information on the position of the detected pathology. Furthermore, the information about the AHA correspondences can be used, and a multiple viewer concept provides the combined inspection of findings from myocardial and angio-

graphic examinations on different levels of abstraction. Thus, if data is aligned, combined views are provided whereas otherwise corresponding regions according to the AHA relations are shown in side-by-side views (see Figure 5.3). Similarly, Kirisli et al. provide an extension

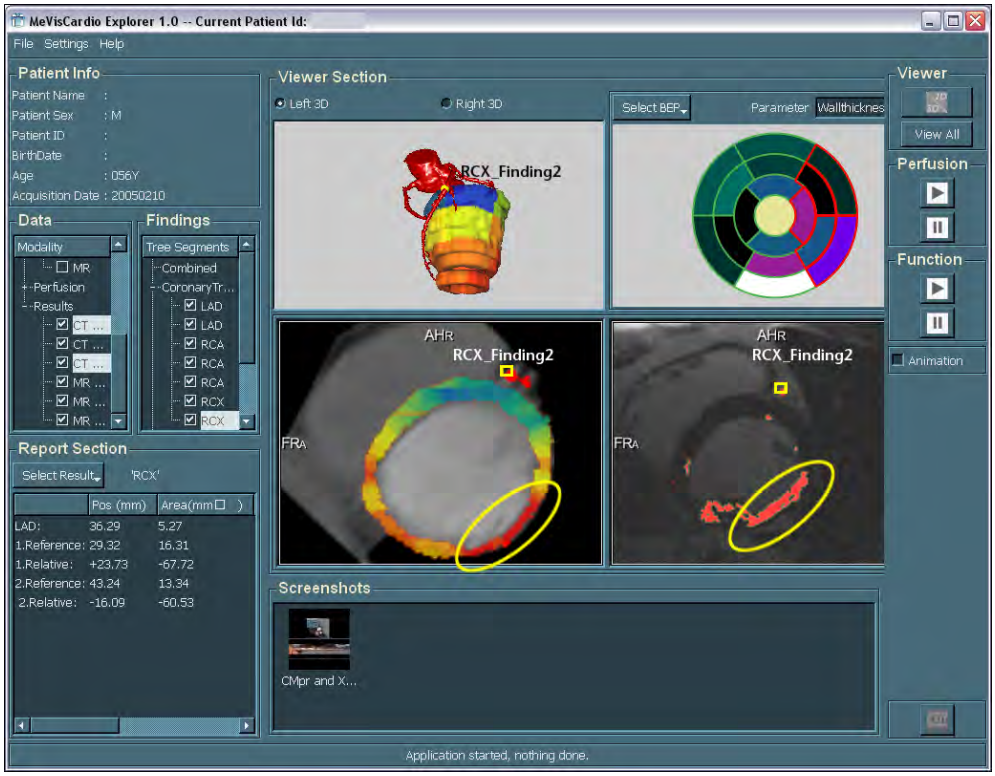

Figure 5.3: CardioExplorer by Kuehnel, Hennemuth, Oeltze, Boskamp, and Peitgen [2008]. Findings related to coronary arteries or myocardium can be selected from the menu on the left, and the visualization is parameterized by selecting the 3D viewing and 2D overlay components. The viewers on the left show a coronary tree and the wallthickness analysis derived from the CT data. On the right side the results of the MR late enhancement analysis are presented. The region corresponding to the selected stenosis measurement according to the AHA model is highlighted.

of *CoViCAD*, which also shows the detected stenoses from the CTCA analysis after aligning CTCA and MRI data [Kirisli et al., 2011] (Fig. 5.2). They provide a *MeVisLab*-based software prototype, which supports the complete workflow of the data analysis and the combined inspection.

5.2 Software Prototype

The aim of the presented software design is to provide analysis functionality for both modalities and to support fused visualizations in order to clarify correspondences between arterial segments and perfusion defects. The developed image analysis components support the fusion of different types of image data, the analysis of MRCA, MR late enhancement and MR perfusion data as well as the analysis of CTCA and CT late enhancement data. It is very difficult to organize these tasks in a universally applicable workflow. In clinical routine actual MR datasets might be combined with previous CT data. Most conventional evaluations only use either MR or CT data, and not all MR examinations provide both late enhancement and perfusion data. Furthermore the time pressure in clinical routine has to be considered. Thus, the major goals in the software design were

1. the integration of the fused exploration into the image analysis workflow

2. the development of an adaptable workflow concept

To address the first goal, the data representation used in this approach is based on the image description and finding concept we proposed in Kuehnel, Hennemuth, Oeltze, Boskamp, and Peitgen [2008], and results are stored in such a way that they can be used within the *CardioExplorer*. The processed data is organized as shown in Figure 5.4.

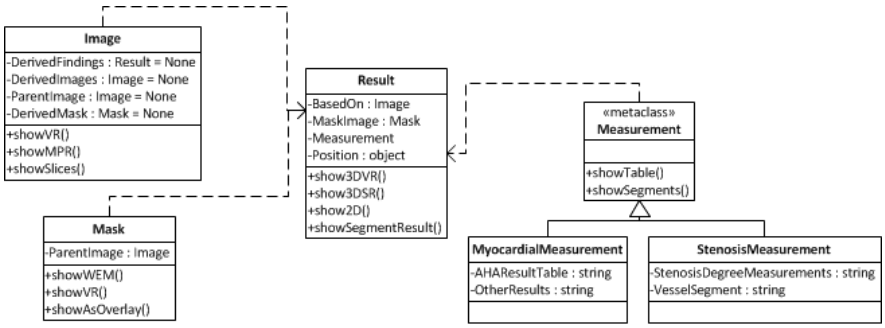

Figure 5.4: Major datastructures for analysis and exploration of CT and MR examinations of CAD patients.

Image data and results provide different visualizations, which are typically selected according to the spatial density of the available data as shown in Figure 5.5. This results from informal interviews with different radiologists, who preferred data representations close to

the image data such as volume renderings over abstract visualizations. Although the rejection of advanced visualizations like the continuous 3D bulls-eye-plot or glyph-based representations proposed by Oeltze et al. [2008] might simply be based on the lack of training in the interpretation of these visualizations, it was accepted here. As an extension of the

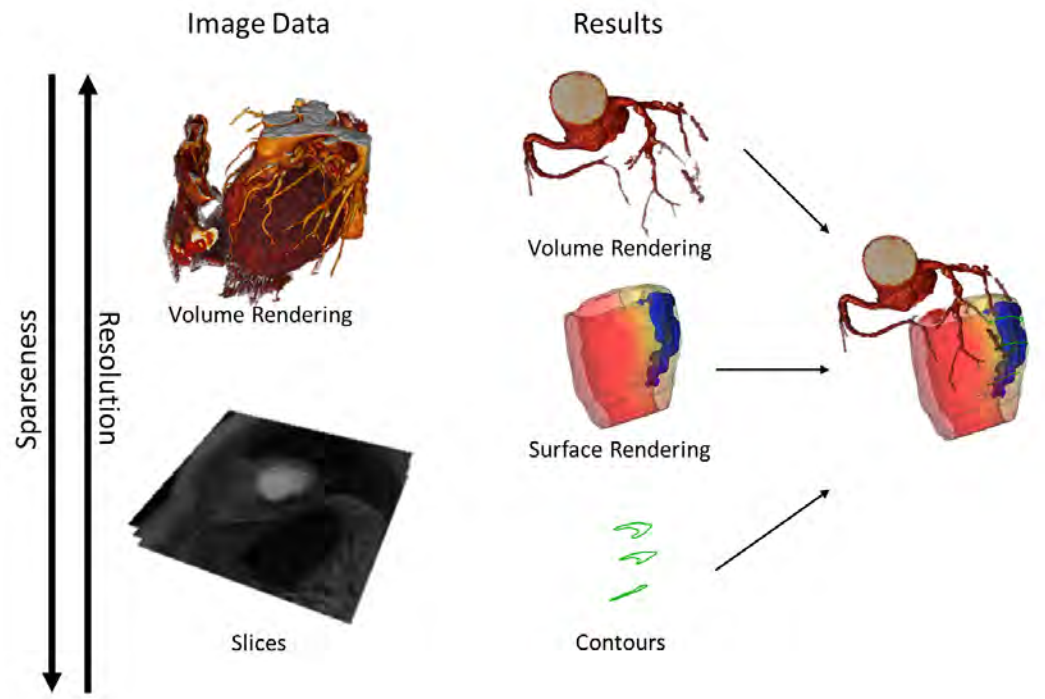

Figure 5.5: Scheme for the selection of the 3D representation of image data and segmentation results.

result fusion construct proposed in previous applications, the concept of the proposed implementation is to provide as much information as possible in all analysis steps. The idea behind this is to support a focussed analysis and shorten the analysis time.

The prototype is implemented within an extension of the *MeVis Application Frame* developed by Rexilius et al. [2006]. This allows the definition of workflow modules with preconditions regarding the type and processing status of available image data. These modules can be configured to workflows via XML-descriptions to define the processing order and the parameterization of the workflow steps. The following workflow modules have been implemented for the developed software prototype:

Alignment Module Functionality for the alignment of the coordinate systems of data from

different acquisitions

Motion Correction Alignment of MRI slice images with a reference image and the motion correction within perfusion sequences

Myocardium Segmentation Interactive segmentation of the myocardium

Late Enhancement Analysis Segmentation and quantification of regions showing late enhancement and microvascular obstructions

Perfusion Analysis Calculation of parameter maps and segmentation of suspicious regions

Rest/Stress Perfusion Analysis Comparison of perfusion parameters from rest/stress perfusion sequences

Coronary Artery Analysis Segmentation and interactive inspection of the coronary arteries

5.2.1 Pre-processing

In the developed application pre-processing means alignment and motion compensation. These tasks are implemented as interactive workflow steps here.

Initial Alignment of Coordinate Systems The initial alignment uses rigid registration initialized via three landmarks and thus consists of three panels. The first panel is dedicated to define corresponding viewing directions. To this end, the user defines the viewing axis, along which the image data is reformatted for the landmark definition. This is typically the long-axis, and images are compared in short-axis orientation. The next panel allows the positioning of the landmarks in the reformatted views as shown in Figure 5.6. The last panel uses the *MeVisLab ManualRegistration* macro module to let the user correct of the initial alignment through moving and rotating the images interactively in overlay views.

Late Enhancement Slice Alignment There are no pre-conditions for these modules. The functionality can be used to align arbitrary images. The result of this module is a transformation matrix, which is stored within the XML-description of the case the processed data belongs to.

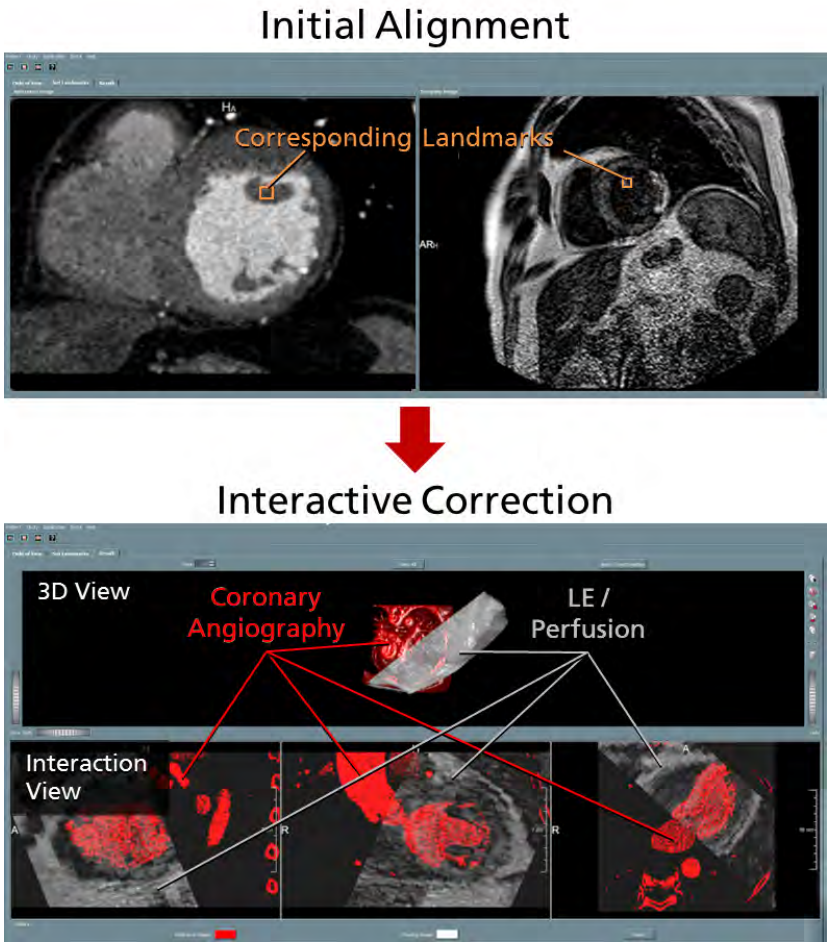

Figure 5.6: Interactive initial alignment of images from different acquisitions. The upper image shows the panel for the landmark definition whereas the lower panel shows the following refinement step.

Motion Correction The motion correction module provides the functionality for the non-rigid registration between or within images, which have already aligned coordinate systems. Thus, slice alignment to correct for patient and breathing motion as well as the correction of perfusion sequences can be performed. After selecting, which image to use, the user determines the spatiotemporal subimage to register and use in further processing steps. The next step is the selection of a reference image in case the slices should be aligned with another image as described in section 3.2.2.2. The correction process consists of

1. matching the slices of the image to correct with the reference image

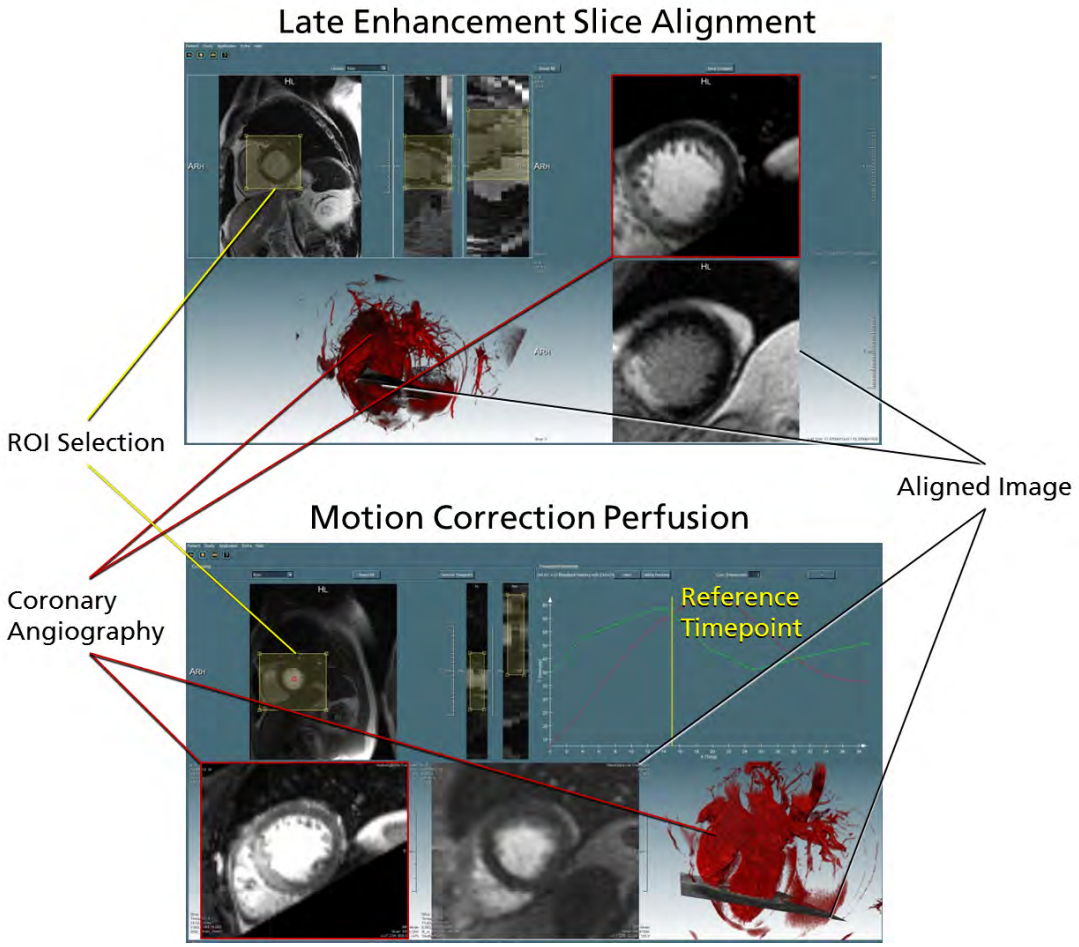

Figure 5.7: Motion correction modules. The images show the user interfaces for the alignment and motion correction of MR late enhancement and perfusion images.

2. matching the time frames of the image sequence onto the corrected reference time frame

Both steps can be performed separately and thus the module can be used to

- align MR late enhancement slices with a CT or MR coronary angiography
- align MR perfusion data with CT or MR coronary angiography or MR late enhancement
- perform a motion correction in a perfusion sequence, which is or is not pre-aligned with a reference image

Through adding pre-conditions regarding the allowed image types for reference image and the image to correct, this module can be adapted to one specific task like, e.g., aligning late enhancement slices with a coronary angiography volume.

Myocardium Segmentation The AHA segmentation as the analysis of intensity or parameter distributions for the detection of suspicious myocardial regions require a preceding segmentation of the myocardium. This is done interactively with the live wire algorithm by Schenk et al. [2000].

5.2.2 Analysis

The workflow modules for the analysis of late enhancement, perfusion and angiography are implemented in such a way that they can be applied to both CT and MRI datasets.

Late Enhancement Segmentation The late enhancement module offers the functionality to perform a segmentation with

1. interactive delineation
2. the conventional 3σ threshold method
3. the proposed mixture model approach

Figure 5.8 shows the user interface of this module. The applied segmentation method is chosen from the selection in the upper row. The segmentation result is then shown in 2D, 3D and in the AHA segment model. The 2D view allows a direct comparison with the underlying image data and provides methods for the interactive manipulation of the result based on the placement of markers or editing contours. Because of the sparseness of the late enhancement images, the 3D visualization uses surface rendering. The segmented defective myocardium is shown in dark blue to indicate, that it is not vivid. The myocardial surface is colored red, where there is no late enhancement. Close to infarcted regions, the surface is colored according to the distance from the late enhancement region to show the transmurality of the infarct. The transparency is also adapted to this distance. If a segmented artery tree is available for the inspected case, this can be added as a volume rendering to allow a visual exploration of correspondences between stenoses and infarct regions.

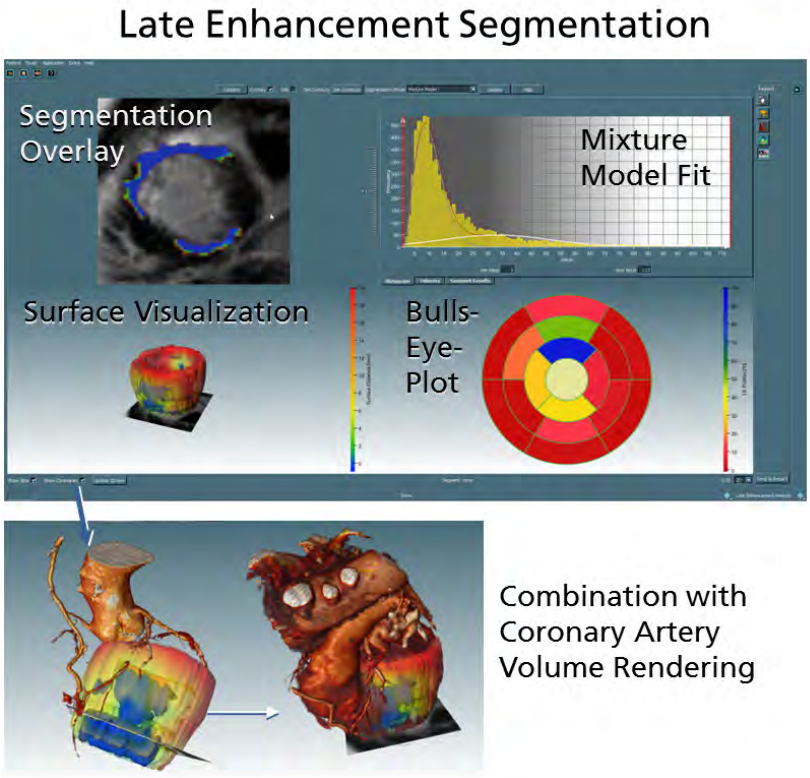

Figure 5.8: Late enhancement analysis with the mixture model approach. The diagram shows the myocardial histogram with the fitted mixture model. The overlay on the left shows the segmentation result with a colorcoding according to the portion of late enhancement in the regarding voxel. General overviews of the result are shown in the lower row.

Perfusion Analysis The perfusion analysis module derives descriptive or quantitative parameters from the input perfusion sequence and allows to display these as color-coded overlays as shown in Figure 5.9. Similar to the late enhancement analysis, perfusion parameters are analyzed according to the AHA parameter model or through deriving segmentations from the parameter images. Because of the images' sparseness, the 3D visualization of the segmented regions is visualized as a combination of a contour set and the corresponding surfaces as shown in Figure 5.9. These surfaces are rendered transparent to ensure the visibility of late enhancement segmentation results, which are expected to be located within underperfused regions.

Coronary Artery Analysis For the detailed inspection of the coronary arteries and the supplied myocardium, an overview visualization is combined with interaction components that allow the inspection of suspicious myocardial regions. The first overview visualization

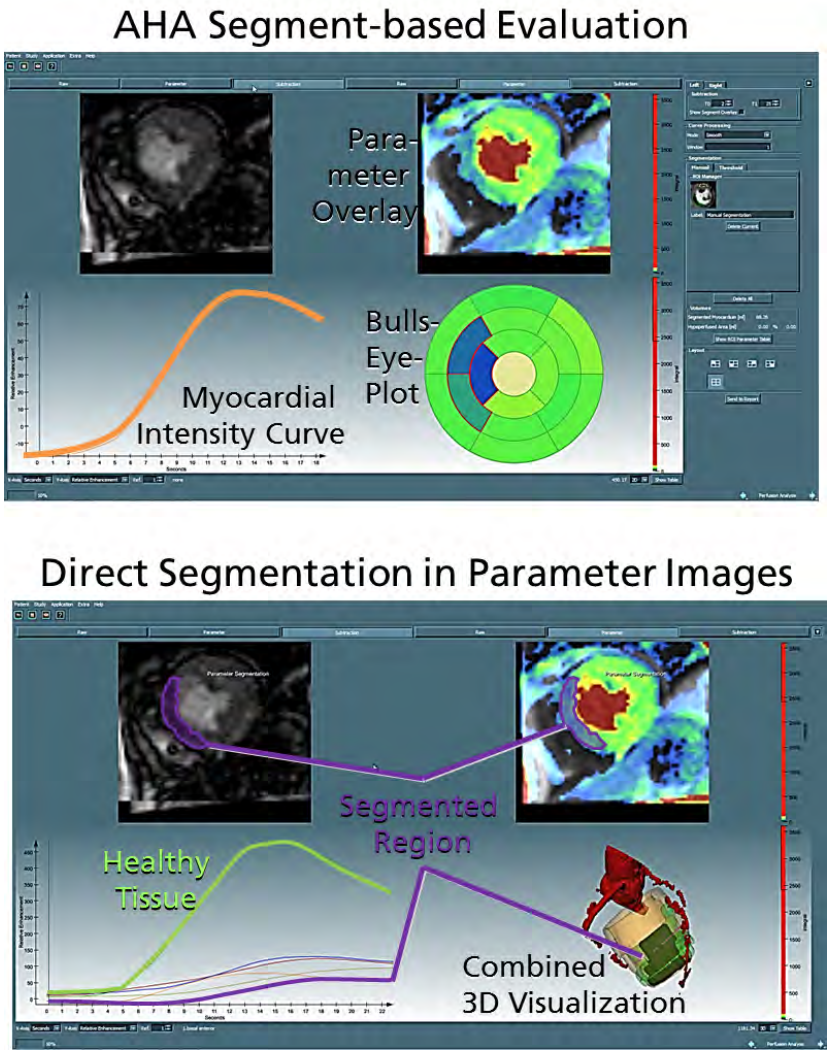

Figure 5.9: Perfusion analysis module. The 2D viewers in the upper row show a subtraction image as well as a color-coded parameter image derived from the perfusion sequence. The lower row shows the analysis results. The curves depict the intensity courses of the AHA segments or the segmented myocardial regions. The upper image shows the parameter analysis for the AHA segment model. The lower image depicts the result of a segmentation performed on the parameter image.

shows a joint volume rendering of the coronary angiography dataset and the fused late enhancement and/or perfusion segmentation. To avoid concealment through surrounding structures, the heart ROI is segmented in the CA dataset for visualization. After the coronary tree segmentation, the artery inspection is performed in reformatted views. The fused myocardial defect segmentations can be overlaid in all 2D and MPR views. Especially, the

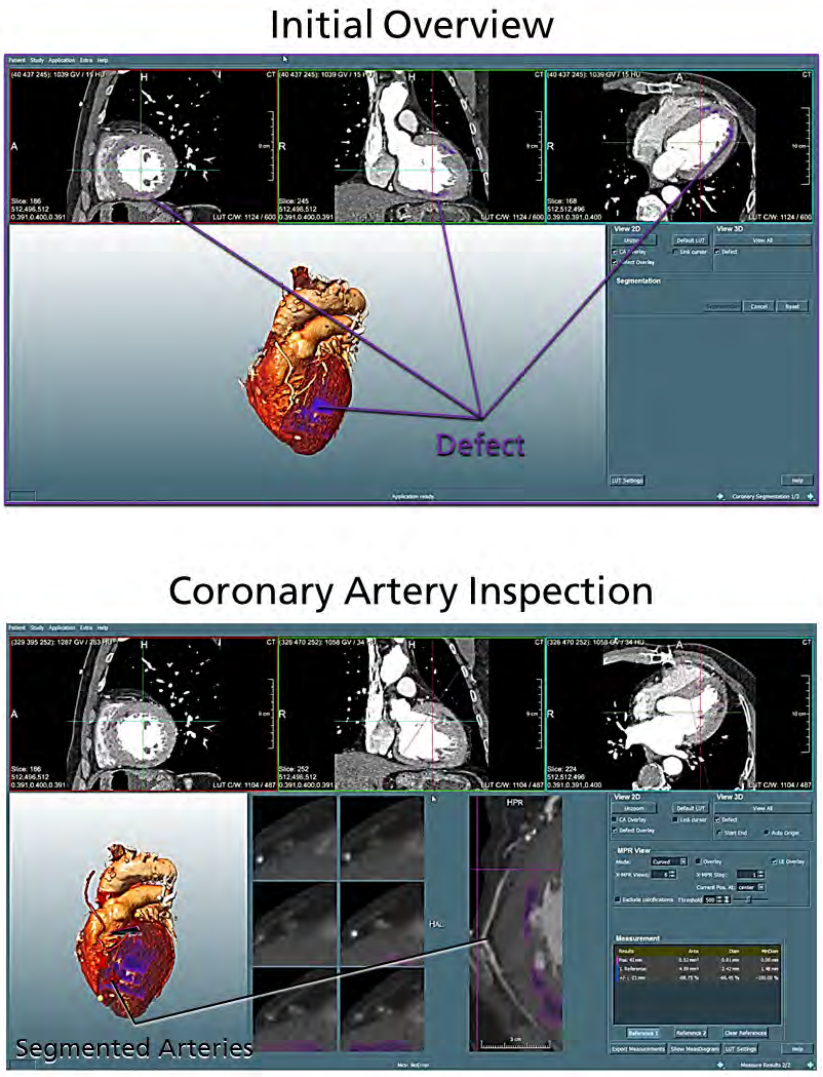

Figure 5.10: Coronary artery inspection. The analysis starts with an overview visualization (upper image). After the segmentation of the coronary artery tree, vessel branches are inspected in reformatted views as shown on the right side (lower image).

curved and cross MPR views provide detailed informations about vessel pathologies and the state of the surrounding myocardium.

5.3 Clinical Evaluation

The problem of the standard AHA segment model providing wrong correspondence information about the supply territories of coronary artery branches in about 23% of patients has been shown in several studies [Ortiz-Perez et al., 2008, Pereztol-Valdes et al., 2005]. Anatom-

ical variation as well as pathological alterations and surgical interventions cause deviations from this standard model. Thus, the introduction of methods to overcome this limitation is of interest in clinical practice. The benefit provided through the developed software has been evaluated in three clinical studies, which were dedicated to the combined analysis of angiographic datasets and examinations of the myocardium. These studies were carried out by different institutions and focussed on different types of data. The combinations, which were evaluated in the different studies were:

1. MR angiography and MR late enhancement
2. CT angiography and CT late enhancement
3. CT angiography, MR perfusion data and MR late enhancement

All studies were carried out with adapted configurations of the software components described above.

5.3.1 Combination of MR Angiography and MR Late Enhancement

The study by Seeger et al. [2011] was dedicated to the evaluation of feasibility and added diagnostic value of the fused analysis of MR coronary angiography and late enhancement with regard to assignment of myocardial infarction areas and supplying coronary artery branches. 25 consecutive patients (20 males, 5 females, mean age 59.9±10.1 years, range 42 to 82 years) with known or suspected CAD were examined with a 1.5T MR scanner. The acquired data included a free-breathing, navigator and ECG-gated T2-prepared 3D whole heart MRCA sequence in axial slice orientation as well as a late enhancement dataset acquired ten minutes after the injection of a gadobutrol bolus with an inversion recovery turbo FLASH 2D sequence. 20 patients also underwent conventional coronary angiography, which served as the standard of reference. Datasets were processed by two observers. First, conventional late enhancement quantification was performed and the AHA segment model was used to provide the standardized assignment of diseased segments to the culprit coronary branches.
The MRCA and MR late enhancement datasets were also processed with the workflow configuration shown in Figure 5.11. The segmentation of the coronary tree was possible in all but three cases, although stents and stenoses regularly impaired the region growing method.

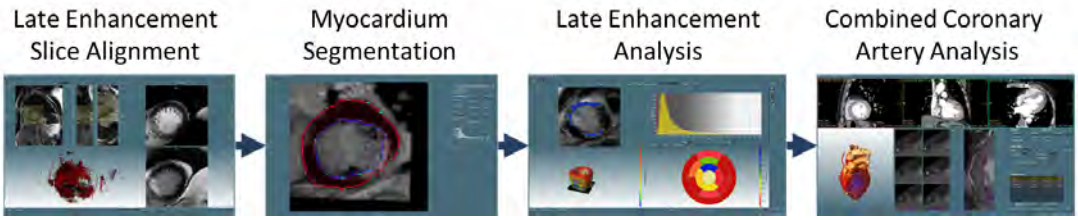

Figure 5.11: Image analysis workflow for the combined analysis of MR coronary angiography and MR late enhancement

Through blurring artifacts there were branches, which could not be detected, in three patients. The vessel segmentation result was graded according to Figure 5.12 depending on the coverage and consistence of the detected branches. For the twenty patients, the ob-

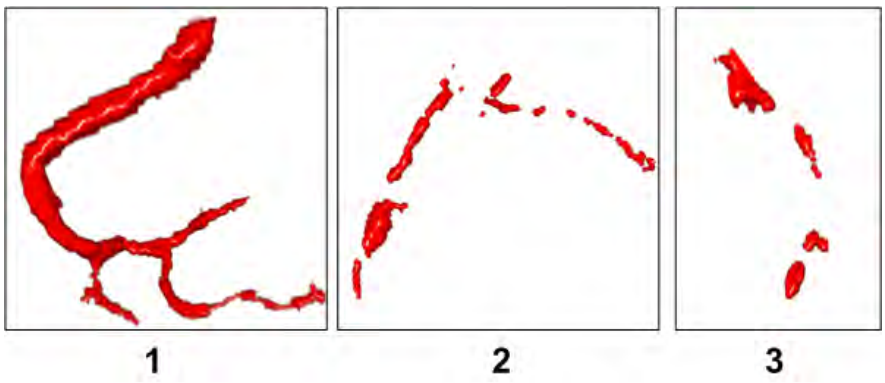

Figure 5.12: Assessment of the coronary artery segmentation quality. The presented branches are examples for a proper segmentation including distal vessel parts (score 1), small gaps in the vessel course (score 2) and a partial segmentation. A score of 4 means that the branch of interest could not be detected.

servers performed an assignment of the corresponding coronary branch based on the fused visualization. To this end, combined tagged volume renderings were produced as shown in Figure 5.13. The MRCA dataset is rendered with a typical lookup table for cardiac datasets, whereas the coronary tree segmentation and the myocardial infarction are shown in red and green respectively. In the three cases, where blurring artifacts impaired the coronary artery segmentation, no assignment was possible. The identified culprit artery branch matched the result of the conventional coronary angiography in all other cases. In four cases, where patients suffered from multivessel disease, the infarction could correctly be assigned to one of the involved vessel branches. No false-positive results were produced. The segmental analysis on the other hand resulted in false-positive results in 6 of the 17 patients, because

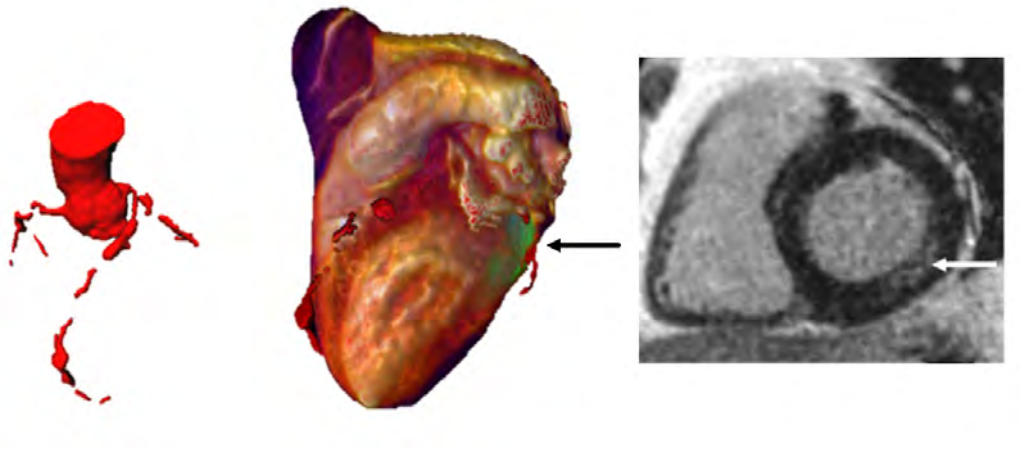

Figure 5.13: Fused visualization of MR coronary angiography and MR late enhancement using tagged volume rendering. The segmented coronary tree is shown in red, whereas the segmented infarction is shown in green.

the late enhancement segmentation expanded into neighboring segments. Thus, the combined approach provided additional information and improved the specificity and the positive predictive value of the assignment of myocardial infarctions to the major coronary arteries.

5.3.2 Combined Analysis of CT Angiography and CT Late Enhancement

Mahnken et al. performed a study to evaluate the benefit of the provided algorithms for the identification of late enhancement as well as for the assignment of the culprit lesion to detected infarct regions. The evaluation was based on animal datasets as well as patient datasets acquired with CT.

Six examined domestic pigs (61.3±6.9 kg) were induced acute reperfused myocardial infarction through the temporal occlusion of the left circumflex or left anterior descending artery with a balloon catheter. Two hours after reperfusion the animals underwent CT imaging. The six consecutive patients (73±12 years; 84±7 kg) had been diagnosed with chronic myocardial infarction and were scheduled for revascularization therapy.

CT imaging was performed with a 64-slice dual source CT system (Siemens SOMATOM Definition), and the examination protocol consisted of an arterial-phase scan and the late enhancement scan. The arterial phase scan was performed after the administration of 120 ml iopromide 300 (Ultravist 300) using a bolus tracking technique. Image volumes with axial

orientation and an effective slice thickness of 0.75 mm were reconstructed at 70% of the RR interval. A field of view of 180 mm^2, a 512 × 212 reconstruction matrix, and a medium-smooth convolution kernel (B26f) were applied.
The late enhancement images were acquired six minutes after the injection of the contrast agent with a lower dosage. These data were reconstructed as short-axis images with 6mm slice thickness from the raw data with a smooth convolution kernel (B20f). The workflow configured for this study consisted of an automatic alignment of the datasets to correct for patient or breathing motion, followed by the interactive late enhancement analysis and the final combined inspection of the coronary arteries and the detected late enhancement (Figure 5.14). To assess the methods performance regarding the accuracy of the late enhance-

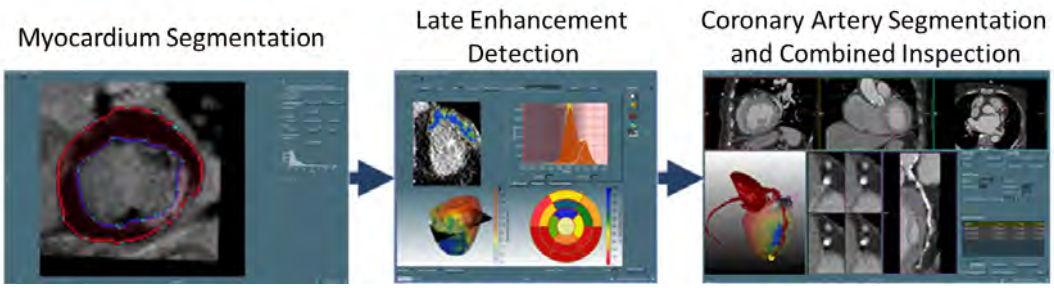

Figure 5.14: Prototype configuration for the combined analysis of CTCA and CT late enhancement

ment segmentation in the CT datasets, late enhancement was also determined with the 3σ-method and manual delineation. The correspondence between coronary artery lesions and regions exhibiting late enhancement was assessed in tagged volume rendering views as well as curved and cross MPRs with overlaid infarction information as shown in Figure 5.15.

The late enhancement segmentation showed a good agreement between mixture-model-based analysis and manual delineation. The comparison of the culprit artery branch matched the position of the balloon catheter during infarct generation in all pigs. In the patient datasets all myocardial infarction territories could be assigned to coronary lesions. These lesions were confirmed by conventional coronary angiography as shown in Figure 5.15. The mismatch between the AHA-segment-based assignment and the result of the fused analysis was 10.4%. From these results it was concluded that the provided method set was suitable for the assessment of coronary lesions and myocardial defects beyond the limitations of the AHA segment model. First, it provides a means for the clear localization of the defective

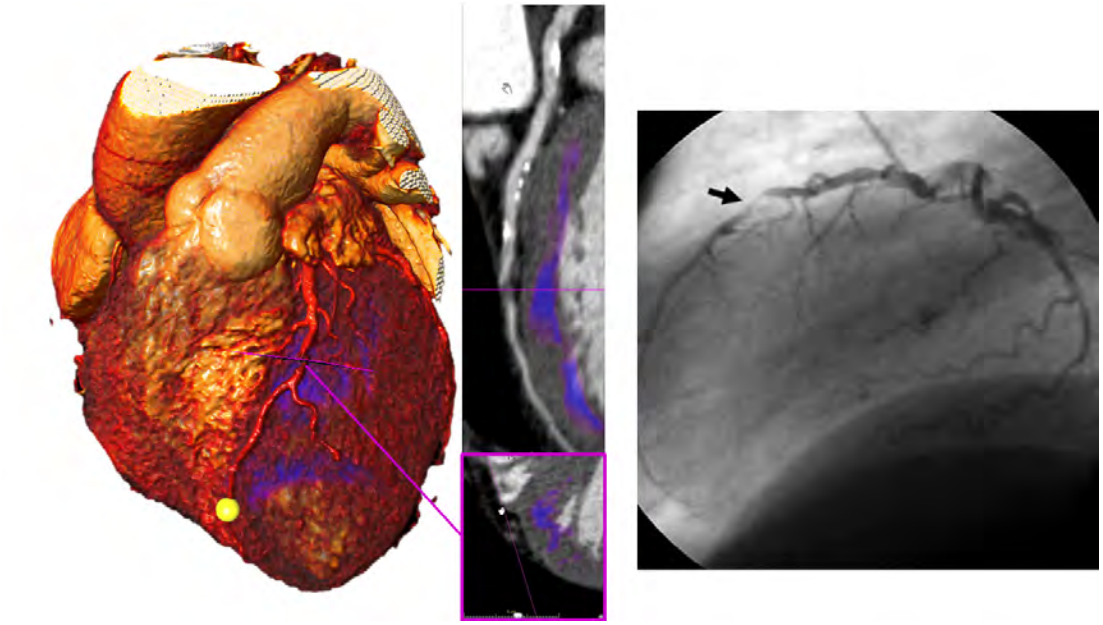

Figure 5.15: Fused volume rendering and corresponding MPR views of the CTCA dataset and the segmentated artery tree and late enhancement. The original data is shown with a typical cardiac lookup table, whereas the artery tree is rendered in red and the late enhancment segmentation is presented in blue. The image on the right shows the conventional angiography of the selected vessel. The arrow marks the position corresponding to the cross MPR .

myocardial tissue, and second it allows an accurate analysis of the correspondence based on dedicated visualizations.

5.3.3 Combination of CT Angiography, MR Perfusion Data and MR Late Enhancement

The study organized by Alkadhi et al. aimed at the evaluation of the added diagnostic value of the fusion of CTCA with MR perfusion and late enhancement data for the assessment of hemodynamically relevant coronary artery diseases. In a first study with five CAD patients the feasibility of the image fusion with the provided methods was demonstrated and a subsequent evaluation of 27 patient datasets assessed the clinical benefit through this fusion [Stolzmann et al., 2010, Donati et al., 2011]. The image fusion and analysis workflow for this study is shown in Figure 5.16. The coronary artery segmentation in the CTCA datasets was performed with the extended algorithm by Bock et al. to achieve a segmentation of as many peripheral branches as possible [Bock et al., 2008].

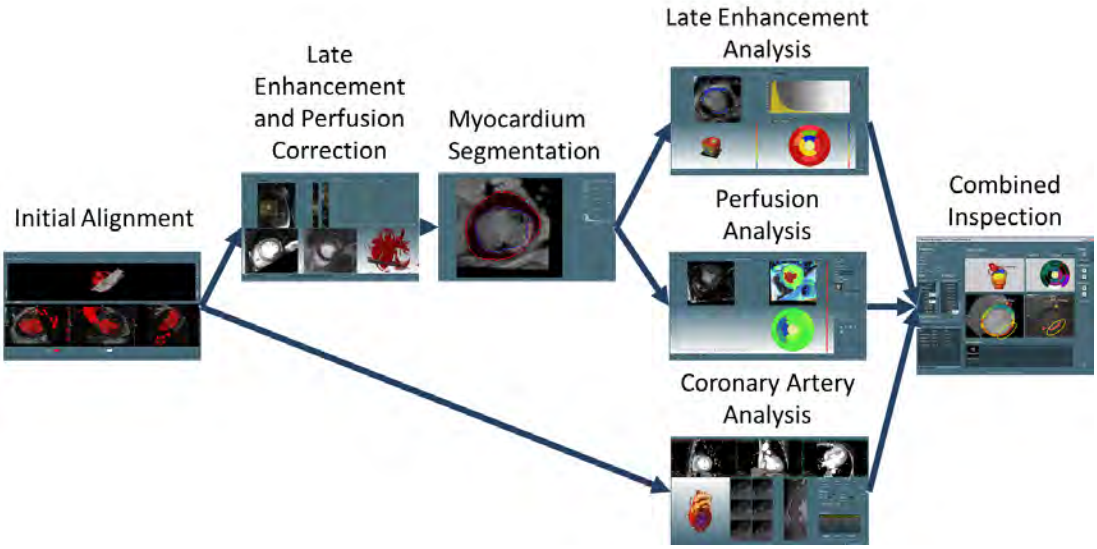

Figure 5.16: Application module workflow for the combined analysis of CTCA, MR late enhancement and MR perfusion

Feasibility Study Five consecutive patients (2 women, 3 men; age 63±12 years; range 52-77) with known CAD were enrolled in this study. All patients underwent low-dose CTCA and CMR on the same day and conventional coronary angiography within 8±5 days. Image alignment as well as the analysis of the coronary tree, late enhancement and perfusion was performed with the proposed software configuration shown in Figure 5.16. For visualization of the data and to show the relation between the coronary artery tree segmented from low-dose CTCA and the myocardium from CMR, the following visualizations were provided:

1. Surface visualization of the segmented coronary artery tree as well as the ventricle and the infarct segmentation from the MR late enhancement image

2. Tagged volume renderings of the CTCA dataset fused with the segmented hypoperfused and late enhancement regions

Examples for both types of visualizations are shown in Figure 5.17. The relation between the perfusion or LGE defects and a coronary artery branch showing significant stenosis was evaluated visually and classified as match or mismatch in consensus by two radiologists.

Data from all five cases could be fused and evaluated with the proposed methods. The comprehensive three-dimensional visualisation of volume-rendered images fused with surface representations of hypo-perfused or scar areas accurately demonstrated the relation-

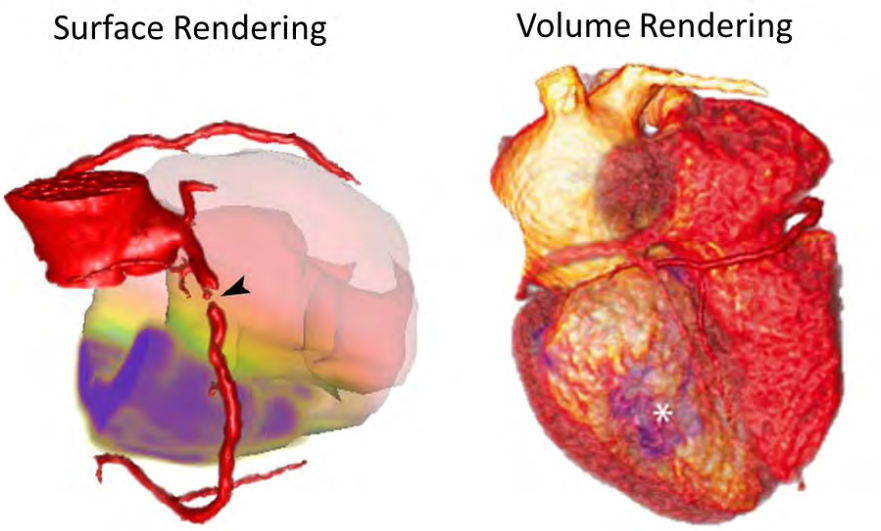

Figure 5.17: Fused CT and MRI visualizations. The left image shows the coronary tree segmentation from CTCA and the left ventricle extracted from the MR late enhancement as surface renderings. The colors of the ventricle surface indicates the distance from the infarction and thus its transmurality. The right image shows a tagged volume rendering of the fused CTCA dataset and the segmented underperfusion. The CTCA is shown with a typical look-up-table whereas the perfusion defect is shown in blue.

ship between coronary artery stenoses and perfusion deficits or late enhancement in all five patients. Thus, these early results were considered promising and another study was initiated to evaluate both the potential clinical benefit of CTCA/CMR image fusion compared with side-by-side analysis and its impact on clinical decision-making.

Clinical Benefit This study focussed on the added diagnostic value of three-dimensional image fusion of computed tomography coronary angiography (CTCA) and functional cardiac magnetic resonance (CMR) for assessing hemodynamically relevant coronary artery disease (CAD). 27 patients with significant coronary artery stenoses proven by catheter angiography underwent low-dose CTCA and CMR as described by Donati et al. [2011]. The accuracy of the image fusion was determined based on the bloodpool segmentations as described in section 3.2.1. The surface distance was 4.1 ± 1.3 mm and the Dice coefficient was 0.78 ± 0.08 mm, which was within the range of one to three perfusion voxels and thus considered accurate enough.
The culprit artery branches and the corresponding lesions were assigned through side-by-side comparison of the CT and MRI datasets as well as based on the above described 3D visualizations. These assignments were carried out by two blinded readers.
In six cases, the side-by-side analysis did not allow to determine a clear correspondence between a diseased artery branch and a perfusion defect. In three of these cases, the 3D visualization provided additional information. In two cases the 3D visualization resulted in a reassignment.

These results showed a clear benefit through the fused 3D visualization in 18% of the inspected cases and indicates, that the presented methods could deliver helpful information for clinical applications such as planning of surgical or interventional procedures in patients having a high prevalence of CAD and for improved topographic assignment of coronary stenoses to corresponding myocardial perfusion defects.

5.4 Discussion

This chapter described the available data and the requirements for the assessment of the correspondences between coronary artery pathologies and myocardial defects based on contrast-enhanced cardiac CT and MRI. The proposed approach consists of a set of software modules, which encapsulate methods for the alignment and the analysis of coronary arteries, myocardial perfusion and late enhancement. These modules can be combined to different workflows.

The clinical evaluation covered three different configurations of image data. The study by Mahnken et al. [2010a] was concerned with CT coronary angiography and CT late enhancement. Seeger et al. examined the combination of late enhancement and coronary angiography from MRI [Seeger et al., 2011]. The study by Donati et al. [2011] included CT coronary angiographies and myocardial examinations from MRI. For all three configurations, suitable workflows could be composed from the developed software components. The provided visualization and interaction concept tries to integrate new types of data combinations in representations, that are closely related to well established exploration concepts. As proposed in several previous publications, corresponding 2D and 3D representations are provided to enable a quick intuitive data exploration. The users learned very quickly, how to explore and interpret the presented data. The concept produced meaningful visualizations for the determination of correspondences between myocardial defects and culprit vessels in all three application settings. Additional information was provided compared to the application of the AHA model and the side-by-side analysis of the complementary datasets. There is high interest in the inspection of so-called vulnerable plaques, which do often not cause relevant stenoses but can result in total vessel blockage in case of rupture. Thus, first steps have been taken towards visualization and analysis concepts for the inspection of the vessel wall in CTCA and MRA data [Glasser, Oeltze, Hennemuth, Kubisch, Mahnken, Wilhelmsen, and Preim, 2010],[Hennemuth et al., 2009]. An integration of these techniques into the inspection of the coronary artery analysis could be a helpful extension towards the assessment of the risk of infarctions.

A clear advantage of the provided method package compared to related approaches is the combination of all necessary steps and the integration of available results from one examination into other analysis steps. This allows to focus the examination in the regions corresponding to known pathologies. In the presented studies data processing could be per-

formed with a single application in reasonable processing time, and no additional software was required. On the other hand, it is highly desirable to combine the provided analysis methods with an inspection of the regional myocardial function. Therefore, future developments should extend the software towards interfaces that allow an easy integration with other complementary software packages as well as PACS systems.

Additional improvements could be achieved through an integration with simulation methods as, e.g., proposed by Termeer et al. [2008]. This would not only enable the determination of the coronary supply territories but also support therapy planning through simulating the expected effect.

6

Summary and Outlook

The presented work is dedicated to the integrated analysis of vascular pathologies and corresponding changes of the viability in the supplied heart muscle tissue in patients with coronary artery disease. This information is crucial for the assessment of disease progression and therapy planning. The current gold standard for the examination of stenosis relevance is the inspection with a catheter. The major drawbacks of this method are the invasiveness and limitations regarding the estimation of the benefit that can be achieved with a vascular intervention.

The approach proposed in this thesis is based on non-invasively scanned 3D and 4D CT and MRI image data. The different types of image data that can be acquired with these modalities have the potential to provide information about the coronary arteries as well as the viability state of myocardial tissue.

Chapter 2 presents a short introduction to the anatomy of the heart and the pathological changes associated with coronary artery disease. A summary of state-of-the-art CT and MRI imaging techniques for coronary artery disease diagnosis is given and limitations regarding image quality are discussed.

Chapter 3 is concerned with the problems that result from the misalignment of image data acquired at different time points and with different modalities. The first step in the fusion of datasets from different modalities is the alignment of the coordinate systems. This has been implemented as an interactive landmark-based registration to allow the application to datasets with arbitrary coverage and orientation. The next task arises from breathing motion during the acquisition of late enhancement MRI data that is often acquired slice-wise. Breathing causes movement of the diaphragm and thus a change of the heart position.

Therefore, an alignment is required before spatial relations of anatomical structures imaged at different time points can be assessed.

The proposed solution uses the 3D angiographic dataset as reference and aligns the sparse late enhancement and perfusion MRI data slice-wise with the dense volumetric images using rigid transformations. The evaluation of this concept with clinical CT and MRI data has shown that the major limitations emerge from the dependency on user input and a mismatch of the heart phases the different images were acquired in. In order to preserve the volume information of defects in the perfusion and late enhancement images, the alignment transformation was restricted to translations. Thus, the deformation occurring between contraction phases is not considered. This type of problem will probably be overcome soon through progress in MR imaging technology. 3D late enhancement imaging sequences already allow the acquisition of motion corrected data, which will hopefully provide a comparable signal-to-noise ratio as conventional 2D-imaging techniques in the near future [Nguyen et al., 2008, Peukert et al., 2007]. Furthermore, with state-of-the-art acquisition techniques, it is possible to reconstruct different heart phases from the acquired raw data, and an adapted reconstruction would be a promising approach to achieve a higher accuracy.

The goal in myocardial perfusion MRI is the analysis of a contrast agent's first pass through the heart muscle tissue. This requires a rapid acquisition with high temporal resolution, and thus navigator gating is not possible. Correction of breathing and contractile motion must be performed on the acquired image sequences. Two deformable registration approaches are suggested for this task: an *NMI*-based motion correction with B-Spline transformations and an implementation of the *Morphon* algorithm by Knutsson and Andersson [2005]. Both methods use a floating reference image and performed almost equally in the evaluation with clinical image datasets. The comparison with previous publications had to be based on the segmentation of the myocardium in several time frames, because these publications used the segmentation overlap and contour distance to assess the quality of the motion compensation. The results achieved here showed a strong improvement of the overlap of the segmentations from different time frames after motion correction. On the other hand, the average gravity center distance of 1.76 mm after registration was even higher than published for rigid registration approaches [Bracoud et al., 2003]. However, the intraobserver variability of the user-defined myocardial contours was three times this distance, and thus this measure is questionable. The quality measures proposed in this thesis

address the distinguishability of the myocardium in the corrected sequence, and the plausibility of the resulting voxel time intensity curves in the myocardium. This is assessed via a comparison with an indicator dilution model that can be performed without user input when combined with an myocardium segmentation. In addition to these measures, derived parameters have been compared with findings from other examinations, such as X-ray angiography and late enhancement MRI. Better correspondences were found after the motion correction with both floating reference methods. Therefore, it can be assumed that the provided methods improve the interpretability of myocardial perfusion MRI.

Chapter 4 describes new approaches for the extraction of the relevant structures for coronary artery disease assessment, namely the coronary artery tree, necrotic myocardial tissue, and underperfused tissue regions. The proposed approach for the coronary tree detection is based on a region growing method, which is combined with an initial aorta recognition and shape assumptions that enable the automatic detection of the coronary ostia. The evaluation with CTCA and MRCA datasets of coronary artery disease patients proved the suitability of the method as a first step in the vessel analysis process. Further improvements are expected from a combination with advanced centerline extraction and lumen quantification methods.

The detection of necrotic and fibrotic tissue, which is important to estimate the achievable benefit through therapy, is based on late enhancement CT and MRI. It is approached with a mixture model that is fitted to the intensity distribution of the myocardium in such a way that one curve represents the healthy tissue intensities and the other one describes the intensity values of the regions showing late enhancement. In addition to the intensity distribution model, assumptions on plausible infarct locations and the appearance of microvascular obstructions have been applied. The method evaluation on laboratory pig datasets and images from clinical routine proved the advantages regarding quantification as well as visualization compared to conventional thresholding techniques, motivating other researchers to take over or adapt the proposed ideas. Furthermore, the algorithms have the potential for an application to other types of cardiac images such as edema images that depict the enhanced water content in damaged tissue [Huellebrand et al., 2012] or left atrial late enhancement images after ablation [Hennemuth et al., 2012b].

The proposed processing pipeline for the detection of perfusion defects consists of a motion correction step followed by a calculation of perfusion parameters. The perfusion

parameter maps are then considered for a segmentation that is based on similar assumptions as the late enhancement detection. In case of a relevant stenosis, dependent tissue is not either unperfused or normally perfused. Tissue is undersupplied to a certain degree depending on the distance to the diseased supplying vessel, and thus a two class mixture model as suggested for the late enhancement images is not suitable here. The determination of candidate voxels for the underperfusion are therefore determined with a threshold based on the standard deviation of the parameter distribution. The segmentation step is then performed with the same method as for the late enhancement detection. The evaluation of this method is difficult, because the available reference data does not allow the assessment of false-positive segmentations. However, all results were plausible when compared with findings from angiography and late enhancement MRI. The generation of suitable reference data for the evaluation of perfusion analysis methods is an important future task here. Furthermore, it is highly desirable to achieve the standardization of imaging protocols in such a way that the calculation of the quantitative parameters enables the comparison of different datasets. This will hopefully also enable the definition of standard values for these parameters.

The major goal in this work was the support of an integrated analysis of the different types of data to enable an inspection of the correspondences between disease-related vessel pathologies and myocardial viability. Therefore, Chapter 5 is dedicated to the integration of the presented image processing methods as well as the development of suitable visualization and interaction concepts. For all types of image data and results, 2D as well as 3D representations are provided. The modular implementation of the different processing and analysis steps enabled the composition of dedicated workflows for three different clinical studies, which were concerned with the value of fused visualizations. All three studies proved the benefit provided by the concept when compared with the conventional assessment methods. Current projects such as the *SMARTVis* software use similar methods for the integrated cardiac image analysis.

Concludingly, this work has presented a new approach for an integrated analysis of coronary pathologies and myocardial viability based on different types of non-invasively acquired image data from CT and MRI. The clinical evaluation of the presented methods with an integrated software application has shown the advantages in comparison to conventional analysis methods and the potential for the assessment of stenosis relevance without invasive catheter examinations.

Appendix A

Datasets and Processing Results

The following sections present the detailed tables and screenshots describing the processed datasets and the corresponding results. The interpretation of the listed results is provided in the corresponding chapters on alignment problems and image analysis.

A.1 MR Perfusion Motion Correction

♯	Scanner	Dimensions	Resolution[mm^2]	Motion OP	Motion IP	Quality
1	Intera	(288,288,3,65)	1.32	X	X	4
2	Intera	(288,288,3,65)	1.32	X	X	4
3	Intera	(256,256,4,45)	1.30		X	4
4	Intera	(256,256,4,45)	1.30		X	3
5	Intera	(256,256,4,60)	1.37	X	X	4
6	Intera	(256,256,4,60)	1.37	X	X	3
7	Intera	(288,288,4,50)	1.32		X	3
8	Intera	(256,256,4,50)	1.37	X	X	3
9	Intera	(256,256,4,65)	1.37		X	4
10	Intera	(256,256,4,65)	1.37		X	4
11	Intera	(256,256,4,60)	1.37		X	4
12	Intera	(320,320,4,20)	1.30		X	4
13	Intera	(320,320,4,20)	1,30		X	3
14	Intera	(240,240,4,30)	1.31	X		4
15	Intera	(240,240,4,30)	1,31		X	4
16	Intera	(256,256,4,30)	1.35		X	4
17	Intera	(256,256,4,20)	1.35		X	4
18	Intera	(320,320,4,40)	1.25			4
19	Intera	(320,320,4,40)	1.25			4
20	Intera	(320,320,4,40)	1.25		X	3
21	Intera	(320,320,4,40)	1.25	X	X	3
22	Intera	(320,320,4,40)	1.25	X	X	2
23	Intera	(320,320,4,40)	1.25	X	X	2
24	Intera	(320,320,4,40)	1.25		X	4
25	Intera	(320,320,4,40)	1.25	X	X	3
26	Intera	(288,288,4,30)	1.33		X	4
27	Intera	(288,288,4,30)	1,33	X	X	4
28	Intera	(240,240,4,40)	1.36		X	4
29	Intera	(240,240,4,40)	1.36		X	3
30	Intera	(320,320,4,40)	1.29			4
31	Intera	(320,320,4,40)	1.29	X	X	4
32	Intera	(320,320,4,40)	1.25		X	3
33	Intera	(320,320,4,40)	1.25		X	3
34	Intera	(320,320,4,40)	1.25		X	3
35	Intera	(320,320,4,40)	1.25		X	3
36	Intera	(320,320,4,40)	1.25		X	3
37	Intera	(320,320,4,40)	1.25		X	3
38	Intera	(320,320,4,40)	1.25		X	4
39	Intera	(320,320,4,40)	1.25		X	4
40	Intera	(320,320,4,40)	1.25		X	4
41	Intera	(320,320,4,40)	1.25		X	3
42	Intera	(320,320,4,40)	1.25		X	4
43	Intera	(320,320,4,40)	1.25		X	4
44	Intera	(320,320,4,40)	1.25	X	X	3
45	Intera	(320,320,4,40)	1.25	X	X	2
46	Intera	(320,320,4,40)	1.25		X	4
47	Intera	(320,320,4,40)	1.25		X	4
48	Intera	(320,320,4,40)	1.25	X	X	4
49	Intera	(320,320,4,40)	1.25		X	3
50	Intera	(320,320,4,40)	1.25	X	X	4
51	Intera	(320,320,4,40)	1.25	X	X	4
52	Intera	(320,320,4,40)	1.25		X	3
53	Intera	(320,320,4,40)	1.25	X	X	3
54	Sonata	(160,192,3,40)	1.56		X	3
55	Sonata	(160,192,3,40)	1.56		X	4
56	Avanto	(144,192,4,40)	1.98	X	X	3
57	SonataVision	(256,192,3,40)	1.25	X	X	3
58	Sonata	(150,150,4,50)	1.41	X	X	3
59	Sonata	(208,256,4,35)	1.45	X	X	4
60	Sonata	(240,256,4,34)	1.45	X	X	3

Table A.1: MR Perfusion Sequences. OP: out-of-plane motion, IP: in-plane motion, Quality levels 0: non-diagnostic via 1: poor to 4: excellent

	Original		Fixed Reference			Floating Reference			Morphon		
♯	Vol	Err[%]	Vol	Err[%]	Diff	Vol	Err[%]	Diff	Vol	Err[%]	Diff
1	1632	9.31	1731	2.83	-0.50	1495	3.00	-0.23	1617	2.84	-0.36
2	1998	3.20	1953	6.44	-1.10	1552	6.61	-0.27	1933	6.01	-1.32
3	1853	2.83	1666	2.80	-0.63	2014	3.31	-0.36	2227	3.39	-0.23
4	2052	4.36	1721	1.99	-0.52	1713	1.88	-0.56	2135	2.15	-0.91
5	1872	5.94	1688	4.46	-1.93	2676	5.28	-1.25	2368	4.47	-1.99
6	1828	5.28	1241	4.59	-2.95	2925	5.07	-1.02	2363	4.65	-1.47
7	1340	7.39	2136	4.10	-2.13	2700	4.21	-2.15	2402	4.63	-1.77
8	1229	6.17	1991	4.79	-0.35	2356	5.94	0.95	1772	6.31	1.16
9	3590	5.73	3379	6.25	-0.01	3535	6.07	-0.01	3382	6.26	-0.06
10	2154	6.35	3296	5.05	-1.78	3981	5.19	-1.67	3741	5.66	-1.00
11	3273	2.02	2221	8.15	-0.23	2310	7.51	-0.64	2257	7.93	-0.30
12	3285	1.78	3019	1.45	-0.35	3512	1.41	-0.44	3273	1.52	-0.33
13	3547	1.65	3817	2.12	-0.23	3716	1.81	-0.62	4079	1.85	-0.43
14	3232	1.91	3458	1.77	-0.21	3431	1.70	-0.44	3616	1.69	-0.31
15	2531	1.95	3513	1.84	-0.03	3429	1.68	-0.18	3518	1.84	-0.05
16	2531	1.46	3332	1.18	-0.25	3011	1.17	-0.26	2814	1.23	-0.20
17	2174	1.32	2589	1.15	-0.18	2678	1.10	-0.20	2568	1.19	-0.15
18	3765	3.32	3848	3.01	-0.37	4641	2.75	-0.42	4028	3.19	0.00
19	3580	3.47	4043	2.98	-0.53	4341	3.12	-0.25	4043	3.33	-0.18
20	2573	3.87	2949	3.54	-0.48	2998	3.34	-0.57	3297	3.44	-0.47
21	3390	5.11	2522	5.50	0.17	3119	4.70	-0.73	3639	4.60	-0.82
22	2173	6.97	3342	7.12	-0.63	3381	7.63	-0.13	3816	7.74	-0.60
23	2029	3.74	3307	5.04	1.20	3735	3.77	-0.17	3902	4.04	-0.09
24	3029	4.47	2639	4.13	-0.53	2303	3.77	-0.64	2399	4.28	-0.32
25	1542	3.91	3264	3.36	-1.25	3335	3.41	-1.04	4194	3.51	-1.00
26	2386	1.73	2516	1.58	-0.09	2917	1.49	-0.31	2642	1.52	-0.08
27	2245	1.92	3123	1.64	-0.19	3106	1.55	-0.56	3576	1.65	-0.27
28	2151	2.36	2079	1.93	-0.31	2598	1.95	-0.44	2354	1.94	-0.32
29	2312	3.37	2113	2.33	-0.96	2633	2.71	-0.76	2498	2.35	-0.98
30	2520	2.07	3038	1.85	-0.31	3245	1.79	-0.34	2539	1.81	-0.27
31	2023	2.54	3454	2.37	-0.46	3284	2.34	-0.35	3305	2.47	-0.17
32	3419	2.68	3640	2.32	-0.44	3788	2.31	-0.47	3499	2.24	-0.56
33	2819	3.24	3564	3.34	-0.30	4587	2.69	-0.84	4406	2.87	-0.59
34	2380	4.10	2749	3.57	-0.23	2734	3.25	-0.40	2515	3.48	-0.38
35	2406	2.75	3024	2.41	-0.35	3095	2.40	-0.35	3160	2.44	-0.25
36	972	3.09	3541	3.57	-0.60	2904	2.84	-0.74	2664	2.69	-0.73
37	2747	4.31	2819	4.35	-0.23	3428	3.88	-0.60	3225	4.06	-0.42
38	1348	2.39	1758	2.13	-0.43	1431	2.04	-0.36	2070	2.15	-0.24
39	1149	3.54	1871	3.25	-0.30	1791	3.07	-0.46	2169	3.24	-0.32
40	4061	2.66	3979	2.43	-0.20	4934	2.29	-0.31	4623	2.40	-0.24
41	4281	3.00	3779	2.90	-0.16	5266	2.71	-0.36	4883	2.88	-0.18
42	2424	2.07	2805	1.81	-0.38	3167	1.85	-0.46	3182	1.92	-0.32
43	1526	3.97	3073	3.62	-0.41	3160	3.57	-0.49	3229	3.75	-0.63
44	1213	3.13	2135	2.70	-1.10	2491	2.56	-1.38	2408	2.77	-1.01
45	1354	2.95	1664	2.83	-0.44	2376	2.83	-0.43	2329	2.81	-0.60
46	979	3.64	1943	2.79	-1.80	2133	3.05	-1.32	1976	2.78	-1.50
47	1878	3.14	1948	3.42	-0.08	2113	2.61	-0.94	2388	2.80	-1.41
48	3335	3.36	5291	2.84	-0.67	5318	2.88	-0.72	4855	2.88	-0.61
49	4433	2.74	4664	2.38	-0.35	5695	2.26	-0.51	5383	2.45	-0.34
50	741	4.47	1616	3.52	-0.77	1627	3.36	-0.90	1768	3.65	-0.72
51	1466	3.31	1792	3.77	0.14	2638	2.98	-0.69	2259	2.88	-0.53
52	3119	4.68	3752	4.34	-0.28	4063	4.26	-0.32	4639	4.45	-0.28
53	335	4.15	4194	4.33	-0.11	3883	3.79	-0.36	4390	3.96	-0.28
54	1993	0.04	1888	3.01	-1.10	2066	2.73	-1.33	2182	3.40	-0.72
55	1824	0.04	1890	3.15	0.27	1813	2.99	-1.23	1971	3.47	-0.69
56	1421	0.02	1383	1.75	-1.04	1833	1.59	-0.90	1802	1.82	-0.68
57	2101	0.01	1518	0.77	-0.11	2403	0.76	-0.33	2940	0.69	-0.60
58	1666	0.02	2355	1.78	-0.20	2892	1.75	-0.22	3282	1.81	-0.19
59	2238	0.01	2846	0.68	-0.08	3204	0.74	0.01	3348	0.50	-0.28
60	1898	0.01	1862	0.52	0.00	3100	0.44	-0.12	3200	0.40	-0.15
Avg	2290	3.18	2739	3.13	-0.50	3043	3.03	-0.56	3051	3.12	-0.51
Stddev		1.92		1.55	0.63		1.57	0.46		1.59	0.49

Table A.2: Improvement of detectable myocardial volume and intensity curves through motion correction. The table shows the volume of the myocardium segmented in the temporal MIPs and the average error of the gamma variate fit in percentage of the images' intensity range. For the corrected sequences, the change of error in the segmented myocardium is also shown.

A.2 Coronary Tree Segmentation

Dataset	Scanner	Resolution	Dimensions	Kernel	Quality
1	Sensation 64	(0.328125 0.328125 0.8)	(512,512,168)	B20f	1
2	Sensation 64	(0.349609375 0.349609375 0.8)	(512,512,161)	B20f	2
3	Sensation 64	(0.43359375 0.43359375 0.5)	(512,512,396)	B20f	2
4	Sensation 64	(0.435546875 0.435546875 0.8)	(512,512,151)	B30f	2
5	Sensation 64	(0.37890625 0.37890625 0.8)	(512,512,169)	B30f	2
6	Sensation 64	(0.373046875 0.373046875 0.8)	(512,512,154)	B30f	2
7	Sensation 64	(0.390625 0.390625 0.5)	(512,512,244)	B25f	2
8	Sensation 64	(0.388671875 0.388671875 0.5)	(512,512,262)	B25f	2
9	Sensation 64	(0.34375 0.34375 0.7)	(512,512,186)	B25f	2
10	Sensation 64	(0.306640625 0.306640625 0.4)	(512,512,362)	B25f	2
11	Sensation 64	(0.318359375 0.318359375 0.5)	(512,512,465)	B20f	2
12	Sensation 64	(0.33203125 0.33203125 0.4)	(512,512,278)	B46f	1
13	Sensation 64	(0.3046875 0.3046875 0.5)	(512,512,254)	B25f	1
14	Sensation 64	(0.36328125 0.36328125 0.4)	(512,512,367)	B36f	1
15	Sensation 64	(0.318359375 0.318359375 0.4)	(512,512,381)	B25f	1
16	Sensation 64	(0.322265625 0.322265625 0.4)	(512,512,309)	B25f	1
17	Sensation 64	(0.353515625 0.353515625 0.4)	(512,512,334)	B25f	2
18	Sensation 64	(0.310546875 0.310546875 0.4)	(512,512,329)	B46f	1
19	Sensation 64	(0.2734375 0.2734375 0.4)	(512,512,283)	B25f	1
20	Sensation 64	(0.248046875 0.248046875 0.6)	(512,512,276)	B30f	1
21	Sensation 64	(0.390625 0.390625 0.4)	(512,512,337)	B25f	1
22	Sensation 64	(0.51171875 0.51171875 0.4)	(512,512,333)	B25f	2
23	Sensation 64	(0.287109375 0.287109375 0.6)	(512,512,213)	B30f	2
24	Sensation 64	(0.414063006639481 0.414063006639481 0.4)	(512,512,419)	B25f	1
25	Sensation 64	(0.3203125 0.3203125 0.6)	(512,512,242)	B30f	1
26	Sensation 64	(0.37109375 0.37109375 0.8)	(512,512,167)	B30f	1
27	Definition	(0.396484375 0.396484375 0.5)	(512,512,373)	B46f	1
28	Sensation 64	(0.28515625 0.28515625 0.6)	(512,512,243)	B30f	1
29	Definition	(0.4375 0.4375 0.4)	(512,512,317)	B26f	1
30	Sensation 16	(0.3515625 0.3515625 1)	(512,512,137)	B30f	3
31	Sensation 64	(0.283203125 0.283203125 0.4)	(512,512,299)	B25f	1
32	Sensation 16	(0.7421875 0.7421875 0.8)	(512,512,151)	B30f	2
33	Definition	(0.42578125 0.42578125 0.4)	(512,512,354)	B26f	1
34	Definition	(0.38671875 0.38671875 0.4)	(512,512,362)	B26f	1
35	Definition	(0.53125 0.53125 0.4)	(512,512,354)	B26f	2
36	Definition	(0.390625 0.390625 0.5)	(512,512,271)	B46f	2
37	Definition	(0.390625 0.390625 0.5)	(512,512,305)	B46f	2
38	Definition	(0.423828125 0.423828125 0.5)	(512,512,293)	B46f	2
39	Sensation Cardiac	(0.375 0.375 0.5)	(512,512,269)	B30f	2
40	Sensation Cardiac 64	(0.30859375 0.30859375 0.4)	(512,512,343)	B25f	1
41	Sensation 64	(0.302734375 0.302734375 0.4)	(512,512,338)	B30f	1
42	Sensation 64	(0.310546875 0.310546875 0.4)	(512,512,304)	B30f	1
43	Sensation 64	(0.240234375 0.240234375 0.5)	(512,512,202)	B20f	2
44	Sensation 64	(0.37890625 0.37890625 0.5)	(512,512,239)	B30f	1
45	Sensation Cardiac 64	(0.3359375 0.3359375 0.6)	(512,512,225)	B25f	1
46	Sensation Cardiac 64	(0.263671875 0.263671875 0.6)	(512,512,237)	B25f	1
47	Sensation Cardiac 64	(0.40234375 0.40234375 0.6)	(512,512,208)	B25f	1
48	Sensation Cardiac 64	(0.40234375 0.40234375 0.6)	(512,512,432)	B25f	1
49	Sensation 64	(0.41015625 0.41015625 0.4)	(512,512,394)	B25f	2
50	Sensation 64	(0.32421875 0.32421875 0.4)	(512,512,270)	B30f	3
51	Sensation 16	(0.3984375 0.3984375 0.5)	(512,512,233)	B20f	1
52	Sensation Cardiac 64	(0.39453125 0.39453125 0.7)	(512,512,163)	B20f	3
53	Sensation 16	(0.3984375 0.3984375 0.5)	(512,512,281)	B30f	2
54	Sensation 16	(0.3515625 0.3515625 0.6)	(512,512,206)	B30f	2

Table A.3: CT Coronary Angiography Datasets 1-54

Dataset	Scanner	Resolution	Dimensions	Kernel	Quality
55	Sensation 16	(0.330078125 0.330078125 0.5)	(512,512,299)	B30f	1
56	Sensation 16	(0.388671875 0.388671875 0.5)	(512,512,100)	B30f	1
57	Sensation 64	(0.390625 0.390625 0.4)	(512,512,368)	B25f	2
58	Sensation 64	(0.29296875 0.29296875 0.5)	(512,512,330)	B30f	1
59	Sensation 16	(0.29296875 0.29296875 0.6)	(512,512,154)	B30f	2
60	Sensation 64	(0.390625 0.390625 0.4)	(512,512,396)	B25f	1
61	Sensation 64	(0.46484375 0.46484375 0.4)	(512,512,332)	B25f	1
62	Sensation 64	(0.390625 0.390625 0.4)	(512,512,333)	B25f	1
63	Definition	(0.3828125 0.3828125 0.5)	(512,512,237)	B46f	2
64	Definition	(0.44921875 0.44921875 0.5)	(512,512,261)	B46f	1
65	Definition	(0.390625 0.390625 0.5)	(512,512,373)	B46f	1
66	Definition	(0.349609375 0.349609375 0.5)	(512,512,237)	B46f	2
67	Definition	(0.4375 0.4375 0.5)	(512,512,237)	B46f	2
68	Definition	(0.439453125 0.439453125 0.5)	(512,512,271)	B46f	2
69	Definition	(0.482421875 0.482421875 0.5)	(512,512,237)	B46f	2
70	Definition	(0.48046875 0.48046875 0.5)	(512,512,305)	B46f	1
71	Definition	(0.41796875 0.41796875 0.5)	(512,512,357)	B46f	1
72	Definition	(0.390625 0.390625 0.5)	(512,512,305)	B46f	2
73	Definition	(0.41796875 0.41796875 0.5)	(512,512,339)	B46f	1
74	Definition	(0.359375 0.359375 0.5)	(512,512,271)	B46f	1
74	Definition	(0.388671875 0.388671875 0.5)	(512,512,251)	B46f	2
76	Definition	(0.390625 0.390625 0.5)	(512,512,271)	B46f	2
77	Definition	(0.416015625 0.416015625 0.5)	(512,512,255)	B46f	1
78	Definition	(0.435546875 0.435546875 0.4)	(512,512,323)	B26f	2
79	Sensation 64	(0.3828125 0.3828125 0.4)	(512,512,301)	B30f	2
80	Sensation 64	(0.390625 0.390625 0.4)	(512,512,366)	B25f	1
81	Sensation 64	(0.3515625 0.3515625 0.4)	(512,512,392)	B25f	1
82	Sensation 64	(0.390625 0.390625 0.4)	(512,512,358)	B25f	1
83	Definition	(0.30859375 0.30859375 0.5)	(512,512,261)	B26f	1
84	Sensation 64	(0.3515625 0.3515625 0.7)	(512,512,230)	B25f	1
85	Sensation 16	(0.283203125 0.283203125 0.5)	(512,512,356)	B30f	1
86	Definition	(0.37304699420929 0.37304699420929 0.4)	(512,512,267)	B26f	2
87	Sensation 64	(0.33203125 0.33203125 0.4)	(512,512,278)	B25f	1
88	Definition	(0.3515625 0.3515625 0.5)	(512,512,421)	B26f	1
89	Definition	(0.3515625 0.3515625 0.5)	(512,512,421)	B46f	1
90	Sensation Cardiac 64	(0.279296875 0.279296875 0.4)	(512,512,326)	B25f	1
91	Definition	(0.37109375 0.37109375 0.5)	(512,512,267)	B26f	2
92	Definition	(0.296875 0.296875 0.5)	(512,512,287)	B26f	1
93	Sensation 64	(0.453125 0.453125 0.5)	(512,512,255)	B25f	2
94	Definition	(0.34375 0.34375 0.5)	(512,512,353)	B26f	1
96	Definition	(0,267578125 0.267578125 0.5)	(512,512,243)	B26f	1
96	Definition	(0.333984375 0.333984375 0.5)	(512,512,271)	B26f	1
97	Definition	(0.421875 0.421875 0.5)	(512,512,227)	B26f	2
98	Definition	(0.30859375 0.30859375 0.5)	(512,512,280)	B26f	1
99	Definition	(0.380859375 0.380859375 0.5)	(512,512,265)	B26f	1
100	Definition	(0.359375 0.359375 0.3)	(512,512,487)	B26f	1
101	Definition	(0.380859375 0.380859375 0.3)	(512,512,462)	B26f	2
102	Definition	(0.371093988418579 0.371093988418579 0.4)	(512,512,293)	B46f	2
103	Sensation 64	(0.3828125 0.3828125 0.4)	(512,512,397)	B25f	2
104	SOMATOM Definition	(0.3515625 0.3515625 0.4)	(512,512,422)	B26f	1
105	Definition	(0.4375 0.4375 0.5)	(512,512,237)	B46f	2
106	Definition	(0.390625 0.390625 0.5)	(512,512,237)	B26f	1
107	Sensation 64	(0.390625 0.390625 0.5)	(512,512,290)	B25f	2

Table A.4: CT Coronary Angiography Datasets 55-107

Dataset	Scanner	Resolution	Dimensions	Kernel	Quality
108	Sensation 64	(0.390625 0.390625 0.5)	(512,512,281)	B25f	2
109	Sensation 64	(0.390625 0.390625 0.5)	(512,512,256)	B25f	1
110	Sensation 64	(0.353515625 0.353515625 1)	(512,512,132)	B30f	1
111	Sensation 64	(0.419921875 0.419921875 0.5)	(512,512,274)	B25f	1
112	Sensation 64	(0.357421875 0.357421875 0.5)	(512,484,284)	B25f	1
113	Sensation 64	(0.3828125 0.3828125 0.5)	(512,512,337)	B25f	3
114	Sensation 64	(0.369140625 0.369140625 0.5)	(512,512,228)	B25f	3
115	Sensation 64	(0.482421875 0.482421875 0.5)	(512,512,284)	B25f	1
116	Sensation 64	(0.5 0.5 0.8)	(512,512,158)	B20f	1
117	Sensation 64	(0.3515625 0.3515625 0.4)	(512,512,427)	B25f	2
118	Aquilion	(0.375 0.375 0.5)	(512,512,231)	FC03	2
119	Aquilion	(0.361000001430511 0.361000001430511 0.5)	(512,512,235)	FC03	1
120	Aquilion	(0.312000006437302 0.312000006437302 0.5)	(512,512,219)	FC03	3
121	Aquilion	(0.351000010967255 0.351000010967255 0.5)	(512,512,221)	FC03	2
122	Aquilion	(0.5 0.5 0.5)	(512,512,239)	FC03	1
123	Aquilion	(0.305000007152557 0.305000007152557 0.5)	(512,512,200)	FC03	1
124	Aquilion	(0.354000002145767 0.354000002145767 0.5)	(512,512,206)	FC03	2
125	Aquilion	(0.337000012397766 0.337000012397766 0.5)	(512,512,210)	FC03	2
126	Aquilion	(0.352999985218048 0.352999985218048 0.5)	(512,512,204)	FC03	2
127	Aquilion	(0.345999985933304 0.345999985933304 0.5)	(512,512,229)	FC03	2
128	Definition	(0.390625 0.390625 0.3)	(512,512,511)	B26f	3
129	Definition	(0.390625 0.390625 0.3)	(512,512,541)	B26f	3
130	Definition	(0.369140625 0.369140625 0.3)	(512,512,471)	B26f	2
131	Definition	(0.427734375 0.427734375 0.3)	(512,512,444)	B26f	2
132	Definition	(0.44921875 0.44921875 0.3)	(512,512,477)	B26f	3
133	Definition	(0.458984375 0.458984375 0.3)	(512,512,491)	B26f	3
134	Definition	(0.396484375 0.396484375 0.3)	(512,512,447)	B26f	2
135	Definition	(0.421875 0.421875 0.3)	(512,512,471)	B26f	1
136	Definition	(0.408203125 0.408203125 0.3)	(512,512,591)	B26f	2
137	Definition	(0.349609375 0.349609375 0.3)	(512,512,471)	B26f	2
138		(0.726562023162842 0.726562023162842 0.8)	(256,256,136)		1
139		(0.726562023162842 0.726562023162842 0.8)	(256,256,169)		1
140		(0.667967975139618 0.667967975139618 0.8)	(256,256,144)		1
141		(0.742187976837158 0.742187976837158 0.8)	(256,256,138)		1
142		(0.632812023162842 0.632812023162842 0.8)	(256,256,137)		1
143		(0.644532024860382 0.644532024860382 0.8)	(256,256,137)		2
144		(0.640626013278961 0.640626013278961 0.8)	(256,256,134)		1
145		(0.574217975139618 0.574217975139618 0.8)	(256,256,152)		2
146		(0.664062023162842 0.664062023162842 0.8)	(256,256,156)		1
147		(0.605467975139618 0.605467975139618 0.8)	(256,256,152)		1
148		(0.546876013278961 0.546876013278961 0.8)	(256,256,115)		1
149		(0.578126013278961 0.578126013278961 0.8)	(256,256,151)		1
150		(0.703126013278961 0.703126013278961 0.8)	(256,256,173)		1
151		(0.683593988418579 0.683593988418579 0.8)	(256,256,167)		1
152		(0.667967975139618 0.667967975139618 0.8)	(256,256,127)		1
153		(0.683593988418579 0.683593988418579 0.8)	(256,256,156)		1
154		(0.609376013278961 0.609376013278961 0.8)	(256,256,157)		1
155		(0.707032024860382 0.707032024860382 0.8)	(256,256,136)		2
156		(0.648437976837158 0.648437976837158 0.8)	(256,256,151)		1
157		(0.65625 0.65625 0.8)	(256,256,144)		1
158		(0.679687976837158 0.679687976837158 0.8)	(256,256,148)		2
159		(0.625 0.625 0.8)	(256,256,141)		1
160		(0.644532024860382 0.644532024860382 0.8)	(256,256,137)		1

Table A.5: CT Coronary Angiography Datasets 108-160

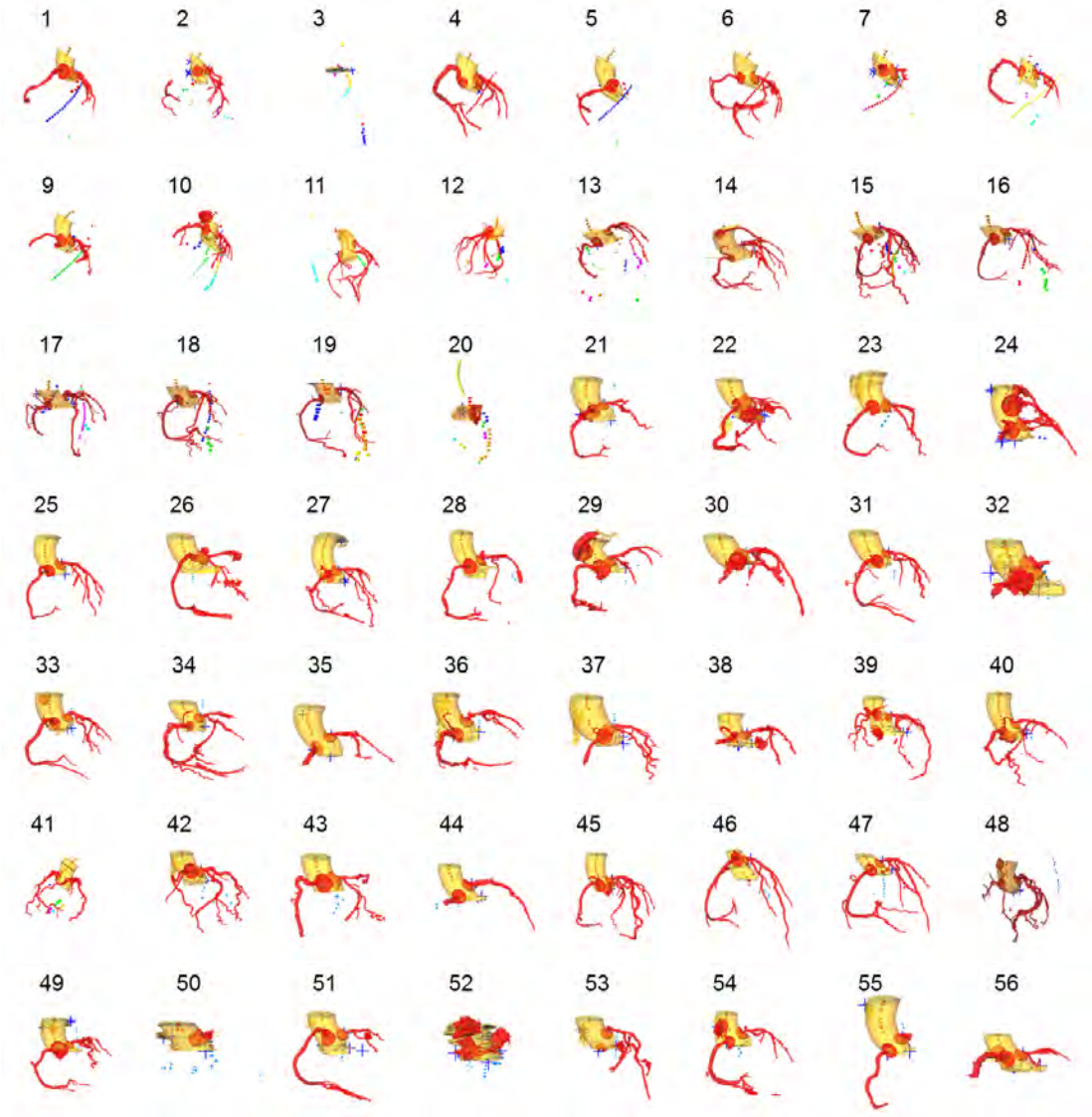

Figure A.1: Results of the automatic coronary tree extraction for dataset 1 to dataset 56. The markers represent the detected circles and are colored according to the clustering. the segmented aorta is shown as a yellow surface, and the coronary branches are colored red.

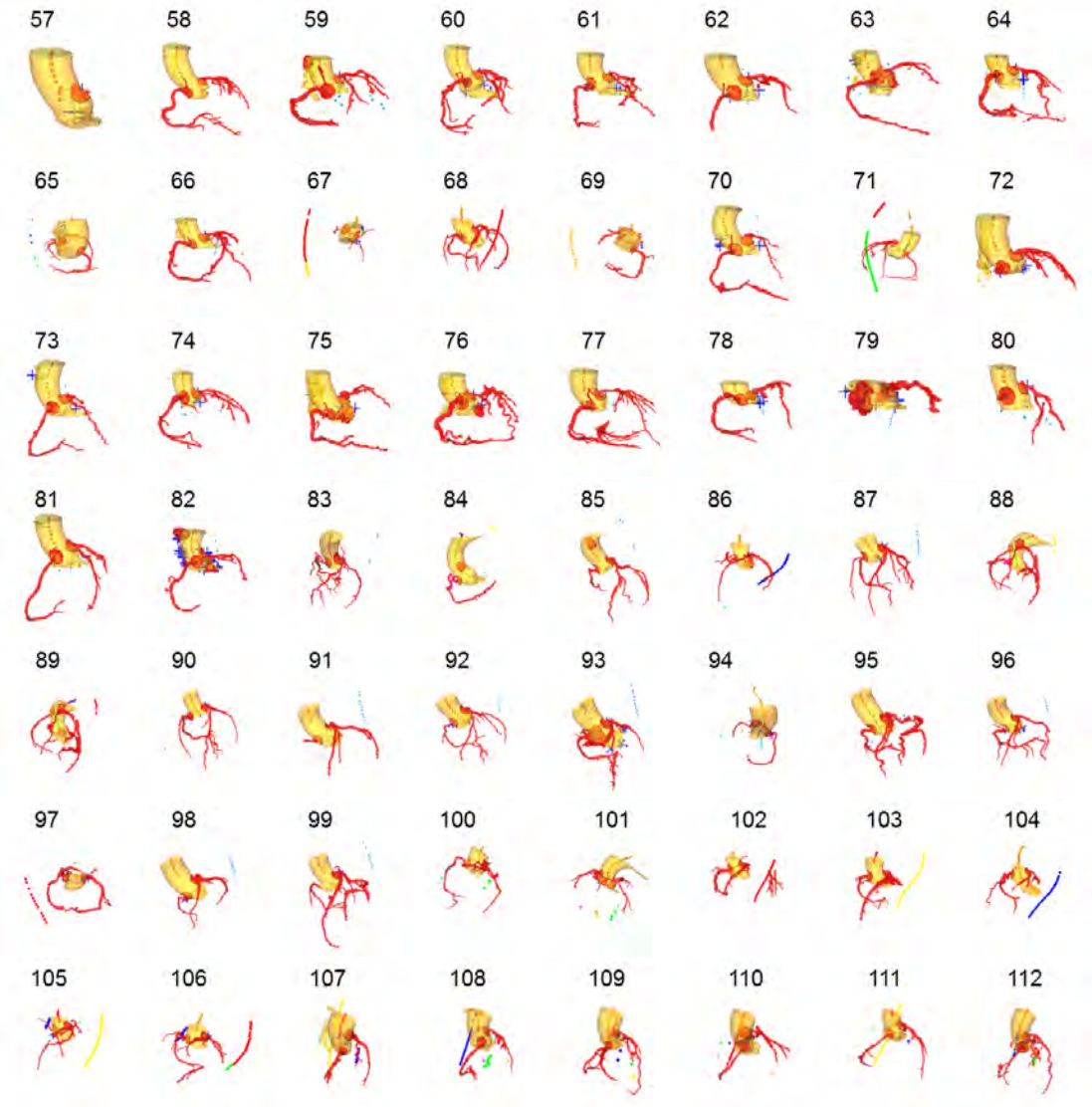

Figure A.2: Results of the automatic coronary tree extraction for dataset 57 to dataset 112. The markers represent the detected circles and are colored according to the clustering. the segmented aorta is shown as a yellow surface, and the coronary branches are colored red.

Figure A.3: Results of the automatic coronary tree extraction for dataset 113 to dataset 160. The markers represent the detected circles and are colored according to the clustering. the segmented aorta is shown as a yellow surface, and the coronary branches are colored red.

MR Angiography Datasets and Segmentation Results

Dataset	MR Scanner	Contrast Agent	Resolution	Dimensions	Quality
1	Avanto	Gadovist	(1,1,1.3)	(320,240,88)	3
2	Avanto	Magnevist	(0.625,0.625,1.1)	(512,368,88)	2
3	Avanto	Magnevist	(0.625,0.625,1.2)	(512,368,112)	2
4	Avanto		(1,1,1.1)	(320,240,120)	2
5	Avanto		(1,1,1.1)	(320,210,120)	3
6	Avanto		(1,1,1.1)	(320,240,120)	2
7	Avanto		(1,1,1.1)	(320,240,120)	3
8	Avanto		(1,1,1.1)	(320,240,120)	2
9	Avanto	Magnevist	(0.625,0.625,2)	(512,368,57)	2
10	Avanto		(1,1,1.1)	(320,240,128)	3
11	Avanto	Magnevist	(0.5,0.5,1.5)	(640,480,72)	2
12	Avanto		(0.8125,0.8125,1.1)	(320,240,112)	3
13	Avanto		(1,1,1.1)	(320,240,160)	2
14	Avanto	with contrast	(1.1,1.1,1.2)	(256,216,96)	2
15	Avanto		(1,1,1.1)	(320,240,128)	3
16	Avanto		(1,1,1.1)	(320,240,128)	2
17	Avanto		(1,1,1.1)	(320,240,120)	3
18	Avanto		(1,1,1.1)	(320,240,128)	2
19	Avanto		(1,1,1.1)	(320,240,128)	3
20	Avanto		(1,1,1.1)	(320,210,144)	2
21	Aera		(0.625,0.625,1)	(512,320,128)	2
22	Avanto	Magnevist	(0.664,0.664,1.3)	(512,368,80)	3
23	Avanto		(0.5,0.5,1.5)	(640,480,88)	2
24	Avanto	Magnevist	(0.625,0.625,1.2)	(512,368,96)	2
25	Avanto	Magnevist	(0.625,0.625,1.1)	(512,400,120)	2
26	Avanto	Magnevist	(0.5,0.5,1.5)	(640,480,80)	2

Table A.6: MR coronary angiography datasets.

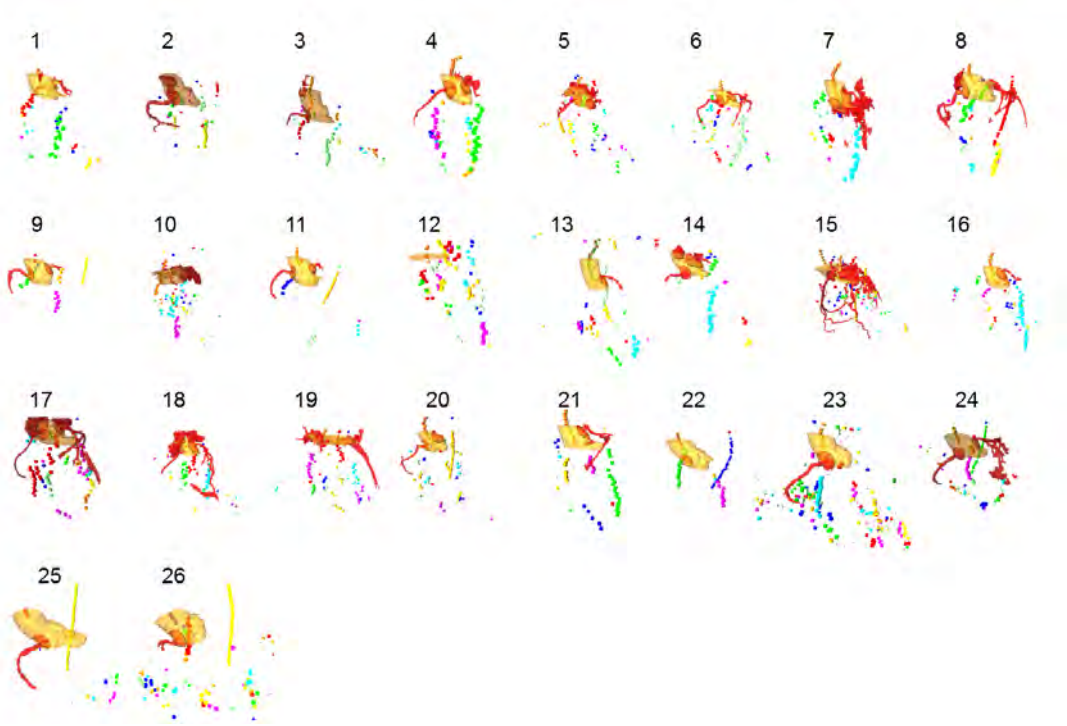

Figure A.4: Automatic segmentation results for MR datasets 1 to 26.

A.3 Late Enhancement Segmentation

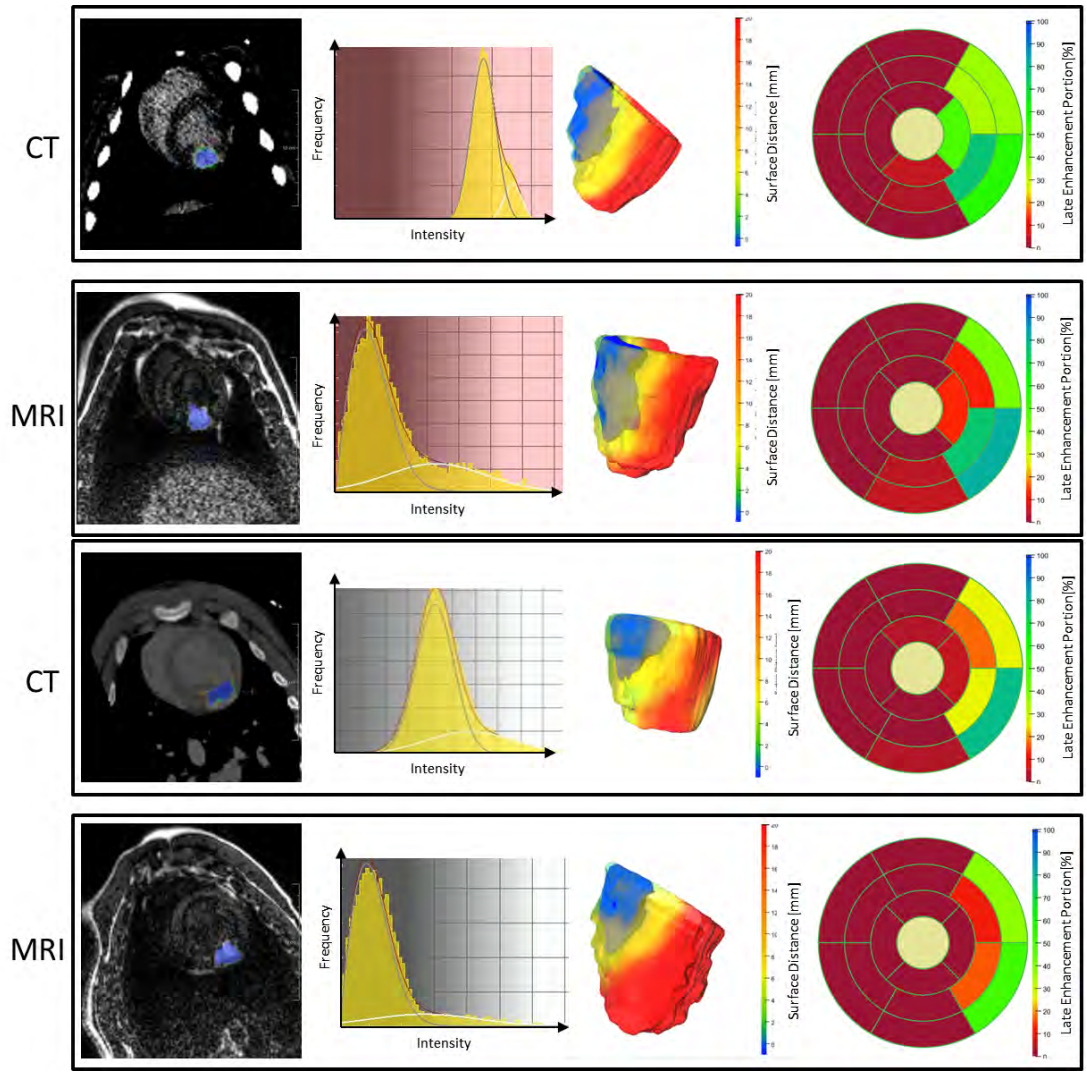

Figure A.5: Late enhancement segmentation results for case 1 and 2. The leftmost column shows the segmented region as an overlay with the original image data. The myocardiums' histogram with the fitted mixture model is shown in the next column. The second column from right depicts the segmentation result in 3D. The late enhancement region is shown in blue and the myocardium surface is color coded according to the distance from the infarction to indicate the transmurality. The rightmost column shows the late enhancement volume portions according to the AHA segment model.

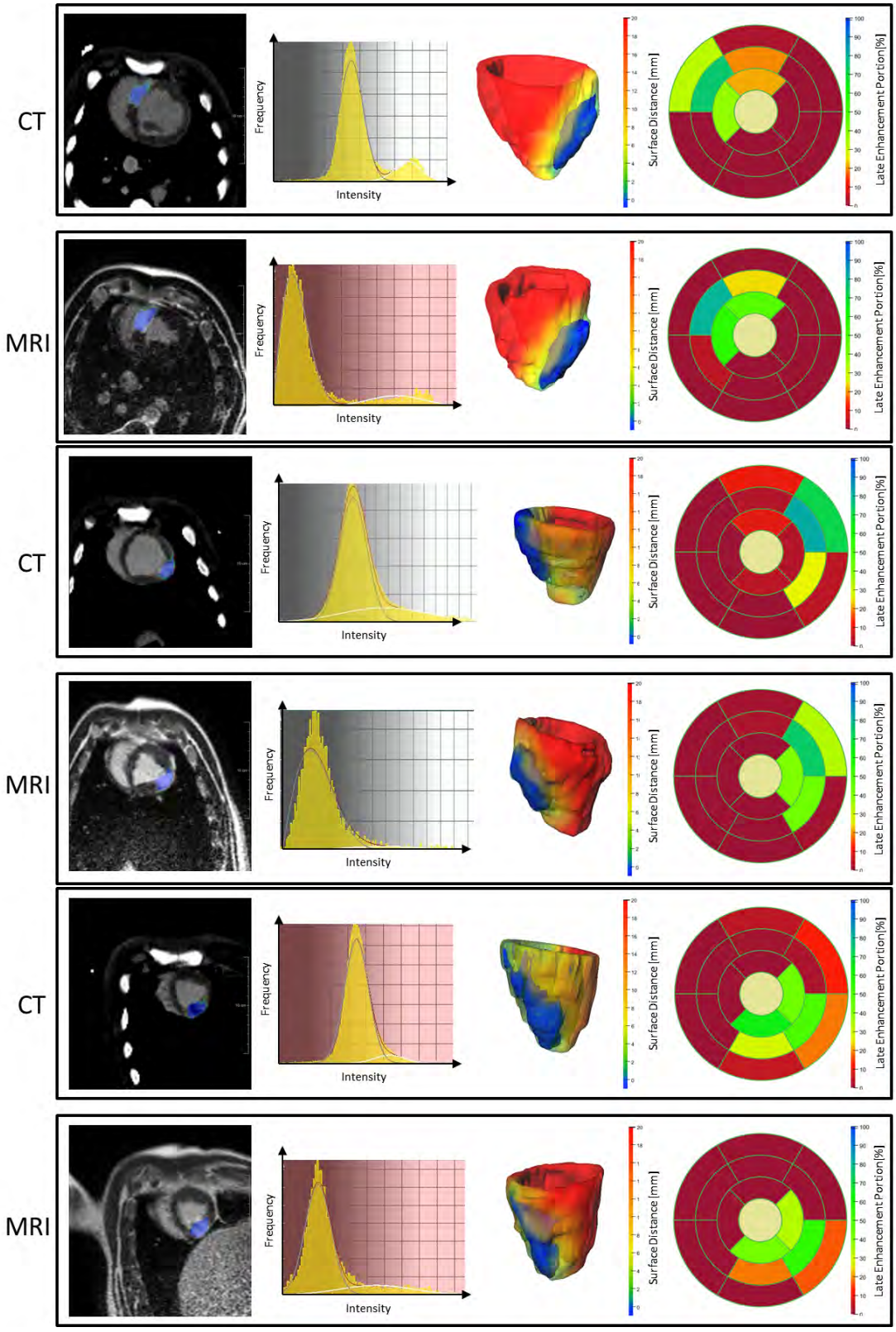

Figure A.6: Late enhancement segmentation results for cases 3 to 5 (see Fig. A.5 for a detailed description of the image content).

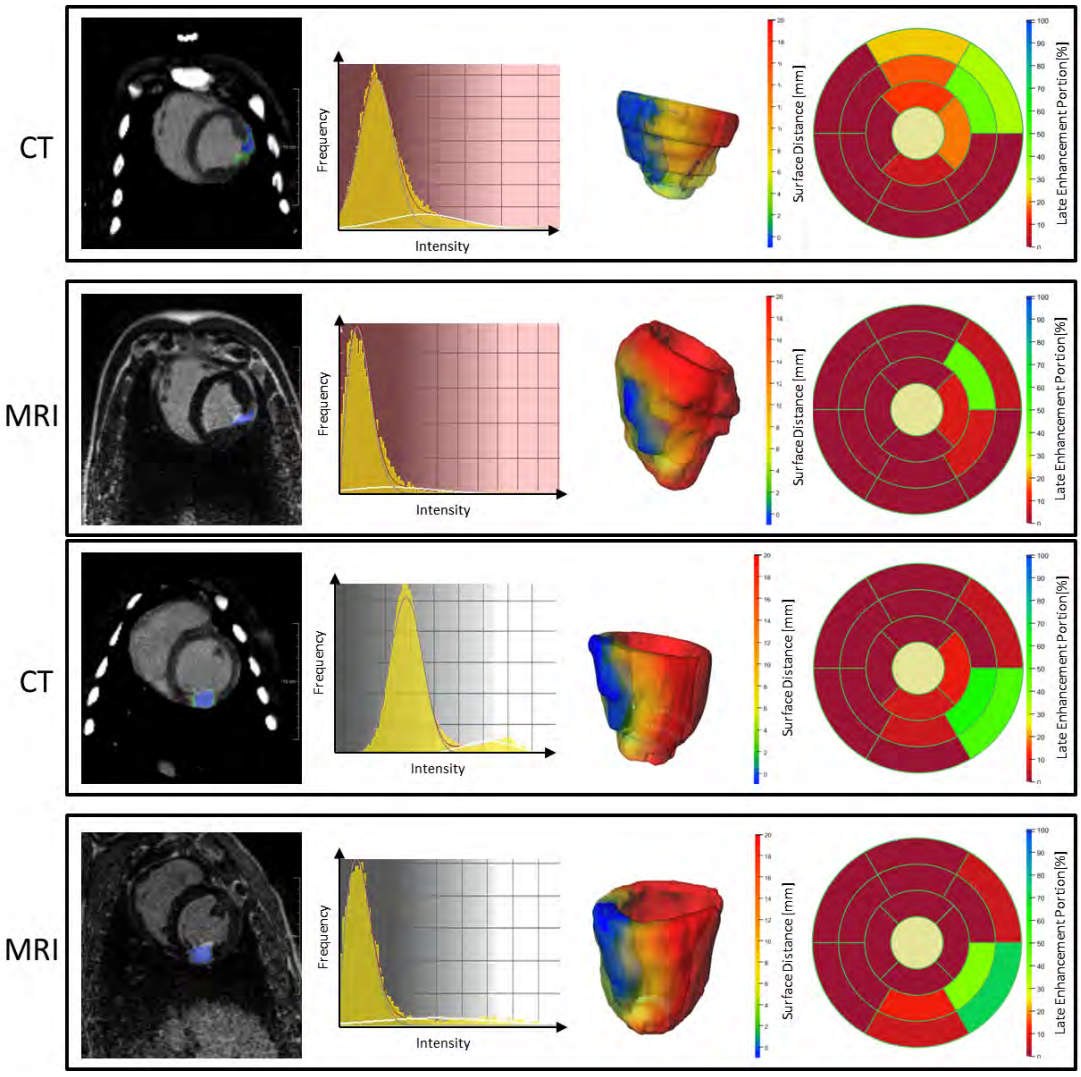

Figure A.7: Late enhancement segmentation results for cases 6 an 7 (see Fig. A.5 for a detailed description of the image content).

A.4 Perfusion Analysis

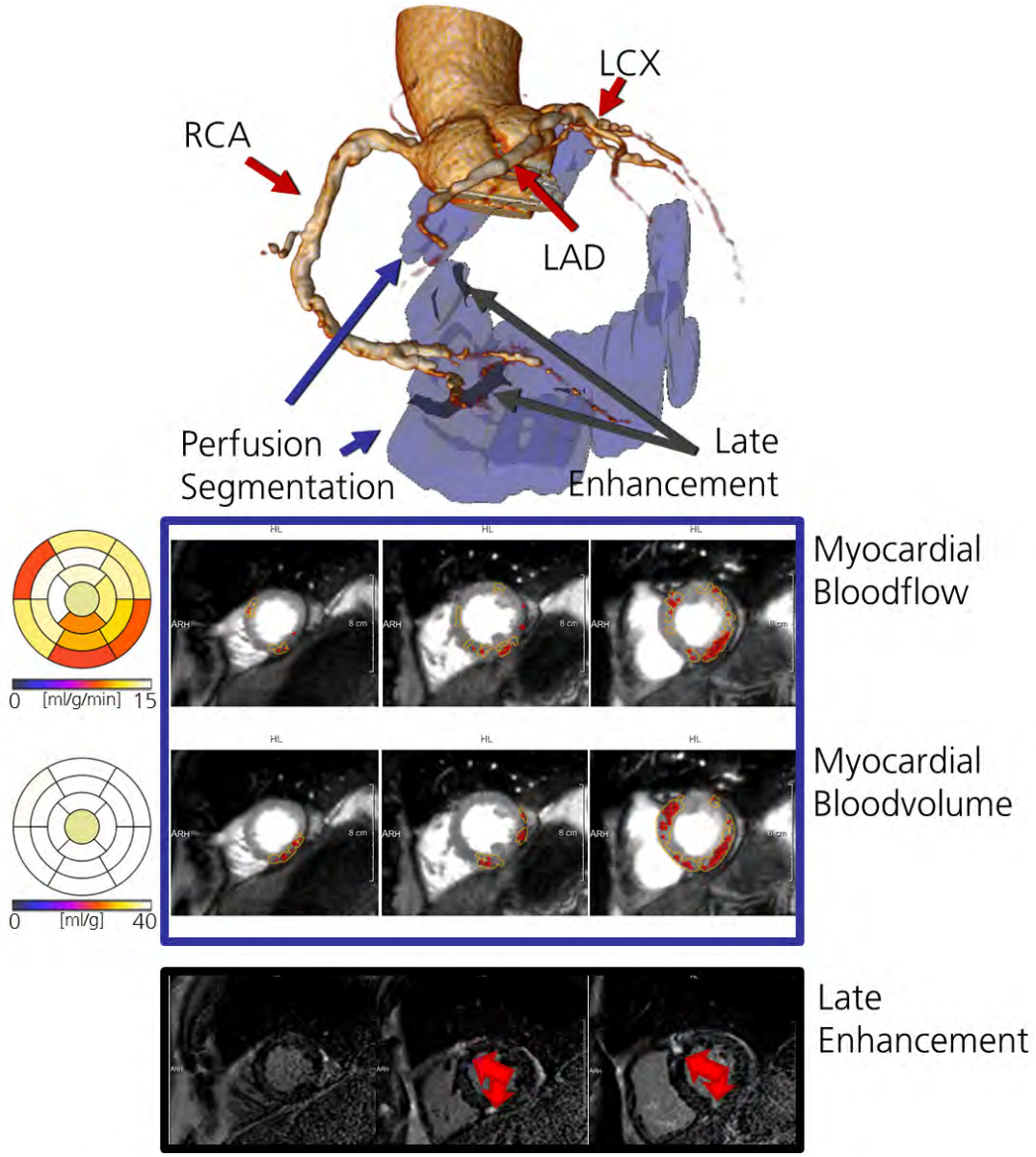

Figure A.8: Comparison of automatic segmentation in perfusion parameter images with findings from coronary artery inspection and late enhancement MRI for sequence 3. The patient suffers from stenoses > 75% in the three main coronary branches, and late enhancement was found in the LAD and RCA region. Perfusion defects were detected in all three supply regions.

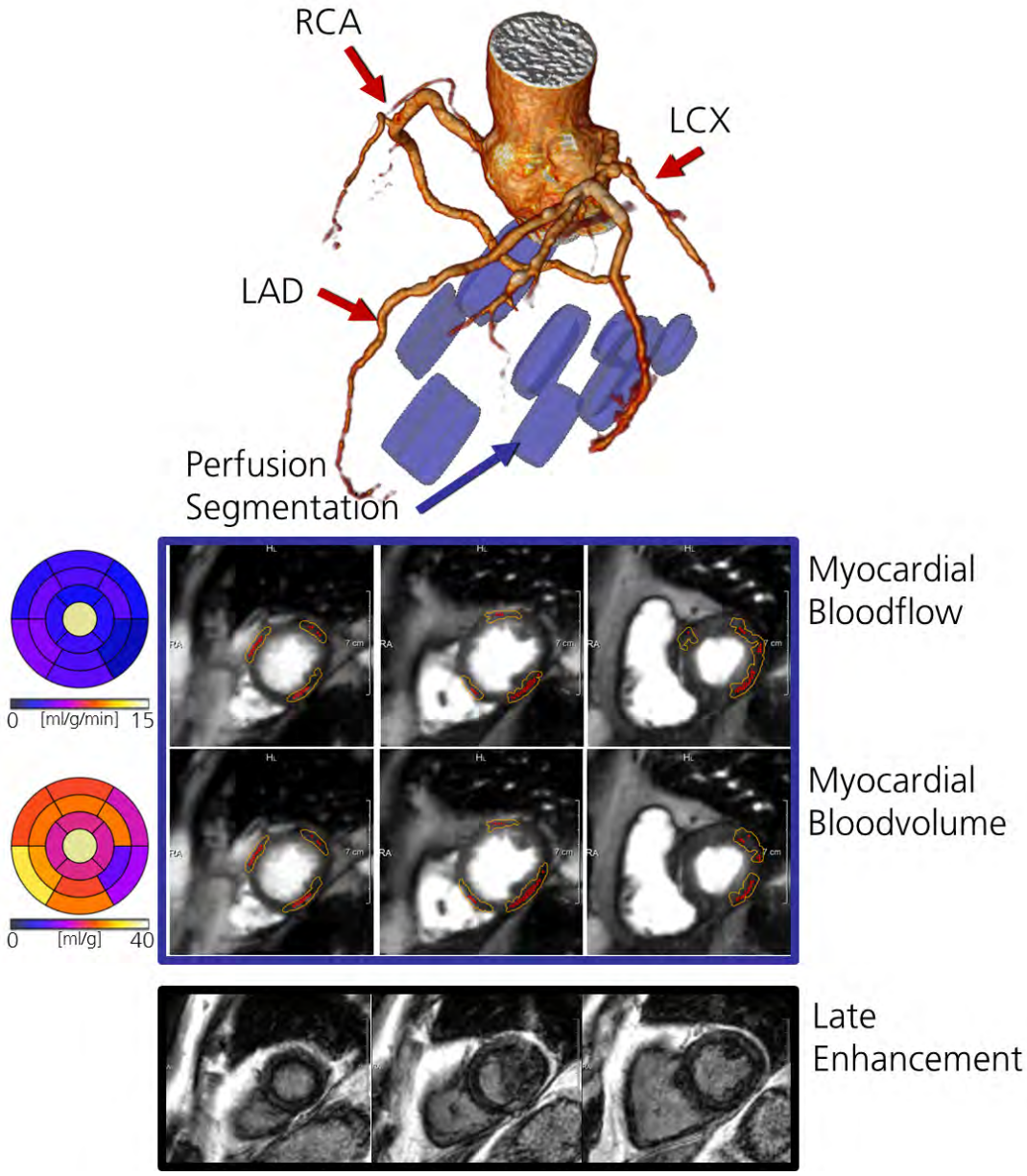

Figure A.9: Comparison of automatic segmentation in perfusion parameter images with findings from coronary artery inspection and late enhancement MRI for sequence 7. The patient has a LCX stenosis > 75%, LAD and RCA stenoses > 50% and no late enhancement. Perfusion defects were mainly detected in the LCX supply regions.

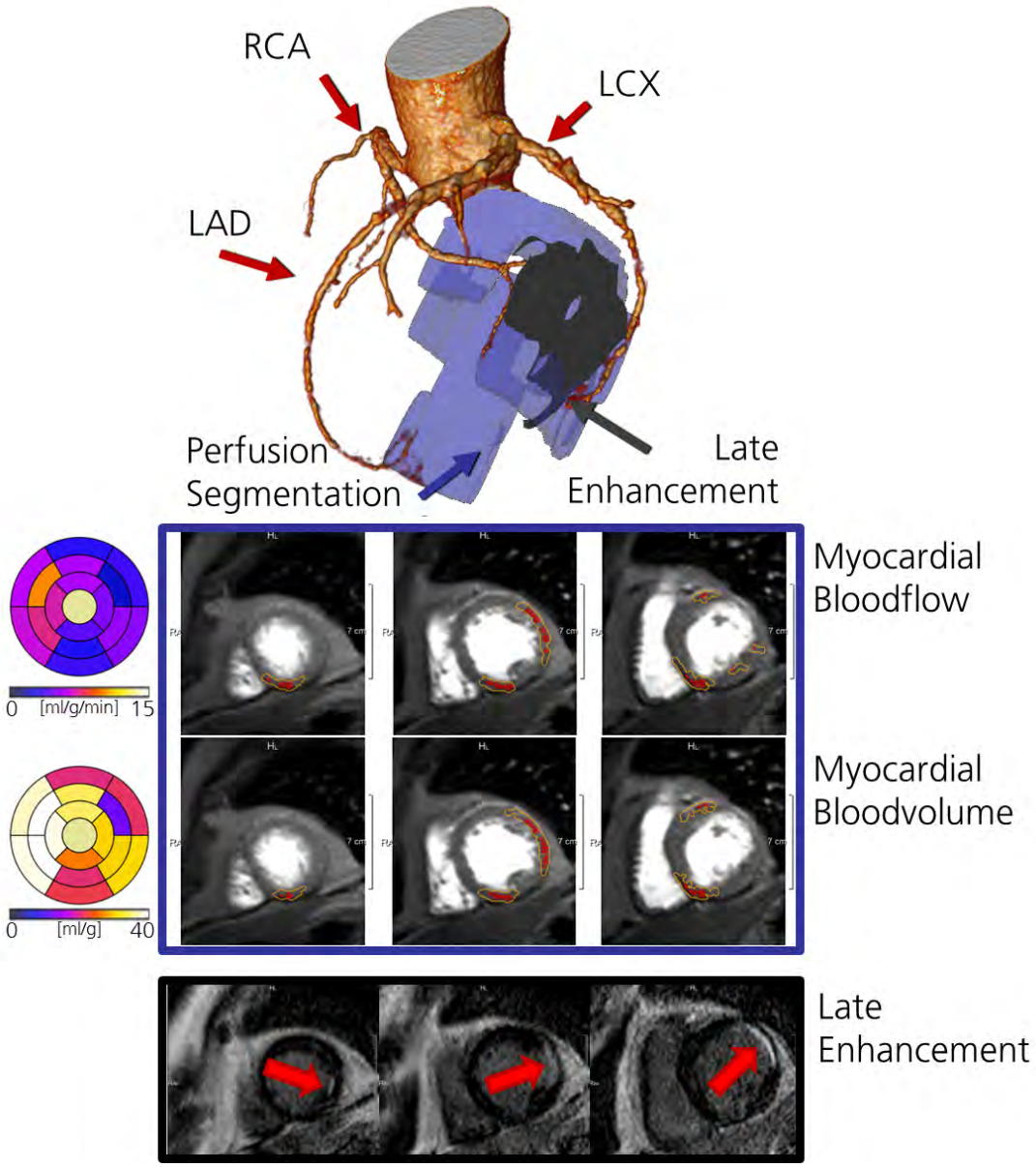

Figure A.10: Comparison of automatic segmentation in perfusion parameter images with findings from coronary artery inspection and late enhancement MRI for sequence 20. The patient has stenoses > 75% in all three major branches, and late enhancement in the LCX region. Detected perfusion defects could be assigned to the LCX and the LAD.

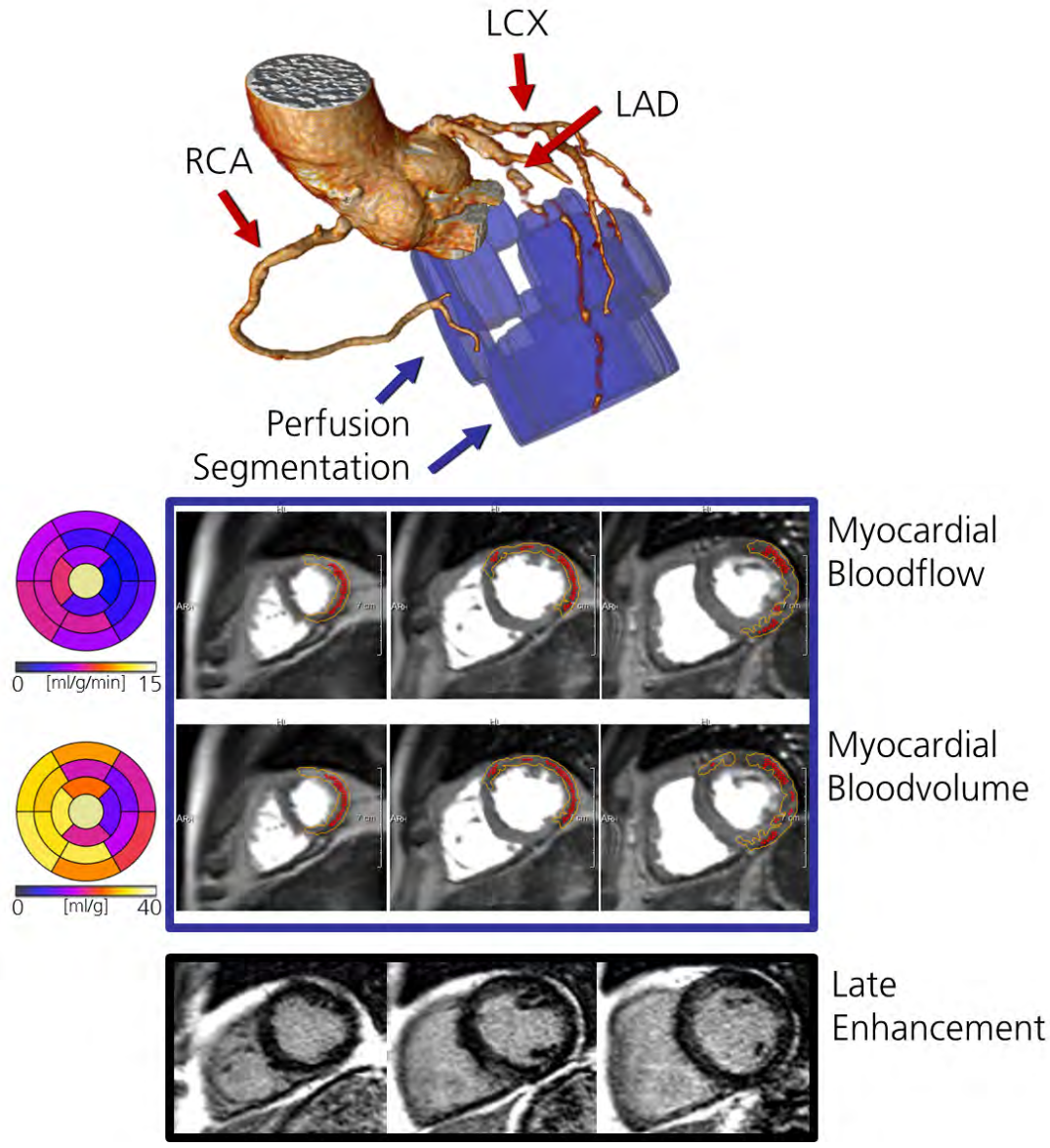

Figure A.11: Comparison of automatic segmentation in perfusion parameter images with findings from coronary artery inspection and late enhancement MRI for case 28. The patient has a LAD stenosis > 75% and no late enhancement. Perfusion defects are detected in the LAD and the RCA supply region.

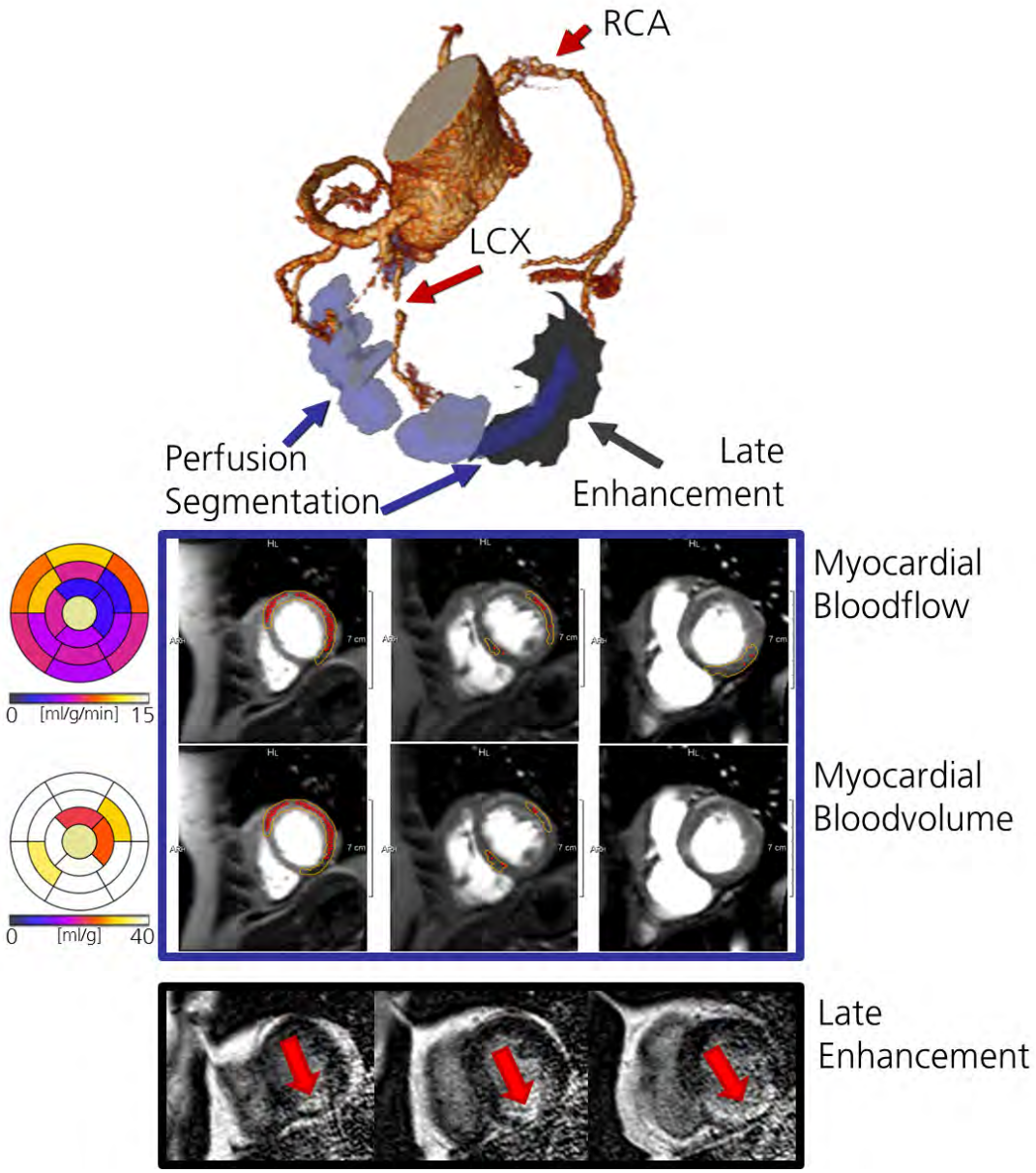

Figure A.12: Comparison of automatic segmentation in perfusion parameter images with findings from coronary artery inspection and late enhancement MRI for case 36. Stenoses > 75% were reported for RCA and LCX, late enhancement was found in the RCA region. Both regions are also detected based on the parameter images.

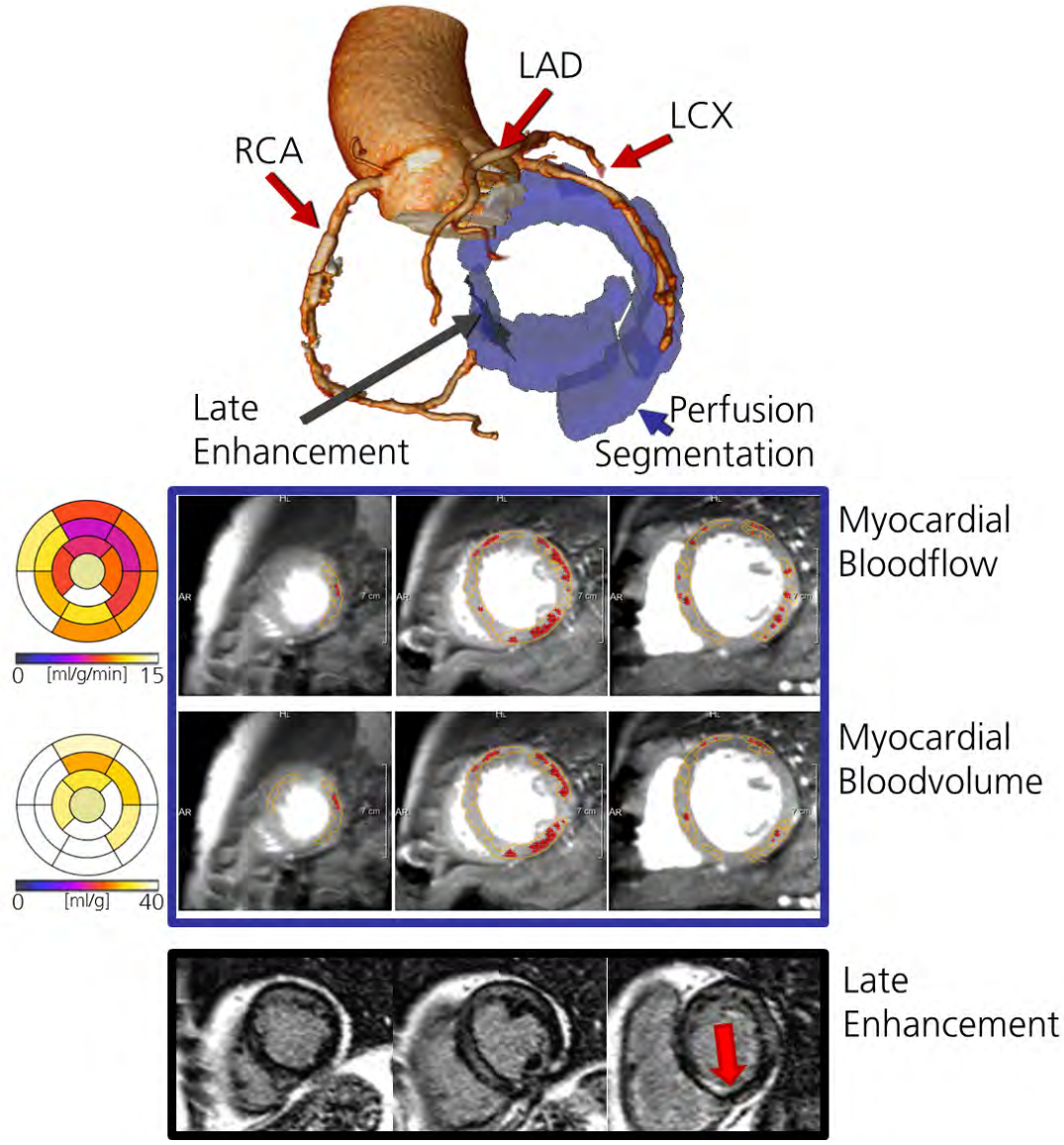

Figure A.13: Comparison of automatic segmentation in perfusion parameter images with findings from coronary artery inspection and late enhancement MRI for case 38. The LAD shows a stenosis > 50%, and late enhancement was found in the RCA region. Both regions are also detected based on the parameter images.

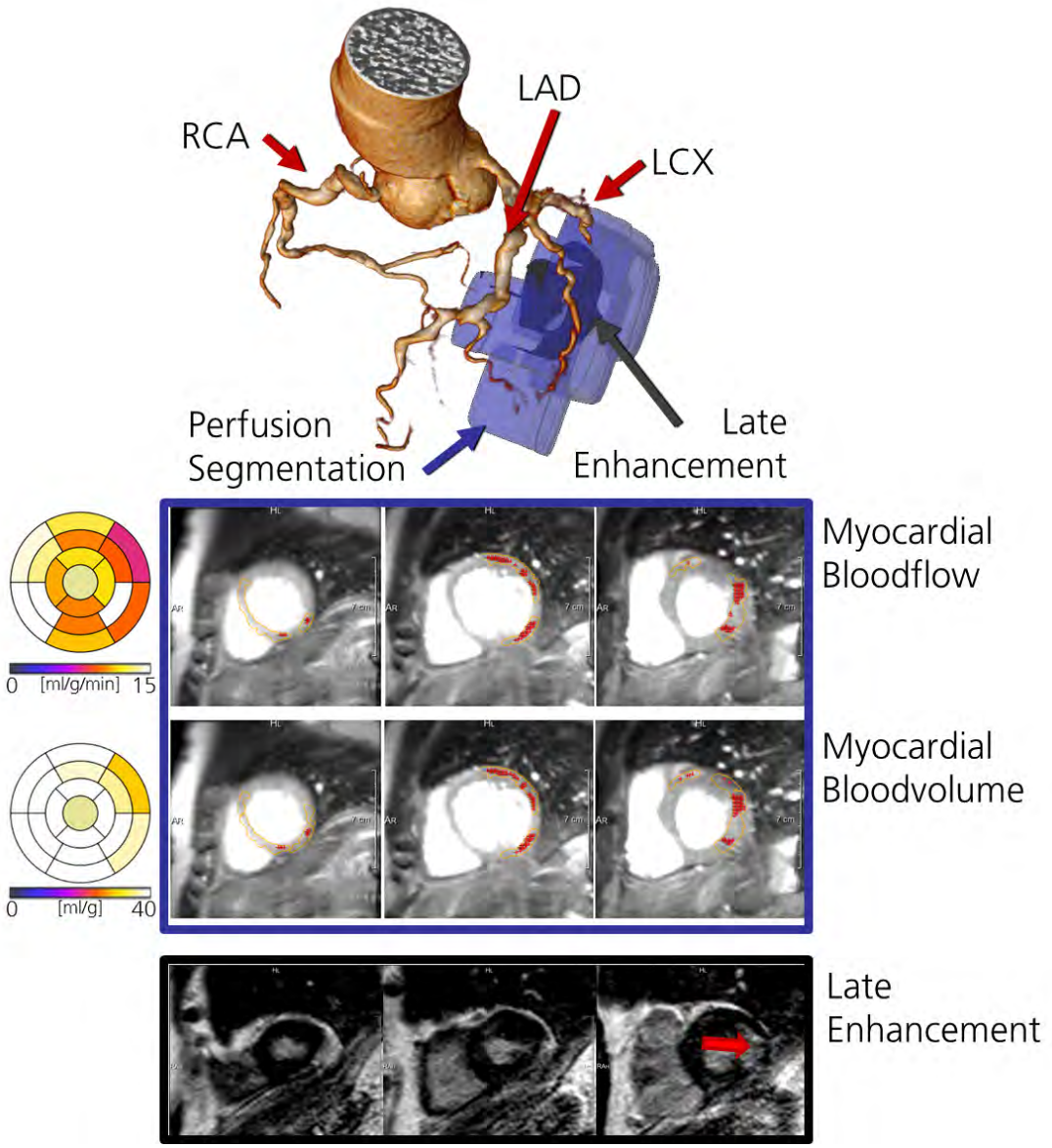

Figure A.14: Comparison of automatic segmentation in perfusion parameter images with findings from coronary artery inspection and late enhancement MRI for case 44. RCA and LCX exhibit stenoses > 75%, the LAD stenosis is > 50% and late enhancement was found in the LCX region. Automatically detected perfusion defects appear in the LCX and the LAD region.

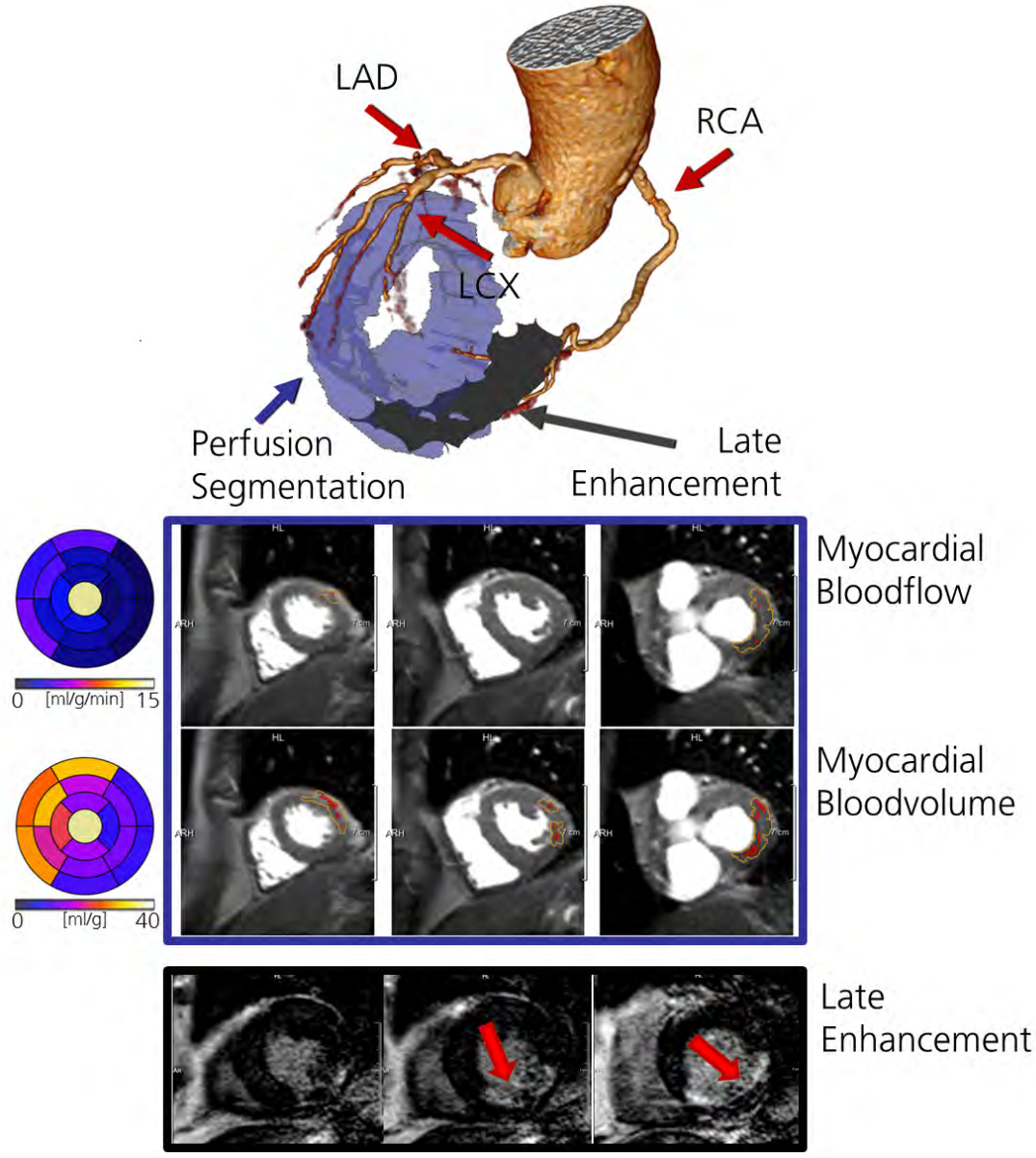

Figure A.15: Comparison of automatic segmentation in perfusion parameter images with findings from coronary artery inspection and late enhancement MRI for case 50. The LCX shows a stenosis > 75%, and late enhancement was found in the LCX and RCA region. Automatically detected perfusion defects match the late enhancement region and show additional small perfusion defects in the LAD region.

Glossary

Notation	Description	
ACC	American College of Cardiology	17
AHA	American Heart Association	1, 9
AIF	The Arterial Input Function describes the intensity profile in the arteries delivering blood to the region of interest after injection of the contrast agent.	116
AMI	Acute Myocardial Infarction caused by necrosis of myocardial tissue due to ischaemia.	10
ARMA	AutoRegressive-Moving Average models are based on linear equation systems. They are used for time series analysis under consideration of noise.	115
CAD	Coronary Artery Disease	10
CMR	Cardiac MRI examination.	37
CT	Computed Tomography: X-ray projections are used to generate absorption profiles of body regions from different directions. With the filtered backprojection method an image volume is created from these profiles.	14
CTCA	CT Coronary Angiography: A contrast enhanced CT volume scan of the heart that is dedicated to the inspection of the coronary artery tree.	17
DSCT	Dual Source Computed Tomography	17
ECG	An ElectroCardioGram is a graph that describes the electric impulse distribution of the heart measured by external sensors	7
EDV	End-Diastolic Volume: The amount of blood that is contained in the ventricle at the end of the filling phase.	7

Notation	Description	
ESV	End-Systolic Volume: The amount of blood in the ventricle at the time when all valves are closed.	8
FFR	The Fractional Flow Reserve is calculated from the pressure drop at a stenosis, which is typically determined with a pressure wire in a catheter examination. It is used to assess the significance of a stenosis.	1
GRE	Gradient Echo MRI sequences use low flip angles that enable a fast recovery and fast acquisitions.	18
HU	Hounsfield Units: Measured attenuation coefficients are converted to Hounsfield units through a linear transformation based on the attenuation of water. The Hounsfield scale for radiodensity is named after Sir Godfrey Newbold Hounsfield.	15
LAD	The Left Anterior Descending artery typically branches from the LCA and supplies 45-55% of the left ventricle of the heart	7
LCA	The Left Coronary Artery typically arises from the aorta above the aortic valve and bifurcates into LAD and LCX.	7
LCX	The Left CircumfleX artery typically branches from the LCA and supplies the posterolateral left ventricle. Depending on the individual anatomy between 15-50% of the left ventricle are supplied via the LCX	7
LE	Late Enhancement: contrast agent accumulates in the extracellular space in necrotic tissue. This effect is visible in CT and MRI images 5 to 30 minutes after contrast agent injection.	17
MBF	Myocardial Blood Flow	57
MBV	Myocardial Blood Volume	57

Notation	Description	
MIP	A Maximum Intensity Projection usually decreases the image dimension by one. The intensity values of the projection image are the maximum values of the original image along the represented projection ray.	51
MMP	Enzymes called Matrix Metalloproteinases, which modulate processes in the vessel wall.	10
Morphon	Registration approach based on the application of quadrature filters.	45
MRI	Magnetic Resonance Imaging is based on the property of nuclear magnetic resonance. Magnetic field gradients cause atomic nuclei to rotate with a location dependent speed. The relaxation after removal of the magnetic field produces a radio frequency signal, which can be measured with a receiver coil.	14
MSL	*Marginal Space Learning* is a machine learning approach, which is organized hierarchically in order to narrow down the search space early and thereby achieve a considerable speed-up.	67
NCC	The Normalized Cross Correlation calculates the probability density of the difference of two independent random variables normalized with the variance. It is used as a similarity measure in image registration.	26
NMI	The Normalized Mutual Information calculates the mutual dependence of the two random variables normalized by their marginal entropies. It is used as a similarity measure in image registration.	27
PACS	A Picture Archiving and Communication System provides storage and access tools for medical image data from different modalities.	146
PDF	Probability Density Function: the PDF describes the relative likelihood for a random variable to take on a given value.	95
RCA	The Right Coronary Artery originates from the aorta above the aortic valve. It supplies the right ventricle 25-35% of the left ventricle.	7

Notation	Description	
SCMR	Society for Cardiac Magnetic Resonance.	20
SNR	The Signal to Noise Ratio $\frac{\mu_{ROI}}{\sigma_{ROI}}$ in a region of interest is calculated from the average intensity μ_{ROI} and the standard deviation σ_{ROI} in this region.	18
SSFP	Steady State Free Precession MRI sequences use steady states of magnetization. They are based on a (low flip angle) gradient-echo MRI sequence with a short repetition time	18
SVD	The Singular Value Decomposition is a factorization of a real or complex matrix,which is often applied in least squares fittion of data.	115
TTC	2,3,5-TriphenylTetrazolin-Chloride is used to differentiate between living and necrotic tissues in pathological examinations. It is enzymatically reduced to red TPF (1,3,5-triphenylformazan) in metabolically active tissue regions. In necrotic tissue the white color of TTC remains unchanged.	104

References

S. Abbara, A. Arbab-Zadeh, T.Q. Callister, M.Y. Desai, W. Mamuya, L. Thomson, and W.G. Weigold. SCCT guidelines for performance of coronary computed tomographic angiography: a report of the Society of Cardiovascular Computed Tomography Guidelines Committee. *J Cardiovasc Comput Tomogr*, 3(3):190–204, 2009. doi: 10.1016/j.jcct.2009.03.004. URL http_//dx_doi_org/10_1016/j_jcct_2009_03_004. 16

M. Abramowitz and I. A. Stegun. *Handbook of Mathematical Functions*. Dover Publications, 1965. 96

G. Adluru, E.V.R. DiBella, and M.C. Schabel. Model-based registration for dynamic cardiac perfusion MRI. *J Magn Reson Imaging*, 24(5):1062–1070, 2006. doi: 10.1002/jmri.20756. URL http_//dx_doi_org/10_1002/_jmri_20756. 61

S. Ait-Aoudia and R. Mahiou. Medical Image Registration by Simulated Annealing and Genetic Algorithms. In *Geometric Modeling and Imaging, 2007. GMAI '07*, pages 145 –148, 2007. doi: 10.1109/GMAI.2007.25. 31

N. Al Saadi, M. Gross, A. Bornstedt, B. Schnackenburg, C. Klein, E. Fleck, and E. Nagel. Comparison of various parameters for determining an index of myocardial perfusion reserve in detecting coronary stenosis with cardiovascular magnetic resonance tomography. *Z Kardiol*, 90(11):824–834, 2001. 114, 116

N. Al Saadi, M. Gross, I. Paetsch, B. Schnackenburg, A. Bornstedt, E. Fleck, and E. Nagel. Dobutamine Induced Myocardial Perfusion Reserve Index with Cardiovascular MR in Patients with Coronary Artery Disease. *Journal of Cardiovascular Magnetic Resonance*, 4(4):471–480, 2002. 116

M. Allard, D. Doucet, P. Kien, B. Bonnemain, and J. M. Caille. Experimental study of DOTA-gadolinium. Pharmacokinetics and pharmacologic properties. *Invest Radiol*, 23 Suppl 1:271–274, 1988. 17

American College of Cardiology Foundation Task Force on Expert Consensus Documents. ACCF/ACR/AHA/NASCI/SCMR 2010 expert consensus document on cardiovascular magnetic resonance: a report of the American College of Cardiology Foundation Task Force on Expert Consensus Documents. *Circulation*, 121(22):2462–2508, 2010a. doi: 10.1161/CIR.0b013e3181d44a8f. URL http_//dx_doi_org/10_1161/CIR_0b013e3181d44a8f. 18

American College of Cardiology Foundation Task Force on Expert Consensus Documents. ACCF/ACR/AHA/NASCI/SAIP/SCAI/SCCT 2010 expert consensus document on coronary computed tomographic angiography: a report of the American College of Cardiology Foundation Task Force on Expert Consensus Documents. *Circulation*, 121(22):2509–2543, 2010b. doi: 10.1161/CIR.0b013e3181d4b618. URL http_//dx_doi_org/10_1161/_CIR_0b013e3181d4b618. 2, 16

H. Arheden, M. Saeed, C. B. Higgins, D. W. Gao, J. Bremerich, R. Wyttenbach, M. W. Dae, and M. F. Wendland. Measurement of the distribution volume of gadopentetate dimeglumine at echo-planar MR imaging to quantify myocardial infarction: comparison with 99mTc-DTPA autoradiography in rats. *Radiology*, 211(3):698–708, 1999. 21

H. Arheden, M. Saeed, C. B. Higgins, D. W. Gao, P. C. Ursell, J. Bremerich, R. Wyttenbach, M. W. Dae, and M. F. Wendland. Reperfused rat myocardium subjected to various durations of ischemia: estimation of the distribution volume of contrast material with echo-planar MR imaging. *Radiology*, 215(2): 520–528, 2000. 21

R. Bansal and G. Funka-Lea. Integrated image registration for cardiac MR perfusion data. In *Proceedings of the 5th International Conference on Medical Image Computing and Computer-Assisted Intervention (MICCAI'02)*, pages 659–666, 2002. 32

J. Barajas, K.L. Caballero, J. Garcia-Barnes, F. Carreras, S. Pujadas, and P. Radeva. Correction of Misalignment Artifacts Among 2-D Cardiac MR Images in 3-D Space. In G. Unal, I.A. Kakadiaris, G. Slabaugh, and A. Tannenbaum, editors, *First International Workshop on Computer Vision for Intravascular and Intracardiac Imaging, MICCAI 2006*, volume 1, pages 114–121, 2006. 32, 37

J.L. Barron, D.J. Fleet, and S.S. Beauchemin. Performance of optical flow techniques. *International Journal of Computer Vision*, 12:43–77, 1994. ISSN 0920-5691. URL http_//dx_doi_org/10_1007/BF01420984. 10.1007/BF01420984. 31

R.W. Bauer, J. M. Kerl, N. Fischer, T. Burkhard, M.C. Larson, H. Ackermann, and T.J. Vogl. Dual-Energy CT for the Assessment of Chronic Myocardial Infarction in Patients With Chronic Coronary Artery Disease: Comparison With 3-T MRI. *Am J Roentgenol*, 195(3):639–646, 2010. doi: 10.2214/AJR.09.3849. URL http_//dx_doi_org/10_2214/AJR_09_3849. 17

A. Becciu, H. Assen, L. Florack, S. Kozerke, V. Roode, and B.M. Haar Romeny. A Multi-scale Feature Based Optic Flow Method for 3D Cardiac Motion Estimation. In *Proceedings of the Second International Conference on Scale Space and Variational Methods in Computer Vision*, SSVM '09, pages 588–599. Springer-Verlag, 2009. ISBN 978-3-642-02255-5. doi: http://dx.doi.org/10.1007/978-3-642-02256-2_49. URL http_//dx_doi_org/10_1007/978-3-642-02256-2_49. 28

F. Benmansour and L.D. Cohen. A new interactive method for coronary arteries segmentation based on tubular anisotropy. In *Proceedings of the Sixth IEEE international Symposium on Biomedical Imaging: From Nano to Macro*, pages 41–44. IEEE Press, 2009. ISBN 978-1-4244-3931-7. URL http_//portal_acm_org/citation_cfm?id=1699872_1699883. 69

J. L. Bernon, V. Boudousq, J. F. Rohmer, M. Fourcade, M. Zanca, M. Rossi, and D. Mariano-Goulart. A comparative study of Powell's and Downhill Simplex algorithms for a fast multimodal surface matching in brain imaging. *Comput Med Imaging Graph*, 25(4):287–297, 2001. 30

L.M. Bidaut and J.P. Vallee. Automated registration of dynamic MR images for the quantification of myocardial perfusion. *J Magn Reson Imaging*, 13(4): 648–655, 2001. 26, 28, 32

D.A. Bluemke, S. Achenbach, M. Budoff, T.C. Gerber, B. Gersh, S.D. Hillis, W.G. Hundley, W.J. Manning, B.F. Printz, M. Stuber, and P.K. Woodard. Noninvasive coronary artery imaging: magnetic resonance angiography and multidetector computed tomography angiography: a scientific statement from the american heart association committee on cardiovascular imaging and intervention of the council on cardiovascular radiology and intervention, and the councils on clinical cardiology and cardiovascular disease in the young. *Circulation*, 118(5):586–606, 2008. doi: 10.1161/CIRCULATIONAHA.108.189695. URL http_//dx_doi_org/10_1161/CIRCULATIONAHA_108_189695. 18, 20, 22

S. Bock, C. Kuehnel, T. Boskamp, and H.-O. Peitgen. Robust vessel segmentation. In *Proceedings of the SPIE*, volume 6915S, pages 391–399, 2008. 68, 92, 142

F.L. Bookstein. Principal warps: thin-plate splines and the decomposition of deformations. *IEEE Trans on Pattern Analysis and Machine Intelligence*, 11(6): 567 –585, 1989. ISSN 0162-8828. doi: 10.1109/34.24792. 28

T. Boskamp, D. Rinck, F. Link, B. Kuemmerlen, G. Stamm, and P. Mildenberger. New vessel analysis tool for morphometric quantification and visualization of vessels in CT and MR imaging data sets. *Radiographics*, 24(1):287–297, 2004. doi: 10.1148/rg.241035073. 70, 71

REFERENCES

T. Boskamp, H.K. Hahn, M. Hindennach, S. Oeltze, B. Preim, S. Zidowitz, and H.-O. Peitgen. *Medical Imaging Systems*, chapter Geometrical and Structural Analysis of Vessel Systems in 3D Medical Image Datasets, pages 1–60. World Scientific, 2005. 79

R.M. Botnar, M. Stuber, P.G. Danias, K.V. Kissinger, and W.J. Manning. Improved coronary artery definition with T2-weighted, free-breathing, three-dimensional coronary MRA. *Circulation*, 99(24):3139–3148, 1999. 22

D. Boukerroui, J.A. Noble, and M. Brady. On the Choice of Band-Pass Quadrature Filters. *J Math Imaging Vis*, 21:53–80, 2004. ISSN 0924-9907. doi: 10.1023/B:JMIV.0000026557.50965.09. URL http_//dl_acm_org/citation_cfm?_id=988238_988277. 28

L. Bracoud, F. Vincent, C. Pachai, E. Canet, P. Croisille, and D. Revel. Automatic Registration of MR First-Pass Myocardial Perfusion Images. In *Functional Imaging and Modeling of the Heart, Second International Workshop, FIMH 2003*, volume 2674, pages 215–223, Lecture Notes in Computer Science, 2003. Springer-Verlag GmbH. 32, 49, 60, 150

M. Breeuwer, I. Paetsch, E. Nagel, R. Muthupillai, S. Flamm, and S. Plein. The detection of normal, ischemic and infarcted myocardial tissue using MRI. In *Proceedings of the 17th International Congress and Exhibition on Computer Assisted Radiology and Surgery (CARS'03)*, pages 1153–1158, 2003. 33, 93, 116

M. Breeuwer, L. Spreeuwers, and M. Quist. Automatic quantitative analysis of cardiac MR perfusion images. *Proceedings of SPIE*, 4322:733, 2004. 32

D.L. Brutsaert. Cardiac endothelial-myocardial signaling: its role in cardiac growth, contractile performance, and rhythmicity. *Physiol Rev*, 83(1):59–115, 2003. doi: 10.1152/physrev.00017.2002. URL http_//dx_doi_org/_10_1152/physrev_00017_2002. 10

J. Cammin and K. Taguchi. Image-based motion estimation for cardiac CT via image registration. In B.M. Dawant and D.R. Haynor, editors, *Proceedings of SPIE*, volume 7623, page 76232G. SPIE, 2010. doi: 10.1117/12.844446. URL http_//link_aip_org/link/?PSI/7623/76232G/1. 29

Centers for Disease Control and Prevention (CDC). Trends in aging–United States and worldwide. *MMWR Morb Mortal Wkly Rep*, 52(6):101–4, 106, 2003. 1

M.D. Cerqueira, N.J. Weissman, V. Dilsizian, A.K. Jacobs, S. Kaul, W.K. Laskey, D.J. Pennell, J.A. Rumberger, T. Ryan, and M.S. Verani. Standardized myocardial segmentation and nomenclature for tomographic imaging of the heart: a statement for healthcare professionals from the Cardiac Imaging Committee of the Council on Clinical Cardiology of the American Heart Association. *Circulation*, 105(4):539–542, 2002. 3, 9, 33, 51

A.G. Chandler, R.J. Pinder, T. Netsch, J.A. Schnabel, D.J. Hawkes, D.L.G. Hill, and R. Razavi. Correction of misaligned slices in multi-slice cardiovascular magnetic resonance using slice-to-volume registration. *J Cardiovasc Magn Reson*, 10:13, 2008. doi: 10.1186/1532-429X-10-13. URL http_//dx_doi_org/10_1186/1532-429X-10-13. 32

P. Chandra and L. Ibanez. ImageIO: design of an extensible image input/output library. *Crossroads*, 7:10–15, 2001. ISSN 1528-4972. doi: http://doi.acm.org/10.1145/372765.372772. URL http_//doi_acm_org/10_1145/372765_372772. 87

K.M. Choi, R.J. Kim, G. Gubernikoff, J.D. Vargas, M. Parker, and R.M. Judd. Transmural Extent of Acute Myocardial Infarction Predicts Long-Term Improvement in Contractile Function. *Circulation*, 104(10):1101–1107, 2001. 93

W.R. Cowell, editor. *Sources and Development of Mathematical Software*. Prentice-Hall Series in Computational Mathematics, Cleve Moler, Advisor. Prentice-Hall, Upper Saddle River, NJ 07458, USA, 1984. ISBN 0-13-823501-5. 50

E. DallArmellina, T.D. Karamitsos, S. Neubauer, and R.P. Choudhury. CMR for characterization of the myocardium in acute coronary syndromes. *Nat Rev Cardiol*, 7(11):624–636, 2010. doi: 10.1038/nrcardio.2010.140. URL http_//dx_doi_org/10_1038/nrcardio_2010_140. 15

M.H. Davis, A. Khotanzad, D.P. Flamig, and S.E. Harms. A physics-based coordinate transformation for 3-D image matching. *IEEE Trans Med Imaging*, 16 (3):317 –328, 1997. ISSN 0278-0062. doi: 10.1109/42.585766. 29

E. De Castro and C. Morandi. Registration of Translated and Rotated Images Using Finite Fourier Transforms. *IEEE Trans Pattern Anal Mach Intell*, 9:700–703, 1987. ISSN 0162-8828. doi: http://dx.doi.org/10.1109/TPAMI.1987.4767966. URL http_//dx_doi_org/10_1109/TPAMI_1987_4767966. 26

J. Declerck, J. Feldmar, M.L. Goris, and F. Betting. Automatic registration and alignment on a template of cardiac stress and rest reoriented SPECT images. *IEEE Trans Med Imaging*, 16(6):727–737, 1997. doi: 10.1109/42.650870. URL http_//dx_doi_org/10_1109/42_650870. 25

A. Dekkers and E. Aarts. Global optimization and simulated annealing. *Mathematical Programming*, 50:367–393, 1991. ISSN 0025-5610. URL http_//dx_doi_org/10_1007/BF01594945. 10.1007/BF01594945. 31

V.S. Deshpande, S.M. Shea, G. Laub, O.P. Simonetti, J. P. Finn, and D. Li. 3D magnetization-prepared true-FISP: a new technique for imaging coronary arteries. *Magn Reson Med*, 46(3):494–502, 2001. 22

M. Dewey. *Coronary CT Angiography*. Springer Berlin / Heidelberg, 2009. doi: 10.1007/978-3-540-79844-6. 17

E.V.R. Di Bella and A. Sitek. Time Curve Analysis Techniques for Dynamic Contrast MRI Studies. In *Proceedings of the 17th International Conference on Information Processing in Medical Imaging (IPMI'01)*, pages 211–217, 2001. 116

L.R. Dice. Measures of the Amount of Ecologic Association Between Species. *Ecology*, 26(3):297–302, 1945. URL http_//www_jstor_org/stable/_1932409. 109

E.W. Dijkstra. A note on two problems in connexion with graphs. *Numerische Mathematik*, 1:269–271, 1959. URL http_//jmvidal_cse_sc_edu/library/dijkstra59a_pdf. 69

A. Discher, N. Rougon, and F. Preteux. An unsupervised approach for measuring myocardial perfusion in MR image sequences. *Proceedings of SPIE*, 5916: 59160C, 2005. 33

O.F. Donati, H. Alkadhi, H. Scheffel, C. Kuehnel, A. Hennemuth, C. Wyss, N. Azemaj, A. Plass, S. Kozerke, V. Falk, S. Leschka, and P. Stolzmann. 3D fusion of functional cardiac magnetic resonance imaging and computed tomography coronary angiography: accuracy and added clinical value. *Invest Radiol*, 46(5):331–340, 2011. doi: 10.1097/RLI.0b013e3182056caf. URL http_//dx_doi_org/10_1097/RLI_0b013e3182056caf. 142, 145, 146

N. Donner-Banzhoff, K. Held, U. Laufs, H.-J. Trappe, K. Werdan, and H.-R. Zerkowski. Nationale Versorgungs-Leitlinien KHK. Leitlinie 1.9, Bundesaerztekammer, Kassenaerztliche Bundesvereinigung, Arbeitsgemeinschaft der Wissenschaftlichen Medizinischen Fachgesellschaften, 2010. URL http_//www_versorgungsleitlinien_de/themen/khk/_nvl_khk. 14

K.A. Eagle, G.S. Ginsburg, K. Musunuru, W.C. Aird, R.S. Balaban, S.K. Bennett, R.S. Blumenthal, S.R. Coughlin, K.W. Davidson, E.D. Frohlich, P. Greenland, G.P. Jarvik, P. Libby, C.J. Pepine, J.N. Ruskin, A.E. Stillman, J.E. Van Eyk, H.E. Tolunay, C.L. McDonald, and S.C. Smith. Identifying patients at high risk of a cardiovascular event in the near future: current status and future directions: report of a national heart, lung, and blood institute working group. *Circulation*, 121(12):1447–1454, 2010. doi: 10.1161/CIRCULATIONAHA.109.904029. URL http_//dx_doi_org/10_1161/CIRCULATIONAHA_109_904029. 15

R.L. Ehman and J.P. Felmlee. Adaptive technique for high-definition MR imaging of moving structures. *Radiology*, 173(1):255–263, 1989. 18, 21

K. Elagouni, C. Ciofolo-Veit, and B. Mory. Automatic segmentation of pathological tissue in cardiac MRI. In *Proceedings of the IEEE International Symposium on Biomedical Imaging*, pages 472–475, 2010. 94, 114, 123

M. Ferrant, A. Nabavi, B. Macq, P.M. Black, F.A. Jolesz, R. Kikinis, and S.K. Warfield. Serial registration of intraoperative MR images of the brain. *Medical Image Analysis*, 6(4):337–359, 2002. 29

J.P. Finn, K. Nael, V. Deshpande, O. Ratib, and G. Laub. Cardiac MR imaging: state of the technology. *Radiology*, 241(2):338–354, 2006. doi: 10.1148/radiol.2412041866. URL http_//dx_doi_org/10_1148/radiol_2412041866. 20

D.J. Fleet. *Measurement of Image Velocity*. Kluwer Academic Publishers, 1992. ISBN 0792391985. 28

T.G. Flohr, C.H. McCollough, H. Bruder, M. Petersilka, K. Gruber, C. Suess, M. Grasruck, K. Stierstorfer, B. Krauss, R. Raupach, A.N. Primak, A. Kuettner, S. Achenbach, C. Becker, A. Kopp, and B.M. Ohnesorge. First performance evaluation of a dual-source CT (DSCT) system. *Eur Radiol*, 16(2):256–268, 2006. doi: 10.1007/s00330-005-2919-2. URL http_//dx_doi_org/10_1007/s00330-005-2919-2. 16

L. Florack and H. van Assen. A new methodology for multiscale myocardial deformation and strain analysis based on tagging MRI. *Int J Biomed Imaging*, page 341242, 2010. doi: 10.1155/2010/341242. URL http_//dx_doi_org/_10_1155/2010/341242. 31

C. Florin, R. Moreau-Gobard, and J. Williams. Automatic Heart Peripheral Vessels Segmentation Based on a Normal MIP Ray Casting Technique. In Christian Barillot, David R. Haynor, and Pierre Hellier, editors, *Proceedings of the 6th International Conference on Medical Image Com- puting and Computer-Assisted Intervention*, volume 3216, pages 483–490. Springer Berlin / Heidelberg, 2004. URL http_//dx_doi_org/10_1007/_978-3-540-30135-6_59. 67

C. Florin, N. Paragios, and J. Williams. Particle filters, a quasi-Monte-Carlo-solution for segmentation of coronaries. *Proceedings of the 7th International Conference on Medical Image Com- puting and Computer-Assisted Intervention*, 8(1):246–253, 2005. 69

A. Frangi, W. Niessen, K. Vincken, and M. Viergever. Multiscale Vessel Enhancement Filtering. In *Proceedings of the 1st International Conference on Medical Image Computing and Computer-Assisted Intervention*, pages 130–137, 1998. 68

H. Fricke, A. Elsner, R. Weise, M. Bolte, J. van den Hoff, W. Burchert, G. Domik, and E. Fricke. Quantitative myocardial perfusion PET combined with coronary anatomy derived from CT angiography: validation of a new fusion and visualisation software. *Z Med Phys*, 19(3):182–188, 2009. 126

O. Friman, M. Hindennach, C. Kuehnel, and H.-O. Peitgen. Multiple hypothesis template tracking of small 3D vessel structures. *Medical Image Analysis*, 14(2):160–171, 2010. doi: 10.1016/j.media.2009.12.003. URL http_//dx_doi_org/10_1016/j_media_2009_12_003. 69, 70, 92

G. Funka-Lea, Y. Boykov, C. Florin, M.-P. Jolly, R. Moreau-Gobard, R. Ramaraj, and D. Rinck. Automatic heart isolation for CT coronary visualization using graph-cuts. In *Proceedings of the IEEE International Symposium on Biomedical Imaging*, pages 614–617, 2006. 67

R.F. Furchgott and P.M. Vanhoutte. Endothelium-derived relaxing and contracting factors. *FASEB J*, 3(9):2007–2018, 1989. 10

L.G. Futterman and L. Lemberg. Hibernating myocardium, stunning, ischemic preconditioning: clinical relevance. *Am J Crit Care*, 9(6):430–436, 2000. 12

O. Gaemperli, T. Schepis, V. Kalff, M. Namdar, I. Valenta, L. Stefani, L. Desbiolles, S. Leschka, L. Husmann, H. Alkadhi, and P. A. Kaufmann. Validation of a new cardiac image fusion software for three-dimensional integration of myocardial perfusion SPECT and stand-alone 64-slice CT angiography. *Eur J Nucl Med Mol Imaging*, 34(7):1097–1106, 2007. doi: 10.1007/s00259-006-0342-9. URL http_//dx_doi_org/10_1007/_s00259-006-0342-9. 126

C.M. Gallippi and G.E. Trahey. Automatic Image Registration for MR and Ultrasound Cardiac Images. In *Proceedings of the 17th International Conference on Information Processing in Medical Imaging*, pages 148–154. Springer-Verlag, 2001. ISBN 3-540-42245-5. URL http_//dl_acm_org/citation_cfm?id=645597_658391. 27, 33

C. Gatta, S. Balocco, V. Martin-Yuste, R. Leta, and P. Radeva. Non-rigid Multimodal Registration of Coronary Arteries Using SIFTflow. In J. Vitria, J. Sanches, and M. Hernandez, editors, *IbPRIA 2011: Pattern Recognition and Image Analysis, Lecture Notes in Computer Science*, pages 159–166. Springer Berlin / Heidelberg, 2011. 26

S. Glasser, S. Oeltze, A. Hennemuth, C. Kubisch, A. Mahnken, S. Wilhelmsen, and B. Preim. Automatic transfer function specification for visual emphasis of coronary artery plaque. *Computer Graphics Forum*, 29(1):191–201, 2010. ISSN 1467-8659. doi: 10.1111/j.1467-8659.2009.01590.x. URL http_//dx_doi_org/10_1111/j_1467-8659_2009_01590_x. 146

R.H. Gong, S. Worz, and K. Rohr. Segmentation of Coronary Arteries of the Human Heart from 3D Medical Images. In T. Wittenberg, P. Hastreiter, U. Hoppe, H. Handels, A. Horsch, and H.-P. Meinzer, editors, *Bildverarbeitung für die Medizin*, Informatik aktuell, pages 66–70. Bildverarbeitung für die Medizin, Springer-Verlag Berlin Heidelberg, 2003. 69

A. Goshtasby. Registration of images with geometric distortions. *IEEE Transactions on Geoscience and Remote Sensing*, 26(1):60 –64, 1988. ISSN 0196-2892. doi: 10.1109/36.3000. 28

P. Gravel, G. Beaudoin, and J.A. De Guise. A method for modeling noise in medical images. *IEEE Trans Med Imaging*, 23(10):1221–1232, 2004. doi: 10.1109/TMI.2004.832656. URL http_//dx_doi_org/10_1109/TMI_2004_832656. 95

J.P. Greenwood, N. Maredia, J.F. Younger, J.M. Brown, J. Nixon, C.C. Everett, P. Bijsterveld, J.P. Ridgway, A. Radjenovic, C.J. Dickinson, S.G. Ball, and S. Plein. Cardiovascular magnetic resonance and single-photon emission computed tomography for diagnosis of coronary heart disease (cemarc): a prospective trial. *Lancet*, 379(9814):453–460, Feb 2012. doi: 10.1016/S0140-6736(11)61335-4. URL http_//dx_doi_org/10_1016/_S0140-6736(11)61335-4. 2

H. Gudbjartsson and S. Patz. The Rician distribution of noisy MRI data. *Magn Reson Med*, 34(6):910–914, 1995. 95

S.N. Gupta, M. Solaiyappan, G.M. Beache, A.E. Arai, and T.K.F. Foo. Fast method for correcting image misregistration due to organ motion in time-series MRI data. *Magn Reson Med*, 49(3):506–514, 2003. 32, 49

Vikas Gupta, Hortense A Kirisli, Emile A Hendriks, Rob J van der Geest, Martijn van de Giessen, Wiro Niessen, Johan H C Reiber, and Boudewijn P F Lelieveldt. Cardiac mr perfusion image processing techniques: a survey. *Med Image Anal*, 16(4):767–785, May 2012. doi: 10.1016/j.media.2011.12.005. URL http_//dx_doi_org/10_1016/j_media_2011_12_005. 126

E. Haber and J. Modersitzki. Intensity gradient based registration and fusion of multi-modal images. *Methods of Information in Medicine*, 46(3):292–299, 2007. 28

A. Hagemann, K. Rohr, H.S. Stiehl, U. Spetzger, and J.M. Gilsbach. Biomechanical modeling of the human head for physically based, nonrigid image registration. *IEEE Trans Med Imaging*, 18(10):875–884, 1999. doi: 10.1109/42.811267. URL http_//dx_doi_org/10_1109/42_811267. 29

H.K. Hahn. *Morphological Volumetry : Theory, Concepts, and Application to Quantitative Medical Imaging*. PhD thesis, University of Bremen, 2005. URL http_//elib_suub_uni-bremen_de/diss/docs/_E-Diss1252_Hahn_pdf. 95

H.K. Hahn and H.O. Peitgen. IWT – Interactive Watershed Transform: A hierarchical method for efficient interactive and automated segmentation of multidimensional grayscale images. In *Proceedings of SPIE*, volume 5032, pages 643–653. SPIE, 2003. 94, 117, 123

M.S. Hansen, H. Ólafsdóttir, K. Sjöstrand, S.G. Erbou, M.B. Stegmann, H.B.W. Larsson, and R. Larsen. Ischemic segment detection using the support vector domain description. *Proceedings of SPIE*, 6512:65120F, 2007. 116

C. Harris and M. Stephens. A combined corner and edge detector. In *Proceedings of the 4th Alvey Vision Conference*, 1988. 25

D.J. Heeger. Optical flow using spatiotemporal filters. *International Journal of Computer Vision*, 1:279–302, 1988. ISSN 0920-5691. URL http_//dx_doi_org/10_1007/BF00133568. 10.1007/BF00133568. 28

REFERENCES

E. Heiberg, J. Sjoegren, M. Ugander, M. Carlsson, H. Engblom, and H. Arheden. Design and validation of Segment–freely available software for cardiovascular image analysis. *BMC Med Imaging*, 10:1, 2010. doi: 10.1186/1471-2342-10-1. URL http_//dx_doi_org/10_1186/1471-2342-10-1. 125

A. Hennemuth, S. Bock, T. Boskamp, D. Fritz, C. Kuehnel, D. Rinck, and M. Scheuering. One-click coronary tree segmentation in CT angiographic images. In *Proceedings of the 19th International Congress and Exhibition on Computer Assisted Radiology and Surgery (CARS'05)*, pages 317–321, 2005. 68, 87

A. Hennemuth, S. Behrens, C. Kuehnel, S. Oeltze, O. Konrad, and H.-O. Peitgen. Novel methods for parameter based analysis of myocardial tissue in MR-Images. In A. Manduca and X.P. Hu, editors, *Proceedings of SPIE*, volume 6511, pages 65111N–1 – 65111N–9. SPIE, 2007. 117

A. Hennemuth, A. Mahnken, C. Kuehnel, S. Oeltze, and H.-O. Peitgen. CT Late Enhancement Segmentation for the Combined Analysis of Coronary Arteries and Myocardial Viability. In C. Botha, G. Kindlmann, W. Niessen, and B. Preim, editors, *Eurographics Workshop on Visual Computing for Biomedicine (VCBM)*, pages 1–9. Eurographics Association, 2008a. URL http_//www_eg_org/EG/DL/WS/VCBM/VCBM08/001-009_pdf. 123

A. Hennemuth, A. Seeger, O. Friman, S. Miller, B. Klumpp, S. Oeltze, and H.-O. Peitgen. A comprehensive approach to the analysis of contrast enhanced cardiac MR images. *IEEE Trans Med Imaging*, 27(11):1592–1610, 2008b. doi: 10.1109/TMI.2008.2006512. URL http_//dx_doi_org/10_1109/TMI_2008_2006512. 49

A. Hennemuth, A. Seeger, O. Friman, S. Miller, and H.-O. Peitgen. Automatic Detection and Quantification of Non-Viable Myocardium in Late Enhancement Images. In *Proceedings of the 16th Scientific Meeting of the International Society for Magnetic Resonance in Medicine (ISMRM 08)*, 2008c. 94

A. Hennemuth, A. Harloff, T. Spehl, N. Pavlov, O. Friman, D. Paul, D. von Elverfeldt, C. Kuehnel, S. Wirtz, H. Goebel, J. Mannheim, H.K. Hahn, B. Pichler, J. Hennig, and M. Markl. Visual classification of complicated plaques based on multidimensional image fusion. In S. Fischer, editor, *GI-Edition - Lecture Notes in Informatics (LNI) - Proceedings 154*, pages 1359–1369. GI, 2009. 146

A. Hennemuth, O. Friman, M. Huellebrand, H.O. Peitgen, and A. Mahnken. Semi-Automatic Quantification of Late Enhancement in CT and MRI Images. In *ISMRM 2012*, page 1251, 2012a. 123

A. Hennemuth, B. Knowles, M. Huellebrand, L. Tautz, and H.O. Peitgen. Automatic Detection of Left Atrial Scar Tissue in DE-MRI using a Mixture Model and Location Constraints. In *cDEMRIS Workshop IEEE ISBI 2012*, pages 1–2, 2012b. 151

K.-T. Ho, K.-C. Chua, E. Klotz, and C. Panknin. Stress and rest dynamic myocardial perfusion imaging by evaluation of complete time-attenuation curves with dual-source CT. *JACC Cardiovasc Imaging*, 3(8):811–820, Aug 2010. doi: 10.1016/j.jcmg.2010.05.009. URL http_//dx_doi_org/10_1016/j_jcmg_2010_05_009. 17

M. Holtzman-Gazit, R. Kimmel, N. Peled, and D. Goldsher. Segmentation of thin structures in volumetric medical images. *Image Processing, IEEE Transactions on*, 15(2):354 –363, 2006. ISSN 1057-7149. doi: 10.1109/TIP.2005.860624. 68

B.K.P. Horn and B.G. Schunck. Determining optical flow. *Artificial Intelligence*, 17:185 – 203, 1981. ISSN 0004-3702. doi: 10.1016/0004-3702(81)90024-2. URL http_//www_sciencedirect_com/science/article/_pii/0004370281900242. 31

L.Y. Hsu, A. Natanzon, P. Kellman, G.A. Hirsch, A.H. Aletras, and A.E. Arai. Quantitative myocardial infarction on delayed enhancement MRI, part I: animal validation of an automated feature analysis and combined thresholding infarct sizing algorithm. *J Magn Reson Imaging*, 23:298–308, 2006. 93, 94

M. Huellebrand, A. Hennemuth, D. Messroghli, and T. Kuehne. An extendable multimodal cardiac analysis plug-in for OsiriX. In *ECR Today*, number 4, page 21, 2012. 151

J. Hugunin and T.E. Oliphant. NumPy scientific computing package for Python. http://numpy.scipy.org/, 2010. URL http_//numpy_scipy_org/. 76

P. Hunold. *Cardiac Imaging: A Multimodality Approach*, chapter Pathophysiology of Delayed Enhancement, page 117. Thieme, 2009. URL http_//books_google_de/books?id=QyM0tsbH8EAC. 15

P. Hunold, T. Schlosser, and J. Barkhausen. Magnetic resonance cardiac perfusion imaging-a clinical perspective. *Eur Radiol*, 16(8):1779–1788, 2006. doi: 10.1007/s00330-006-0269-3. URL http_//dx_doi_org/10_1007/_s00330-006-0269-3. 101

L. Husmann, S. Leschka, L. Desbiolles, T. Schepis, O. Gaemperli, B. Seifert, P. Cattin, T. Frauenfelder, T.G. Flohr, B. Marincek, P.A. Kaufmann, and H. Alkadhi. Coronary artery motion and cardiac phases: dependency on heart rate – implications for CT image reconstruction. *Radiology*, 245(2):567–576, 2007. doi: 10.1148/radiol.2451061791. URL http_//dx_doi_org/10_1148/radiol_2451061791. 16

S.T. Hussain, M. Paul, S. Plein, G.P. McCann, A. Shah, C. Amedeo, G. Morton, A. Schuster, M. Westwood, D. Perera, M. Marber, and Nag. Design and rationale of the mr-inform study: stress perfusion mri to guide the management of patients with stable coronary artery disease. *Journal of Cardiovascular Magnetic Resonance*, 14(1):O19, 2012. 122, 124

B. Jaehne. *Local Wave Number and Phase*, chapter 13.4, pages 375–384. Springer, 2005. 28

M. Jerosch-Herold. Quantification of myocardial perfusion by cardiovascular magnetic resonance. *Journal of Cardiovascular Magnetic Resonance*, 12(57):1–16, 2010. URL http_//www_jcmr-online_com/content/12/1/57. 117

M. Jerosch-Herold, C. Swingen, and R.T. Seethamraju. Myocardial blood flow quantification with MRI by model-independent deconvolution. *Med Phys*, 29(5):886–897, 2002. 115, 116

M. Jerosch-Herold, R.T. Seethamraju, C.M. Swingen, N.M. Wilke, and A.E. Stillman. Analysis of myocardial perfusion MRI. *J Magn Reson Imaging*, 19(6):758–770, 2004. doi: 10.1002/jmri.20065. URL http_//dx_doi_org/10_1002/jmri_20065. 50

J. Jomier, V. LeDigarcher, and S.R. Aylward. Automatic vascular tree formation using the Mahalanobis distance. *Proceedings of the 7th International Conference on Medical Image Com- puting and Computer-Assisted Intervention*, 8(2):806–812, 2005. 70

J.T. Keijer, A.C. van Rossum, M.J. van Eenige, A.J. Karreman, M.B. Hofman, J. Valk, and C.A. Visser. Semiquantitation of regional myocardial blood flow in normal human subjects by first-pass magnetic resonance imaging. *Am Heart J*, 130(4):893–901, 1995. 114

R. Kim, D. Fieno, T. Parrish, K. Harris, E.L. Chen, O. Simonetti, J. Bundy, J. Finn, F. Klocke, and R. Judd. Relationship of MRI delayed contrast enhancement to irreversible injury, infarct age, and contractile function. *Circulation*, 100(19):1992–2002, 1999. 93, 94

H.A. Kirisli, V. Gupta, S.W. Kirschbaum, A. Rossi, C.T. Metz, M. Schaap, R. J. van Geuns, N. Mollet, B.P.F. Lelieveldt, J.H.C. Reiber, T. van Walsum, and W.J. Niessen. Comprehensive visualization of multimodal cardiac imaging data for assessment of coronary artery disease: first clinical results of the SMARTVis tool. *Int J Comput Assist Radiol Surg*, 2011. doi: 10.1007/s11548-011-0657-2. URL http_//dx_doi_org/10_1007/_s11548-011-0657-2. 33, 126, 128

P. Kitslaar, M. Frenay, E. Oost, J. Dijkstra, B. Stoel, and J.H.C. Reiber. Connected Component and Morphology Based Extraction of Arterial Centerlines of the Heart (CocomoBeach). In *The MIDAS Journal - Grand Challenge Coronary Artery Tracking (MICCAI 2008 Workshop).*, 2008. URL http_//hdl_handle_net/10380/1460. 68, 71

S. Klein, M. Staring, and J.P.W. Pluim. Evaluation of optimization methods for nonrigid medical image registration using mutual information and B-splines. *IEEE Trans Image Process*, 16(12):2879–2890, 2007. 31

F. Klocke, O. Simonetti, R. Judd, R. Kim, K. Harris, S. Hedjbeli, D. Fieno, S. Miller, S. Chen, and M. Parker. Limits of detection of regional differences in vasodilated flow in viable myocardium by first-pass magnetic resonance perfusion imaging. *Circulation*, 104(20):2412–2416, 2001. 114

H. Knutsson and M. Andersson. Morphons: Paint on Priors and Elastic Canvas for Segmentation and Registration. In H. Kalviainen, J. Parkkinen, and A. Kaarna, editors, *Image Analysis*, volume 3540 of *Lecture Notes in Computer Science*, pages 46–55. Springer Berlin / Heidelberg, 2005. ISBN 978-3-540-26320-3. 45, 63, 150

A. Kolipaka, G. Chatzimavroudis, R. White, T. O'Donnell, and R. Setser. Segmentation of non-viable myocardium in delayed enhancement magnetic resonance images. *Int J Cardiovasc Imaging*, 21(2–3):303–311, 2005. 93

T. Kovacs, P. Cattin, H. Alkadhi, S. Wildermuth, and G. Szekely. Automatic Segmentation of the Vessel Lumen from 3D CTA Images of Aortic Dissection. In H. Handels, J. Ehrhardt, A. Horsch, H.-P. Meinzer, and T. Tolxdorff, editors, *Bildverarbeitung fuer die Medizin*, Informatik aktuell, pages 161–165. Springer Berlin Heidelberg, 2006. ISBN 978-3-540-32137-8. URL http_//dx_doi_org/10_1007/3-540-32137-3_33. 72

C.M. Kramer, J. Barkhausen, S.D. Flamm, R.J. Kim, E. Nagel, and Society for Cardiovascular Magnetic Resonance Board of Trustees Task Force on Standardized Protocols. Standardized cardiovascular magnetic resonance imaging (CMR) protocols, society for cardiovascular magnetic resonance: board of trustees task force on standardized protocols. *J Cardiovasc Magn Reson*, 10: 35, 2008. 20, 21, 22

C. Kuehnel, A. Hennemuth, S. Oeltze, T. Boskamp, and H.-O. Peitgen. Enhanced Cardio Vascular Image Analysis by Combined Representation of Results from Dynamic MRI and Anatomic CTA. In *Proceedings of the SPIE*, volume 6918, page 69180S, 2008. 126, 127, 128, 129

C.D. Kuglin and D.C. Hines. The phase correlation image alignment method. In *Proceedings of IEEE Conference on Cybernetics and Society*, pages 163–165, 1975. 26

A. Larralde, C. Boldak, M. Garreau, C. Toumoulin, D. Boulmier, and Y. Rolland. Evaluation of a 3D Segmentation Software for the Coronary Characterization in Multi-slice Computed Tomography. In I. Magnin, J. Montagnat, P. Clarysse, J. Nenonen, and T. Katila, editors, *Functional Imaging and Modeling of the Heart*, volume 2674 of *Lecture Notes in Computer Science*, pages 1005–1005. Springer Berlin Heidelberg, 2003. 69, 71

H.B. Larsson, M. Stubgaard, L. Soendergaard, and O. Henriksen. In vivo quantification of the unidirectional influx constant for Gd-DTPA diffusion across the myocardial capillaries with MR imaging. *J Magn Reson Imaging*, 4(3): 433–440, 1994. 115

T.M. Lehmann, C. Goenner, and K. Spitzer. Survey: interpolation methods in medical image processing. *IEEE Trans Med Imaging*, 18(11):1049–1075, 1999. doi: 10.1109/42.816070. URL http_//dx_doi_org/10_1109/42_816070. 31

T. Lei and W. Sewchand. Statistical approach to X-ray CT imaging and its applications in image analysis. I. Statistical analysis of X-ray CT imaging. *IEEE Trans Med Imaging*, 11(1):53–61, 1992. doi: 10.1109/42.126910. URL http_//dx_doi_org/10_1109/42_126910. 95

D. Lesage, E.D. Angelini, I. Bloch, and G. Funka-Lea. Bayesian maximal paths for coronary artery segmentation from 3D CT angiograms. *Proceedings of the11th International Conference on Medical Image Com- puting and Computer-Assisted Intervention*, 12(1):222–229, 2009a. 69, 70

D. Lesage, E.D. Angelini, I. Bloch, and G. Funka-Lea. A review of 3D vessel lumen segmentation techniques: models, features and extraction schemes. *Medical Image Analysis*, 13(6):819–845, 2009b. doi: 10.1016/j.media.2009.07.011. URL http_//dx_doi_org/10_1016/j_media_2009_07_011. 66

C. Li and Y. Sun. Nonrigid registration of myocardial perfusion MRI using pseudo ground truth. *Proceedings of the11th International Conference on Medical Image Com- puting and Computer-Assisted Intervention*, 12(1): 165–172, 2009. 49

H. Li and A. Yezzi. Vessels as 4D Curves: Global Minimal 4D Paths to Extract 3D Tubular Surfaces. In *Proceedings of Computer Vision and Pattern Recognition Workshop*, page 82, 2006. doi: 10.1109/CVPRW.2006.210. 69

P. Libby and P. Theroux. Pathophysiology of coronary artery disease. *Circulation*, 111(25):3481–3488, 2005. doi: 10.1161/CIRCULATIONAHA.105.537878. URL http_//dx_doi_org/10_1161/CIRCULATIONAHA_105_537878. 11

C. Lorenz, S. Renisch, T. Schlathoelter, and T. Buelow. Simultaneous segmentation and tree reconstruction of the coronary arteries in MSCT images. In *Proceedings of SPIE*, volume 5031, page 167. SPIE, 2003. 68, 71

C. Lorenz, J. Lessick, G. Lavi, T. Bulow, and S. Renisch. Fast automatic delineation of cardiac volume of interest in MSCT images. In Fitzpatrick, J.M. & Sonka, M., editor, *Proceedings of SPIE*, volume 5370, pages 456–466, 2004. doi: 10.1117/12.533463. 67

L.M. Lorigo, O.D. Faugeras, W.E.L. Grimson, R. Keriven, R. Kikinis, A. Nabavi, and C.-F. Westin. CURVES: Curve evolution for vessel segmentation. *Medical Image Analysis*, 5(3):195 – 206, 2001. ISSN 1361-8415. doi: DOI:10.1016/S1361-8415(01)00040-8. URL http_//www_sciencedirect_com/science/article/B6W6Y-43T1Y9R-3/_2/229d15c2ca0c7d3bc459a658401722b1. 68

J. Lotjonen, M. Pollari, S. Kivisto, and K. Lauerma. Correction of movement artifacts from 4-D cardiac short-and long-axis MR data. In *Proceedings of the 7th International Conference on Medical Image Computing and Computer-Assisted Intervention*, pages 405–412, 2004. 32, 37

D.G. Lowe. Object recognition from local scale-invariant features. In *Proceedings of the 7th IEEE International Conference on Computer Vision*, volume 2, pages 1150 –1157, 1999. doi: 10.1109/ICCV.1999.790410. 25

B.D. Lucas and T. Kanade. An iterative image registration technique with an application to stereo vision. In *Proceedings of the 7th international joint conference on Artificial intelligence - Volume 2*, pages 674–679. Morgan Kaufmann Publishers Inc., 1981. URL http_//dl_acm_org/citation_cfm?_id=1623264_1623280. 31

M.T. Madsen. A simplified formulation of the gamma variate function. *Physics in Medicine and Biology*, 37(7):1597, 1992. URL http_//stacks_iop_org/0031-9155/37/i=7/a=010. 50

F. Maes, A. Collignon, D. Vandermeulen, G. Marchal, and P. Suetens. Multimodality image registration by maximization of mutual information. *IEEE Trans Med Imaging*, 16(2):187–198, 1997. doi: 10.1109/42.563664. URL http_//dx_doi_org/10_1109/42_563664. 27

F. Maes, D. Vandermeulen, and P. Suetens. Comparative evaluation of multiresolution optimization strategies for multimodality image registration by maximization of mutual information. *Medical Image Analysis*, 3 (4):373 – 386, 1999. ISSN 1361-8415. doi: 10.1016/S1361-8415(99)80030-9. URL http_//www_sciencedirect_com/science/article/_pii/S1361841599800309. 30

A.H. Mahnken, R. Koos, M. Katoh, J.E. Wildberger, E. Spuentrup, A. Buecker, R.W. Guenther, and H.P. Kuehl. Assessment of myocardial viability in reperfused acute myocardial infarction using 16-slice computed tomography in comparison to magnetic resonance imaging. *J Am Coll Cardiol*, 45(12): 2042–2047, 2005. doi: 10.1016/j.jacc.2005.03.035. URL http_//dx_doi_org/10_1016/j_jacc_2005_03_035. 17

A.H. Mahnken, P. Bruners, C.M. Bornikoel, N. Kraemer, and R.W. Guenther. Assessment of myocardial edema by computed tomography in myocardial infarction. *JACC Cardiovasc Imaging*, 2(10):1167–1174, 2009a. doi: 10.1016/j.jcmg.2009.05.014. URL http_//dx_doi_org/10_1016/j_jcmg_2009_05_014. 94, 104

A.H. Mahnken, G. Jost, P. Bruners, M. Sieber, P.R. Seidensticker, R.W. Guenther, and H. Pietsch. Multidetector computed tomography (MDCT) evaluation of myocardial viability: intraindividual comparison of monomeric vs. dimeric contrast media in a rabbit model. *Eur Radiol*, 19(2):290–297, 2009b. doi: 10.1007/s00330-008-1150-3. URL http_//dx_doi_org/10_1007/s00330-008-1150-3. 17

REFERENCES

A.H. Mahnken, P. Bruners, O. Friman, and A. Hennemuth. The culprit lesion and its consequences: combined visualization of the coronary arteries and delayed myocardial enhancement in dual-source CT: a pilot study. *Eur Radiol*, 20(12):2834–2843, 2010a. doi: 10.1007/s00330-010-1864-x. URL http_//dx_doi_org/10_1007/s00330-010-1864-x. 111, 146

A.H. Mahnken, E. Klotz, H. Pietsch, B. Schmidt, T. Allmendinger, U. Haberland, W.A. Kalender, and T. Flohr. Quantitative whole heart stress perfusion CT imaging as noninvasive assessment of hemodynamics in coronary artery stenosis: preliminary animal experience. *Invest Radiol*, 45(6):298–305, 2010b. doi: 10.1097/RLI.0b013e3181dfa3cf. URL http_//dx_doi_org/10_1097/RLI_0b013e3181dfa3cf. 17

T. Makela, Clarysse. P., O. Sipila, N. Pauna, Q.C. Pham, T. Katila, and I.E. Magnin. A review of cardiac image registration methods. *IEEE Trans Med Imaging*, 21(9):1011–1021, 2002. doi: 10.1109/TMI.2002.804441. URL http_//dx_doi_org/10_1109/TMI_2002_804441. 24, 26

S.S. Mao, N. Ahmadi, B. Shah, D. Beckmann, A. Chen, L. Ngo, F.R. Flores, Y.L. Gao, and M.J. Budoff. Normal thoracic aorta diameter on cardiac computed tomography in healthy asymptomatic adults: impact of age and gender. *Acad Radiol*, 15(7):827–834, 2008. doi: 10.1016/j.acra.2008.02.001. URL http_//dx_doi_org/10_1016/j_acra_2008_02_001. 72

R. Mastouri, S.G. Sawada, and J. Mahenthiran. Current noninvasive imaging techniques for detection of coronary artery disease. *Expert Rev Cardiovasc Ther*, 8(1):77–91, 2010. 2

C.M. Matter, M. Stuber, and M. Nahrendorf. Imaging of the unstable plaque: how far have we got? *Eur Heart J*, 30(21):2566–2574, 2009. doi: 10.1093/eurheartj/ehp419. URL http_//dx_doi_org/10_1093/_eurheartj/ehp419. 15

E.H. Meijering, W.J. Niessen, and M.A. Viergever. Quantitative evaluation of convolution-based methods for medical image interpolation. *Medical Image Analysis*, 5(2):111–126, 2001. 32

C. Metz, M. Schaap, A. van der Giessen, T. van Walsum, and W. Niessen. Semi-automatic coronary artery centerline extraction in computed tomography angiography data. In *Proceedings of 4th IEEE International Symposium on Biomedical Imaging: From Nano to Macro*, pages 856 –859, 2007. doi: 10.1109/ISBI.2007.356987. 68, 70

J. Mille and L.D. Cohen. Deformable tree models for 2D and 3D branching structures extraction. In *Proceedings of IEEE Computer Vision and Pattern Recognition Workshops*, pages 149 –156, 2009. doi: 10.1109/CVPRW.2009.5204049. 70

J.M. Miller, C.E. Rochitte, M. Dewey, A. Arbab-Zadeh, H. Niinuma, I. Gottlieb, N. Paul, M.E. Clouse, E.P. Shapiro, J. Hoe, A.C. Lardo, D.E. Bush, A. de Roos, C. Cox, J. Brinker, and J.A.C. Lima. Diagnostic performance of coronary angiography by 64-row CT. *N Engl J Med*, 359(22):2324–2336, 2008. doi: 10.1056/NEJMoa0806576. URL http_//dx_doi_org/10_1056/NEJMoa0806576. 2, 16

J. Milles, R.J. van der Geest, M. Jerosch-Herold, J.H.C. Reiber, and B.P.F. Lelieveldt. Fully automated motion correction in first-pass myocardial perfusion MR image sequences. *IEEE Trans Med Imaging*, 27(11):1611–1621, 2008. doi: 10.1109/TMI.2008.928918. URL http_//dx_doi_org/_10_1109/TMI_2008_928918. 49, 54, 61

M. Mischi, J. den Boer, and H. Korsten. On the physical and stochastic representation of an indicator dilution curve as a gamma variate. *Physiol Meas*, 29(3):281–294, 2008. doi: 10.1088/0967-3334/29/3/001. URL http_//dx_doi_org/10_1088/0967-3334/29/3/001. 50

M. Muehling, O.and Jerosch-Herold, M. Naebauer, and N. Wilke. Assessment of Ischemic Heart Disease Using Magnetic Resonance First-Pass Perfusion Imaging. *Herz*, 28(2):82–89, 2003. 116

D. Mueller and A. Maeder. Robust semi-automated path extraction for visualising stenosis of the coronary arteries. *Computerized Medical Imaging and Graphics*, 32(6):463 – 475, 2008. ISSN 0895-6111. doi: DOI:10.1016/j.compmedimag.2008.05.003. URL http_//www_sciencedirect_com/science/article/B6T5K-4SXRYBW-1/_2/bcd74cbf857dff5797e3e1a3adaa95bb. 68

H.-H. Nagel. Displacement vectors derived from second-order intensity variations in image sequences. *Computer Vision, Graphics, and Image Processing*, 21(1):85 – 117, 1983. ISSN 0734-189X. doi: 10.1016/S0734-189X(83)80030-9. URL http_//www_sciencedirect_com/science/article/_pii/S0734189X83800309. 31

D. Nain, A. Yezzi, and G. Turk. Vessel Segmentation Using A Shape Driven Flow. In *Proceedings of the 7th International Conference on Medical Image Computing and Computer-Assisted Intervention*, pages 51–59, 2004. 68

T. Nakaura, D. Utsunomiya, S. Shiraishi, S. Tomiguchi, T. Honda, H. Ogawa, K. Awai, and Y. Yamashita. Three-dimensional cardiac image fusion using new CT angiography and SPECT methods. *Am J Roentgenol*, 185(6):1554–1557, 2005. doi: 10.2214/AJR.04.1401. URL http_//dx_doi_org/_10_2214/AJR_04_1401. 126

J.A. Nelder and R. Mead. A simplex method for function minimization. *Computer Journal*, 7(4):308–313, 1965. 30, 37

R.W. Nesto and G.J. Kowalchuk. The ischemic cascade: temporal sequence of hemodynamic, electrocardiographic and symptomatic expressions of ischemia. *Am J Cardiol*, 59(7):23–30, 1987. 12

B. Neyran, M.F. Janier, C. Casali, D. Revel, and E.P. Canet Soulas. Mapping myocardial perfusion with an intravascular MR contrast agent: robustness of deconvolution methods at various blood flows. *Magn Reson Medicine*, 48 (1):166–179, 2002. 115

T.D. Nguyen, P. Spincemaille, J.W. Weinsaft, B.Y. Ho, M.D. Cham, M.R. Prince, and Y. Wang. A fast navigator-gated 3D sequence for delayed enhancement MRI of the myocardium: comparison with breathhold 2D imaging. *J Magn Reson Imaging*, 27(4):802–808, 2008. doi: 10.1002/jmri.21296. URL http_//dx_doi_org/10_1002/jmri_21296. 150

G. Niccoli, F. Burzotta, L. Galiuto, and F. Crea. Myocardial no-reflow in humans. *J Am Coll Cardiol*, 54(4):281–292, 2009. doi: 10.1016/j.jacc.2009.03.054. URL http_//dx_doi_org/10_1016/j_jacc_2009_03_054. 15

N. Noble, D. Hill, M. Breeuwer, and R. Razavi. The Automatic Identification of Hibernating Myocardium. In *Proceedings of the 7th International Conference on Medical Image Computing and Computer-Assisted Intervention (MICCAI'04)*, pages 890–898, 2004. 93

J. Nocedal and S.J. Wright. *Numerical Optimization*. Springer, 2 edition, 2006. 30

T.P. O'Donnell, N. Xu, R.M. Setser, and R.D. White. Semi-automatic segmentation of nonviable cardiac tissue using cine and delayed enhancement magnetic resonance images. *Proceedings of SPIE*, 5031:242, 2003. 93

S. Oeltze, F. Grothues, A. Hennemuth, and B. Preim. Integrated Visualization of Morphologic and Perfusion Data for the Analysis of Coronary Artery Disease. In *Eurographics / IEEE VGTC Symposium on Visualization*, volume 6, pages 131–138, 2006. 126

S. Oeltze, A. Hennemuth, S. Glasser, C. Kuehnel, and B. Preim. Glyph-Based Visualization of Myocardial Perfusion Data and Enhancement with Contractility and Viability Information. In *VCBM*, pages 11–20, 2008. 130

S.D. Olabarriaga, M. Breeuwer, and W.J. Niessen. Evaluation of Hessian-based filters to enhance the axis of coronary arteries in CT images. In *Proceedings of the 17th International Congress on Computer Assisted Radiology and Surgery*, volume 1256, pages 1191 – 1196, 2003. doi: DOI:10.1016/S0531-5131(03)00307-8. URL http_//www_sciencedirect_com/science/article/B7581-48PK9S7-6S/_2/6d54dd6c27e4cac4d8707c2a93425dd0. CARS 2003. Computer Assisted Radiology and Surgery. Proceedings of the 17th International Congress and Exhibition. 68, 69

J.T. Ortiz-Perez, J. Rodriguez, S.N. Meyers, D.C. Lee, C. Davidson, and E. Wu. Correspondence between the 17-segment model and coronary arterial anatomy using contrast-enhanced cardiac magnetic resonance imaging. *JACC Cardiovasc Imaging*, 1(3):282–293, 2008. doi: 10.1016/j.jcmg.2008.01.014. URL http_//dx_doi_org/10_1016/j_jcmg_2008_01_014. 3, 137

L. Ostergaard, R.M. Weisskoff, D.A. Chesler, C. Gyldensted, and B.R. Rosen. High resolution measurement of cerebral blood flow using intravascular tracer bolus passages. Part I: Mathematical approach and statistical analysis. *Magn Reson Med*, 36(5):715–725, 1996. 117

K. Palagyi and A. Kuba. A 3D 6-subiteration thinning algorithm for extracting medial lines. *Pattern Recognition Letters*, 19(7):613 – 627, 1998. ISSN 0167-8655. doi: DOI:10.1016/S0167-8655(98)00031-2. URL http_//www_sciencedirect_com/science/article/_B6V15-3VW2XHV-Y/2/b6898bd5daab16f3fffad044c80c955e. 70

M. Pechaud, I. Vanzetta, T. Deneux, and R. Keriven. Sift-based sequence registration and flow-based cortical vessel segmentation applied to high resolution optical imaging data. In *Proceedings of 5th IEEE International Symposium on Biomedical Imaging: From Nano to Macro*, pages 720 –723, 2008. doi: 10.1109/ISBI.2008.4541097. 26

C.A. Pelizzari, G.T. Chen, D.R. Spelbring, R.R. Weichselbaum, and C.T. Chen. Accurate three-dimensional registration of CT, PET, and/or MR images of the brain. *J Comput Assist Tomogr*, 13(1):20–26, 1989. 25

O. Pereztol-Valdes, J. Candell-Riera, C. Santana-Boado, J. Angel, S. Aguade-Bruix, J. Castell-Conesa, E.V. Garcia, and J. Soler-Soler. Correspondence between left ventricular 17 myocardial segments and coronary arteries. *Eur Heart J*, 26(24):2637–2643, 2005. doi: 10.1093/eurheartj/ehi496. 9, 121, 137

D. Perperidis, A. Rao, R. Mohiaddin, and D. Rueckert. Non-rigid Spatio-Temporal Alignment of 4D Cardiac MR Images. In J. Gee, J. Maintz, and M. Vannier, editors, *Biomedical Image Registration*, volume 2717 of *Lecture Notes in Computer Science*, pages 191–200. Springer Berlin / Heidelberg, 2003. ISBN 978-3-540-20343-8. 29

D. Peukert, M. Laule, M. Taupitz, N. Kaufels, B. Hamm, and M. Dewey. 3D and 2D delayed-enhancement magnetic resonance imaging for detection of myocardial infarction: preclinical and clinical results. *Acad Radiol*, 14(7):788–794, 2007. doi: 10.1016/j.acra.2007.03.006. URL http_//dx_doi_org/10_1016/j_acra_2007_03_006. 150

N.H.J. Pijls, W.F. Fearon, P.A.L. Tonino, U. Siebert, F. Ikeno, B. Bornschein, M. van't Veer, V. Klauss, G. Manoharan, T. Engstrom, K.G. Oldroyd, P.N. Ver Lee, P.A. MacCarthy, B. De Bruyne, and F. A. M. E. Study Investigators. Fractional flow reserve versus angiography for guiding percutaneous coronary intervention in patients with multivessel coronary artery disease: 2-year follow-up of the FAME (Fractional Flow Reserve Versus Angiography for Multivessel Evaluation) study. *J Am Coll Cardiol*, 56(3):177–184, 2010. 2

J. Pintaske, P. Martirosian, H. Graf, G. Erb, K.-P. Lodemann, C.D. Claussen, and F. Schick. Relaxivity of Gadopentetate Dimeglumine (Magnevist), Gadobutrol (Gadovist), and Gadobenate Dimeglumine (MultiHance) in human blood plasma at 0.2, 1.5, and 3 Tesla. *Invest Radiol*, 41(3):213–221, 2006. doi: 10.1097/01.rli.0000197668.44926.f7. URL http_//dx_doi_org/_10_1097/01_rli_0000197668_44926_f7. 51

S. Plein, J.P. Ridgway, T.R. Jones, T.N. Bloomer, and M.U. Sivananthan. Coronary artery disease: assessment with a comprehensive MR imaging protocol–initial results. *Radiology*, 225(1):300–307, 2002. 18

V. Positano, M. Santarelli, A. Pingitore, M. Lombardi, L. Landini, and A. Benassi. Quantitative 3D assessment of myocardial viability with MRI delayed contrast enhancement. In *Proceedings of the 30th Annual Conference on Computers in Cardiology*, pages 629–632, 2003a. doi: 10.1109/CIC.2003.1291234. 93

V. Positano, M.F. Santarelli, and L. Landini. Automatic Characterization of Myocardial Perfusion in Contrast Enhanced MRI. *EURASIP Journal on Applied Signal Processing*, 2003(5):413–421, 2003b. 116

V. Positano, A. Pingitore, A. Giorgetti, B. Favilli, M. Santarelli, L. Landini, P. Marzullo, and M. Lombardi. A Fast and Effective Method to Assess Myocardial Necrosis by Means of Contrast Magnetic Resonance Imaging. *Journal of Cardiovascular Magnetic Resonance*, 7(2):487–494, 2005. 93

V. Positano, A. Pingitore, B. Scattini, M.F. Santarelli, D. De Marchi, B. Favilli, M. Lombardi, and L. Landini. Myocardial perfusion by first pass contrast magnetic resonance: a robust method for quantitative regional assessment of perfusion reserve index. *Heart*, 92(5):689–690, 2006. 116

M.J.D. Powell. An efficient method for finding the minimum of a function of several variables without calculating derivatives. *The Computer Journal*, 7(2):155–162, 1964. doi: 10.1093/comjnl/7.2.155. URL http_//comjnl_oxfordjournals_org/content/7/2/155_abstract. 30

L.R. Ramos-Duran, J.F. Kalafut, M. Hanley, and U.J. Schoepf. Current contrast media delivery strategies for cardiac and pulmonary multidetector-row computed tomography angiography. *J Thorac Imaging*, 25(4):270–277, 2010. doi: 10.1097/RTI.0b013e3181efe8b0. URL http_//dx_doi_org/10_1097/RTI_0b013e3181efe8b0. 72

J. Rexilius, J.-M. Kuhnigk, H.K. Hahn, and H.-O. Peitgen. An Application Framework for Rapid Prototyping of Clinically Applicable Software Assistants. In *GI Jahrestagung*, pages 522–528, 2006. 130

C. Ritter, A. Brackertz, J. Sandstede, M. Beer, D. Hahn, and H. Koestler. Absolute quantification of myocardial perfusion under adenosine stress. *Magnetic Resonance in Medicine*, 56(4):844–849, 2006. ISSN 1522-2594. doi: 10.1002/mrm.21020. URL http_//dx_doi_org/10_1002/mrm_21020. 115, 116

W.J. Rogers, E.P. Shapiro, J.L. Weiss, M.B. Buchalter, F.E. Rademakers, M.L. Weisfeldt, and E.A. Zerhouni. Quantification of and correction for left ventricular systolic long-axis shortening by magnetic resonance tissue tagging and slice isolation. *Circulation*, 84(2):721–731, 1991. 41

R. Rohr, H.S. Stiehl, R. Sprengel, T.M. Buzug, J. Weese, and M.H. Kuhn. Landmark-based elastic registration using approximating thin-plate splines. *IEEE Trans Med Imaging*, 20(6):526–534, 2001. doi: 10.1109/42.929618. URL http_//dx_doi_org/10_1109/42_929618. 29

A. Rosset, L. Spadola, L. Pysher, and O. Ratib. Informatics in radiology (infoRAD): navigating the fifth dimension: innovative interface for multidimensional multimodality image navigation. *Radiographics*, 26(1):299–308, 2006. doi: 10.1148/rg.261055066. URL http_//dx_doi_org/10_1148/_rg_261055066. 125

J.M. Rouet, J.J. Jacq, and C. Roux. Genetic algorithms for a robust 3-D MR-CT registration. *IEEE Trans Inf Technol Biomed*, 4(2):126–136, 2000. 31

N. Rougon, A. Discher, and F. Preteux. Region-driven statistical non-rigid registration: application to model-based segmentation and tracking of the heart in perfusion MRI. In *Proceedings of SPIE*, volume 5916, pages 148–159, 2005. URL http_//www-artemis_int-evry_fr/Publications/_library/Rougon-SPIE-SanDiego2005-5916-15_pdf. 33

D. Rueckert, L.I. Sonoda, C. Hayes, D.L. Hill, and M.O. Leach. Nonrigid registration using free-form deformations: application to breast MR images. *IEEE Trans Med Imaging*, 18 1999. ISSN 29

M. Saeed, G. Lund, M. F. Wendland, J. Bremerich, H. Weinmann, and C.B. Higgins. Magnetic resonance characterization of the peri-infarction zone of reperfused myocardial infarction with necrosis-specific and extracellular nonspecific contrast media. *Circulation*, 103(6):871–876, 2001. 3

D. Saering, J. Ehrhardt, A. Stork, P.M. Bansmann, G. Lund, and H. Handels. Analysis of the Left Ventricle after Myocardial Infarction combining 4D Cine-MR and 3D DE-MR Image Sequences. In *Bildverarbeitung fuer die Medizin*, pages 56–60, 2006. 94

E.J. Sainsbury and J.J. Ashley. Curve-fitting in pharmacokinetics–a comparison between gamma- and biexponential fits. *Eur J Clin Pharmacol*, 30(2):243–244, 1986. 116

S. Saur, C. Kuehnel, G. Szekely, and P. Cattin. Automatic Ascending Aorta Detection in CTA Datasets. In T. Tolxdorff, J. Braun, T.M. Deserno, H. Handels, A. Horsch, and H.P. Meinzer, editors, *Bildverarbeitung für die Medizin*, pages 323–327. Springer-Verlag, 2008. 67

REFERENCES

M. Schaap, C.T. Metz, T. van Walsum, A.G. van der Giessen, A.C. Weustink, N.R. Mollet, C. Bauer, H. Bogunovic, C. Castro, X. Deng, E. Dikici, T. O'Donnell, M. Frenay, O. Friman, M. Hernandez Hoyos, P.H. Kitslaar, K. Krissian, C. Kuehnel, M.A. Luengo-Oroz, M. Orkisz, O. Smedby, M. Styner, A. Szymczak, H. Tek, C. Wang, S.K. Warfield, S. Zambal, Y. Zhang, G.P. Krestin, and W.J. Niessen. Standardized evaluation methodology and reference database for evaluating coronary artery centerline extraction algorithms. *Medical Image Analysis*, 13(5):701–714, Oct 2009a. doi: 10.1016/j.media.2009.06.003. URL http_//dx_doi_org/10_1016/j_media_2009_06_003. 70, 87

M. Schaap, L. Neefjes, C. Metz, A. van der Giessen, A. Weustink, N. Mollet, J. Wentzel, T.W. van Walsum, and W. Niessen. Coronary lumen segmentation using graph cuts and robust kernel regression. *Inf Process Med Imaging*, 21:528–539, 2009b. 70

A. Schenk, G. Prause, and H.-O. Peitgen. Efficient Semiautomatic Segmentation of 3D Objects in Medical Images. In *Proceedings of the 3rd International Conference on Medical Image Computing and Computer-Assisted Intervention*, pages 186–195, 2000. 95, 117, 134

C. Schmid, R. Mohr, and C. Bauckhage. Evaluation of Interest Point Detectors. *Int. J Comput Vision*, 37:151–172, 2000. ISSN 0920-5691. doi: 10.1023/A:1008199403446. URL http_//dl_acm_org/citation_cfm?id=350676_350678. 25

M. Schmitt, O.K. Mohrs, S.E. Petersen, K.F. Kreitner, T. Voigtlander, T. Wittlinger, G. Horstick, S. Ziegler, J. Meyer, M. Thelen, and W.G. Schreiber. Evaluation of myocardial perfusion reserve in patients with CAD using contrast-enhanced MRI: a comparison between semiquantitative and quantitative methods. *RoeFo - Fortschritte auf dem Gebiet der Roentgenstrahlen und der bildgebenden Verfahren*, 174(2):187–195, 2002. 116

J. Schwitter. Myocardial perfusion. *J Magn Reson Imaging*, 24(5):953–963, 2006. doi: 10.1002/jmri.20753. 115

A.D. Scott, J. Keegan, and D.N. Firmin. Motion in cardiovascular MR imaging. *Radiology*, 250(2):331–351, 2009. doi: 10.1148/radiol.2502071998. URL http_//dx_doi_org/10_1148/radiol_2502071998. 21

A. Seeger, A. Hennemuth, B. Klumpp, M. Fenchel, U. Kramer, C. Bretschneider, S. Mangold, A.E. May, C.D. Claussen, H.-O. Peitgen, and S. Miller. Fusion of MR coronary angiography and viability imaging: Feasibility and clinical value for the assignment of myocardial infarctions. *Eur J Radiol*, 81(1):71–76, 2011. doi: 10.1016/j.ejrad.2010.12.005. URL http_//dx_doi_org/10_1016/j_ejrad_2010_12_005. 138, 146

D. Selle. *Analyse von Gefaessstrukturen in medizinischen Schichtdatensaetzen fuer die computergestuetzte Operationsplanung.* PhD thesis, University of Bremen, 1999. 79

D. Selle, B. Preim, A. Schenk, and H.O. Peitgen. Analysis of vasculature for liver surgical planning. *IEEE Trans on Med Imaging*, 21(11):1344–1357, 2002. 79

R. Setser, T. O'Donnell, N. Smedira, J. Sabik, S. Halliburton, A. Stillman, and R. White. Coregistered MR imaging myocardial viability maps and multidetector row CT coronary angiography displays for surgical revascularization planning: initial experience. *Radiology*, 237(2):465–473, 2005. doi: 10.1148/radiol.2372040236. 33

D.J. Shah, R.M. Judd, and R.J. Kim. Technology insight: MRI of the myocardium. *Nat Clin Pract Cardiovasc Med*, 2(11):597–605; quiz 606, 2005. doi: 10.1038/ncpcardio0352. URL http_//dx_doi_org/10_1038/ncpcardio0352. 20

S. Sinha, U. Sinha, J. Czernin, G. Porenta, and H.R. Schelbert. Noninvasive assessment of myocardial perfusion and metabolism: feasibility of registering gated MR and PET images. *Am J Roentgenol*, 164(2):301–307, 1995. 25

P.J. Slomka, G.A. Hurwitz, J. Stephenson, and T. Cradduck. Automated alignment and sizing of myocardial stress and rest scans to three-dimensional normal templates using an image registration algorithm. *J Nucl Med*, 36(6):1115–1122, 1995. 26

R. Smolíková-Wachowiak, M. Wachowiak, A. Fenster, and M. Drangova. Registration of Two-Dimensional Cardiac Images to Preprocedural Three-Dimensional Images for Interventional Applications. *Journal of Magnetic Resonance Imaging*, 22(2):219–228, 2005. 33, 37

L. Spreeuwers and M. Breeuwer. Automatic Detection of Myocardial Boundaries in MR Cardio Perfusion Images. In *Proceedings of the 4th International Conference on Medical Image Computing and Computer-Assisted Intervention*, pages 1228–1231, 2001. 40, 49

M.B. Stegmann, H. Ólafsdóttir, and H.B.W. Larsson. Unsupervised motion-compensation of multi-slice cardiac perfusion MRI. *Medical Image Analysis*, 9(4):394–410, 2005. 33

P. Stolzmann, H. Alkadhi, H. Scheffel, A. Hennemuth, C. Kuehnel, S. Baumueller, S. Kozerke, V. Falk, B. Marincek, and O.F. Donati. Image fusion of coronary CT angiography and cardiac perfusion MRI: a pilot study. *Eur Radiol*, 20(5):1174–1179, 2010. doi: 10.1007/s00330-010-1746-2. URL http_//dx_doi_org/10_1007/s00330-010-1746-2. 142

C Studholme and D Hill, D.and Hawkes. An overlap invariant entropy measure of 3D medical image alignment. *Pattern Recognition*, 32:71–86, 1999. 27, 37

K.A. Sturm, B.and Powell and A.E. Stillman. Registration of 3D CT angiography and cardiac MR images in coronary artery disease patients. *Int J Cardiovasc Imaging*, 19(4):281–293, 2003. ISSN 33

A. Suinesiaputra, L. Florack, J.J.M. Westenberg, B.M. ter Haar Romeny, J.H.C. Reiber, and B.P.F. Lelieveldt. Optic Flow Computation from Cardiac MR Tagging Using a Multiscale Differential Method: A Comparative Study with Velocity-Encoded MRI. In *Proceedings of the 6th International Conference on Medical Image Computing and Computer-Assisted Intervention*, pages 483–490, 2003. 31

Y. Sun, M. Jolly, and J. Moura. Contrast-Invariant Registration of Cardiac and Renal MR Perfusion Images. In *Proceedings of the 7th International Conference on Medical Image Computing and Computer-Assisted Intervention*, pages 903–910, 2004. 32, 33

C. Swingen, R.T. Seethamraju, and M. Jerosch-Herold. An approach to the three-dimensional display of left ventricular function and viability using MRI. *Int J Cardiovasc Imaging*, 19(4):325–336, 2003. 33

A. Szymczak. Vessel tracking by connecting the dots. *The Midas Journal*, 2008 MICCAI Workshop - Grand Challenge Coronary Artery Tracking.:1406, 2008. URL http_//hdl_handle_net/10380/1406. 70

A. Szymczak, A. Tannenbaum, and K. Mischaikow. Coronary vessel cores from 3D imagery: a topological approach. In J.M. Fitzpatrick and J.M. Reinhardt, editors, *Proceedings of SPIE*, volume 5747, pages 505–513. SPIE, 2005. doi: 10.1117/12.593837. 70

Q. Tao, J. Milles, K. Zeppenfeld, H.J. Lamb, J.J. Bax, J.H.C. Reiber, and R.J. van der Geest. Automated segmentation of myocardial scar in late enhancement MRI using combined intensity and spatial information. *Magn Reson Med*, 64(2):586–594, 2010. doi: 10.1002/mrm.22422. URL http_//dx_doi_org/_10_1002/mrm_22422. 94, 114

L. Tautz, A. Hennemuth, M. Andersson, A. Seeger, H. Knutsson, and O. Friman. Phase-based non-rigid registration of myocardial perfusion MRI image sequences. In *Proceedings of IEEE International Symposium on Biomedical Imaging: From Nano to Macro*, pages 516 – 519, 2010. doi: 10.1109/ISBI.2010.5490297. URL http_//ieeexplore_ieee_org/xpl/freeabs_all_jsp?arnumber=5490297. 45, 47, 49

A.J. Taylor, M. Cerqueira, J.M. Hodgson, D. Mark, J. Min, P. O'Gara, G.D. Rubin, American College of Cardiology Foundation Appropriate Use Criteria Task Force, Society of Cardiovascular Computed Tomography, American College of Radiology, American Heart Association, American Society of Echocardiography, American Society of Nuclear Cardiology, North American Society for Cardiovascular Imaging, Society for Cardiovascular Angiography and Interventions, and Society for Cardiovascular Magnetic Resonance. ACCF/SCCT/ACR/AHA/ASE/ASNC/NASCI/SCAI/SCMR 2010 Appropriate Use Criteria for Cardiac Computed Tomography. . *Circulation*, 122(21):e525–e555, 2010. doi: 10.1161/CIR.0b013e3181fcae66. URL http_//dx_doi_org/10_1161/CIR_0b013e3181fcae66. 17

H. Tek, M.A. Gulsun, S. Laguitton, L. Grady, D. Lesage, and G. Funka-Lea. Automatic coronary tree modeling. *The Midas Journal*, 2008 MICCAI Workshop – Grand Challenge Coronary Artery Tracking.: <http://hdl.handle.net/10380/1426>, 2008. 68, 71

M. Termeer, J.O. Bescos, M. Breeuwer, A. Vilanova, F. Gerritsen, and E. Groeller. CoViCAD: comprehensive visualization of coronary artery disease. *IEEE Trans Vis Comput Graph*, 13(6):1632–1639, 2007. doi: 10.1109/TVCG.2007.70550. URL http_//dx_doi_org/10_1109/TVCG_2007_70550. 126, 127

M. Termeer, J.O. Bescós, M. Breeuwer, A. Vilanova, F. Gerritsen, E. Gröller, and E. Nagel. Visualization of Myocardial Perfusion Derived from Coronary Anatomy. *IEEE Trans Vis Comput Graph*, 14(6):1595–1602, 2008. ISSN 1077-2626. URL http_//www_cg_tuwien_ac_at/research/publications/_2008/termeer-2008-vis/. 147

H.K. Thompson, C.F. Starmer, R.E. Whalen, and H.D. McIntosh. Indicator Transit Time Considered as a Gamma Variate. *Circ Res*, 14:502–515, 1964. 50, 116

C. Tobon-Gomez, F.M. Sukno, C. Butakoff, M. Huguet, and A.F. Frangi. Simulation of late gadolinium enhancement cardiac magnetic resonance studies. *Conf Proc IEEE Eng Med Biol Soc*, 2010:1469–1472, 2010. doi: 10.1109/IEMBS.2010.5626854. URL http_//dx_doi_org/10_1109/IEMBS_2010_5626854. 123

P.A.L. Tonino, B. De Bruyne, N.H.J. Pijls, U. Siebert, F. Ikeno, M. van' t Veer, V. Klauss, G. Manoharan, T. Engstrom, K.G. Oldroyd, P.N. Ver Lee, P.A. MacCarthy, W.F. Fearon, and F. A. M. E. Study Investigators. Fractional flow reserve versus angiography for guiding percutaneous coronary intervention. *N Engl J Med*, 360(3):213–224, 2009. doi: 10.1056/NEJMoa0807611. URL http_//dx_doi_org/10_1056/NEJMoa0807611. 122

C. Toumoulin, C. Boldak, M. Garreau, and D. Boulmier. Coronary characterization in multi-slice computed tomography. In *Proceedings of Computers in Cardiology*, pages 749 – 752, 2003. doi: 10.1109/CIC.2003.1291264. 68

M. Tsukiji, P. Nguyen, G. Narayan, J. Hellinger, F. Chan, R. Herfkens, J.M. Pauly, M.V. McConnell, and P.C. Yang. Peri-infarct ischemia determined by cardiovascular magnetic resonance evaluation of myocardial viability and stress perfusion predicts future cardiovascular events in patients with severe ischemic cardiomyopathy. *J Cardiovasc Magn Reson*, 8(6):773–779, 2006. doi: 10.1080/10976640600737615. 3

M. Unser, A. Aldroubi, and M. Eden. Fast B-spline transforms for continuous image representation and interpolation. *IEEE Transactions on Pattern Analysis and Machine Intelligence*, 13(3):277 –285, 1991. ISSN 0162-8828. doi: 10.1109/34.75515. 29

S. W. M. van den Borne, J. Diez, W. M. Blankesteijn, J. Verjans, L. Hofstra, and J. Narula. Myocardial remodeling after infarction: the role of myofibroblasts. *Nat Rev Cardiol*, 7(1):30–37, 2010. 13

A. Vasilevskiy and K. Siddiqi. Flux maximizing geometric flows. *IEEE Transactions on Pattern Analysis and Machine Intelligence*, 24(12):1565 – 1578, 2002. ISSN 0162-8828. doi: 10.1109/TPAMI.2002.1114849. 68

J. Velut, C. Toumoulin, and J.-L. Coatrieux. 3D coronary structure tracking algorithm with regularization and multiple hypotheses in MRI. In *Proceedings of IEEE International Symposium on Biomedical Imaging: From Nano to Macro*, pages 37 –40, 2010. doi: 10.1109/ISBI.2010.5490421. 69

M.P. Wachowiak, R. Smolikova, Yufeng Zheng, J.M. Zurada, and A.S. Elmaghraby. An approach to multimodal biomedical image registration utilizing particle swarm optimization. *IEEE Transactions on Evolutionary Computation*, 8(3):289 – 301, 2004. ISSN 1089-778X. doi: 10.1109/TEVC.2004.826068. 31

M. Wagner, R. Roesler, A. Lembcke, C. Butler, M. Dewey, M. Laule, A. Huppertz, C. Schwenke, C. Warmuth, M. Rief, B. Hamm, and M. Taupitz. Whole-heart coronary magnetic resonance angiography at 1.5 Tesla: does a blood-pool contrast agent improve diagnostic accuracy? *Invest Radiol*, 46(3):152–159, 2011. doi: 10.1097/RLI.0b013e3181fac6ef. URL http_//dx_doi_org/10_1097/RLI_0b013e3181fac6ef. 22

C. Wang and O. Smedby. An Automatic Seeding Method For Coronary Artery Segmentation and Skeletonization in CTA. *The Midas Journal*, 2008 MICCAI Workshop – Grand Challenge Coronary Artery Tracking.:126, 2008. URL http_//coronary_bigr_nl/pdf/124_wang_pdf. 67, 91, 123

W.M. Wells, P. Viola, H. Atsumi, S. Nakajima, and R. Kikinis. Multi-modal volume registration by maximization of mutual information. *Medical Image Analysis*, 1(1):35–51, 1996. 27

S. Wesarg and E.A. Firle. Segmentation of vessels: the corkscrew algorithm. *Proceedings of SPIE*, 5370:1609–1620, 2004. 69

O. Wink, W.J. Niessen, and M.A. Viergever. Minimum cost path determination using a simple heuristic function . In *Proceedings of the15th International Conference on Pattern Recognition*, volume 3, pages 998 –1001 vol.3, 2000. doi: 10.1109/ICPR.2000.903713. 69

O. Wink, A.F. Frangi, B. Verdonck, M.A. Viergever, and W.J. Niessen. 3D MRA coronary axis determination using a minimum cost path approach. *Magn Reson Med*, 47(6):1169–1175, 2002. doi: 10.1002/mrm.10164. URL http_//dx_doi_org/10_1002/mrm_10164. 68

G. Wollny, M.J. Ledesma-Carbayo, P. Kellman, and A. Santos. Non-rigid motion compensation in free-breathing myocardial perfusion magnetic resonance imaging. In *Proceedings of Computers in Cardiology*, pages 465 –468, 2008. doi: 10.1109/CIC.2008.4749079. 28

World Health Organization. Global Health Observatory: Causes of death in 2008, 2011. URL http_//www_who_int/gho/mortality_burden_disease/causes_death_2008/en/index_html. 1

S. Wörz and K. Rohr. Segmentation and Quantification of Human Vessels Using a 3-D Cylindrical Intensity Model. *IEEE Transactions on Image Processing*, 16(8):1994–2004, 2007. 69

O. Wu, L. Ostergaard, R.M. Weisskoff, T. Benner, B.R. Rosen, and A.G. Sorensen. Tracer arrival timing-insensitive technique for estimating flow in MR perfusion-weighted imaging using singular value decomposition with a block-circulant deconvolution matrix. *Magn Reson Med*, 50(1):164–174, 2003. doi: 10.1002/mrm.10522. URL http_//dx_doi_org/10_1002/_mrm_10522. 117

H. Xue, J. Guehring, L. Srinivasan, S. Zuehlsdorff, K. Saddi, C. Chefdhotel, J.V. Hajnal, and D. Rueckert. Evaluation of rigid and non-rigid motion compensation of cardiac perfusion MRI. *Proceedings of the 11th International Conference on Medical Image Computing and Computer-Assisted Intervention*, 11(2):35–43, 2008. 49, 52, 60

A. Yan, A. Shayne, K. Brown, S.N. Gupta, C. Chan, T. Luu, M. Carli, H. Reynolds, W. Stevenson, and R. Kwong. Characterization of the peri-infarct zone by contrast-enhanced cardiac magnetic resonance imaging is a powerful predictor of post-myocardial infarction mortality. *Circulation*, 114(1):32–39, 2006. 3, 93

C. Yang and G. Medioni. Object modelling by registration of multiple range images. *Image and Vision Computing*, 10(3):145 – 155, 1992. ISSN 0262-8856. doi: 10.1016/0262-8856(92)90066-C. URL http_//www_sciencedirect_com/science/article/pii/026288569290066C. 25

G. Yang, J. Zhou, D. Boulmier, M.-P. Garcia, L. Luo, and C. Toumoulin. Characterization of 3-D coronary tree motion from MSCT angiography. *IEEE Trans Inf Technol Biomed*, 14(1):101–106, 2010. doi: 10.1109/TITB.2009.2032333. URL http_//dx_doi_org/10_1109/TITB_2009_2032333. 16

Y. Yang, A. Tannenbaum, D. Giddens, and W. Coulter. Knowledge-based 3D segmentation and reconstruction of coronary arteries using CT images. *Conf Proc IEEE Eng Med Biol Soc*, 3:1664–1666, 2004. doi: 10.1109/IEMBS.2004.1403502. URL http_//dx_doi_org/10_1109/IEMBS_2004_1403502. 69

S. Zambal, J. Hladuvka, A. Kanitsar, and K. Buehler. Shape and Appearance Models for Automatic Coronary Artery Tracking. *Insight Journal*, 2008. URL http_//hdl_handle_net/1926/1926/1420. 68, 69, 71

REFERENCES

Y. Zheng, M. John, R. Liao, J. Boese, U. Kirschstein, B. Georgescu, S.K. Zhou, J. Kempfert, T. Walther, G. Brockmann, and D. Comaniciu. Automatic aorta segmentation and valve landmark detection in C-arm CT: application to aortic valve implantation. *Proceedings of the 13th International Conference on Medical Image Computing and Computer-Assisted Intervention*, 13(1): 476–483, 2010a. 89, 91

Y. Zheng, F. Vega-Higuera, S.K. Zhou, and D. Comaniciu. Fast and automatic heart isolation in 3D CT volumes: optimal shape initialization. In *Proceedings of the first international conference on machine learning in medical imaging*, MLMI'10, pages 84–91, Berlin, Heidelberg, 2010b. Springer-Verlag. ISBN 3-642-15947-8, 978-3-642-15947-3. URL http_//portal_acm_org/citation_cfm?id=1889135_1889146. 68

C. Zhou, H.-P. Chan, A. Chughtai, S. Patel, L.M. Hadjiiski, B. Sahiner, J. Wei, and E.A. Kazerooni. Automated segmentation and tracking of coronary arteries in cardiac CT scans: comparison of performance with a clinically used commercial software. In N. Karssemeijer and R.M. Summers, editors, *Proceedings of the SPIE*, volume 7624, page 76240O. SPIE, 2010. doi: 10.1117/12.844391. URL http_//link_aip_org/link/?PSI/7624/76240O/1. 68